An Open-architecture Laser Powder Bed Fusion System and its use for In-situ Process Measurements

Prveen Bidare

Submitted for the degree of Doctor of Philosophy

Heriot-Watt University

School of Engineering and Physical Sciences

June 2018

Abstract

Design and development of an open-architecture laser powder bed fusion (LPBF) system for in-situ process measurements of the build process during additive manufacture is described. The aim of this work is to create new knowledge and contribute towards further understanding of complex laser powder interaction through in-situ process monitoring. The designed system is sufficiently automated to enable single tracks and high density multiple layer components to be built. It is easily transportable to enable measurements at different measurement facilities and its modular design enables straightforward modification for specific measurements to be made. The system produces components with >99% density, hence, the build conditions are representative to observe process fundamentals and to develop process control strategies.

Open-architecture design enabled access to the build area allowing a range of in-situ measurements such as high energy flash x-ray imaging, camera-based high-speed imaging, schlieren imaging and temperature measurements. High speed imaging of the LPBF process results reveal that the process is more dynamic than is generally appreciated and can involve considerable motion of powder particles and agglomerates in and above the powder bed. Many critical process regimes were observed for the first time, such as changes in inclination of the laser with varying power and scan speed; and denudation became less severe with respects to an increase in layer number. Schlieren imaging results enabled the visualisation of the argon gas flow and laser plume propagation in the atmosphere above the powder bed.

In-situ monitoring has been extended to study the effect of ambient pressures from a high vacuum to 5 bar positive pressure on the LPBF. Considerable disruption to the powder bed is observed at pressures below 20 mbar. As the pressure decreases, the expansion of the laser plume prevents particles reaching the melt pool: profiles and cross-sections of the track reveal a drastic reduction in its cross-sectional area. At above atmospheric pressure, argon (up to 5 bar), the process was further disrupted by severe plasma formation along with an increase in size and number of spatter. The particle entrainment and resulting denudation was reduced, and single-track continuity was enhanced. In further study, it has been found that helium, used as shielding gas at higher pressure, mitigates negative effects of argon; generates smooth and uniform tracks and islands. The smoothness and continuity of built layers at 5 bar in helium was comparable to argon at atmospheric pressure, with considerable increase in scan speed.

Dedicated to my adorable parents and my lovely wife

मेरे प्यारे माता-पिता और मेरी पत्नी को समर्पित

Acknowledgements

A PhD project, and the resulting thesis, is not something which can be undertaken entirely independently. As such, there are a number of people who I would like to acknowledge for their input in making this thesis a reality.

First and foremost, I would like to express my deep appreciation to my supervisor Professor Andrew Moore for his support and encouragement throughout this PhD. His enthusiasm was the main driving force of this project. I would also like to thank Dr Robert Maier, Dr Jonathan Shephard and Dr. Rainer Beck for their assistance, ideas and opinions at the beginning of this PhD. Without their input, this project would not have progressed nearly as quickly or smoothly as it did.

Special thanks go to my supporters and collaborators, Prof. Moataz Attallah and Dr Mark Ward (University of Birmingham); Nick Jones and Dr Nick Weston (Renishaw plc); Prof. Phil Prangnell (University of Manchester); Dr Joe Kelleher and Dr Ceri Brenner (STFC, Harwell); Dr Marco Endrizzi (University College London), Jolyon Cleaves (Vision Research, UK), Toby Scrivener (Laser 2000, UK). Their support, through loans of equipment, use of facilities and invaluable expertise, was vital for many aspects of the project.

I would like to thank the School of Engineering and Physical Sciences, Heriot Watt University for providing me prestigious James Watt Scholarship towards my research, bursary and conferences expenditures during this project in UK.

I do acknowledge my officemates Dr Peter Schemmel, Ioannis Bitharas (John), Gilles Diederich, Dr Yuvraj Madhukar, Danny Etieve and Alex Ross for rendering all kinds of help and technical discussion necessary for this work. I would also like to thank the workshop staff here at Heriot-Watt University, particularly Alistair Blyth, Richard Kinsella and Camron Smith for tolerating my endless requests for making and ordering parts in a jovial manner.

Finally, I would like to thank my parents for constant support and blessings. I also thank my sisters Anita, Pramila, brother Deepak and my wife Jyoti for continuous encouragement and moral support during these years.

ACADEMIC REGISTRY
Research Thesis Submission

Name:	Prveen Bidare		
School:	School of Engineering and Physical Sciences		
Version: *(i.e. First, Resubmission, Final)*	Final	Degree Sought:	Doctor of Philosophy in Mechanical Engineering

Declaration

In accordance with the appropriate regulations I hereby submit my thesis and I declare that:

1) the thesis embodies the results of my own work and has been composed by myself
2) where appropriate, I have made acknowledgement of the work of others and have made reference to work carried out in collaboration with other persons
3) the thesis is the correct version of the thesis for submission and is the same version as any electronic versions submitted*.
4) my thesis for the award referred to, deposited in the Heriot-Watt University Library, should be made available for loan or photocopying and be available via the Institutional Repository, subject to such conditions as the Librarian may require
5) I understand that as a student of the University I am required to abide by the Regulations of the University and to conform to its discipline.
6) I confirm that the thesis has been verified against plagiarism via an approved plagiarism detection application e.g. Turnitin.

* *Please note that it is the responsibility of the candidate to ensure that the correct version of the thesis is submitted.*

Signature of Candidate:		Date:	

Submission

Submitted By *(name in capitals)*:	Prveen Bidare
Signature of Individual Submitting:	
Date Submitted:	

For Completion in the Student Service Centre (SSC)

Received in the SSC by *(name in capitals)*:			
Method of Submission *(Handed in to SSC; posted through internal/external mail)*:			
*E-thesis Submitted (**mandatory for final theses**)*			
Signature:		Date:	

Please note this form should be bound into the submitted thesis.
Academic Registry/Version (1) August 2016

Table of Contents

List of Symbols & Abbreviations

LPBF/PBF	-	Laser Powder Bed Fusion
AM	-	Additive Manufacturing
SLM	-	Selective Laser Melting
E-Beam	-	Electron Beam Melting (Powder Bed)
Ar	-	Argon (gas)
He	-	Helium (gas)
cw	-	Continuous wave
ND	-	Neutral-Density
PD	-	Packing Density
NIR	-	Near-Infrared
R_a	-	Linear surface roughness (arithmetic)
R_z	-	Average maximum peak to valley
SCAPS	-	SCanner APplication Software
SEM	-	Scanning Electron Microscopy
CMM	-	Coordinate Measuring Machine
STFC	-	Science and Technology Facilities Council
XCT	-	X-ray Computed Tomography
PCX	-	Phased Contrast X-rays
M^2	-	Beam quality index
D4σ	-	Beam diameter (ISO method)
D%pk	-	Beam diameter ($1/e^2$ method)
t_p	-	Powder layer thickness
t_{sp}	-	Height of the spreader above the build plate
t_m	-	Melted layer thickness
z	-	Build plate down movement step
c	-	Consolidation ratio
s	-	Scanning space (hatch distance)
d	-	Spot diameter
LSAW	-	Laser Supported Absorption Waves
FPS	-	Frames Per Second
K_n	-	Knudsen number
P	-	Pressure
T	-	Temperature

Δv	-	Specific volume of phase transition
L	-	Latent heat of phase transition
L_{vap}	-	Latent heat of vaporisation
$T_{liquidus}$	-	Melting temperature
P_c	-	Pressure in the keyhole
σ	-	Surface tension
r	-	Radius of the keyhole
k	-	Boltzmann constant
E_i	-	Ionization potential of the iron
T_e	-	Electron temperature
m_e	-	Electron mass
h	-	Planck constant
N_e	-	Electron density
g_e	-	Degeneracy of electron
λ	-	Wavelength

List of Publications

Journal Publications:

P. Bidare, I. Bitharas, R.M. Ward, M. M. Attallah, A. J. Moore, *Laser powder bed fusion at sub-atmospheric pressures*, International Journal of Machine Tools and Manufacture, 130-131, 65-72, 2018.
https://doi.org/10.1016/j.ijmachtools.2018.03.007

P. Bidare, I. Bitharas, R.M. Ward, M. M. Attallah, A. J. Moore, *Fluid and particle dynamics in laser powder bed fusion*, Acta Materialia, 142, 107-120, 2018.
https://doi.org/10.1016/j.actamat.2017.09.051

P. Bidare, R.R.J. Maier, R.J. Beck, J.D. Shephard and A.J. Moore, *An open-architecture metal powder bed fusion system for in-situ process measurements*, Additive Manufacturing, 16,177-185, 2017. https://doi.org/10.1016/j.addma.2017.06.007

P. Bidare, I. Bitharas, R.M. Ward, M. M. Attallah, A. J. Moore, *Laser Powder Bed Fusion in High Pressure Atmosphere,* Submitted to The International Journal of Advanced Manufacturing Technology, 2018.

Conference Contributions:

P. Bidare, I. Bitharas, R.M. Ward, M. M. Attallah, A. J. Moore, *High-Speed Imaging of the Powder-bed and Shield Gas during Metal PBF Additive Manufacture*, Annual International Solid Freeform Fabrication Symposium, 2017, Austin, USA.

P. Bidare and A.J. Moore, *Open-architecture system for in-situ x-ray imaging during selective laser melting (SLM)*, Additive Manufacturing Workshop by AILU, 22 March 2016, Cranfield University, Cranfield, UK.

Chapter 1. Introduction

Cost-effective and sustainable manufacturing processes which can deliver components and complex assemblies in the shortest possible time frame, providing a quick solution to frequently changing industrial needs are highly desirable. *Additive Manufacturing (AM)* has attracted many industries in recent years because of its simplicity and less time to market. *AM* is also known as digital manufacturing wherein three-dimensional CAD models, a computer drawing, is printed to form a final functional part. Metal-based AM parts have broader application in aerospace components, medical implants and tools, precious metal jewellery, high-value automobile engines, aircraft assemblies, customised tools and fixtures.

AM offers multiple benefits over conventional manufacturing processes, including reduced material waste, reduced time to market and manufacturing of intricate shapes that are not possible with conventional processes. AM's layer by layer manufacturing approach allows the manufacture of complex geometries in one go, this ability provides designers with significantly greater design freedom by reducing manufacturing constraints, enabling built parts to be closer to the optimum functional design. Many different types of AM processes exist, each has their advantages and disadvantages. These techniques can be differentiated by the material, principle, joining mechanism and heat source used [1]. AM techniques which use an arc as heat source and wire as material (Wire Arc Additive Manufacture-Cranfield University, Hybrid Layered Manufacturing-IIT Bombay) allow large components to be made much faster, but at the cost of dimensional accuracy. The parts made using WAAM or HLM are called near net shapes, and they need extensive post-processing to be used in real application. An AM method uses an electron beam as a heat source within in a vacuum chamber is called an Electron Beam Melting (E-Beam) process. In E-Beam, electromagnetic coils raster the electron beam across each layer of powder. The process relies on two-step sequence, first lightly sintering each layer of powder to prevent electrostatic charging and repulsion of powder particles followed by an additional pass fusing the region defined by the part volume. E-beam produces near-net shape parts which further require extensive post processing. AM methods which use a laser as a heat source and powder as materials are classified as laser powder blown and Laser Powder Bed Fusion (LPBF) processes. In powder blown process, the laser beam melts co-axially flowing powder through the nozzle, depositing material forming a 3D component. This technique has a limitation in making intricate shapes and overhangs in parts because of the lack of support mechanisms during fabrication. In contrast, laser powder bed fusion (LPBF) has

an inherent support system, while building intricate shapes and overhangs the un-sintered powder act as support. LPBF is the most used rapid manufacturing process in industry and one of the fastest growing AM process [2]. LPBF is capable of making components within tighter tolerance than other AM processes, although typically associated with smaller (<0.064 m^3) build volumes.

1.1 Overview of Laser Powder Bed Fusion

Laser powder bed fusion produces objects from the powdered material using one or more lasers to fuse or melt powder particles on the build surface selectively, layer by layer, in an enclosed chamber. It is often referred to by manufacturers' names and sometimes trademarked, for example, selective laser melting (SLM^{TM}). LPBF enables the production of complex parts matching the mechanical properties of parts produced through conventional manufacturing methodologies. A 3D volumetric CAD model is sliced down in layers and transferred to the scanner (2-axis deflection unit) through control software. Subsequently, the powder material is spread by a hopper on the substrate and levelled by a powder scraper. The geometric information of each layer is transmitted to the laser-scan system where a focused laser beam is directed onto the powder bed. The laser beam scans the specified area on the layer and melts the powder to make a solid layer. The entire process part building takes place inside an enclosed chamber filled with inert gas such as Ar which helps in minimising oxidation, removing process by-products and degradation of the remaining metal powder. After lowering the powder bed by one-layer thickness, the process steps are repeated for each layer respectively until the part is finished.

Currently, LPBF has been employed to manufacture functional prototypes and small production runs of the complicated parts in exotic materials. The processing of different materials depends on the availability of the material in powder form. LPBF is commercially highly preferable for sectors like aviation that involve low volume manufacturing, because of the reduced costs in producing bespoke parts. It can produce internal honeycomb or lattice structures with optimised topology, offering weight reduction whilst maintaining mechanical strength as well as internal cooling channels, which are not possible using conventional processes. SpaceX's SuperDraco Inconel rocket chamber [3], GE's fuel nozzle LEAP-1A engines [4], Renault Truck rocker arms [5] and structural bracket for Airbus Eurostar spacecraft [6] are some complex components that were manufactured using LPBF, shown in Figure 1.1. In order to enter into series production; increased process productivity is necessary while maintaining consistent quality.

Figure 1.1: Famous components produced through LPBF, top left SpaceX's SuperDraco Inconel rocket chamber [3]; top right GE's fuel nozzle LEAP-1A engines [4], bottom left Renault Trucks rocker arms [5]; bottom right structural bracket for Airbus Eurostar spacecraft [6].

1.2 Issues with the LPBF Process

Industries are hesitating to replace conventional processes with AM because of inconsistent quality and the high capital cost. The current commercial LPBF machines are also limited by smaller build volumes, normally 400 x 400 x 400 mm^3 and slow deposition rates (long build times). The quality of components produced by LPBF is mainly affected by surface roughness, porosity, residual stresses, cracking, delamination, part shrinkage and distortion.

The surface roughness is one of the major limitations in LPBF. Accuracy and surface finish of LPBF are typically inferior to conventional manufacturing processes such as machining. The built part surface finish depends on the powder particle size and the layer thickness used. The fine particle powder sizes and the smaller layer thicknesses produce smoother parts but on the cost of longer build time and operator health risk of handling smaller particles (<1 μm) [7]. LPBF components need additional and expensive post-processing operations to finish the mating surfaces. On the inclined and angled surfaces, the roughness is mainly driven by the well-known "staircase effect" which also directly depends on the layer thickness. The predominate area of current research is in-process surface finishing of LPBF components i.e. laser polishing.

In LPBF, the high energy localised heat input and inherent high-temperature gradient induce a significant amount of residual stress in part. The residual stress has been found to cause dimensional inaccuracies, distortions, cracks and delamination during building and post-processing stages. There are two stages of stress accumulation [8]; the first is the temperature gradient mechanism (TGM) which occurs due to rapid heating from the laser beam spot which develops a steep temperature gradient around its perimeter. The second mechanism which induces residual stresses is the cool-down phase of the molten top layer; as it shrinks due to thermal contraction. In order to minimise the effect of residual stresses (distortion), parts are built with a support structure and heated bed. The current research is going on in-process mitigation of these stresses, and one of the significant challenges is to measure meltpool temperatures in-situ.

An undesirable porosity is also one of the major damaging factor in LPBF. Many factors can contribute to pore formation, including instability of the melt pool [9], the lack of fusion between powder particles [10], the laser keyhole leaving a trail of voids [11], the narrow powder particle size distribution reducing packing density in a layer [12,13], the scanning strategy with insufficient overlap between adjacent tracks [8,14] and the spatter and oxidation due to insufficient shielding gas flow [15]. These pore formation mechanisms can be eliminated completely by using appropriate process parameters, scanning strategies, suitable shielding gas, effective cross flow and minimising O_2 in process [8,16,17]. In current LPBF machines, however, the major reason causing undesirable porosity is in-process dynamics such as spatter ejection, plasma generation, beam distortion and metal vapor generation, which can drastically reduce the energy availability to the powder bed [18]. In order to reduce in-process dynamic issues, either the process can be made robust by understanding these dynamics or a feedback control should be developed to capture the in-process dynamics and correct for process variances in real time. In both cases, an in-depth understanding of the process is needed and that can be achieved through in-situ process measurements, as presented in this thesis.

1.3 Aim & Objectives

The overall objective of the work contained within this thesis is to expand on current limited knowledge of the in-process dynamics of the LPBF processes which affect build quality. The primary objective includes the design and development of an open-architecture powder bed fusion system which allows for easy access to different in-situ and post process measurements. In contrast to the commercial LPBF systems, where access is difficult and

modification to the system for specific measurements is expensive. The use of different in-situ monitoring techniques such as x-ray imaging, high-speed imaging, schlieren imaging and thermal imaging have been detailed including results on different shielding environments. In-situ observations will create additional knowledge for making the process more robust for in-process dynamics and will provide suitable input parameters for sophisticated feedback control.

This project was started as a short-term feasibility study funded by the EPSRC Centre for Innovative Manufacturing in Additive Manufacturing. The principal aim of the study was to determine if x-rays can be used for in-situ imaging of the melt pool during LPBF. If feasible, such images might yield new insight into fundamental physical processes that occur during LPBF, including how the laser beam couples with the powder bed, the powder melting and solidifying processes as well as insight into the formation of pores. The x-ray source at STFC is set up for approximately two weeks each summer for imaging applications. Experiments were scheduled in the summers of 2015 and 2016 but unfortunately issues with the x-ray source meant that on both occasions no imaging with the LPBF system could be attempted. However, some preliminary x-ray tests have been conducted which are discussed in detail in Chapter 3. In the meantime, the aim and objective of the work evolved after reviewing several state of art research LPBF systems and discussing with industrial players like Renishaw, SPI lasers, BOC gases etc. Aim and objectives pertaining to this project are detailed below.

In order to achieve the desired objective, the project is further divided into following tasks.

1) Design, development and characterisation of an open-architecture LPBF system: Modular for easy modifications; smaller in size for easy transportation; self-sustained automation for operating remotely (for high power x-rays); can produce single tracks, islands, cubes (multilayer builds) and complex parts with density >99%.

2) In-situ measurements to study in-process dynamics.

    (a) XCT Imaging; develop setup to do in process x-ray computed tomography to understand powder packing density as spread.

    (b) X-ray Imaging: a feasibility study of flash x-rays and phased contrast x-rays for in-situ imaging in the LPBF process.

(c) Camera based high-speed imaging: Establish a high-speed imaging setup with suitable illumination for the powder bed visualisation at particle level magnification; adjustable magnification for imaging of single tracks, island and multilayer builds; study effects of different parameters including shielding environments with and without shielding gas cross flow.

(d) Schlieren imaging: to study gas flow visualisation with and without shielding gas cross flow; study on laser plume formation and expansion above the powder bed.

3) Effect of pressure: extend in-situ measurement work to study the effect of ambient pressure: LPBF in vacuum down to 10 μbar and high pressure up to 5 bar.

1.4 Summary of Chapters

- Chapter 1 provides an introduction to the thesis, including the primary motivation and key ambitions for the work presented.

- Chapter 2 introduces background information on the laser powder bed fusion process and past work on the development of modular LPBF systems, with an extended focus on the literature surrounding the use of modular LPBF systems for in-situ measurements. Furthermore, different process signatures (features) that are important in understanding the in-process status of the process and the past research on the development of in-situ measurements are discussed in detail. In the end the Chapter summarises the literature and highlighted gaps in the literature.

- Chapter 3 provides details on the design and development of an open-architecture laser powder bed fusion system. It details the design requirements and benchmarking of the x-ray sources for in-situ imaging. Then, it details full system characterisation from single track to high density 3D component build.

- Chapter 4 covers the work done on high-speed imaging in the LPBF from single track to multilayer builds. It explains the setup modification for direct imaging as well as schlieren imaging. It discusses the effect of process parameters on in-process dynamics and highlights several new regimes observed in the laser powder fusion.

- Chapter 5 discusses effect of sub-atmospheric pressure on the LPBF; single tracks and island scans in different vacuum conditions from 20 mbar to 10 µbar are reported. Results in form of videos, micrographs and surface profiles are included and compared with atmospheric pressure results.

- Chapter 6 discusses the effect of positive ambient pressure up to 5 bar for argon and helium for single layer tracks to multilayer builds. Results in the form of direct high-speed imaging videos, schlieren imaging videos, surface profiles and micrographs and their comparison are detailed.

- Chapter 7 presents the outcomes of the investigations discussed in this thesis and possible areas of future research are also suggested.

Chapter 2. Literature Review

This Chapter aims to provide a background of laser powder bed fusion (LPBF) including operating principle, applications, process variants, process parameters and defect formation. It will then provide a review of the past work on the development of modular powder bed fusion systems for in-situ process studies. Subsequently, it will give details of different process signatures (features) that are important in understanding the in-process status and the past research on the development of in-situ measurements of these features. Background knowledge on some of the post process measurements will also be given in this Chapter. The conclusion of this Chapter will then identify the gap in the past research based on the literature review and establishes the motivation for conducting this research as was discussed in the Introduction Chapter.

2.1 Laser Powder Bed Fusion

Powder bed fusion was developed by the University of Texas, Austin USA during the mid-1980's, it became the first commercialised system known as Selective Laser Sintering (SLS). The process used laser light to selectively sinter powder particles to build a solid structure layer by layer. SLS is one of the first 3D printing processes to print components directly from CAD models. The powder bed process was initially developed to manufacture plastic/ABS prototypes for visualisation purposes in automobile industries and later the process had been used for metals and ceramics printing [19,20]. In recent times, each new powder bed machine developer has introduced competing terminology to describe the process through fusion mechanism, with variants of sintering and melting being the most popular. Some of the popular names are Selective Laser Sintering (SLS), Selective Laser Melting (SLM), Direct Metal Laser Sintering (DMLS), Laser Beam Melting (LBM) and Direct Metal Laser Melting (DMLM). However, the use of a single word to describe the powder bed fusion is inherently problematic as multiple mechanisms are possible. The recently formed ASTM standard for additive manufacturing terminology defines it as laser powder bed fusion (LPBF). There are a variety of powder bed fusion techniques which can be differentiated by the material, principle joining mechanism and heat source used in [8]. In LPBF, a high-power laser is used to sinter or melt specified regions of a layer of metal powder spread on a build platform.

There is a similar metal powder-bed fusion technology where the input energy is provided by an electron beam instead of the laser and is called an Electron Beam Melting (E-Beam). Both the E-Beam and LPBF are powder-bed fusion processes that work on the

same melting principle. However, there are some differences between the LPBF and the E-Beam, for instance E-Beam typically requires a vacuum and preheating of the powder bed in comparison to LPBF, where the atmosphere is an inert gas at atmospheric pressure without preheating. The surface finish of LPBF manufactured components is better compared to E-Beam manufactured components. E-Beam is a hot process due to a preheated bed, the resulting microstructure is different from LPBF [4,21,22]. Compared to other powder AM processes such as the blown powder process, LPBF has an inherent support system, while building intricate shapes and overhangs, here un-sintered powder acts as support.

In LPBF, a focused laser beam melts and fuses submicron size randomly distributed powder particles in the form of a layer with the speed of 100's of millimetres per second [9]. LPBF is layer by layer process, in which every layer represents a cross-sectional geometry of the component with a thickness equal to the metal powder layer thickness. A 2-axis deflection unit (Galvo-scanner) coupled with a laser system scans the two-dimensional geometry (component's contour and filling pattern) over the deposited powder layer and repeats for further layers. LPBF enables the production of complex parts and assemblies matching the mechanical properties of parts manufactured using conventional processes such as casting and forging [23]. Unlike other manufacturing processes, LPBF does not need part specific drawing tooling and pre-production costs. Currently, LPBF is popular in high-value manufacturing areas like the medical, aerospace, and tools and die making industries where parts are small in quantity but complex in geometry. LPBF gives unlimited geometrical freedom to design, allowing engineers to design cost-effective complex parts. Although, LPBF has a significant amount of pre and post-processing operations.

Figure 2.1 illustrates the operating principle of the SLM process; first, the 3D CAD volume model is sliced down into layers and transferred to a scanner (2-axis deflection unit). Subsequently, the powder material is spread by the hopper on the substrate mounted on the piston that moves vertically up and down in the process. The hopper contains a roller or knife edge scraper which levels the powder bed; the extra powder is overflowed to container. The geometric information of each layer is transmitted to the laser scan system where a focused laser beam is directed onto the powder bed. The laser beam scans the specified area on the layer and melts the powder to make a solid layer. The entire part building process takes place inside an enclosed chamber filled with inert gas such as argon (Ar) which helps to minimise oxidation and degradation of the remaining metal powder.

After lowering the powder bed mounted on the piston by one layer thickness, the process steps are repeated until the part is finished. The f-theta lens ensures uniform focus (flat field image) along the plane of interest.

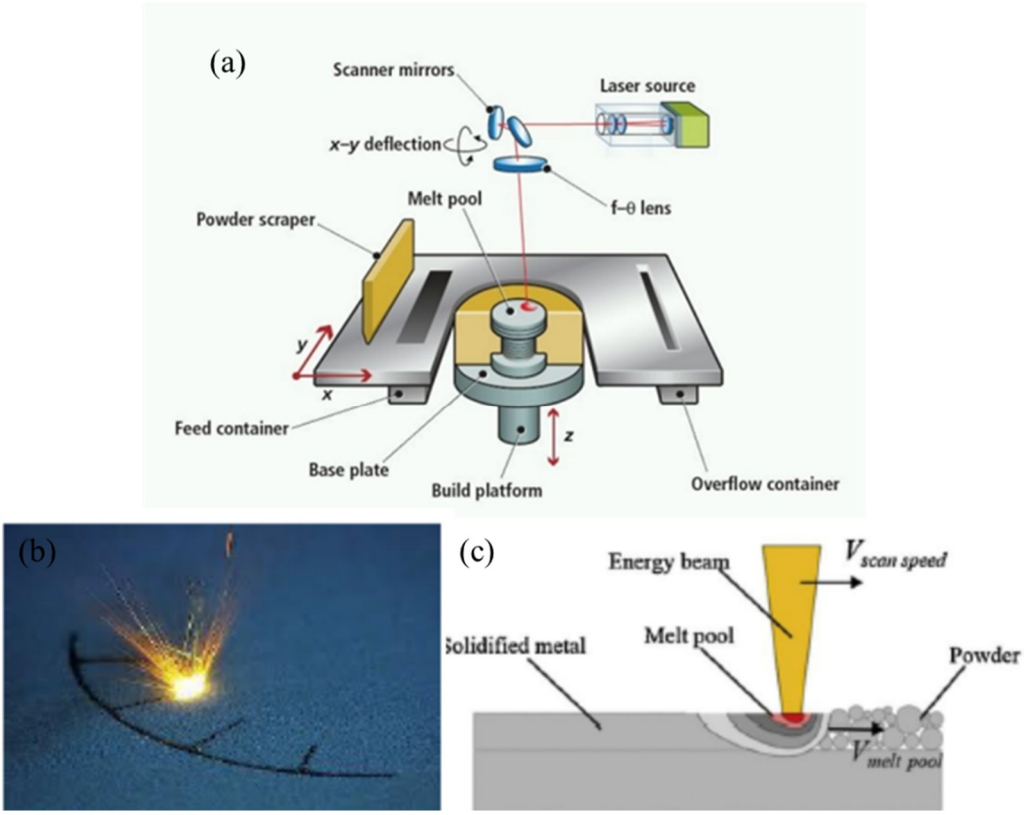

Figure 2.1: Laser powder bed fusion (a) schematic of general LPBF system [8], (b) LPBF in-process photograph (c) schematic of laser-powder interaction [24].

The laser melting of the metal powder is a complex process that is highly sensitive to the material properties, powder size distribution, packing density and process parameters. The bed looks like a random distribution of spheres. Due to the uncompressed nature of the metal powder, the packing density varies between 40% to 60% [25]. As the laser irradiates the powder; it is absorbed by the top layer particles and some of the scattered radiation is also absorbed by lower particles. Although much of the incident radiation is absorbed by the powder particles, a significant portion is reflected. The laser radiation absorbs, reflects and scatters multiple times in the powder particles which create pseudo-volumetric heating [26]. As the powder particles melt, viscous flow due to surface tension fuse them together into a melt pool. Once a melt pool is formed, the energy flows into the melt pool, which further transfers it to the surrounding powder through conduction, radiation, and convection. In the melt pool, several other complex fluid dynamic elements also influence the formation and movement of the melt pool such as the Marangoni convection, the Bernoulli effect and recoil pressure [27]. A depiction of this process can be seen in Figure 2.1(c) [20].

Table 2.1: List of commercial machine manufacturer and claimed fusion mechanisms.

Short Form	Full Form	Company	Fusion Mechanism
SLS	Selective Laser Sintering	3D Systems, USA	Sintering
SLM	Selective Laser Melting	SLM Solution, Germany	Melting
DMLS	Direct Metal Laser Sintering	EOS, Germany	Sintering/Melting
DMLM	Direct Metal Laser Melting	GE, USA	Melting
LPBF	Laser Powder Bed Fusion	Additive Industries, Netherlands	Melting
DMP	Direct Metal Printing	3D Systems, USA	Sintering
LaserCUSING	-	Concept Laser GmbH, Germany	Melting
MPBF	Metal Powder Bed Fusion	Renishaw, UK	Melting

Unique advantages such as reduced time to market, design freedom, complex assembly consolidation of LPBF enable a wide range of applications. The powder bed fusion was limited to prototyping parts for a quite long time after its invention through the mid to late 1980's. In the 2000's, after seeing what additive manufacturing can do, along with improvements in materials and parameters used to make parts, various industries have adopted additive manufacturing as a way to build real parts and not just prototypes [28]. However, over the last five years, the process has significantly improved in terms part quality and mechanical strength. Thus, the application in high-value manufacture where the material is expensive, complex geometry and limited quantity such as aerospace, luxury automobiles, and biomedical industries are the main areas of current application. In addition, the future generation LPBF systems are being developed to make the process affordable for series production with added mass customisation. The main advantages of LPBF are topology optimisation, multi-materials, lattice structures which helps significantly in mass reduction of parts which is critical in aerospace applications. Aerospace manufacturers such as Rolls-Royce, EADS-AIRBUS, Bombardier, Boeing, GE, Air Force Research Lab-US, Aerosud, GKN Aerospace have already started using LPBF for manufacturing various complex components. The other key advantages associated with

LPBF are porous structures, customisable porosity and hollow geometries which help in adapting the technology extensively in biomedical industries. Customised implants for example dental crowns, cranial implants, orthopaedics surgery such as the knee and hip replacement, have been manufactured using the LPBF. Other potential industries taking an interest in LPBF are the luxury automobile and sports vehicle. Renishaw's lightweight mountain bike is one of the examples of it [29].

There have been significant technological advancements in LPBF in last few years, as such, the process has improved a lot after the introduction of gas atomised powder particles due to their spherical nature, flowability and higher packing density [30]. On the other hand, as future systems are targeting high volume manufacture, new techniques such as quad laser systems are enhancing productivity by approximately four times and helping in mitigating the residual stresses in manufactured components [31]. Currently, researchers are working to develop a multi-laser system with more than four lasers to increase productivity further. Other future improvements include advancements in gas flow systems to optimise consumption and process by-products removal. Another advancement is an integrated LPBF system with auto powder cleaning, laser machining, heat treatments aim to improve productivity and reduce the operator health risk form handling harmful metal powders. Additive Industries has integrated multi-build chamber to utilise the laser downtime, heat treatment module and cleaning module and surface treatment module to enable the process for series productions [32].

Processing different metal alloy powders in LPBF must meet requirements such as it being formed into spherical powder particles by using any of the atomisation processes. A wide range of materials meet these broad requirements, but only a few have been commercialised and validated for building high-density components. Recently, a handful more have been developed, but there remains a tremendous amount of opportunity in processing new material and developing new alloys specifically for the LPBF. Some of the materials researched for LPBF are FeTiNi, TiZrNbMoV, ceramics, CoCrMo, WC-Co, Inconel 718, Inconel 625, Al 2024, high purity copper, GRCop-84, Niobium, bulk metallic glass, stainless steel 316L, TiAl, CMSX-4, Tantalum, W-Ni, AlSi10Mg, Bronze, Gold (18 carat), Platinum alloy, Silver alloy. The commercially available materials are mostly steels, stainless steel 316l, stainless steel 17-4, sports and defence utility maraging steel, tool steel (1.2709), structural aerospace material (Ti–6Al–4V), biocompatible implant materials (Ti, Ti–6Al–4V, CoCr), high-temperature materials (Inconel 626, Inconel 625, Inconel 718, CoCr), Aluminium (AlSi10Mg, AlSi9Cu3) [33,34].

There are several commercial metal LPBF system manufacturers available today. Each manufacturer master either one or several variations of these printers. Many of these systems are available for advanced prototyping and can also be used for producing real application functional parts. Currently to make these machines more reachable to series production, many companies are developing multi-laser systems with automatically integrated systems for powder handling, recycling, cleaning and heat treatment. Table 2.2 gives details about the top machine manufacturers, their different models, laser power capacity, both single and multi-laser, build volume, build rate and the integrated modules available.

LPBF for metals is getting more and more mature every day for many industrial applications. However, it cannot be said that it is plug and play technology for functional part production. For each new application, the process parameters have to be fine-tuned for best performance in terms of part material properties. The manufactured parts are affected by a large number of different process parameters with around 130 parameters being apparent [35]. In LPBF, process parameters can be lumped into four categories:

- Laser-related: laser power, spot size and laser properties (wavelength, polarisation etc.)
- Powder related: particle shape, size and distribution, powder packing density, layer thickness, spreader type, spreader speed and powder reuse cycle
- Scan related: scan speed, scan spacing, scan angle and space pattern, scanner properties (delays, acceleration) and F-theta lens properties (thermal lensing, internal reflection, threshold)
- Environment-related: bed temperature, gas flow rate properties, O2 level and chamber pressure.

Table 2.2: List of LPBF systems

Manufacturer	Models	Laser	Build volume	Build Rate	Intigrated Modules
3D System, USA	ProX DMP Series (100, 200, 300, 320)	50W - 500 W	100 x 100 x 100 mm^3 to 275 x 275 x 420 mm^3	.-	Recyling Module (Optional)
SLM Solutions, Germany	SLM 125, 280 ,500	400W - Quad Laser (4x700 W)	125 x 125 x 125 mm^3 to 500 x 280 x 365 mm^3	25 - 105 cm^3/h	Automatic Powder Recyling, Meltpool Monitoring, Heated Bed 550 Deg. C
EOS, Germany	EOS M (100, 290, 400, 400-4), EOSINT M 280 and Precious M080	200 W - Quad Laser (4 x 400 W)	Phi100x 95 mm to 400 x 400 x 400 mm^3	up to 100 cm^3/h	Modular Plaform (Control station, Process station and Setup station), Special machines for preciuous metals
Concept Laser, Germany	Mlab (cusing, cusing 200R), M1 cusing, M2 cusing, M Line factory, X LINE 2000R and X LINE PCG	100 W - Quad Laser (4 x 1000W)	50 x 50 x 80 mm^3 to 400 x 400 x 425 mm^3	5 - 120 cm^3/h	Modular Platoform (Setup and dismantling module), 2 build chamber, Interized process and powdewr stations
Renishaw, UK	AM 250, 400, 500M	200 W - Quad Laser (4 x 400W)	250 x 250 x 300 mm^3 to 250 x 250 x 350 mm^3	20 cm^3/h-	Real time powder recycling
Realizer	SLM 50, 125, 300i	120 W-1000 W	Phi 70 x 40 mm^3 to 300 x 300 x 300 mm^3	.-	Intergtarted powder recycling system
Additive Industries	Metalfab1 & Metalfab process and application development tool	500 W - Quad Laser (4 x 1000 W)	420 x 420 x 400 mm^3 - 420 x 420 x 400 mm^3	.-	Intergarted modules (automatic powder handling and extraction, heattreatment, 2 build chamber)
Trumpf, Germany	TruPrint 1000, 3000	200 W	Phi 100 x 100 - Phi 300 x 400 mm^3	.-	Powder removal station separte
Farsoon, China	FS271M	200 W - 500 W	120 x 120 x 100 - 275 x 275 x 320 mm^3	5 cm^3/h	Open parameters and materials
Matsuura, Japan	Lumex Avance-25, 60	400 W - 1000 W	256 x 256 x 185 - 600 x 600 x 500 mm^3		Hybrid System (Milling every layer)
Sisma, Italy	MYSINT 100, 300	200 W - 500 W	Phi 100x100 - Phi 300x400 mm^3		.-
Shining 3D, China	EP-M250	400 W	250 x 250 x 300 mm^3 to 250 x 250 x 350 mm^3		.-

All the parameters are interdependent and specific to material, machine and component, they mutually interplay to affect build part quality. Primary defects which are governed by process parameters are porosity, residual stresses, micro-cracks, oxide formation, layer delamination, material vaporisation, lack of fusion, part shrinkage and poor surface finish.

The effects of process parameters have been reported many times by researchers such as increase in laser power with an increase in scan speed and a decrease in the laser beam spot size leads to the fast and dense processing of metal parts [36]. Whereas, surface finish, material properties, the residual stress of final parts are affected strongly by scan spacing, scan pattern and scan speed [37,38]. A reduce scan spacing, and higher scan speed will lead to lower surface roughness and opposite parameter lead to excessive melting and porosity [14,39,40]. The larger the powder particle size means the higher the layer thickness and so higher the productivity of the process [41]. However, larger particles size leads to higher surface roughness, so optimal powder size distribution is needed to achieve higher productivity and improved surface roughness [42]. In recent research, it was found that the powder reusability also affects the powder packing density, after the 17^{th} cycle, the distribution changes drastically and leaves only big particles in the powder [43,44]. Auxiliary system and accessories parameters such as gas flow direction and flow rate also influence the final part quality, poor gas flow rate and inappropriate direction lead to delamination of layers [45]. In contrast, to maintain the consistent quality of LPBF parts, all the possible affecting parameters have to be studied and optimised. Selecting appropriate parameters enable acquisition of desired characteristics regarding surface quality, productivity and the mechanical properties of the final product.

As discussed, several defects and issues originate in the process; some can be eliminated by post-processing such as porosity by hipping and residual stresses by heat treatment but most of them cannot. To mitigate these defects; and to develop control strategies to avoid the formation of these defects, robust and in-depth understanding of in-process dynamics is needed. For this, the process needs to be studied in-situ. In order to do in-situ measurements, the commercial system's modification is difficult for specific measurements. Whereas, the current in-situ measurement systems on commercial machines are limited to basic build chamber monitoring such as build plate and chamber ambient temperature, chamber oxygen concentration, powder bed layer quality. The chamber pressure, the gas-scrubbing filter monitoring etc. In the next section, commercial in-situ monitoring systems are discussed.

2.2 In-situ Measurement Systems on Commercial Machines

The fundamental issues addressed by current in-situ monitoring systems focus on the variability in the state of AM machines, which in turn can lead to build failure. In-chamber conditions such as the build plate temperature, the chamber ambient temperature, the chamber oxygen concentration, the chamber pressure, the gas-scrubbing filter and the recycling powder quality play a vital role in process shifts and the formation of defects. In-situ monitoring of these properties is critical, is one of the primary aspects of ensuring high quality builds, and the first aspect of "process monitoring" to be implemented on commercial AM tools. In the last 3 years, a couple of advanced monitoring systems have been introduced by major LPBF machine manufacturers.

Renishaw plc, UK, has recently introduced an in-situ process monitoring system called InfiniAM Spectral for their newly launched RenAM500Q and M quad laser machine. The system combines a chamber camera with synchronous sensing of laser power, galvo position and multi-spectral melt pool sensing. The system monitors melt pool emissions across a wide spectral range including laser frequency using co-axially mounted photodiodes. Then “MeltVIEW” software combines all the data from the sensors with galvanometer position so that all the information can be accurately mapped and visualised [46].

Concept Laser's “QM Coating” monitors powder bed layer distribution over the build surface. It uses a high-resolution camera and flash light to take a picture of the build surface before and after layer application. An algorithm calculates a difference image from the recorded data. The analyser then decides whether the powder application was sufficient and whether the powder dose factor needs to be increased, reduced or renewed coatings need to be carried out. “QM atmosphere” module [47] regulates the chamber O_2 concentration and continuously analyses the filter status. regulates the chamber O_2 concentration and continuously analyses the filter status. The machines are fitted with several oxygen sensors that monitor the process gas circulation.

EOS’s EOSTATE monitoring suite is a multi-monitoring tool which comprises four different monitoring modules: System and Laser, PowderBed, MeltPool and Exposure OT (optical tomography). The powder module monitors powder coating after each layer using an integrated camera; MeltPool measures the light emissions from the melt pool by means of sensors (photodiodes). In addition, Exposure OT uses an optical tomography technique which deploys an eCMOS camera to capture high resolution images of the energy

application in the melt pool from the entire build area. It monitors the system status if a value deviates from within a pre-defined range, the process is stopped, and the operator is informed. [48].

SLM Solutions' in-situ monitoring module [49] monitors temperature at several locations throughout the machine as well as filter conditions and O_2 concentration in the build chamber, logging these data every two seconds. Quality Assurance System (QAS) of SLM solutions provides in-situ information of layer spreading quality by image documentation after powder spreading and after exposure offering the possibility of manual adjustment of conditions and limits for error detection. In addition, the critical sensing places are the platform, build chamber, pumps, cabinet, optical bench, ambience. QAS enables automatic data monitoring of all sensors every two seconds. Control and output of temperatures, oxygen control, inert gas pressure and filter conditions [49].

As discussed above, many of these in-situ measurement systems provide basic measurements towards machine and build failures. They do not provide information on process- particle level understanding. In addition, commercial in-situ systems generate tremendous amount of data for every layer; analysing and comparing these large data with the particle level interaction is challenging. In order to do specific measurements for fundamental study of laser-powder interaction, open and modular architecture LPBF systems are needed. Where one can easily use any kind of sensor without excessive modification to the machine to monitor the LPBF processes. Some modular LPBF systems reported by researchers for in-situ process studies are discussed below.

2.3 Modular AM Systems for In-process Studies

In order to create enhanced process understanding of complex physical interactions through in-situ process monitoring, an open architecture modular LPBF system is needed offering accessibility whilst remaining compact; since commercial systems are costly and offer limited flexibility. An open architecture system enables complete control over various operations such as toolpath generation, control of laser power, travel speed, position of beam, beam diameter, triggering of sensors, tracking of the X, Y position of the beam (to track sensor data) and access to the beam delivery path etc. Current strategies for process optimisation still rely on expensive and time-consuming trial and error iterations. In order to minimise such iterations and enhance the critical knowledge base for in-process variations, researchers are working on developing high fidelity physics-based simulation models, and that too needs a sophisticated LPBF system to validate models. A perfect open-

architecture system should not only accommodate various sensors and instrumentation used to support in-process measurements but also enable implementation of control strategies.

The in-situ setups proposed in the literature can be grouped into the following major categories: (i) open-architecture modular powder bed systems (i.e. developed for specific need or general-purpose measurements), (ii) modified commercial systems (i.e. modified optical path, modified building chamber) (iii) external in-situ systems (i.e. external sensors mounting especially from viewing window of commercial system). A further important categorisation regards the sensor mounting strategy, which involves either 'co-axial' or 'off-axis' systems. In co-axial configurations, sensors exploit the optical path of the power source. In off-axial configurations, sensors are placed outside the optical path, with a given angle-of-view with respect to the region of interest. In this section only the open-architecture powder bed systems are discussed; other types of in-situ setups are discussed in the next section with details of in-situ measurement techniques.

The National Institute of Standards and Technology (NIST), USA [50] has designed a LPBF testbed with dual purpose: (i) to assess in-process and process intermittent metrology methods and real-time process control algorithms aimed to enhance process repeatability, reliability, and part quality; and (ii) to establish foundations for traceable radiance-based temperature measurements that support high-fidelity process modelling and model validation efforts, as well as to study methods for real-time thermometry in the production environment. In addition, it also provides a temperature controlled heated bed up to 80 ºC with the capability of heating the system chamber wall up to 250 ºC. Figure 2.2 shows a CAD model of NIST BPF system for in-situ measurements. Figure 2.2(a) shows build mode, where in-process, process-intermittent metrology methods and real-time process control algorithms can be tested. Figure 2.2(b) shows radiance-based metrology mode for post process measurements. The system has in-line coaxial continuous monitoring for thermal measurements using a single point high-speed filtered photodetector as well as a coaxial IR imaging system to detect melt pool geometry.

The system is still in development phase and has not been built completely, this project was started since 2014. A recent conference paper published in SPIE journal [51] from the group mentioned that: analysis is carried out on a baseline experiment with no powder material added, melt pool size measurements collected in-situ are compared to ex-situ measurements, and results are discussed in terms of temporal bandwidth. Other

limitations are: the base plate is manually adjusted to allow powder spread and the size is large which may not suit for low quantity powder characterisation.

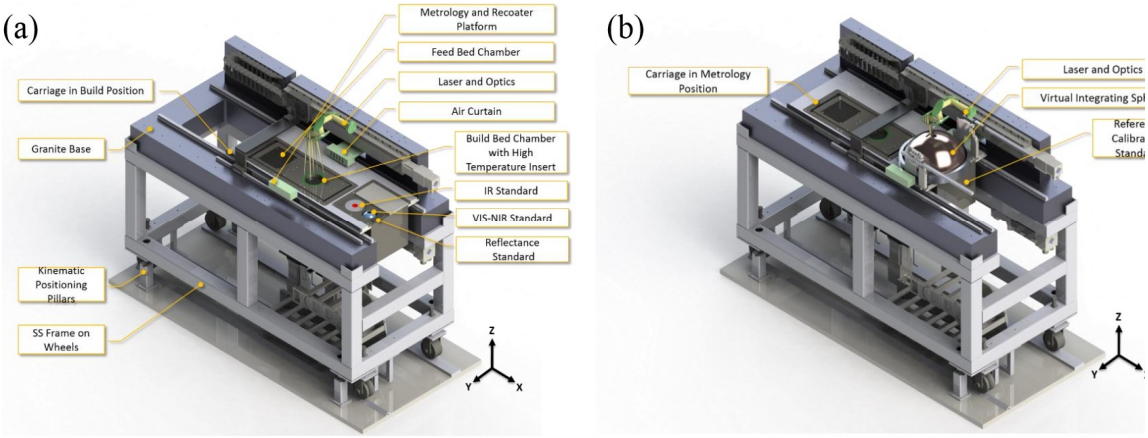

Figure 2.2: CAD of LPBF system developed by NIST [50], (a) Build mode and (b) Radiance based metrology mode.

Edison Welding Institute, USA (EWI) [52] has designed and developed a modular powder bed fusion system to demonstrate the importance of in-process sensing in LPBF and how it can lead to breakthroughs in improving numerical model prediction. The author suggested that LPBF must be treated in the similar way conventional manufacturing processes are tightly monitored and controlled to ensure quality. The primary objective was to evaluate and mature in-process sensing techniques on LPBF test bed to enable quality monitoring. The measurements include process deviations, geometry, distortions, bed flatness, metallurgical properties, pores, lack of fusion, cracking and validation of numerical models. In addition, the test bed was developed to allow sensor evaluation without physical or software constraints as it is challenging to install sensors in a commercial system. Furthermore, the test bed enables installation of the local sensor as near as possible to material fusion. Popular local sensors are (melt pool) photodetector, spectrometer, high-speed camera, pyrometer and global sensors, high-resolution imaging, laser line scan, global thermal camera (FOV and working area). Figure 2.3(a) shows a CAD model of EWI's test bed with detailed monitoring accessories whereas Figure 2.3(b) shows the actual system in place.

The use of the EWI system for in-situ measurements has been reported few times in the literature. Jamshidinia et al. [53] reported the use of the system for in-situ measurement of cross contamination in LPBF; three sensors including a spectrometer, a photodetector, and a low speed optical camera were used to monitor the process. Other applications of the system were reported in powder layer thermal imaging for numerical model validation [52], high resolution powder layer imaging [54]. The individual in-

process studies related to this system are discussed in detail in further section of this Chapter.

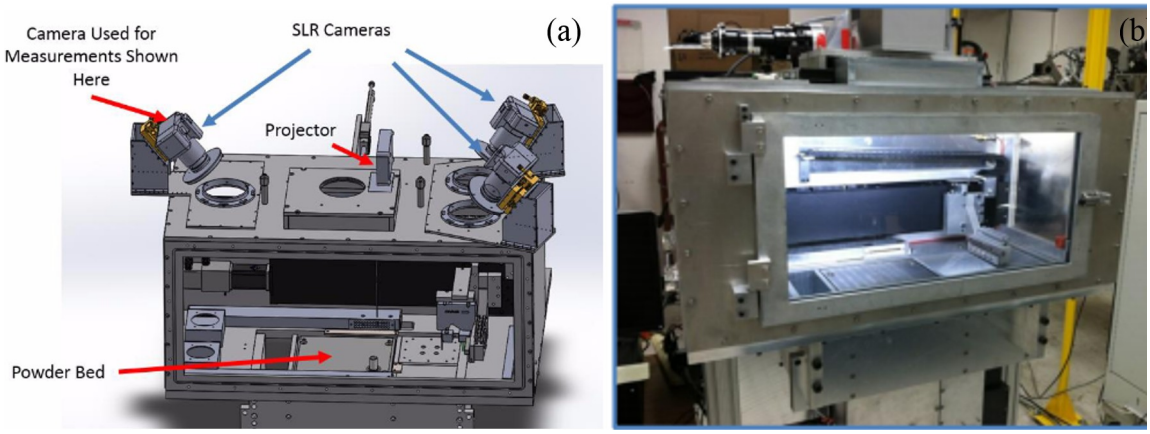

Figure 2.3: EWI LPBF test bed, (a) CAD model with all the accessories and (b) actual LPBF system in place [52].

Fraunhofer ILT [55] has developed a modular powder bed system for development and testing of new laser beam sources and optical components. In addition, it can also be used for precise laser-based metrology, testing technologies and individual processes studies. It is believed that such LPBF system helps in expanding the material database and can enable feasibility and process qualification study of variables in the powder bed fusion, as the small system needs small amount powder. The rig has additional feature of a heated powder bed which can go up to 1700° C. It also supports modification in shielding gas flow system to use it to validate simulation and design optimisation. Figure 2.4 shows, the system as build, left, scanner and the powder bed, right is the complete system in place. The system is newly developed and no results have been reported. However, the system is currently being used for feasibility studies towards larger powder bed size.

Figure 2.4: Fraunhofer ILT's LPBF system, left, scanner and the powder bed, right is the complete system in place [55].

MIT [56] has reported an open-architecture LPBF system shown in Figure 2.5. The project was started with constructing a single-layer, 1-degree of freedom linear test platform for initial testing, and then continued to create a multi-layered, galvanometer operated system. In order to maximise the use of commercial-off-the-shelf components both to leverage as much pre-existing engineering as possible as well as to make modifying and reproducing the system rapidly. An open-source, modular software platform from a combination of readily available and custom software was used to operate the system, which further helped in the rapid modification, reconfiguration, and distribution of the control system. This system is also a newly developed system and no results are reported anywhere. However, author have claimed that the system will be used to study effect of high ambient pressure in LPBF.

Masmoudi et al. [57] have used a customised LPBF system which allowed LPBF under vacuum down to 0.1 mbar in a controlled atmosphere. The system was fitted with stepper motor built scanning system inside the vacuum chamber. The author demonstrated validation of multiphysics models by comparing temperature profile of melt pool, size and depth with simulated profile. Combined with laser-powder and atmosphere interaction for vacuum and argon atmosphere.

In the literature, simple LPBF systems have been reported for example single base plate and manual powder spreading with an open optical system for co-axial melt pool imaging. One of such systems was reported by Matthews et al. [58]. They have developed a powder test chamber which can handle vacuum up to 0.6 mbar. In this, the spreading system was manually operated and can only do single layers. The gas flow system is also a handheld one to blow argon over the powder bed. The system was used to understand the denudation mechanism of single tracks in the vacuum. Islam et al. [59] developed a test bed setup and characterised the powder bed fusion process of stainless steel with two different test setups. The first setup comprises a simple processing chamber with a mechanical powder spreading system and a 200 W IPG Fiber laser with Scanlab scanner optics. The second setup utilised an EOS research system EOS M270 with 200 W IPG fibre laser. In both the setups, the process chamber was filled with a nitrogen atmosphere and for monitoring a Thyssen Laser-Technik TCS pyrometer and a Baumer CMOS camera with Cavitar CAVILUX diode laser illumination was used. The author demonstrated that both setups showed similar results of the build quality [59].

Most of the modular LPBF systems reported in the literature are in the development phase and no detailed study or results are available except for the EWI LPBF system. However, the individual in-process studies are reported in the next section which also describes the type of LPBF system used.

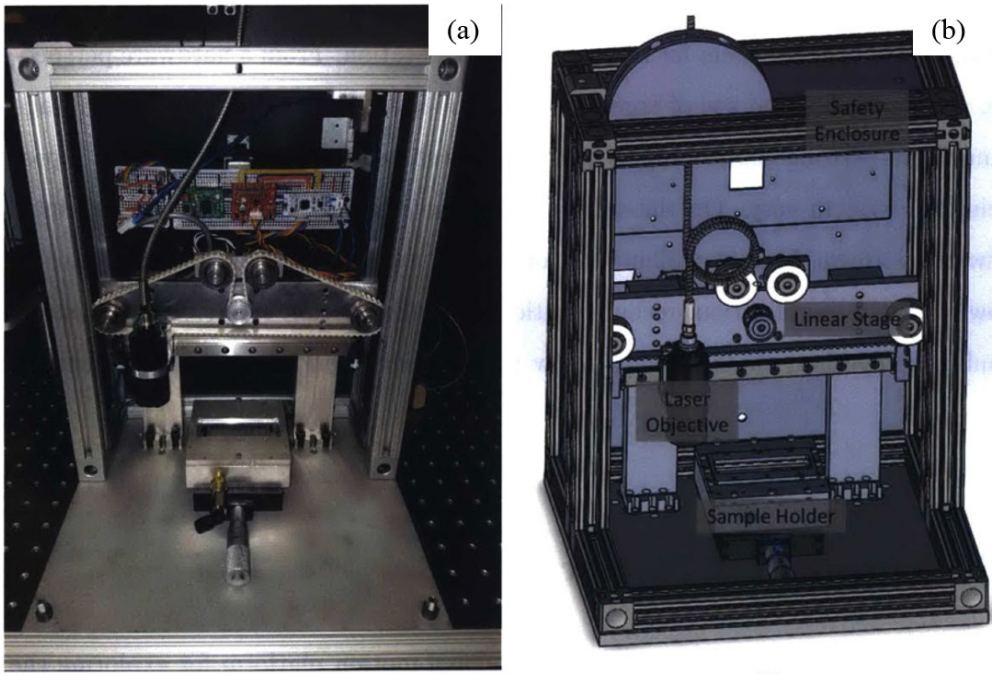

Figure 2.5: MIT's LPBF system, (a) actual systems in place and (b) CAD model [56].

2.4 In-process Studies

The reviewed literature is mapped with respect to different process signatures, process features, associated defects and in-process measurement done either on the modular LPBF systems or the modified commercial LPBF system. In addition, challenges that deserve further research efforts such as large amounts of data handling, the high sampling rate needed to capture fast process dynamics and the lack of variety of samples for highly customised products are also discussed.

In literature, the process signatures can be grouped into four major categories, depending on the level of detail required for process measurements. These categories are: (i) the melt-pool, (ii) the build chamber, (iii) the powder bed (iv) and, the part. The term "build chamber" refers to the closed environment where the part is built: it comprises shielding gas, metal vapour, fumes, plasma, base plate etc. Whereas the term "powder bed" refers to the thin layer of loose powder deposited by the recoating system. The term 'part' refers to consolidated material after laser melting such as a single track, area and multilayer built. Benchmarking of these signatures and respective in-process studies are important to

this work to find gaps in the research, understanding signature characteristics and limitations of different optical sensors. This will further help in establishing a motivation and building a robust open-architecture LPBF system for in-situ process measurements.

2.4.1 Melt Pool

The melt pool is a primary feature of interest in any process that involves a laser beam-material interaction aimed to achieve local fusion of the material. The stability, dimensions and fluctuations of the melt pool determine the stability of the process and quality of the parts [60]. In the literature, four fundamental melt pool-related quantities were considered for measurement purposes: (i) the size (i.e. the area top and side, depth area), (ii) the shape (ellipticity), (iii) the temperature intensity (average or cumulative), and (iv) the temperature profile (1D profiles along the transversal and longitudinal direction or 2D profile over the entire area). The size, shape and temperature of the melt pool are predominantly affected by the process parameters. They strongly influence the porosity, the presence of un-melted particles and the partial melting of powder particles within the bulk material, cracking and delamination together with the development of residual stresses [61,62]. The melt pool features the highest level of detail for in-process monitoring, which also imposes several challenges from the measurement aspects. First, the in-process measurement system must be able to measure the characteristics of a small region (a few microns) with a sufficient spatial resolution and contrast. Second, a very high sampling frequency is needed, since the scanning speed in LPBF is in the order of thousands of millimetres per second.

Size and shape:

Melt pool depth, width and length are known to be the most important dimensions which are often being measured and compared with process instability. A research group from the Katholieke Universiteit Leuven [63–65] has developed a co-axial monitoring system which is shown in Figure 2.6(a). The optical set-up included a high-speed NIR CMOS camera and a photodiode. The laser beam was reflected by a partially reflective mirror towards the scanner, and the same mirror enabled the radiation emitted by the melt pool to be captured by the two sensors. The partially reflective mirror reflects the laser (1064 nm) towards the laser source, whereas the radiation at other wavelengths passes through the mirror. This radiation was then split towards the two sensors, which were both sensitive to wavelengths in the range. The incoming radiation was integrated into one value representing the melt pool intensity. The NIR camera was equipped with a 1280 × 1024 pixel CMOS sensor that enables determination of the geometry and temperature distribution of the melt pool. The

camera was used to determine the shape and size of the melt pool. The sample rate for both the sensors was 10 kHz [66]. Kruth et al. [67] and Craeghs et al. [68] have developed similar setup on commercial systems. Figure 2.6 shows melt pool monitoring (a) co-axial imaging setup for LPBF (b) thermal camera image of melt pool [62] and (c) CCD camera profile of melt pool [66]. This kind of co-axial setups with CCD or CMOS camera can be great tool for visualisation for laser-powder interaction, though, these studies have only focused on the melt pool emission mapping for part-process failure.

Zhao et al. [69] used synchrotron radiation to image the interaction of 1 ms laser pulses with a powder layer at 50,000 fps. The entire process of melt pool evolution and the keyhole cavity formation deep inside the base metal is revealed in considerable detail using high-speed x-ray imaging. The dimensions of the melt pool as a function of the laser heating time is reported.

Temperature intensity and profile:

A co-axial monitoring setup was presented in [70,71], a two-wavelength pyrometer connected to the optical unit of laser scanning system by an optical fibre was used to capture the melt pool temperature intensity. The pyrometer includes two InGaAs photodiodes with a temperature range of 1200–2900 K, a transmission spectrum at central wavelength 1260 nm with a 100 nm bandwidth; spot diameter area was 560 μm. In addition, a CCD camera with a resolution of 560 x 760 pixels was used to measure the image brightness profiles along the transversal and longitudinal directions. The sampling frequency used was 20 kHz [1], with a scanning velocity of 0.12 m/s. Similar setups were implemented on commercial systems by [72,73]. Figure 2.7 shows the temperature intensity of the melt pool (a) distribution of the brightness temperature along the laser scanning direction at 50 W and 0.1 m/s [70] and (b) temperature distribution during melting of SS316L at 30 W and 0.3 m/s [73].

Similarly, a co-axial set-up was proposed by Gestel [62] where one or two CMOS cameras (with wavelength sensitivity between 400 and 1000 nm) were used to determine the melt pool size, shape and intensity. Another version of the co-axial monitoring set-up for LPBF was proposed in [74,75] with two major differences: the presence of a co-axial laser illumination source and a pre-focusing unit. The pre-focusing unit was applied to avoid axial and lateral chromatic aberrations due to the different imaging properties of f-theta lens at wavelengths different from the processing one. Specifically, it enables the focal plane to be the same at every wavelength of interest. The illumination beam is

deflected by a beam splitter and transmitted to the dichroic mirror. The radiation emitted by the melt pool is transmitted through the dichroic mirror and the beam splitter towards a high-speed camera and a pyrometer.

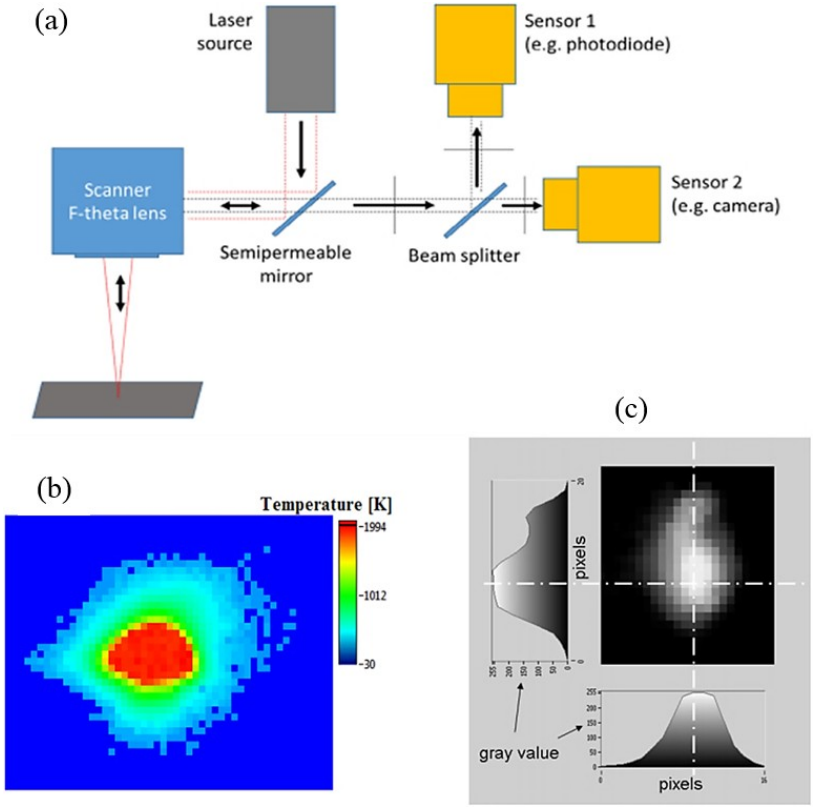

Figure 2.6: Melt pool monitoring (a) co-axial imaging setup for LPBF (b) thermal camera image of melt pool [62] (c) CCD camera profile of melt pool [66].

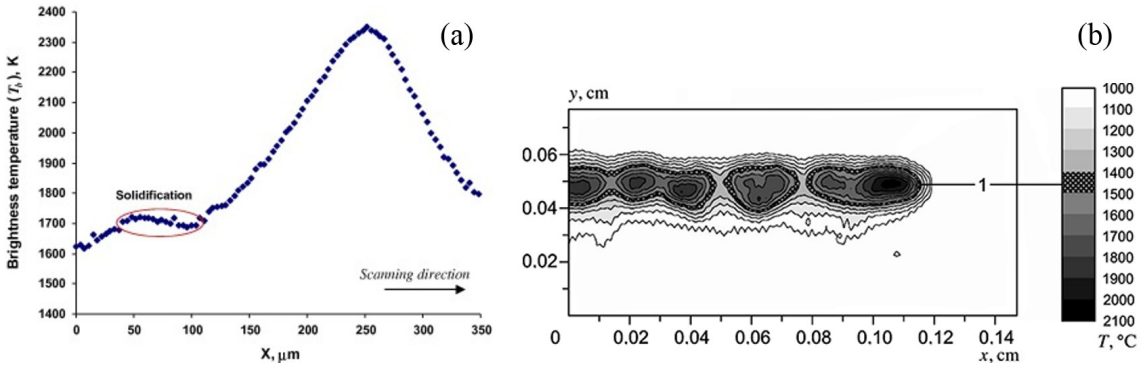

Figure 2.7: Temperature intensity of melt pool (a) distribution of the brightness temperature along the laser scanning direction at 50W and 0.1 m/s [70] (b) temperature distribution during melting of SS316L at 30W and 0.3 m/s [73].

Light emitted from meltpool and plasma is the primary source for in-process monitoring for shape, size and temperature measurement; so mainly photodiodes and optical cameras are used for such measurements. Meltpool and plasma above emits light in broad spectrum range from visible to infrared wavelengths. In order to measure the correct meltpool shape,

size and temperature, the light from the plasma needs to be avoided. Such setups with high magnification optics can generates better images for laser-powder interaction, which is missing in these studies.

2.4.2 Build Chamber

Functional performances of the part are not only affected by the melt pool but also severely affected by the build chamber properties. In addition, the build chamber healthiness also affects the machine itself in the long run; deteriorate machine's performance and can damage lenses, the base plate and filtrations systems which could further affect the process [76]. The build chamber is an enclosed pressure regulated box made of metal mainly steel, which constitutes gas flow inlet and outlet systems, laser input window, lighting systems, baseplate, powder scraper. In the literature, four main build chamber signatures were considered for in-situ, and post-process monitoring: (i) spatter, (ii) fumes and metal vapour, (iii) shielding gas, (iv) base plate temperature/strain. The direction of spatter and the amount of spatter provide relevant information for the determination of balling phenomena, lack-of fusion or melt pool depth (keyhole or conduction mode) and porosity formation [77]. The metal vapour, fumes and plasma ejection are relevant to characterise process stability in terms of denudation and process disruptions that affect the quality of the part. Shielding gas not only protect the melting material from oxidation but also help in removing the process by-products [78]. In addition to the shielding gas flow rate, the height of the flow straightener from the powder bed and the type of shielding gas affects the build quality mainly porosity and microstructure [76]. Other features such as baseplate temperature and strain measurement help in minimising the residual stress in the built part [79]. Analogously to the monitoring of these process features imposes challenges in terms of required spatial and temporal resolution of the in-situ sensing system.

Spatter:

Spatter are the molten metal balls ejected from the melt pool. In the literature, many different mechanisms for the formation of the spatter have been mentioned. The spatter are entrained in the induced gas flow and move over the powder bed, the direction of movement depends on specific scanning parameters. More spatter show the unstable process. Furthermore, this spatter can form inclusion in the build parts and inhibit different microstructure as they cool faster than the bulk part. In addition, it affects surface finish of the top layer as these are 3-5 times larger than the powder particle and stick to the surface

[80,81]. In the literature, monitoring of spatter was mainly done by high imaging direct/thermal imaging techniques.

Bayle et al. [82] measured the spatter ejection (ejection of liquid droplets) at different operating conditions mainly stable and unstable conditions. For this, experiments were carried out on PHENIX-PM100 machine equipped with a 50 W CW fibre laser with laser spot size 80 µm. The powder used was stainless steel 904L powder from OspreyTM, with granulometry 95% of powder with less than 16 µm size and powder layer thickness was set to 40 µm. For imaging, an infrared camera and pyrometer were mounted inside the build chamber. In addition, a 25 mm objective was used, coupled to a ring lengthening piece in order to increase magnification and improve spatial resolution. The acquisition frequency was varied from 2031 Hz up to 3556 Hz by reducing the size of the imaging window. In the process, the beginning of the scanning line, intensive removal of liquid metal droplets was visible. As it can be seen in Figure 2.8, droplets are ejected mainly in the direction of the laser beam scanning, the size observed was much larger than the size of the deposited powder and measured velocity was in the range 0.5–5 m/s. The author suggested that particles are emitted in the direction of beam displacement, similar to billiards game, except very few of them, which are emitted in the opposite direction (Figure 2.9). Further results show the velocities of the particles travelling backwards were much lower than those travelling forward. These are important observations by the author and relevant to the work done in this thesis. However, captured images lack magnification and show poor contrast making it difficult to see individual powder particles.

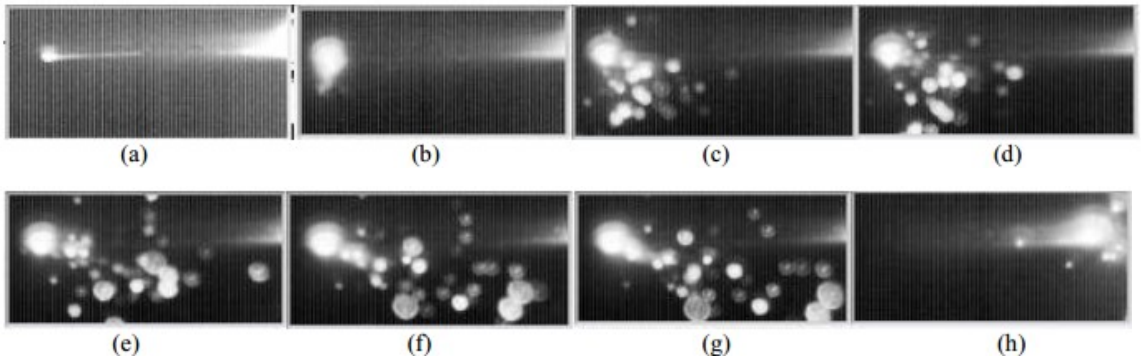

Figure 2.8: Thermal camera image of the spatter (a-d) beginning of melting and spatter balls ejection, (c-g) explosion and ejection of larger balls from the melt pool, (h) end of scanning vector [82] .

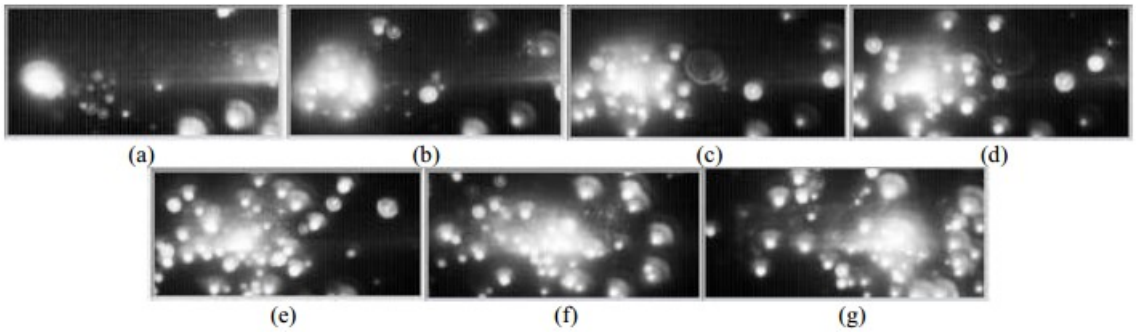

Figure 2.9: Thermal camera images captured with acquisition frequency f=2031, (a-g) Spatter travelling in forward and backward during laser melting [82].

Repossini et al. [77] developed off-axial setup to acquire and characterise the spatter-related information during the LPBF process on Renishaw AM 250 machine. The spatter formation was imaged in under, over and normal melting conditions. In-situ image acquisition equipment consisted of a high-speed camera (Olympus I-speed 3 with CMOS sensor) in the visible range (about 400–700 nm) placed outside the protective window of the build chamber as shown in Figure 2.10(a). The high-speed camera was equipped with a Tamron SP 17–50 mm F/2.8 lens, images were acquired at 1000 frames per second. Patterns of spatter spatial spread under different melting conditions in the two builds were included in experimentation. It has been shown that the number of spatters observed in normal melting conditions was lower than the number in under- and over-melting. In addition, the under-melting state yields a similar number of spatters to the one in the normal melting state, with a comparable spatial spread but with a smaller average area. Whereas, the over-melting state yields a more substantial number of spatters than the normal-melting state with a larger spatial spread, but with a smaller average area (Figure 2.10(b)).

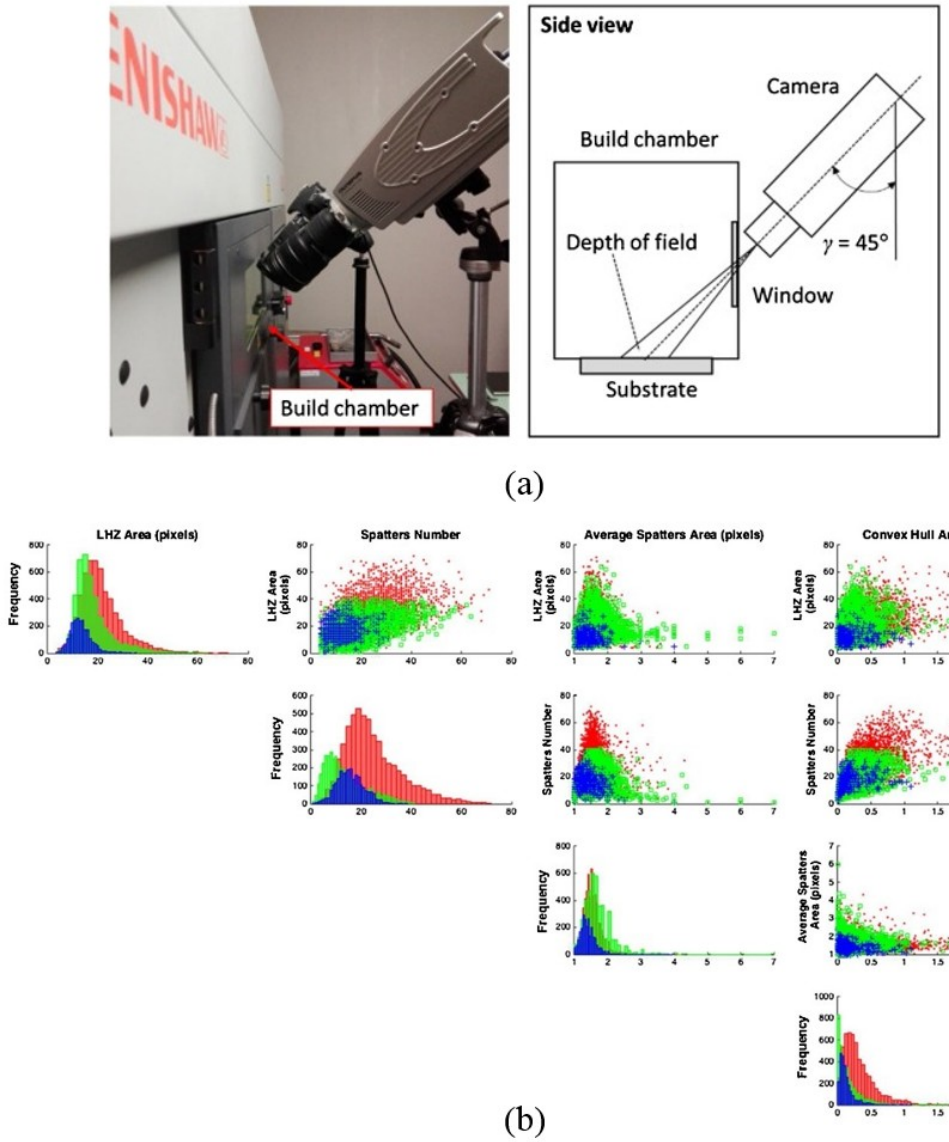

Figure 2.10: Fig. 10. (a) Off-axial setup (b) Scatterplot of spatter and LHZ descriptors; blue crosses: under-melted, green squares: normal-melted, red circles: over-melted. (scan direction left to right) [77].

Lane et al. [83] developed off-axial setup (45° viewport) on EOSINT M270 machines. Experiments were carried out using an extended sensitivity range InSb camera (< 1 μm to 5.3 μm) to measure lower temperature phenomena. In order to measure at shorter wavelengths, a commercial off-the-shelf (COTS) 50 mm short-wave infrared (SWIR) lens and filters were used. In the results, hot particles could be seen being ejected from the melt pool generally opposite the laser scan direction. In addition, based on motion blur elongation and camera integration time, particle velocities were calculated and observed to range from almost stationary to between 11.7 m/s and 15.3 m/s. In the setup optical resolution was limited to measurement of smaller particles, though some ejected particles were observed that exceed 200 μm diameter.

Liu et al. [81] experimented on SLM machine DiMetal-100 fitted with a 200W fibre laser. High-speed photography was used to understand spatter behaviour during single track experiments. Furthermore, the influence of energy input on spatter behaviour (size, scattering and jetting height) was investigated by adjusting the laser power. Consequently, two different types of spatter were identified: droplet spatter and powder (sideways) spatter. Author reported that energy input affects spatter behaviour, including spatter size, scattering state and jetting height significantly. The general trend was that the higher energy input leads to intense spatter generation.

Qiu et al. [61] undertook a systematic study of the effect of laser scan speed and powder layer thickness on porosity using a commercial Concept Laser M2 system. SEM images of sample surfaces revealed an increase in surface roughness and weld track irregularity when either the scan speed or powder layer thickness were increased above certain (process-specific) thresholds. Increases in surface roughness were correlated with an increase in internal porosity. High-speed videos were recorded at 10,000 frames per second (fps) through the system viewing window. The optical resolution of ~150 µm per pixel was insufficient to resolve individual powder particles and their interaction with the laser, although the number of incandescent powder particles ejected backwards from the melt pool was observed to increase with increased thickness of the powder layer.

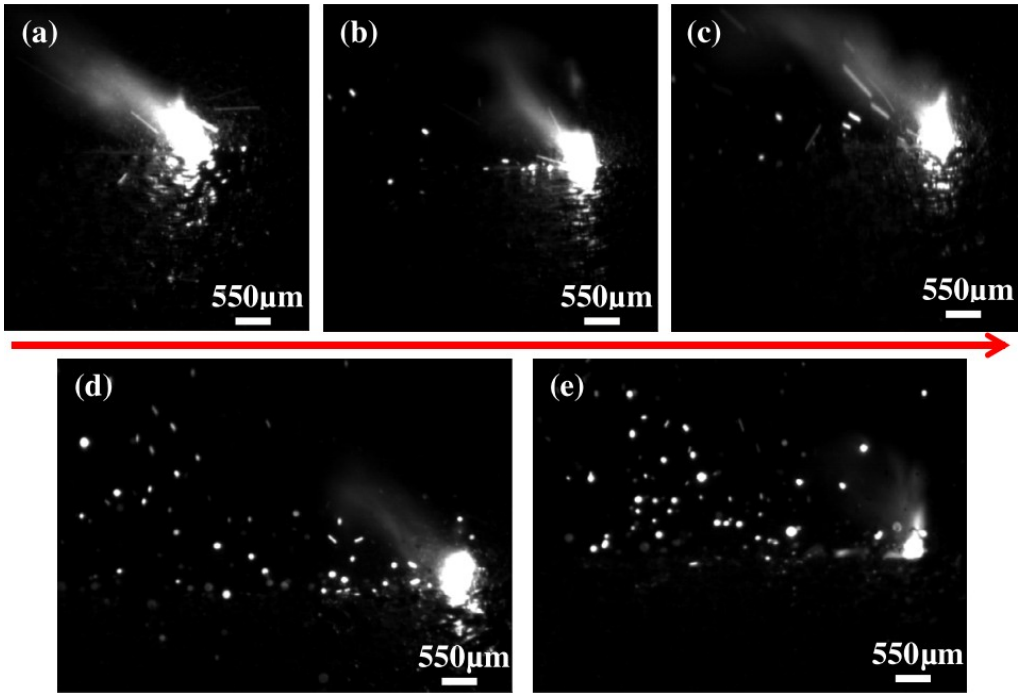

Figure 2.11: High speed imaging showing the interaction between the laser beam and powder layers at specific settings [47], the images show increase spatter with increase in layer thickness (a) 20 µm; (b) 40 µm; (c) 60 µm; (d) 80 µm; (e) 100 µm. The arrow shows the laser scan direction [61].

After reviewing the literature, it is clear that, it is extremely challenging to record images through the viewing window of commercial LPBF systems with sufficient magnification or contrast to see individual powder particles in the powder bed.

Fumes and metal vapour:

After the shielding gas, build chamber comprises fumes and metal vapour ejected from the melt pool, though, quantity is small in the build chamber compared to shielding gas, but concentration above the melt pool is significant. In common, generation of these products are associated with laser material processing; generation quantity is dynamic and mainly depends on processing parameters. In LPBF, the shielding gas blows the fumes and metal vapour away from the build chamber continuously through the outlet. However, sometimes due to unexpected process dynamics and inefficient gas flow, the extraction is not entirely 100%. It is known from the literature [60], that the fumes and generated metal vapour absorb the laser power and could further go into a stage of ionisation and resulting in plasma. Furthermore, the laser absorption in plasma can further reduce the laser power availability at the powder bed. Metal vapour and fumes also could contaminate the powder, the optical window and the build part. In-situ measurement of metal vapour or fumes has not been reported yet for LPBF. There are significant measurement challenges for the application of sensors and their limitation of installation near to the melt pool. There are few cases in the literature where researchers have observed and highlighted the generation of metal vapour which is explained below.

Ly et al. [84] reported metal vapour jet which causes induced gas flow and particle movements. The author carried out experiments, creating ultra high-speed image sequences of the laser-driven melt pool motion for tracks produced on a flat metal substrate recorded and compared them to those recorded for a substrate covered by a layer of metal powder and with the simulation results. The author claimed that the effect of a vertically-oriented metal vapour jet is causing a low-pressure region and pulling in the surrounding gas. The setup includes, a 600 W fibre laser (JK lasers, model JK600FL) was directed through a 3-axis galvanometer scanner into a $15 \times 15 \times 15$ cm^3 vacuum chamber through a high purity fused silica window. Then, the vacuum chamber was evacuated using a pump and subsequently purged with Ar.

An ultra high-speed camera with an optical resolution of ~5 μm with microscope optics was placed outside the chamber to image the melt pool. Imaging was performed at up to 100k fps frames per second (fps) using either a 700 mW, 638 nm CW diode laser or

a low coherence 810 nm to illuminate on the surface. Author claimed that, the inward flow of the ambient gas is sufficient to entrain powder particles, which can become incorporated into the melt pool or ejected with the metal vapour. Imaging of the melt pool with an optical resolution of ~5 μm per pixel enabled this particle motion to be observed, with particles ejected backwards with respect to the scan direction (Figure 2.12) or vertically upwards, depending on the process setting. These single track and single spot measurements prove useful for informing powder-level numerical models but are not part of a characterised build process. The experimental system for imaging comprised scanning a single laser track in a powder layer that had been spread manually on to a metal substrate, protected with an inert gas from a localised jet.

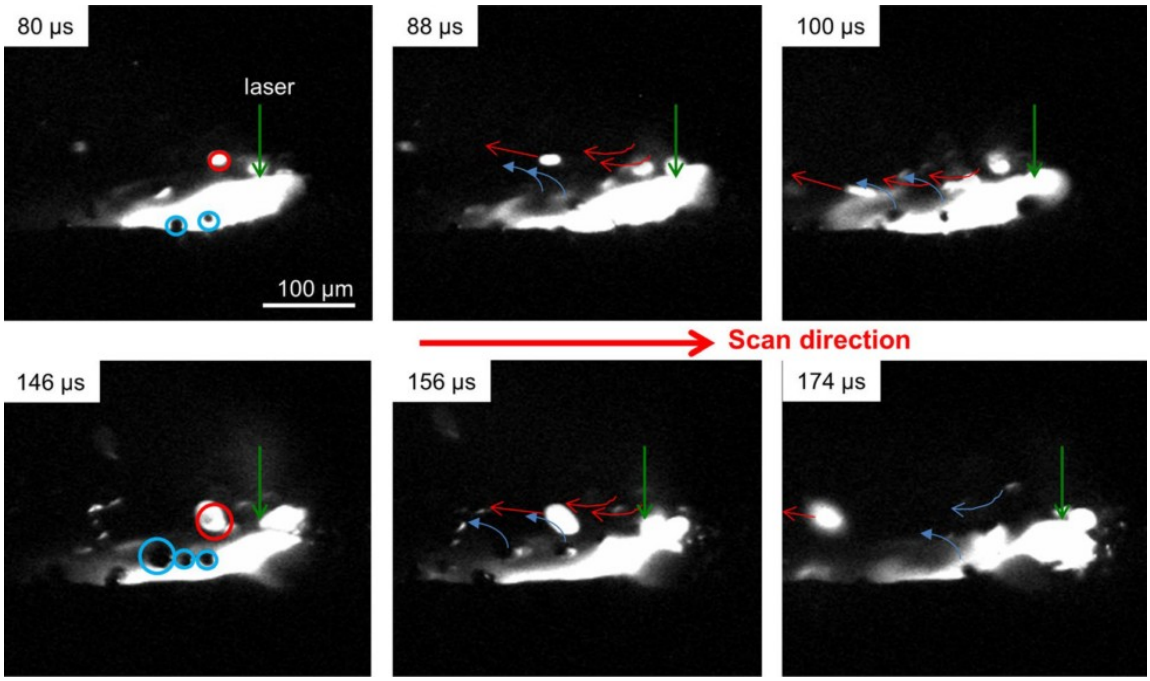

Figure 2.12: High resolution images of the melt pool formation and ejection recorded at 100k fps by [84], the images show rapid heating and incandescence of the entrained particles, As the laser is scanned from left to right, particles are observed being swept up and backward with the arrow denoting the movement.

Matthews et al. [58] reported high-speed imaging at 500K frames per second, exhibit that the metal vapour flux emitted from the melt pool at low pressures may sufficiently expand into a wide plume as compared to a narrower jet at higher pressures. Typical experimental parameters show intensive evaporation of metal within the melt pool. The author also observed that the metal vapour was expelled normal to the surface with a velocity close to the thermal velocity associated with the surface temperature. The author further investigated in the same article that the depletion of metal powder particles in the zone immediately surrounding the solidified track (denudation), which can affect porosity and surface roughness. It was proposed that denudation at ambient pressure is caused by the

intense evaporation of metal vapour from the melt pool, which produces an inward flow of the ambient gas towards the melt track due to the Bernoulli effect (Figure 2.13). Images recorded shown poor contrast and are focussed on the melt pool whilst scanning a single laser track in a representative powder layer.

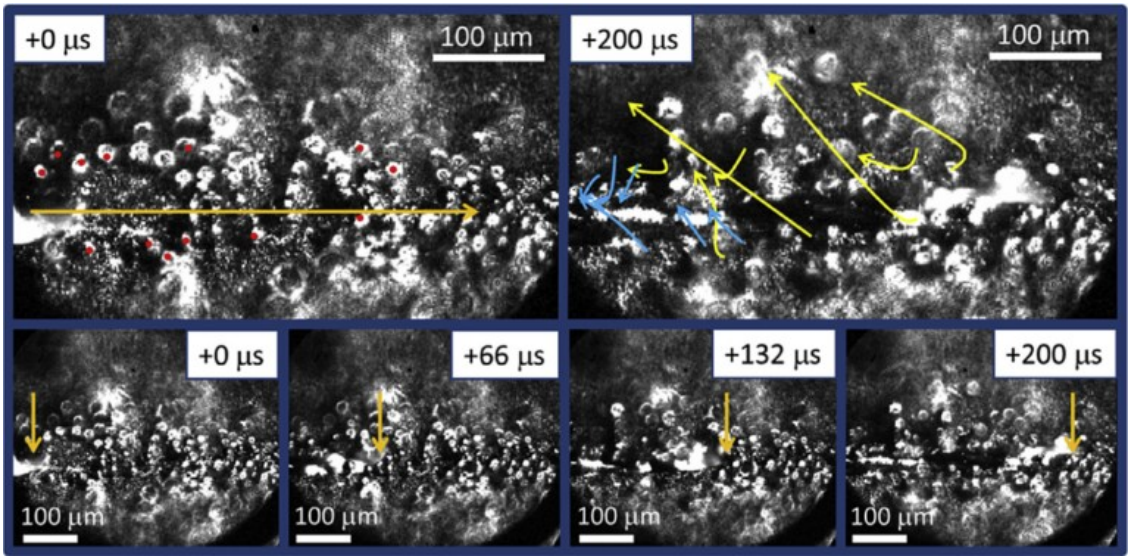

Figure 2.13: High speed imaging of melt track progression and powder movement under the influence of the metal vapour Bernoulli effect. The images show particles being incorporated into the meltpool and ejecting rearward direction relative to laser scan direction [58].

Gunenthiram et al. [85] noted the complexity of performing diagnostics during the LPBF build process and so recorded single track images in a similar system to [58] but with a powder layer that moved on a translation stage below the laser. The motion of powder particles towards the melt pool due to the metal vapour was again observed, but again high magnification on the melt pool prevented the formation of the denuded region from being imaged

Zhao et al. [69] used synchrotron radiation to image the interaction of 1 ms laser pulses with a powder layer at 50,000 fps. Vapour-driven particle motion was observed and, additionally, the dynamic keyhole development beneath the powder bed could be seen. In this case, the powder bed was only 450 µm wide to enable transmission of the x-rays and a single laser spot was illuminated.

As seen in the literature, higher magnification images have so far focussed on the melt pool whilst scanning a single laser track in a representative powder layer, and have been published since the start of this PhD. To date, the behaviour of the powder bed away from the melt pool has not been imaged, nor have the effects of scanning adjacent tracks and multiple layers during a full build been investigated, apart from the work reported in this thesis.

Shielding Gas:

Shield gas is used to create an inert atmosphere which protects metal from oxidation during laser melting. Researchers also claimed that it increases weldability and enhance the quality of weld significantly [86,61]. The most common shielding gases used in the laser melting are argon (Ar), Nitrogen (N), Helium (He), Carbon dioxide (CO_2) and mixtures of all these gases. In the LPBF, shielding gas serves dual purpose, first, protect the melted metal from oxidation and second, remove process byproducts like smoke, spatter, metal vapour and ensure the chamber is clear. There are several features of shielding gas and gas flow system which affect the part significantly such as the type of shielding gas, ionisation potential, flow rate, inlet system design (nozzle diameter and height), outlet temperature and recycling efficiency. Standard systems are available for in-situ monitoring of the shielding gas general properties such as temperature, flow rate etc. The more challenging is the in-situ monitoring of interaction of the melt-pool and shielding gas during the build. In the literature, in-situ visualisation (monitoring) of LPBF is not reported, but there is some work from welding gas flow visualisation which is explained in the next paragraph.

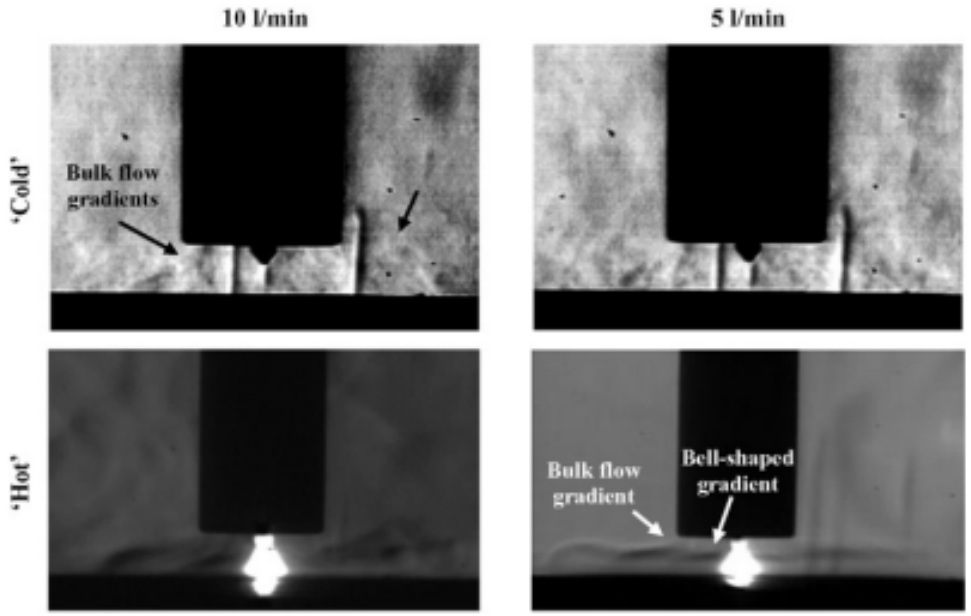

Figure 2.14: Gas flow visualisation mainly density gradient using schlieren imaging during TIG welding of hot and cold flows [87].

Bitharas et al. [87] reported a high-speed schlieren imaging setup to visualise alternating shielding gas flow in GTAW welding process. Schlieren imaging facilitates observation of transient flow features during GTAW, due to change in refractive index gradient. Setup includes, two 100 mm diameter, parabolic field mirrors with a focal length of 1.27 m were located approximately two focal lengths apart. The system was aligned in a Z-type arrangement; the first mirror collimated the light from the light-emitting diode (LED)

source whereas the other mirror focused it to a spot. In the results, a 13% increase in weld penetration was observed with the alternating shielding gas method compared to the 'pre-mixed' case reported. Figure 2.14 shows the steady-state schlieren images of shielding gas flow (argon) during TIG welding process, with the arc (hot) and without the arc (cold). Furthermore, flow gradients, bulk flow and turbulence near to the melt pool are visible in the Figure 2.14.

Dadbakhsh et al. [88] have done a post process study on effects of gas flow in LPBF using a commercial system MCP Realizer SLM machine. Argon gas was pumped into the chamber, and a cross draft is maintained in order to keep the O_2 level below 0.9 percent. The study showed that gas flow direction can influence the quality and mechanical properties of stainless steel parts produced by the LPBF process. Furthermore, the temperature distribution and cooling rate fo the part affected by the build layout; gas flow influence deformations appearing in final parts. However, homogeneous temperature distribution could be achieved by laying the parts perpendicular to the gas flow, the results into decreased delamination.

In the laser powder bed fusion, no such in-situ shielding gas flow visualisation and optimisation techniques have been reported.

Base plate (Temperature/Strain):

The build plate also known as the base plate is the support plate where the part is built layer by layer. Its primary purpose is to support part from delamination or warpage. Temperature and strain (deformation) are the two most important features associated with the base plate and to be continuously monitored to produce geometrically accurate parts. The key challenge is accessibility for such sensors if it is not part of commercial systems. In order to keep the build chamber sealed, no measurement equipment or wires can breach the seal that surrounds the build chamber without significantly modifying the machine. A few of such in-situ measurements reported in the literature are explained in next paragraph.

Dunbar et al. [89] reported an enclosed instrumented system named "vault", is designed to be used in the LPBF machines. The vault was designed to bolt into the build plate without requiring modification to the machine. The machines and material used in this experiment were EOSINT M 280 AM machine and Inconel 718. The vault, shown in Figure 2.15, is designed in such way that all measurement systems can be placed inside of the machine while keeping it separated from the metal powder. Furthermore, a 0.81 mm thin substrate is used to maximise distortion from the build. Distortion measurements are

completed using the M-DVRT-3 Lord Microstrain differential variable reluctance transducer (DVRT) displacement sensor. The DVRT produces in-situ measurements of the displacement in the build direction throughout the build process. Temperature measurements were completed using K-Type thermocouples. The results were recorded for the systems using a small low power computer placed inside the vault. All measurement systems were attached to the lower face of the substrate to prevent obstruction of the LPBF build process. The experimental results show that using a constant scan pattern causes increased distortion in the build by 37.6% as compared with the rotating scan pattern for the build geometry. Furthermore, the results of the experiment are compared with the simulated distortion.

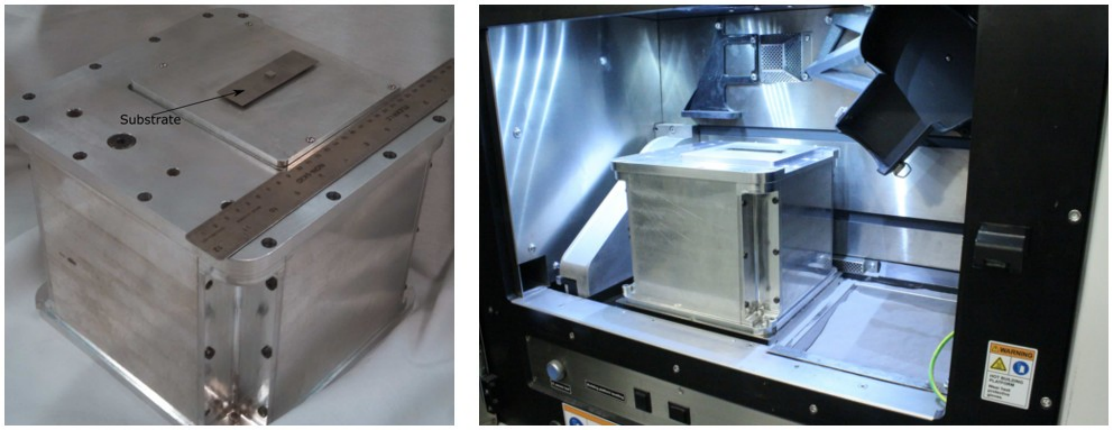

Figure 2.15: The "vault" system designed for in-situ temperature and strain monitoring from the commercial powder bed machine [89].

Sutcliffe et al. [90] reported a built in residual stress dynamometer for in-situ strain measurement, was designed to be fit in with the baseplate of Renishaw AM machine. The base plate built in dynamometer comprises 16 load cells mounted in parallel and two thermocouples under the base plate. Results were recorded at 100 Hz sampling rate for building pillars on induvial load cell, then building a solid block on the pillars. The measured results show that, stress was predominantly in the direction of scan; the order in which scan vectors are deposited had an effect on the residual stresses; and residual stresses are not just dependent on the material but also on the developed material parameters. Similar experiments for LPBF in-situ strain measurements using strain gauges in the bottom of the build plate have been reported by Shiomi et al. [91] and Van Belle et al. [92].

Wu et al. [93] reported post process residual stress measurement of the parts built using a Concept Laser M2 and stainless steel 316l. A digital image correlation method for measuring surface level residual stresses was presented and used in conjunction with the neutron diffraction method to assess the effect of specimen geometry and process

parameters, explicitly scanning strategies and laser power/speed, on residual stress development. Two types of specimens were built; first, L-shaped specimens were designed to facilitate neutron diffraction measurements. Secondly, prism specimens were built to highlight the effect of length scale on residual stress development. The 5 x 5 mm^2 island scanning strategy was adopted in the preparation of the L-shaped specimens. In the case of prisms, the scanning pattern was varied between a continuous scan, 3 x 3 mm^2 islands, and 5 x 5 mm^2 islands (with a hatch angle perpendicular to the base in both cases. The author claimed that combined stress-relief-via-sectioning and digital image correlation provide surface residual stress measurements without surface conditioning or finite element analysis. Results obtained using this approach are in good agreement with near-surface neutron diffraction measurements made on the same part Figure 2.16(a) and (b). Consequently, the author demonstrated the ability of this method to provide not only qualitative insight into process-induced residual stresses but also quantitative surface level residual stress measurements.

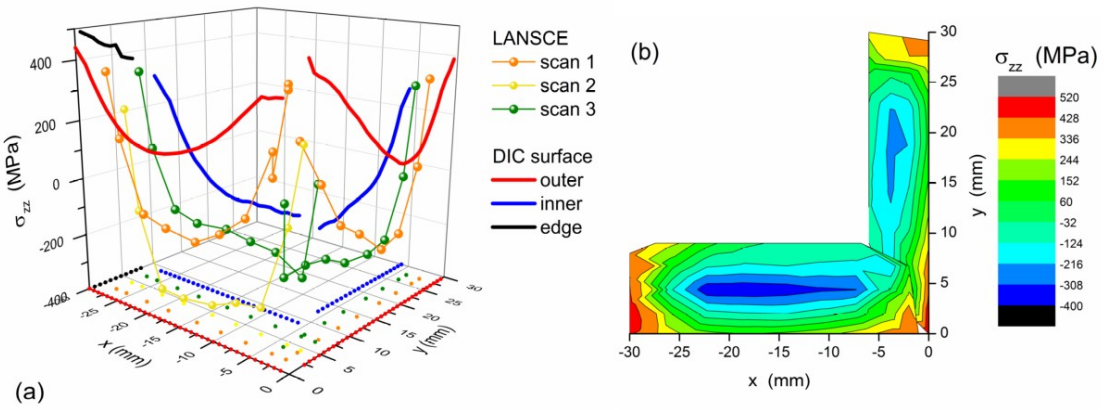

Figure 2.16: Residual stress measurement by DIC (sectioning) method and neutron diffraction for L shaped bracket at 400W and 1.8 m/s. (a) Contour plot (b) 3d plot [93].

2.4.3 Powder Bed

This category of observable signatures consists of the powder bed. In this case, in-situ acquisition can be performed after or during the deposition of the powder itself. The main quantities of interest are: (i) uniformity, (ii) temperature intensity/profile (iii) packing density (iv) laser absorption/scattering. In situ determination of these properties are important to detect defects caused in powder spreading due to recoater bouncing or particles/spatter dragging or other recoating system damages. In addition, the temperature stability from one layer to another and the temperature profile of each layer are additional features to be used to identify important process characteristics. A poor packing density,

inhomogenous powder bed and non-uniform temperature distribution can be a reason for increased porosity which can also change the powder bed laser absorptivity which could further result into over or under melting [94].

Homogeneity:

Homogenous thickness powder layer is vital for high density builds. However, measurement of such properties of the powder bed is not as difficult as the other process features discussed earlier. A simple low frame rate visual camera can be used, but still, the location of the camera is critical as the best suitable location is where the scanner is mounted.

Foster et al. [54] used an image-processing approach for the detection of local powder bed defects and the edge detection of the slice. These defects included unfused particles dragged across the bed and irregularities caused by a bouncing effect of the recoater (Figure 2.17). In the setup, a 36.3-megapixel single lens reflex (Nikon D800E SLR) camera in visible range was used, mounted inside the EOS M280 build chamber with multiple flash modules to collect multiple pictures with varying illumination both after the powder bed deposition and melting.

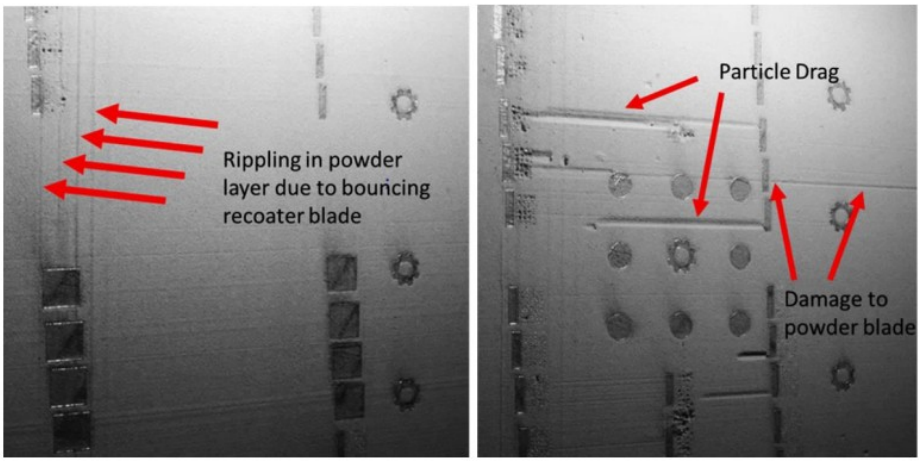

Figure 2.17: In-situ image showing powder layer spread defects due to recoater blade failure and sintered particle drag [54].

Erler et al. [95] proposed a topographic reconstruction of the powder bed for in-situ inhomogeneity measurement. For this, a 2D laser displacement sensor was used to form a 3D powder bed topography, aimed at detecting both the powder bed non-uniformity and the scanned surface irregularities. The sensor operates on the principle of optical triangulation, with a spot area of 40 × 25 μm. A linear axis system to move the sensor over the powder bed surface was used. In principle, the in-process detection of powder bed defects can be used to activate corrective actions, like a re-deposition of the powder bed

and, when possible, the substitution of a worn recoating system. It has been shown in the Figure 2.18 that the topography images, and histograms of good (Figure 2.18(a)) and inferior (Figure 2.18(c)) powder layer spread with a standard deviation of (Figure 2.18(b)) 6 um and (Figure 2.18(d)) 9.7 um.

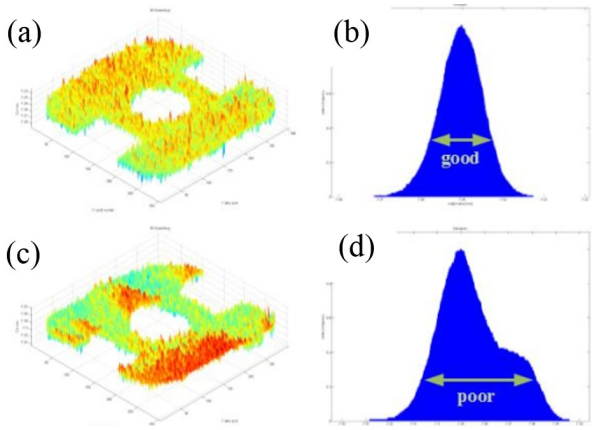

Figure 2.18: In-situ topography images and histograms of good (a) and inferior (c) powder layer spread; standard deviation of (b) 6 um and (d) 9.7 um [95].

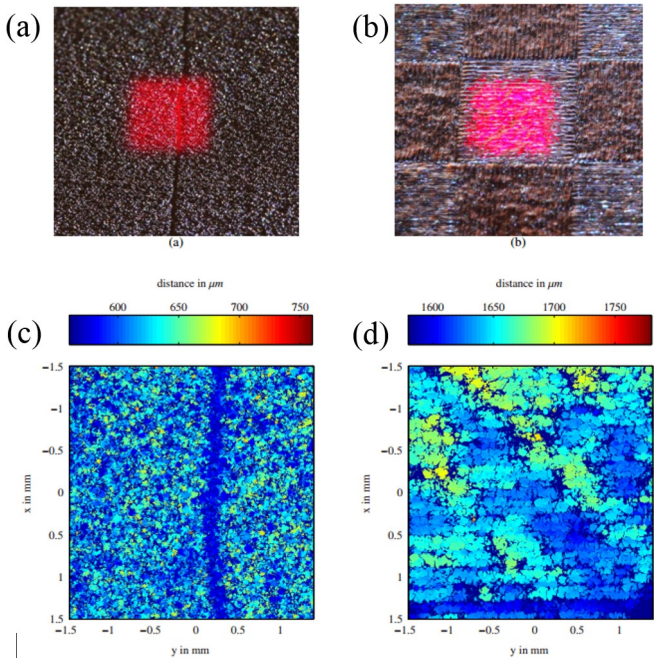

Figure 2.19: Low-coherence interferometric, (a) on powder layer, (b) on melted layer; resulting coloured profile plots, (c) on powder layer, (d) on melted layer [96].

Neef et al. [96] reported a co-axial sensing technique low-coherence interferometric also termed inline coherent imaging (ICI), suitable for co-axial monitoring of the LPBF process at high frequency. A typical ICI system consists of a low-power broadband light source, a high-speed spectrometer and fibre based Michelson interferometer. These sensors were integrated into an EOS M250 machine production setup. This approach is for powder bed uniformity analysis and monitoring of the surface slice patterns. The proposed setup is based on the sensor with a maximum scan rate of 70kHz. Results showed an example of

surface topology reconstruction for both loose powder and molten material as shown in Figure 2.19. A similar setup was used by Kanko et al. [97].

EOS GmbH [48] recently released software, called EOSTATE, that utilises an integrated a 1.3 Megapixel industrial camera in the ceiling of an EOS machine processing chamber. Images are taken after each layer and run through edge detection algorithms. Furthermore, data on the edges are stored to create a record of part layers. In the sequence, the recoating step is completed and a second image is taken and run through an edge detection algorithm. If any edges are detected, it signifies insufficient recoating. In the outcome, the process can be paused for evaluation or recoating can be repeated before continuing.

Temperature Intensity/profile:

The temperature of the powder bed can give us critical information about the build status, as one can compare the temperature throughout the process to understand how temperature is increasing. Furthermore, inhomogeneity in the powder bed temperature leads to change in microstructure and resultant anisotropic material properties. To some extent, it also affects the side surface roughness as a hotter region can attract loose powder particle from the bed.

Islam et al. [59] compared two different test setups by measuring temperature profiles and using on-line photography of the powder bed. The first setup was in-house developed and second used a commercial EOS M270. Both the setups included similar lasers and monitoring equipment (Thyssen Laser-Technik TCS pyrometer and a Baumer CMOS camera with Cavitar CAVILUX diode laser illumination). The process chamber had a nitrogen atmosphere, and the process parameters were kept the same in both cases. In the results, two test setups showed similar behaviour in the process temperatures according to the changes of energy input. Whereas, the maximum process temperatures were attained with energy inputs of approximately 1000 J/mm^3.

Wenger et al. [98] proposed two different setups by mounting two thermal cameras at different places aiming to integrate a thermal imaging system for the powder bed and melt pool into a laser sintering system (DTM Sinter station 2500). The first experimental setup allowed for observation of the entire powder bed surface for measuring the temperature distribution Figure 2.20(a). The scanner head was replaced by the thermal imaging system to observe the surface through the laser window. A wide-angle lens with a focal distance of 12 mm, resulting optical resolution of 1.5 mm per pixel on the powder

bed surface was used. This resolution was sufficient to analyse the temperature distribution. In the second setup, the camera was placed adjacent to the scanner head with an observation angle of 23°. This setup permitted measurement of the melt pool's temperature while the process was on. A telephoto lens with a focal distance of 50 mm was used. It has been shown in Figure 2.20(b) and (c), a camera image showing non-uniform temperature on the bed and the average temperature for single scan lines.

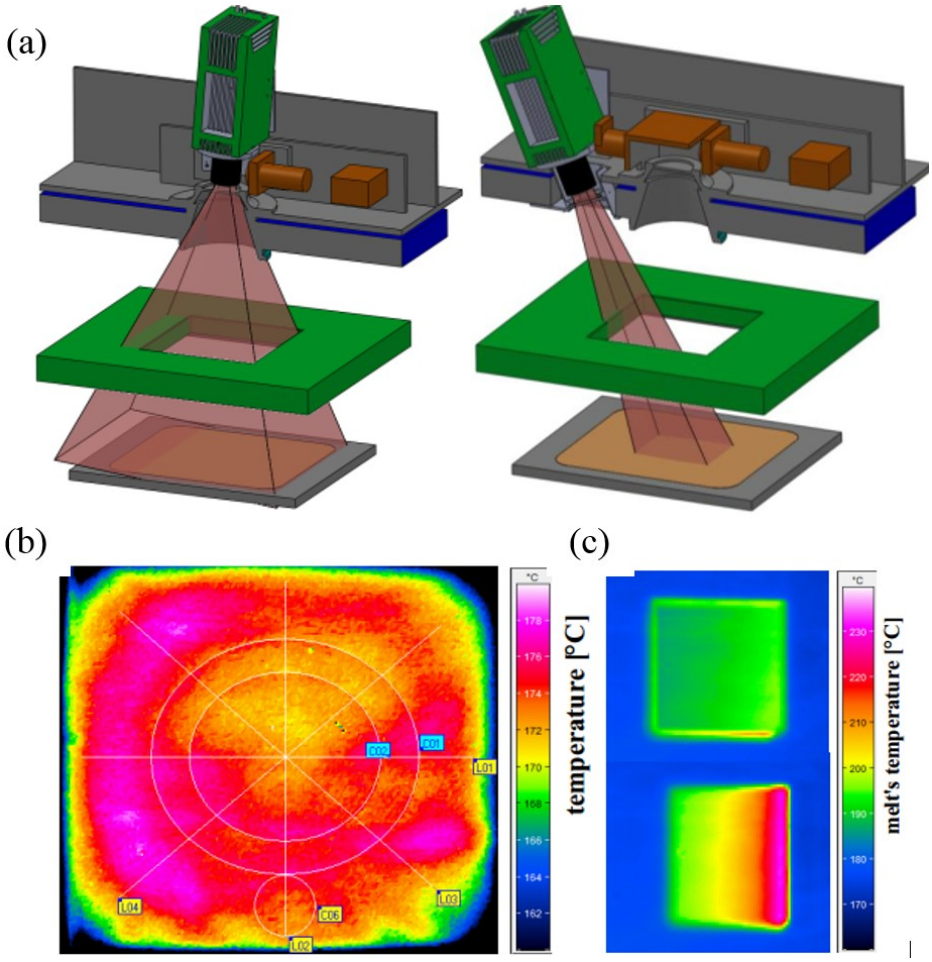

Figure 2.20: Temperature profile measurement; (a) setup, left after melting and right in-situ before melting. (b-c) thermal camera image of powder layer and the average temperature for single scan lines [98].

Packing density

Packing density (PD) of powder is critical as the higher PD leads to less porosity and high-quality parts [99]. In the literature, it is clear that PD mainly depends on the powder particle distributions and to some extent on the type of spreader. In-situ measurement of PD is challenging as the only the top is visible and visual cameras are not suitable for such measurements.

Jacob et al. [100] developed an in-situ specimen used to determine the powder bed density on the build plate inside a LPBF machine. In this approach, packing density was

measured by using a special container (Figure 2.21) which captures the powder spread over the build plate during the LPBF process, such that the powder can be removed without losing any powder or damaging the container shell. The author claimed that such an enclosed specimen would also protect the powder from the effects of post-machining, as well as any climate conditions until the density measurements could be performed. The container was a hollow cylinder with a conical lid which allowed the user to capture the metal powder from different locations on the build plate. This design also enabled the user to open the lid manually without removing any solid material from the specimen body and without contaminating the enclosed powder. The author described that the measurement method using the closed container approach is a robust and reliable in-situ method to determine the packing density of a LPBF machine.

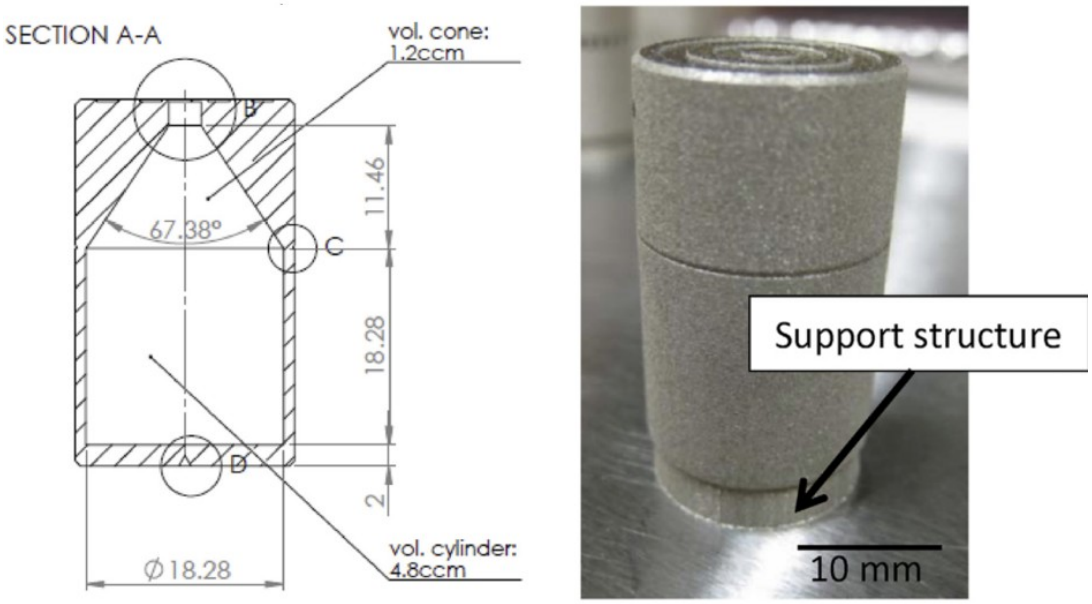

Figure 2.21: Container for packing density measurement, left cross-section and right specimen on build plate [100].

Kallman et al. [101] used the XCT (x-ray computed tomography) technique for powder packing density measurement. For this, two different powder materials were packed into 24 specimens of several physical densities that were independently measured using the total mass-volume method. The specimens were then scanned by the MicroCT system, the data analysed and compared in order to study the effects of powder characteristics on x-ray attenuation.

Absorption/scattering

Variability of laser radiation absorption can alter the part quality especially increased porosity due to under melting or over melting conditions. Furthermore, the absorption characteristics of powder layers in LPBF are dynamic and need to be monitored to select

optimal processing parameters. McVey et al. [102] conducted experiments to measure the amount of energy reflected and transmitted through the range of thicknesses of a preplaced powder layer using an integrating sphere. This technique was used to estimate the attenuation coefficients for pure Fe and pure Cu powders, each with three powder size distributions, during Nd:Yag and CO_2 laser irradiation. The laser power used was 8 and 12 W with an unfocused spot size of 0.5 cm diameter for CO2 and Nd:YAG laser respectively. A ZnSe beam splitter was used for the CO_2 laser, and a fused silica beam splitter was used for the Nd:YAG laser. An integrating sphere was used to integrate the laser energy obtained during transmission through, or reflectance from, the powder layer. In addition, a thermopile detector, in conjunction with a low noise amplifier, was used with the integrating sphere. A specially designed sample holder made of stainless steel was built to enable reproducible placement of varying powder layer thicknesses. Furthermore, the stainless steel holder utilised ZnSe cover glass and fused silica during CO2 and Nd:YAG laser irradiation, respectively, as a transparent coupling media between the powder and the integrating sphere. The holder employed an annular ring that allows the accurate thickness of the powder layer by "scraping" the powder layer across the ring. It has been shown that the greater beam penetration and a decrease in the estimated attenuation coefficients with the larger powder particles, the copper powder, and the lower wavelength of the Nd:YAG laser.

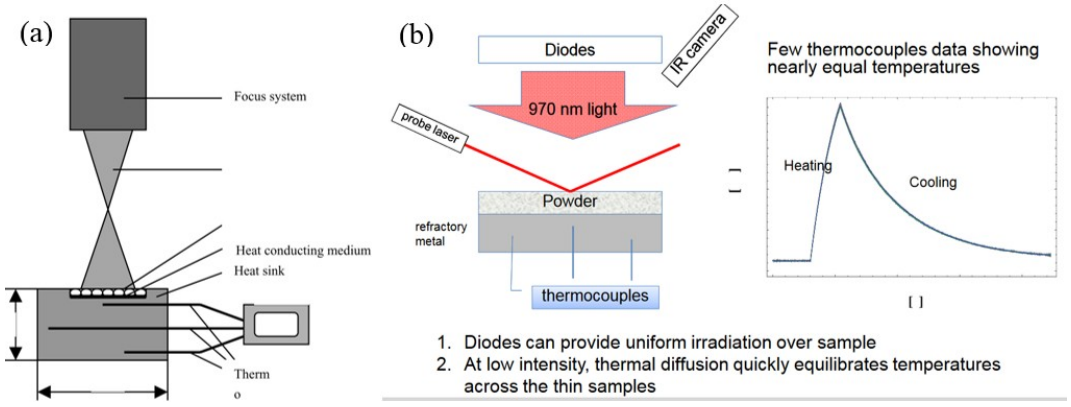

Figure 2.22: Absorption measurement test setups, (a) Shao et al. [103] (b) Wu et al. [104].

Shao et al. [103] presented a lumped method based on heat transfer for laser absorptivity measurement. The absorptivity of some powder materials such as Cu, Fe, Al, NiO, Al_2O_3, ZrO_2, SiC, to YAG laser was investigated. A test device was developed as shown in Figure 2.22(a). The powder materials to be measured were put onto a copper-made heat sink, a YAG laser was irradiated onto the powder material layer, and the temperature of the heat sink was measured. In order to control the measurement accuracy, three thermocouples were embedded to the top, the middle and the bottom of the heat sink. The laser was

irradiated for 20 s with power ranging up to 150 W. The results show that the absorptivity of powder materials to a YAG laser is higher than the bulk materials.

Wu et al. [104] developed a ray-tracing model and compared data with experiments to estimate absorptivity of material powder. The measurement was performed during heating and cooling period. Figure 2.22(b) explains the setup: diode laser radiates on to the powder layer and resulting increase in temperature was measured using three thermocouples in the bottom and IR camera from the top. A similar setup was reported by Rubenchik et al. [105].

2.4.4 Part

The part is the output of the process, is always crucial to monitor the condition of it while building. However, the part is buried in the powder, and only the top layer is visible for measurements. The layer (slice) dimensions and the melted layer properties such as flatness, surface roughness affect the overall part quality in terms of geometric dimensions and induced porosity. In the literature four main quantities related to build part are considered for in-situ measurements; (i) top and bottom temperature (ii) top surface roughness and edge effect (iii) deformation/strain (iv) single track geometry. There are several challenges to measure these features as one need a high-speed and high-resolution optics and a camera system. It is similar to fitting the high-speed microscope into the machine. Researchers have used different techniques to measure these features and more explanation can be seen in the next section.

Top and bottom temperature:

Temperature of the slice (top layer) can give information about the part stability with increasing height and if the temperature increases or decreases or shows nonuniformity; it can lead to process failure. High-temperature gradients and thermal nonuniformities of the part's slice cause residual stresses, distortions and influence the microstructure.

Furthermore, variations in wall thickness over the height can cause heat accumulation; mainly in the filigree part areas and can be detected by utilising thermographic monitoring during the build process either on-axis or off-axis [106,107]. In addition, necessary adjustments in the process parameters to achieve a homogeneous temperature field perpendicular to the build direction can be identified. Figure 2.23 shows the in-situ temperature measurement of turbine blade and investigations on macro scale simulations.

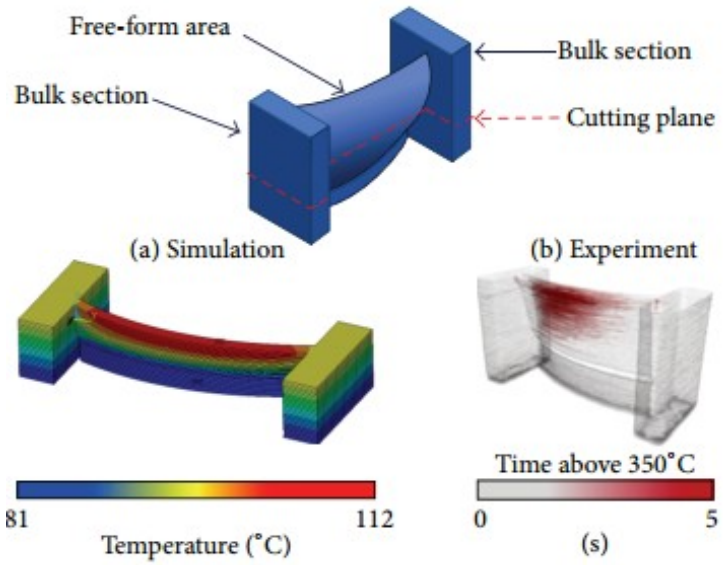

Figure 2.23: In-situ part temperature measurement and comparison, (a) simulated results (b) experimental results [106].

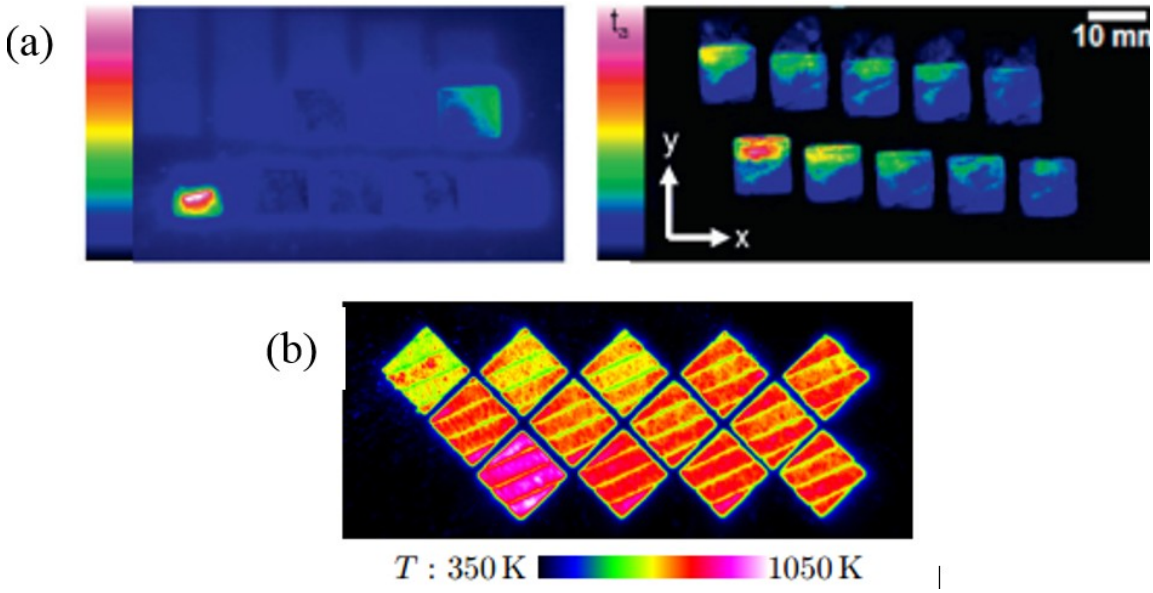

Figure 2.24: Top surface thermography, (a) single frame – melting start and finish, (b) maximum temperature measurement [108].

Krauss et al. [108] performed layer-wise monitoring of the temperature distribution of the part slice to gather information about the process stability. For this, integration of an off-axis mounted uncooled thermal detector to the build chamber of EOS M270 commercial AM machine (200W Yb fibre laser, the spot diameter of 70 µm) was done. The microbolometer thermal detector aimed at a view angle of 55 degrees on this platform, reached a pixel resolution of approx. 250 µm per pixel and operated at 50 Hz. In addition, the solidification of the layer was monitored that enabled the identification of hot areas in an early stage of built and helped to avoid process interruptions. Potential quality indicators

were identified from spatially resolved data, and these have been correlated to the resulting part properties as shown in Figure 2.24.

Surface roughness & Edge effect

Surface roughness is one of the major hindrances in rapid production because of LPBF components must go through time-consuming post-processing operations. Since, only the top layer is visible, in-situ measurements of side surfaces are not possible because of the surrounding powder. Furthermore, an in-situ measurement of the top layer surface pattern exposes irregularities that may be caused by different defects, including spattering, balling, porosity and local distortions. Eventually, this information can be further used to implement a real-time correction system to reconstruct the printed slice [109]. In addition, top layer characteristics also allow detecting elevated edges and other surface irregularities that may have a substantial impact on the wear of the recoater blade and the consequent defect propagation within the building area [110]. The primary challenge in such in-situ measurements is requirements of high-resolution long-distance optics.

Zur Jacobsmuhlen et al. [111] proposed an in-situ surface roughness measurement using a thresholding method by comparing the monitored descriptor image against an empirical threshold. The author proposed a fast image processing operation of images captured at the end of each layer through the high-resolution off-axis camera in the visible range. For this, a high-resolution monochrome CCD camera in combination with a tilt and shift lens was used. The descriptor was defined as the product of the area and the mean intensity of the region of interest. The proposed approach involved the estimation of different descriptors, including the relative elevated area and the number of detected elevated regions. Furthermore, both 2D and 3D mappings of the spatial locations of pixels corresponding to the elevated areas were constructed to visualise the regions of the produced parts where this kind of defect was detected in-situ.

Zhang et al. [88] proposed a fringe projection system for in-situ surface roughness measurement for the top layer; the experiments were conducted on the testbed structure of the LPBF machine designed and developed by the Edison Welding Institute, USA (EWI). The full setup of the fringe projection system on this machine chamber is shown in Figure 2.25. A machine vision camera (PointGray Flea3, resolution 4096 × 2160 pixels) with a 50 mm lens for high-resolution imaging of the build process was used. In addition, a DLP projector was mounted on top of the chamber, illuminating the powder bed at an angle of approximately 35° through an anti-reflection coated window. The author claimed that this

kind of system is suitable for measurement of the profile height of each layer and surface patterns of the scanned slice.

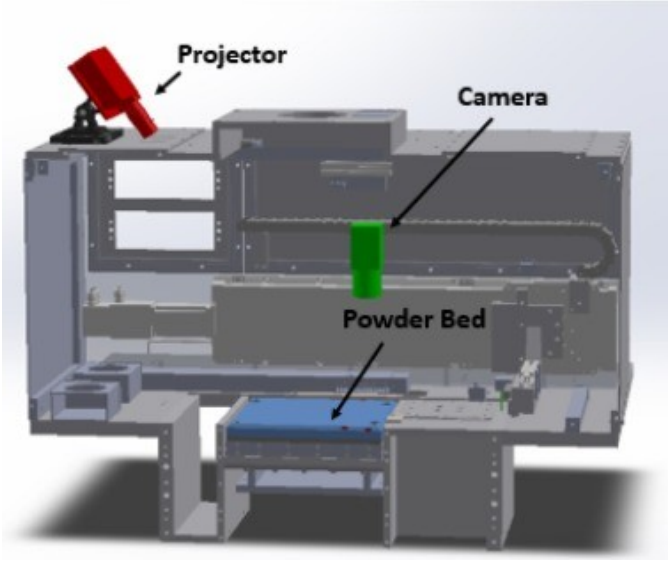

Figure 2.25: Fringe projection system for powder bed surface roughness measurement [88].

Deformation/Strain (Residual stresses)

The LPBF parts may show different kinds of dimensional inaccuracies and geometric deviations from the nominal model. Regarding the size of the part especially the height and shrinkage measurements were reported by various authors, even some time opposite effect expansion of the part (larger than the nominal) was also reported. Furthermore, these distortions show a common source of inaccuracy in LPBF. In some cases, a combination of both shrinkage and distortion can form a curved profile on down-facing surfaces which are intended to be flat. These undesirable deformations strongly impact the quality and functionalities of the part for different reasons. First, it deteriorates the dimensional accuracy of the part, second, it may interfere with the recoating system, increasing wear and affecting the powder layer uniformity [112]. Measuring the distortion in part in-situ is challenging because only the top layer is visible, although slice by slice measure can give overall part deformation at the end of the process.

Dunbar [89] proposed a setup for in-situ distortion measurement of the part during the process. These measurements were performed using a Lord Micro strain differential variable reluctance transducer (DVRT) displacement sensor attached to the underside of the baseplate. This allowed the author to investigate the effect of scanning strategies on the build distortions. Figure 2.26(a) shows the substrate with sensors and Figure 2.26(b) shows results of distortions captured for the first three layers for accumulated distortion in the vertical direction (z) due to rotating scan patterns.

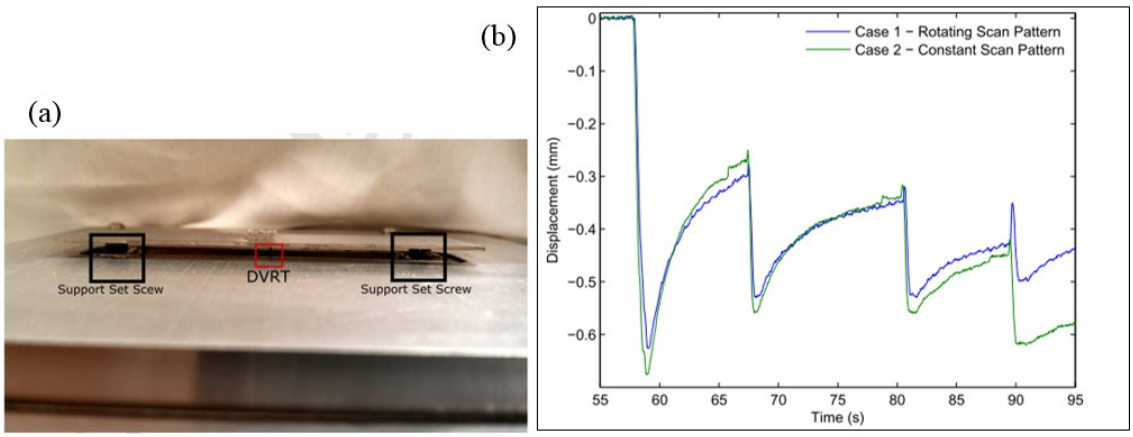

Figure 2.26: Part deformation measurements, (a) post build substrate with sensors, (b) comparison of distortions in Z direction accumulated by changing scan patterns for three layers [89].

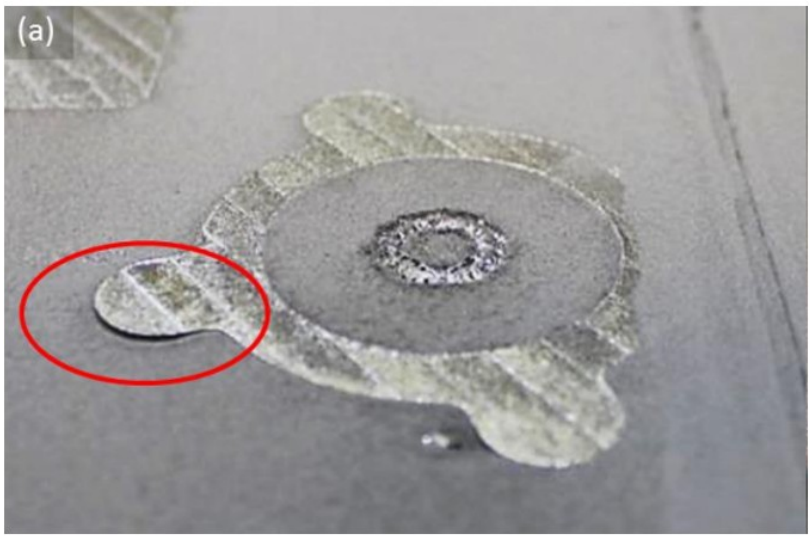

Figure 2.27: Image captured in-situ of thermal distortion during build [54].

Another in-situ measurement of deformation measurement was reported by Foster et al. [54], it used a 36.3-megapixel single lens reflex camera (SLR) mounted inside the build chamber with multi-flash modules to collect multiple pictures with varying illumination both after the powder bed deposition and again after melting. In addition, a 28 mm focal length lens which allowed resolution of about 50 μm/pixel across the entire 250 × 250 mm^2 baseplate was used. In the results, Figure 2.27 shows the image captured in-situ of thermal distortion during the build which can be a potential cause for recoater blade failure.

Track Geometry

Single tracks are critical to the overall quality of the components. In addition, its characteristics such as smoothness, full melting, width, wetting angle are the primary to study process stability. Analogously to the monitoring of the melt pool, the monitoring of the process along the scan path imposes challenges in terms of required spatial and temporal resolution of the in-situ sensing system.

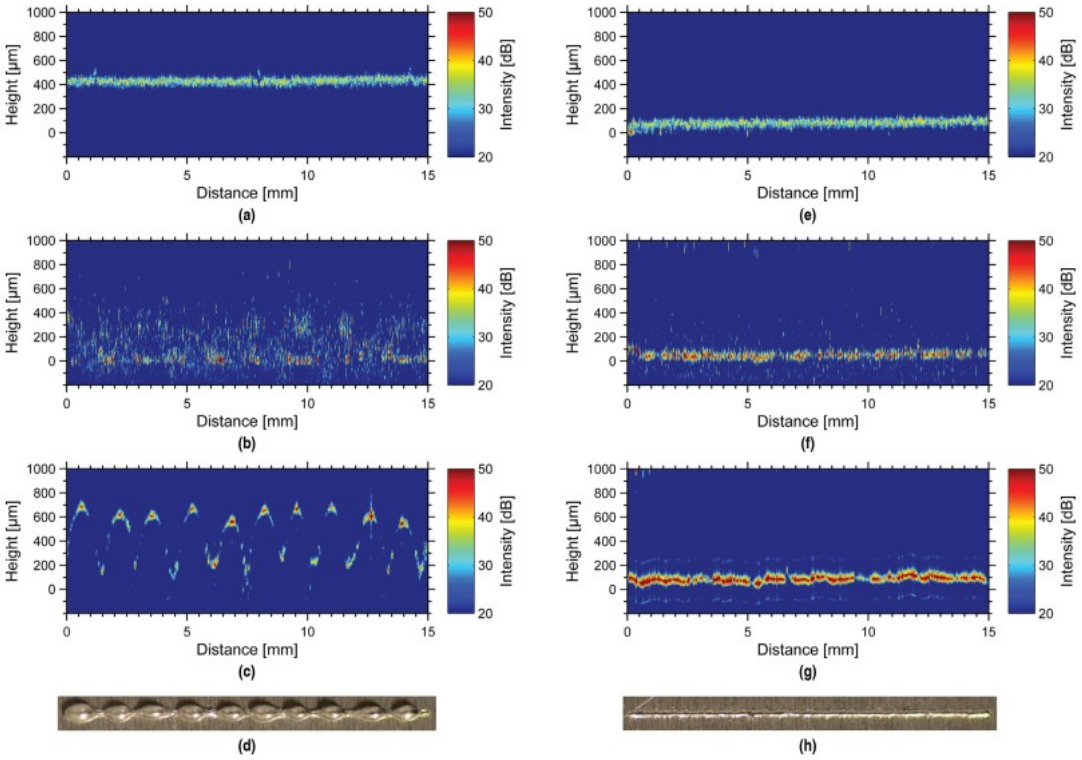

Figure 2.28: ICI imaging of single track profile, (a-d) 430 um layer thickness, (e-h) 80 um thick powder. (a) and (e) before laser melting, (b) and (f) in-situ data laser melting, (c) and (g) after melting, (d) and (h) Post photographs of tracks [97].

A co-axial sensing technique was proposed by Kanko et al. [97]; it consists of a low-coherence interferometric technique, also known as inline coherent imaging (ICI). A typical ICI system consists of a low-power broadband light source, a high-speed spectrometer and fibre-based Michelson interferometer as previously stated. ICI systems were assembled into the two different powder LPBF systems; one to investigate the melt pool and surrounding area where the imaging beam passes through the scanner and whereas in the other setup, imaging is in line with the fibre laser beam for higher speed measurements. It allows detecting different kinds of single track defects, including balling, under melting, over melting and other surface irregularities. Furthermore, a spatial mapping of melt pool morphological properties was created to highlight regions of the scan path where deviations from the normal melting state occurred. Figure 2.28(a-d) show results of single track co-axial inline measurement ICI imaging of 403 um thick layer and Figure 2.28(e-h) shows results of 80 um thick layer.

Another in-situ measurement of a single track was done by Bertoli et al. [113], they reported off-axial high-speed imaging systems (250000 fps) for LPBF for two different powders: gas atomised and water-atomised. The obtained experimental results were compared with simulation results. This study was done to quantify simulated cooling rates and compare then with experimentally determined ones.

2.5 LPBF in Vacuum

To date, very few papers have investigated the laser powder bed fusion (LPBF) of metals at sub-atmospheric pressures [57,58,114,115]. The perceived advantages of sub-atmospheric pressure include reduced porosity and surface roughness in the fabricated part, similar to that achieved with laser welding. Remaining pores that are not filled with shielding gas would be removed more effectively by hot isostatic pressing. Other potential advantages stated by these authors include reduced oxidation and the control of crystal orientation.

Zhang et al. [114] melted single layers of pure Ti powder with a fibre laser at 100 μbar. At this single pressure, the authors varied the laser power and scan speed; and found acceptable density (close to 100%) and surface porosity only at very low scan speeds, ≤0.02 m/s. The density was already reduced to 95% at a laser scan speed of 0.1 m/s, decreasing steadily to 70% at 0.6 m/s. The width and height of a single melted track were both significantly reduced, this was attributed to the increasing metal vaporisation due to the reduction in boiling temperature at low pressure. The authors claimed that balling was completely avoided at low pressure.

In a subsequent publication, the same group scanned single tracks in stainless steel powder and investigated the effect of reducing the chamber pressure from 1 bar to 1 mbar whilst again varying the laser scan speed [57]. This time, consolidated tracks were only observed at pressures ≥100 mbar for 0.1 m/s scan speed: below 100 mbar, no powder was consolidated and only re-melting of the solid substrate occurred (Figure 2.29). The lack of powder consolidation below 100 mbar was again explained in terms of increasing metal vaporisation due to the reduced vaporisation temperature at low pressure. The authors concluded that reduced pressure requires an increase in scan speed (or a decrease in laser power) to limit material vaporisation. The apparent contradiction with their previous observations [114] at 100 μbar and low scan speeds was not addressed.

Sato et al. [115] melted single layers of Ti-6Al-4V powder on to stainless steel substrates at 50 nbar. At a very low scan speed of 0.01 m/s, they observed a surface roughness (Ra = 0.40 μm) which was significantly lower than the most abundant powder diameter of 35 μm and the largest powder diameter of 88 μm. Imaging at 60 frames per second (fps) revealed that no spatter was produced from the melt pool at this low scan speed. At 0.01 m/s, the surface roughness (Ra = 25 μm) and spatter had both increased to

resemble the LPBF process more closely. The authors concluded that, at sub-atmospheric pressures, the sputter free process at low laser scan speeds improves the surface roughness.

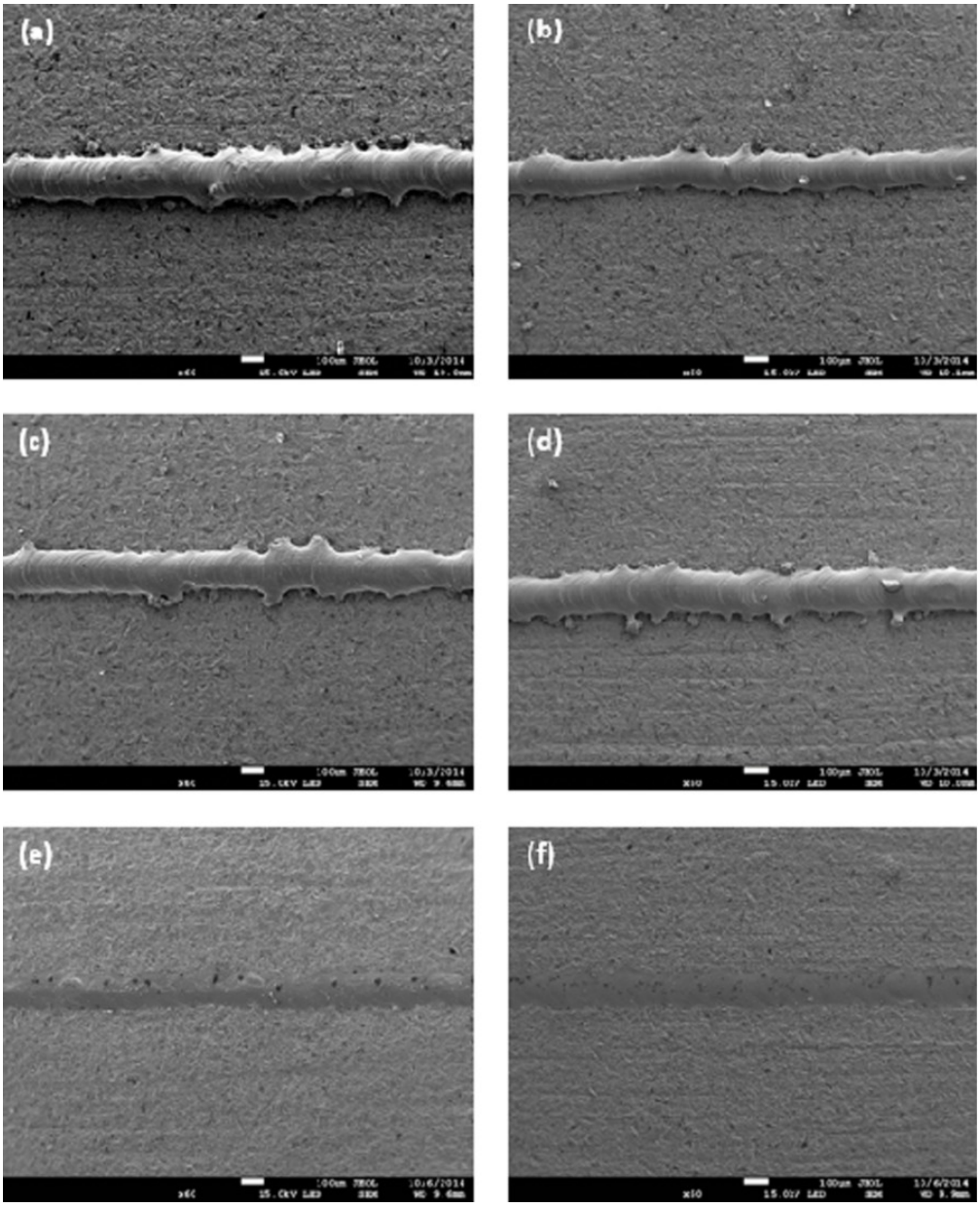

Figure 2.29: Effect of vacuum on SS 316L tracks prepared by the SLM process (a) 995mbar, (b) 500mbar, (c) 250mbar, (d) 100mbar, (e) 10mbar, (f) 1mbar at 0.1 m/s [57].

Matthews et al. [58] investigated the depletion of metal powder particles (denudation) in the zone immediately surrounding the solidified track, which can affect the porosity and surface roughness of built parts. The width of the denuded region was measured after scanning laser tracks across layers of Ti64 powder in a vacuum chamber. The width increased as the pressure was reduced from 1 bar down to 13 mbar (Figure 2.30), and was attributed to the increased velocity of the evaporation plume from the melt pool and the associated increase in particles entrained towards the melted track by the inward flow of the ambient gas.

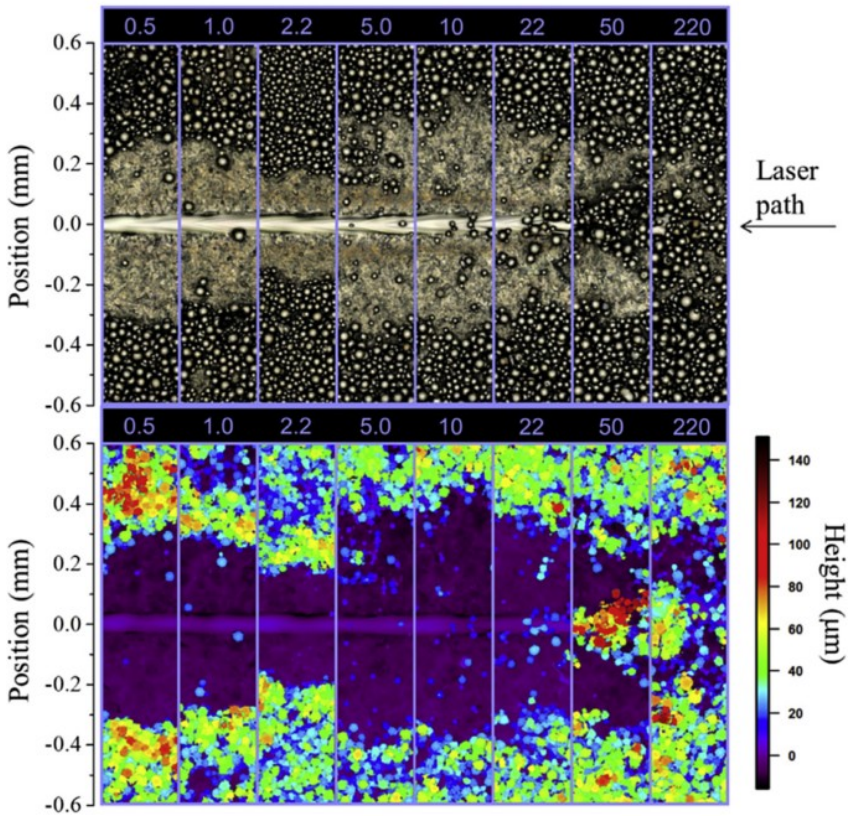

Figure 2.30: Montage of 1.2 x 0.25 mm optical micrographs (top) and height maps (bottom) of the solidified melt track within a powder layer at 225W and 1.4 m/s as a function of ambient Ar pressure (shown above image slices in Torr) [58].

The width then decreased from 13 mbar to a local minimum at 3 mbar, before increasing again as the pressure was further reduced to 660 µbar. The decrease and subsequent increase in the denuded zone width was attributed to the onset of molecular (or rarified) flow and the outward expansion of the evaporation plume counter-acting and eventually dominating any inward flow of the ambient gas. An alternative explanation involved asymmetrical heating of particles close to the laser spot which were then propelled away by the vapour flux generated, transferring momentum to remove adjacent powder particles. However, this second explanation was not preferred because smaller diameter particles were preferentially removed below 3 mbar, whereas asymmetrical heating should affect particles of all diameters equally. High-speed images were recorded close to the melt pool at atmospheric pressure using a localised jet of inert gas, and so this mechanism at lower pressures was not confirmed.

Laser welding at sub-atmospheric pressure is well established in the literature [116] and has received increased attention recently for joining thick materials using solid state fibre and disk lasers. The penetration of a keyhole weld is typically twice that achieved at atmospheric pressure, with an associated reduction in voids in the weld seam and an increase in weld pool stability. The deep, narrow weld is similar to that achieved with

electron beam welding but without the production of harmful x-rays associated with that technique. The improved penetration at reduced pressure is attributed to two principal effects: the reduction in the metal vaporisation temperature, so that less energy is required to create and maintain the keyhole; and the increase in laser energy reaching the workpiece due to reduced absorption and scattering of the beam by the atmosphere. Clearly it is not the objective to introduce a keyhole during LPBF, but the effects of laser processing at sub-atmospheric pressures are informative for this study.

In laser welding, the keyhole depth increases as the ambient pressure decreases [116,117] due to the decrease in vaporisation temperature at reduced pressure: the mean temperature of the molten keyhole surface is reduced [118] so that the same incident laser power is absorbed along the surface of a deeper keyhole. The penetration depth becomes independent of the ambient pressure below some threshold pressure (Figure 2.31). This effect has been explained in terms of the total pressure acting inside the keyhole to keep it open, which is the sum of the atmospheric pressure, surface tension, hydrostatic pressure and weld speed pressure [118]. Ignoring the relatively small contribution from the hydrostatic pressure, the lowest pressure that can exist in the keyhole occurs for low weld speeds under a complete vacuum and is the pressure P_C due to the surface tension only. Hence reducing the atmospheric pressure below ~P_c/10 has no noticeable effect on the penetration depth. At sub-atmospheric pressures, the reduced vaporisation temperature accounts for ~40% of the increase in penetration depth seen in laser welding [117,118].

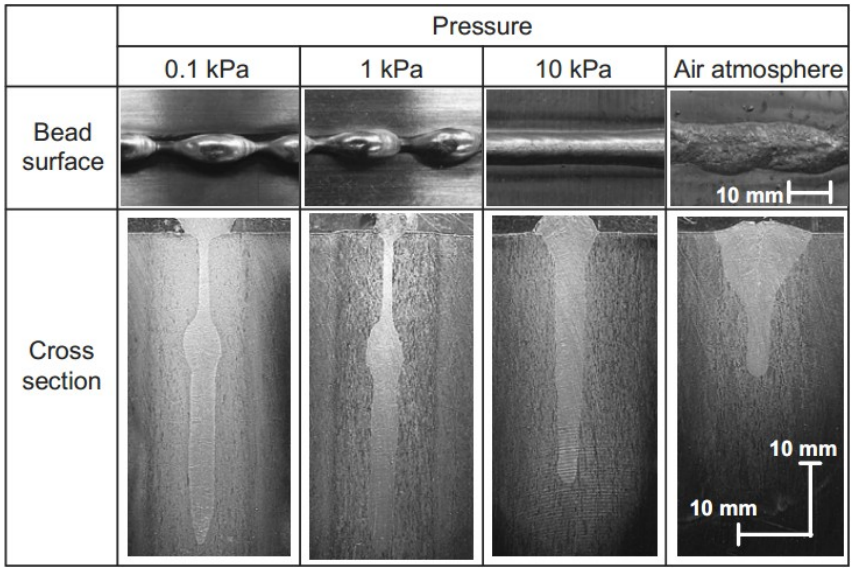

Figure 2.31: Bead surfaces and cross sections of disk laser welds in SUS304 stainless steel plate at different speeds under various pressures [118].

Absorption of the incident laser beam in the laser evaporation plume (metal vapour and plasma) occurs via the inverse Bremsstrahlung process. The improved penetration depth at

reduced pressure for CO_2 lasers operating at a wavelength $\lambda \approx 10$ μm has been explained in terms of reduced inverse Bremsstrahlung absorption [119]. The lower temperature of the vapour plume, combined with its reduced density, reduced the degree of ionisation to the extent that the plasma was almost completely suppressed at low pressure. However, the solid-state fibre and disk lasers used for welding and LPBF operate at $\lambda \approx 1$ μm. They produce weakly ionised plasmas (< 5%) and the inverse Bremsstrahlung absorption, which varies with λ^2, is therefore 100 times less significant than for a CO_2 laser. Kawahito et al. [120] measured the attenuation of a probe laser beams propagating through the laser plume above a keyhole and showed that it scaled with λ^{-4}. They therefore concluded that Rayleigh scattering dominates due to small particles of condensed metallic atoms with diameter ~100 nm, at least in the plume above the keyhole; neither Mie scattering from larger agglomerations of condensation particles (which has no λ dependence) nor inverse Bremsstrahlung absorption are significant. At sub-atmospheric pressures, reduced Rayleigh scattering due to the reduced density of small condensation particles accounts for an increase of 10–20% in the incident laser power [118,120]. This effect, combined with the reduced vaporisation temperature discussed in the previous paragraph, accounts for the doubling of the penetration depth observed in practice.

2.6 LPBF in High-pressure Atmosphere

Recent high-speed imaging of the laser powder bed fusion (LPBF) has shown that the laser plume of metal vapour and plasma from the melt pool induces a flow in the shielding gas, which entrains powder particles towards the track [58,69]. The resulting depletion of powder (denudation) increases the likelihood of porosity and the surface roughness of built parts. If the pressure is decreased in the transition region between hydrodynamic and molecular flows, particle entrainment increases due to the increased speed of the laser plume [58]. Eventually the expansion of the laser plume prevents the entrained particles from reaching the melt pool. Further pressure decreases into the molecular flow regime cause particles to be only repelled away from the melt pool by the laser plume. In some of the gas assisted laser drilling processes, it has been observed that he laser plume velocity reduces with an increase in pressure [121].

An increase in ambient pressure might reduce denudation, due to a decrease in the laser plume velocity and the resulting induced flow in the shielding gas leading to less entrainment of powder particles. A reduction in the recoil pressure from the laser plume might lead to a more stable melt pool and a smoother build. It might also reduce

condensation coating on machine windows from evaporation of metal from the melt pool. It increases the vaporisation temperature that might allow use of higher energy densities and increased scan speed without boiling the material. To the best of the authors' knowledge, few researchers have reported the use of above atmospheric pressure in laser LPBF. Gieseke at al. [122] reported the development of 3 bar pressure capable laser LPBF system to process low boiling point metals such as magnesium. It has been said that the 3 bar pressure will increase the boiling point by 127 ºC to 1220 ºC allowing for wider range of laser power and scan speed to increase the build speed and improve material properties. Although. the authors have not reported any experimental results or studies so far in this area.

2.7 Summary

A detailed literature review on modular laser powder bed systems and in-situ measurements studies performed on both the modular LPBF systems and the commercial machines have been presented. In addition, few papers available on LPBF feasibility in vacuum and positive ambient pressure have also been discussed. Despite the number of papers on in-situ process measurements, little research has been presented regarding the in-situ micro laser-powder-atmosphere interactions.

The design of an open architecture LPBF system was primarily determined by the requirements for in-situ x-ray access as explained in Chapter 1, however from the literature, several other gaps have been found in the research. The current in-built, in-situ sensing systems are limited to basic process monitoring for build failure detection. In contrast, the modular LPBF systems have shown tremendous potential for such measurements and most of the current state of art research investigating critical process interactions came from such systems. However, as seen in the literature, many systems just represent AM for producing single layer and single tracks only. A few other systems are still in the development and characterisation phase by research groups such as NIST [36] and Fraunhofer ILT [41] and no results are available.

Regarding the in-situ measurements using the high-speed imaging techniques, the research is limited to single layer builds; and the recorded images through the viewing window of commercial LPBF systems shown insufficient magnification and poor contrast to see individual powder particles in the powder bed. Whereas, higher magnification images from the modular LPBF systems have so far focussed on the melt pool whilst

scanning a single laser track. Despite the direct impact of ambient gas on the process, no study on in-situ gas flow interaction and visualisation have been reported.

Very few researchers have investigated the LPBF process of metals at sub-atmospheric pressures. The perceived advantages of sub-atmospheric pressure include reduced porosity and surface roughness in the fabricated part, similar to that achieved with laser welding. Research in this area is insufficient to explain the complex laser powder interactions under vacuum: the pressure and laser settings required for a successful process have not been established and no multi-layer builds have been undertaken.

No literature is available for LPBF in positive ambient pressure up to 5 bar. Though, there are few papers explaining powder particle movement and denudation. The primary aim of this work is to explore the unknown regimes in the process including minimising such particle movements and denudation.

Considering the limitations mentioned above and gaps in the research, motivation of this work was established as explained in Chapter 1. In the following paragraphs, a chapterwise description of the work contained within this thesis is discussed with the aim of mitigating limitations associated with the LPBF processes interactions.

Chapter 3 reports the design of a compact and fully automated open-architecture LPBF system for in-situ measurements. It discusses the flexibility of the LPBF system to enable access to a range of in-situ measurement techniques including x-rays. It further discusses, the calibration and characterisation of the LPBF system for building single tracks and high density >99% multiple layer builds. Chapter 4 details the high-speed imaging of the laser-powder-atmosphere interaction whilst building multiple layer builds with best magnification and contrast to date in order to see individual powder particles. Several regimes of the laser-powder interactions which have never been reported and/or visualised are discussed. In addition, schlieren imaging for shielding gas flow visualisation including cross draft in LPBF is discussed. Chapter 5 reports on the high-speed imaging to investigate the interaction of the laser beam with the powder bed at sub-atmospheric pressures to provide some process understanding for future implementation in LPBF. Several regimes are visualised for the first time; analytical solutions and micrograph results supporting arguments made within this thesis are discussed. Chapter 6 discusses the use of high pressure atmosphere up to 5 bar in LPBF which have not been reported before. The results obtained using the high-speed direct and the schlieren imaging, micrographs and area profile measurements for single track and multiple layer builds are discussed. The Chapter

also discusses the use of helium atmosphere at high pressure in LPBF, the results are visualised and compared with argon atmosphere results, and the outcomes are discussed in detail.

Chapter 3. LPBF System Design and Calibration

3.1 Introduction

The LPBF system described in this Chapter was designed as part of a feasibility study to use x-rays for in-situ imaging of the melt pool during metal LPBF. The open-architecture design of the system also enables flexible access for other process measurements in addition to x-ray imaging, including high-speed imaging, shielding gas flow and temperature. In this Chapter, the design of the open-architecture LPBF system and its performance validation are described. The results of specific process monitoring applications, and the understanding of process fundamentals provided by them, will be reported in further Chapters. As an outcome of this work, a journal article entitled "**An open-architecture metal powder bed fusion system for in-situ process measurements**" was published in the peer-reviewed Additive Manufacturing journal as an open access [17].

The design of the LPBF system was determined by the requirements for x-ray access. The aim of the x-ray measurements in the feasibility study is to yield process understanding, rather than validating the quality of parts during their build. Such images will yield new insight into the physical processes that occur during LPBF, including the powder melting and solidifying, fluid dynamics in the melt-pool and the formation of pores. One example where this insight might be useful is in improving the high-cycle fatigue life of titanium components produced by AM, which is dominated by cracks that nucleate at near-surface pores. A better systematic understanding of the relationships between the process parameters and the size, density, and three-dimensional spatial distribution of pores might be used to eliminate their detrimental effect on fatigue life, without resorting to additional costly process steps such as hot isostatic pressing [123].

As explained in Chapter 2 (Literature Review), x-ray access to the powder bed is extremely difficult in a commercial LPBF machine. Obviously the complex and compact machinery is not optimised for x-ray passage to the powder bed and modifications to the powder delivery system, build platform and laser delivery would be prohibitively expensive. In the literature, nobody reported a multilayer capable LPBF system for in-situ x-ray imaging. Initial x-ray imaging experiments were conducted at STFC (Science and Technology Facilities Council, UK) in 2015 with the Vulcan laser to understand the feasibility of flash x-ray monitoring in the powder bed fusion. Sufficient intensity and spatial resolution for imaging were achieved. However, the broadband source produced high-energy x-rays that were absorbed by the detector but not by the stainless-steel powder

particles, producing insufficient contrast to image individual particles. Alternatively, the long-exposure phase contrast x-ray source at UCL (University College London, UK) explored and found to best to provide sufficient contrast to see individual particles.

3.2 Requirements for the LPBF system

Our objective is to record in-process x-ray images around the melt pool in a metal powder bed. We are interested in imaging a region ~500 μm long that incorporates the melt pool with un-melted powder in front and solidifying material behind. Of particular importance is realistic heat conduction away from the melt-pool and the ability to monitor pores through multiple build layers. A short exposure time is required to effectively freeze the motion of the melt-pool as it moves across the powder bed at speeds up to several hundred mm/s. Successful x-ray imaging therefore requires that:

- the intensity of the x-ray source is sufficient to record short exposure images through the build plate and any other metal in the beam path;
- the spatial resolution is sufficient (~1 μm) for individual powder particles to be imaged;
- the image contrast is sufficient to resolve small variations in x-ray absorption in the powder layer above the noise in the image.

X-ray sources with these characteristics can be set up at the Science and Technology Facilities Council Central Laser Facility (STFC CLF) in the UK. The ultra-high intensity Vulcan laser (power ~1015 W, light intensity 1021 W/cm^2 pulses) can drive a compact particle accelerator when focussed on a solid foil target [124]. The short laser pulse (~few ps) produces a plasma and drives electrons at relativistic energies through the foil. These electrons interact with the solid material of the foil to generate high-energy Bremsstrahlung x-rays that emerge from the rear surface of the foil in a diverging cone from a spot of less than 100 μm across. These x-rays have a broad energy spectrum (10's keV to 5 MeV), a duration of a few picoseconds and sufficient intensity to record projection images through thick metallic objects [125,126]. The time between x-ray pulses is ~15 minutes, determined by the repetition rate of the Vulcan laser. The diverging x-ray beam emerges horizontally into a test room, with an included angle of approximately 40° as seen in Figure 3.1. The operator is stationed in a separate control room to avoid exposure to the burst of x-rays, gamma rays and charged particles produced by the compact accelerator.

Clearly then, the LPBF system must be sufficiently portable to operate in the x-ray test room with automated operation from the control room. Its design should minimise the amount of metal in the x-ray path to the melt-pool. Experiments require a small number of fully fused layers to be deposited, over which a powder layer is spread in readiness for the x-ray pulse. The x-ray pulse is requested from the Vulcan control room, and LPBF system laser is synchronised to scan across the powder bed and to be at the centre of the imaging region when the x-ray pulse arrives. It must be possible to deposit multiple layers automatically and remotely in order to monitor the development of pores between successive layers.

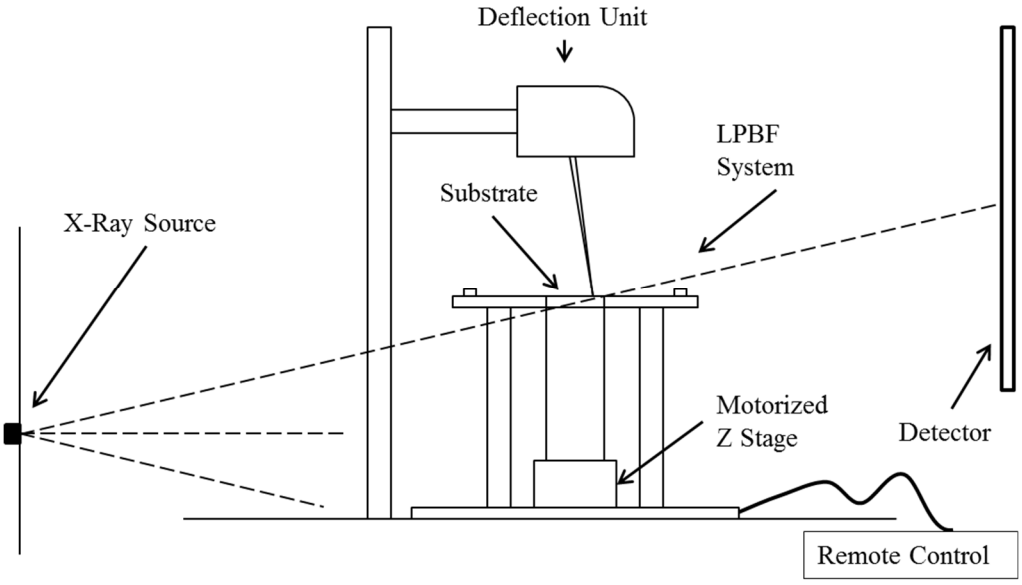

Figure 3.1: In-situ flash x-ray imaging setup and the powder bed setup

3.3 LPBF system design

The open-architecture LPBF system is shown in Figure 3.2 and 3.3. It comprises a powder reservoir and spreader block that are moved as a single unit by a stepper motor and lead screw. The powder is gravity-fed and deposited in the build area as the spreader block moves linearly in one direction; the excess powder is removed as the spreader block returns. The build plates are 80 × 40 mm^2 coupons that are bolted to a rectangular support assembly that is rigidly connected to the vertical stage (z-axis). A circular hole in the support assembly leaves clear passage for the x-rays to pass from below the powder bed. Powder layers of the desired thickness are produced by lowering the support assembly with the vertical stage (Standa 8MVT40-13-1, ~10 nm resolution). The rectangular support assembly moves as a 'piston' within the surface plate: a Teflon O-ring around the edge of the rectangular support prevents powder falling through the gap with the surface plate.

As noted above, the STFC Vulcan x-ray beam emerges horizontally into the test room with a total included angle of 40°: the desired x-ray beam diameter and direction are selected from within that cone with lead bricks. Two x-ray imaging directions are accommodated in the current design. The length of the slot in the spreader block can be set to <1 mm in the y-direction so that a thin line of powder is deposited in the x-direction. In this case, the LPBF system is positioned so that the central region of the x-ray cone passes horizontally through the test region, as shown in Figure 3.2(b). However, a thin powder stripe is not representative of the heat flow away from the melt pool in the standard process, especially for multiple layer deposition. Hence a second mode of operation is enabled by the circular hole in the support assembly. In this case, the LPBF system is raised so that the upper portion of the diverging cone of x-rays passes through the hole in the support assembly. X-rays making an angle of between 12 and 57 degrees to the powder bed pass directly through the build coupon and powder layer, as shown in Figure 3.2(b). X-rays out with this range of angles are absorbed by the support assembly. This observation direction enables a powder layer of full width to be spread and the vertical 'edges' of the powder at the front and one side of the melt-pool to be imaged. For both imaging directions, the detector is placed ~1.5 m behind the LPBF system to yield a spatial resolution in the image of approximately 1 μm.

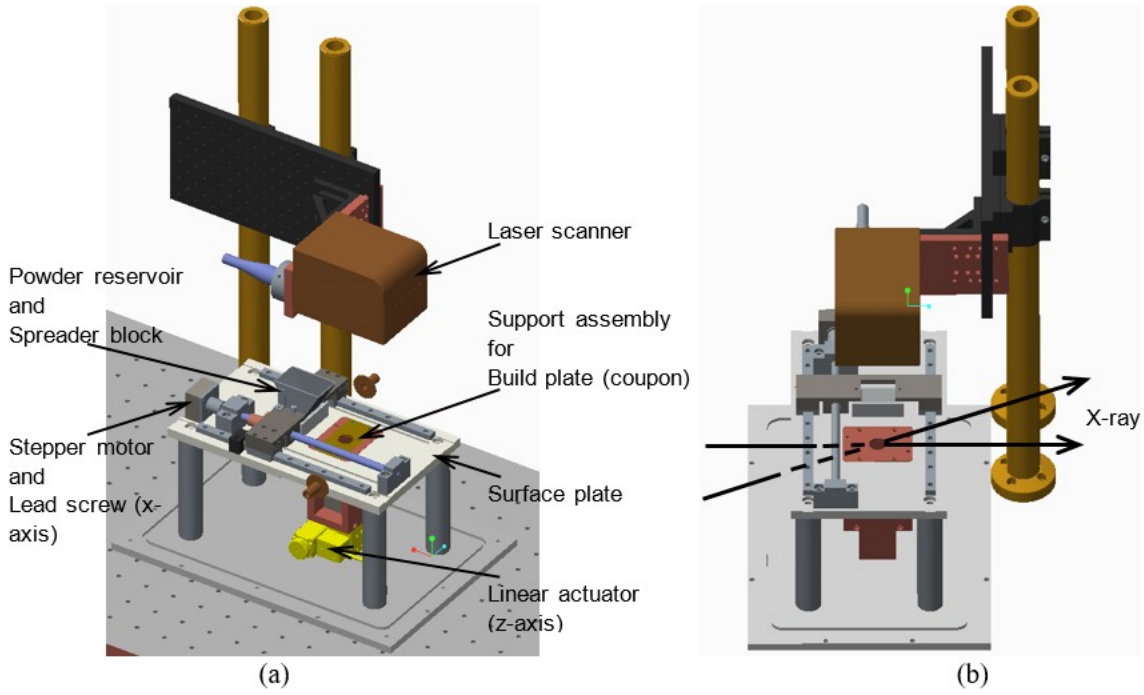

Figure 3.2: (a) Schematic of the open-architecture powder bed fusion system. (b) Passage of x-rays, either at 12° to 57° to the horizontal, or horizontally, through the powder-bed.

The powder in each layer is melted with light from a single mode fibre laser (SPI 400 W continuous wave, 1070 nm) which is scanned over the powder surface (Raylase MS-II-14

scanner with 163 mm focal length f-theta lens). A PC remotely controls the vertical movement of the support assembly, the movement of the powder spreader and the laser illumination and scanning. The build area on the coupon is approximately 30 × 30 mm^2. The maximum build depth is approximately 10 mm for the motion limit of the vertical stage. After processing, the metal coupons are removed for analysis.

The LPBF system is enclosed in a detachable shielding gas chamber made of clear 5 mm thick Perspex sheet, of size 350 × 230 × 220 mm^3 (Figure 3.3). The shielding gas chamber is sealed to a baseplate using a Perspex flange and a silicon gasket (diameter 4 mm) that fits into a groove that runs completely around the baseplate. The chamber has inlet and exhaust ports for filling the shielding gas and providing a gas flow across the powder bed during builds. For a shielding gas that is heavier than air, the chamber is filled from a port close to the baseplate and the lighter air is exhausted from the port in the top surface of the chamber.

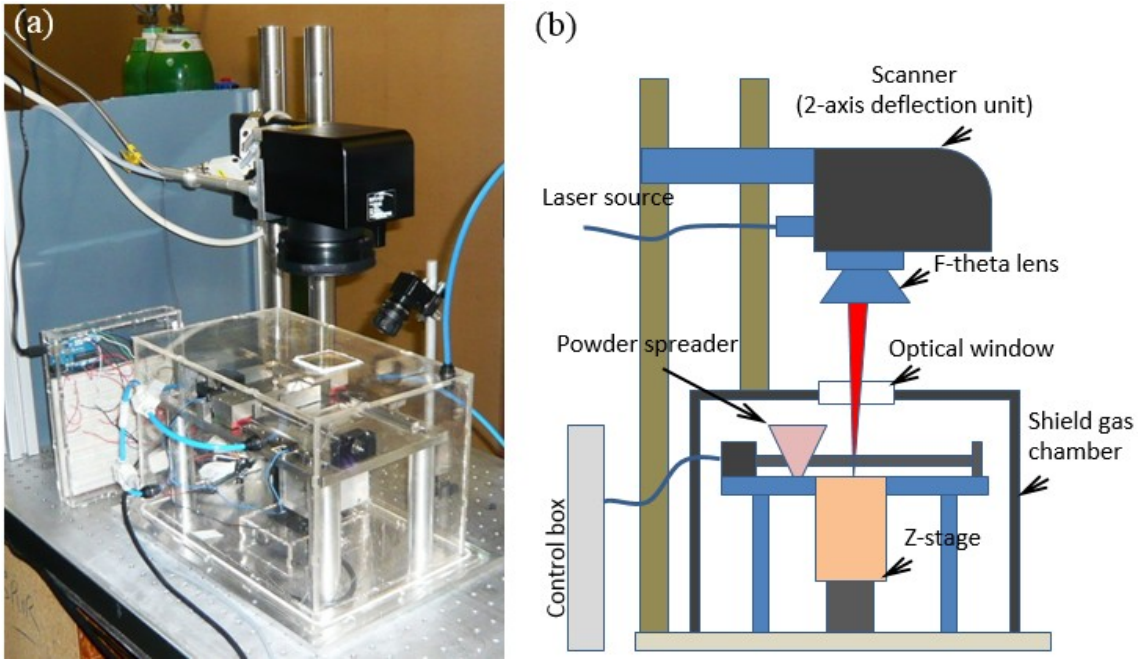

Figure 3.3: The open-architecture LPBF system with the shielding gas chamber in position (a) photograph and (b) schematic

When using a shielding gas that is lighter than air, the ports are reversed so that the lighter shielding gas enters at the top and expels the denser air from the bottom port. Once the oxygen concentration is reduced to <0.5% (measured using a Grove O_2 gas sensor) the shielding gas inlet is switched by an external valve to a second inlet port that is midway up the side of the shielding gas chamber to provide a constant flow across the powder bed during the build. A removable flow straightener (not shown) can be connected to the inlet port and mounted adjacent to the powder bed if required. The exhaust gas runs through a

water bath to remove potentially harmful nanoparticles produced by the process. The laser beam passes through an anti-reflection coated UV-grade fused silica window in the top surface of the shielding gas chamber.

The key requirement of the spreading system is that it produces an accurate and repeatable powder layer thickness, and does not create excessive shear forces on previously deposited layers. Figure 3.4 shows a cross-section of the spreading system at its midpoint. It comprises two main components: the carriage is supported on the rails and is driven backwards and forwards across the build coupon by the stepper motor and lead screw; and the spreader block that is connected to the carriage by fine pitch screws. The spreader block contains a V-shaped reservoir from which the powder is fed by gravity to sit between the two cylindrical spreaders. Clearly moving the whole reservoir is slower than spreading the powder with a separate wiper arm but an additional mechanism to deliver a metered dose of powder is avoided. Hence, gravity feed was chosen for simplicity and because build speed is not the primary concern for investigations into the process that involve single tracks and small build volumes. The design incorporates a piezoelectric shaker attached to the spreader block that can agitate the powder during spreading, but it has not been used in practice to date.

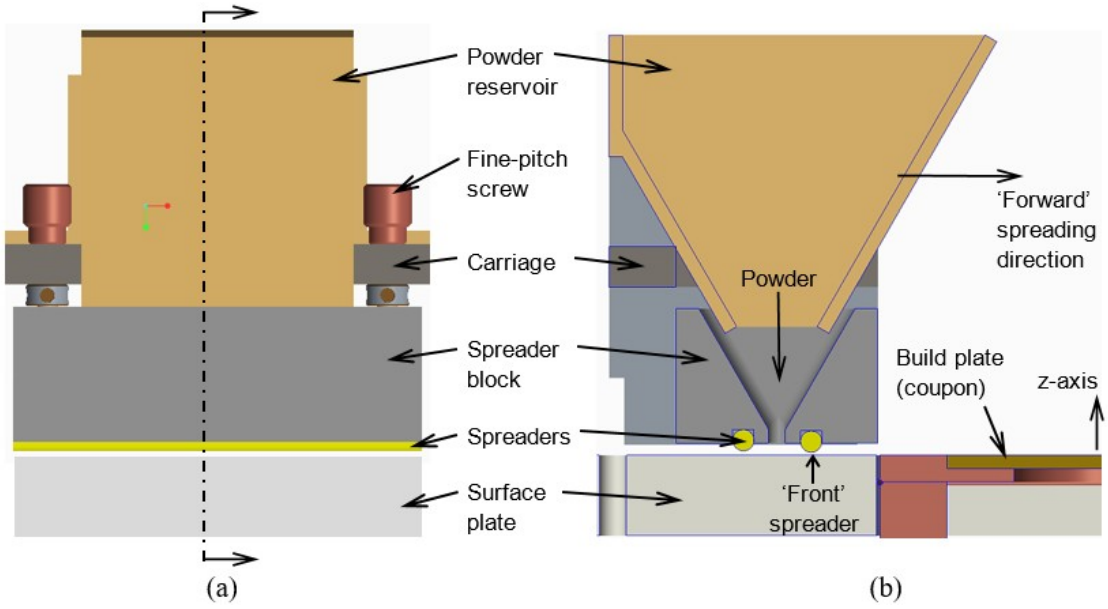

Figure 3.4: Detail of powder spreading system. (a) Front view showing the powder spreader block mounted on its carriage with the fine pitch screws to adjust the height of the spreaders above the surface plate. (b) Side view (cross-section) showing the relative height of the spreader above the surface plate

To deposit a layer, the carriage and spreader block move across the build plate in the forward spreading direction from the start position indicated in Figure 3.4(b), and then return to the start position. The 'rear' spreader with respect to the forward spreading

direction, on the left in Figure 3.4(b), is 100 µm higher than the 'front' spreader. Hence the forward pass of the spreader block leaves an excess depth of 100 µm of powder that is scraped off by the front spreader as it returns to the start position. The depth of each powder layer is determined by the height of the front spreader above the surface plate, the amount the z stage moves down between layers plus the consolidation of the powder from the previous layer. The height of the front spreader is set by adjusting the height of the spreader block below the carriage with the fine pitch screws (0.5 µm per degree rotation): feeler gauges are inserted between the front spreader and the build plate to determine the height. We have tested tungsten carbide spreaders in the form of knife edges and cylinders. In both cases the spreader motion was jammed by the build-up of particles between the rigid spreader and the build plate. Therefore, we currently use silicon cord of diameter 3 mm.

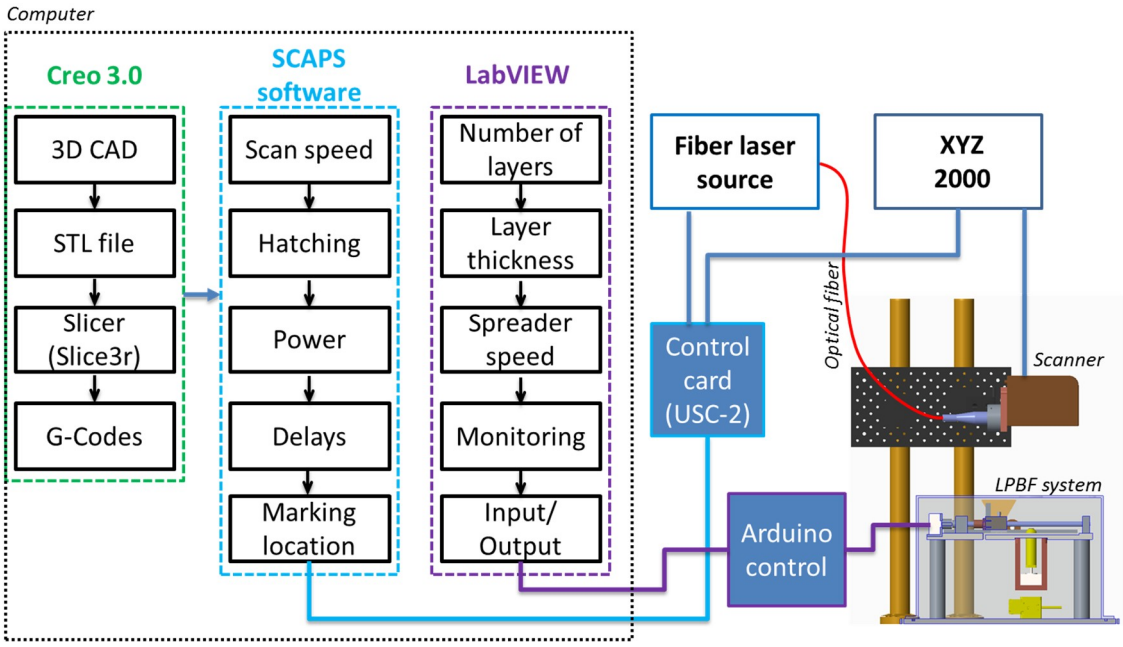

Figure 3.5: Process flow diagram

The vertical movement of the platform, the movement of the powder spreader and the laser illumination and scanning are controlled remotely by a computer, a block diagram of process flow is shown in Figure 3.5. LabVIEW code takes as input the LPBF process requirements such as number of layers and layer thickness and controls all aspects of depositing each powder layer. To start a build, the shielding gas valves are activated remotely to fill the shielding chamber: when the O_2 sensor reports the desired concentration the shielding gas is switched to flow across the build area. The code then drives the z-stage controller to lower by the amount required for a given powder layer depth. The motion of the powder spreader system is initiated: an Arduino Uno drives the lead screw forwards and then backwards until micro-switches attached to the extreme positions on the guide rail

are activated. With a powder layer deposited, LabVIEW passes control to a SCAPS USC-2 [127] card and SAMlight laser marking software [128] which control the laser power and scanning unit. Hence the system has complete flexibility for laser power and speed, and scan geometry including hatching.

3.4 System Calibrations

3.4.1 Beam Profiling

Laser beam characteristics such as spot size, focal point, beam quality (M^2) and power distribution are critical to producing high quality repeatable parts through the LPBF process. These properties need to be checked regularly and must be controlled if deviate from the nominal value. In our system, it is further critical, as high-quality results need to be produced every time. For this measurement, a camera-based beam profiler consists of a camera SP928 [129], profiler software Beam Gage Professional [129], beam attenuation accessories LBS 300s and set of ND filters were used to profile the laser beam. In the setup, as shown in Figure 3.6(a), the beam from the f-theta lens was coupled with the camera using a LBS-300-NIR wedge that passes 1% of the beam to the camera. The wedge consists of a beam splitter lens and a mirror as shown in the Figure 3.6(a). A thermopile beam dump was used to dump the rest (99%) of the laser beam. A combination of two stackable neutral density filters provided by Ophir was employed in front of the camera, each with different attenuation capacity to reduce the laser power further. The beam splitter is designed in such way that the preferential polarisation selection effect of a single wedge is cancelled out and the resulting beam image is polarisation corrected to restore the polarisation components of the original beam [129].

ND filters were changed when the beam image gets saturated with an increase in laser power. The profiler was mounted on the vertical motorised stage (Standa 8MVT40-13-1, ~10 nm resolution). In the primary setting, the motorised stage was set in such a way that the camera sensor was on focus of the beam (smallest beam size). Then, the beam was scanned in the direction of propagation as shown in Figure 3.6(b) and results were obtained. Figure 3.7(a) showed the image of beam profile at 100 W laser power taken at the focus; it details gaussian distribution and spot diameter in D4σ (ISO definition) and D%pk ($1/e^2$-diameter definition) in X and Y direction. Subsequently, the motorised stage was moved to ~1 mm up and the beam diameter was measured; the corresponding image is shown in Figure 3.7(b). In conjunction with beam profiling, the beam propagation Eq. (3.1) [130]

was used to calculate the theoretical beam diameters *d(z)* at different distances *z* from the beam waist d_0 (from focus).

$$d(z) = d_0\sqrt{1 + \left(\frac{4\lambda z}{\pi d_0^2}\right)^2} \tag{3.1}$$

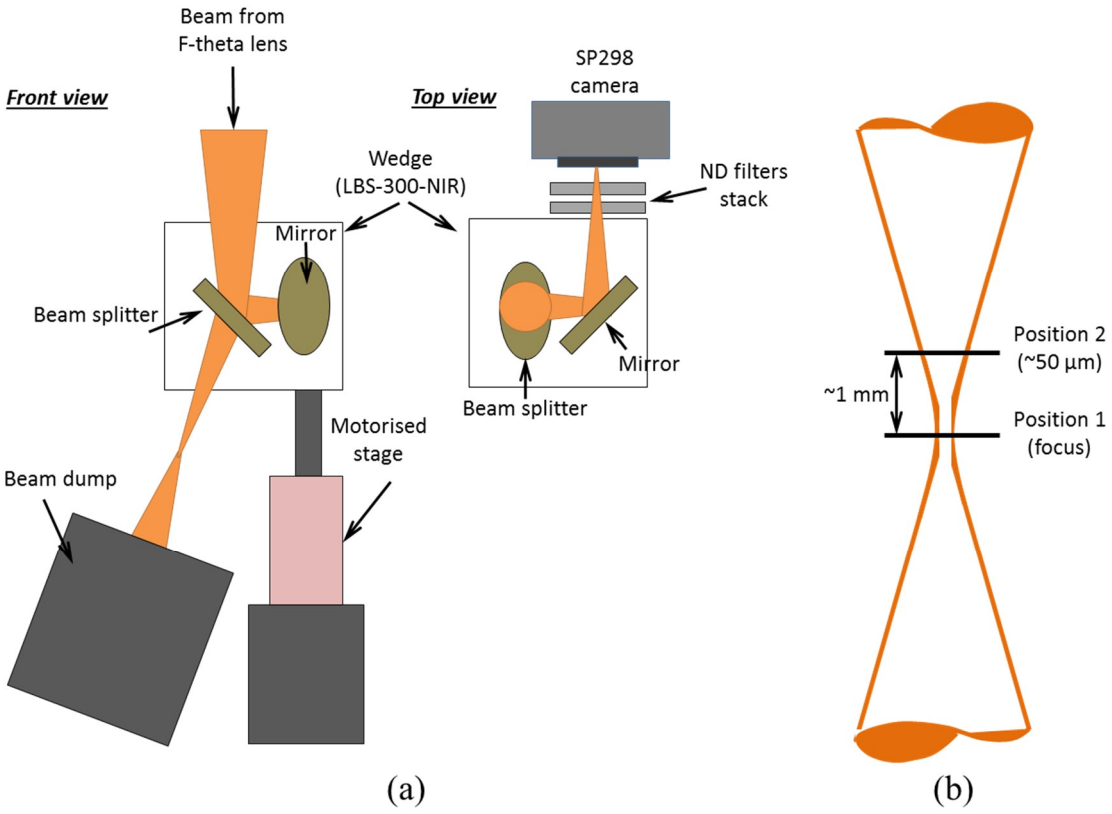

Figure 3.6: Schematic of the laser beam profile measurements, (a) front and top view of Ophir camera based beam profile setup used (b) beam size measurement as a function of distance

For determining the focus position, SPI Laser's marking procedure [131] was used. Sets of lines of 10 mm length were marked on stainless steel substrate at different z positions (0.2 mm steps in z height). Marked lines were analysed using a Leica microscope: best focus was identified as a thin line between wider lines on either side of the focus.

For these experiments (reported in the thesis), the build plate of LPBF system was set accordingly to have the spot diameter of ~50 µm on the powder bed.

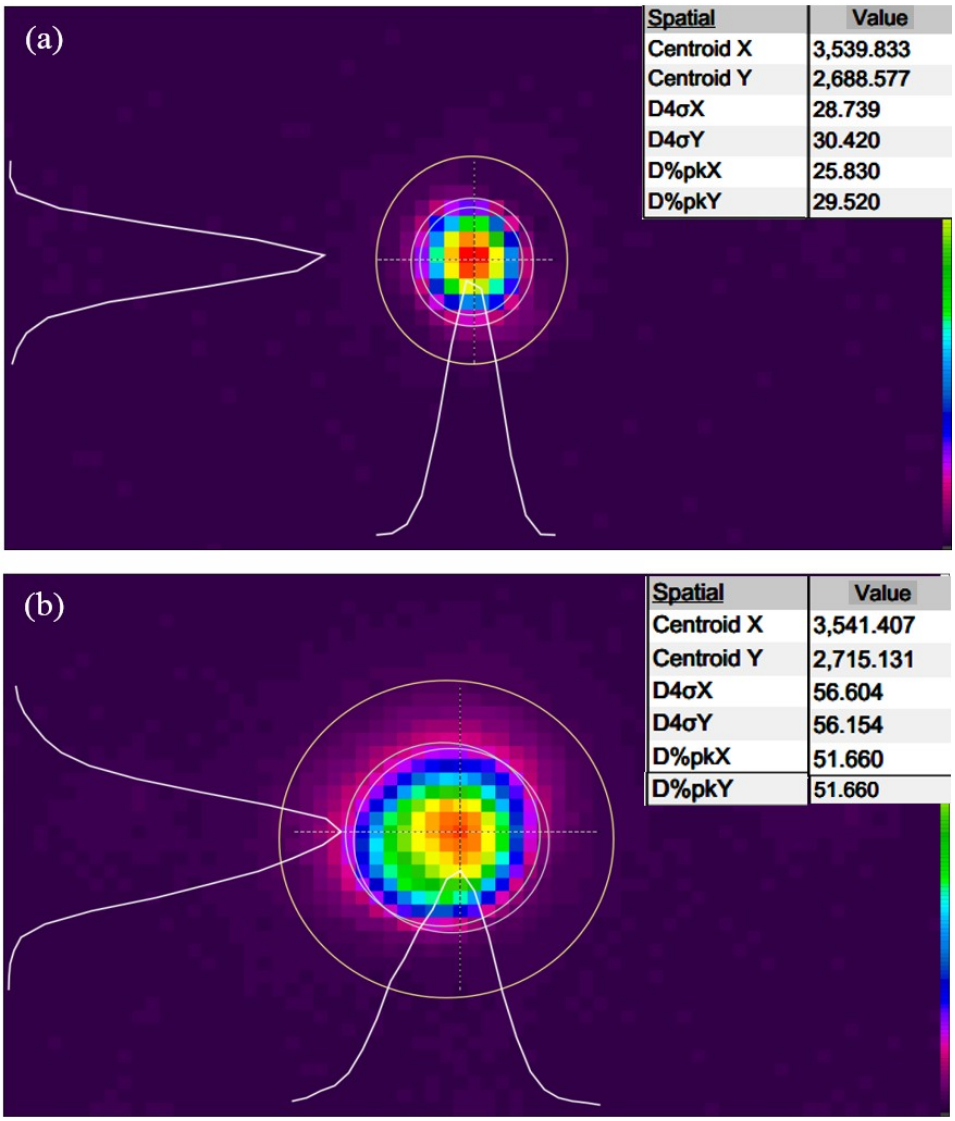

Figure 3.7: Beam profile at (a) position 1 (focus) (b) position 2(~50 µm)

3.4.2 Beam Distortion and F-theta Effect

The scanner consists of two mirrors mounted on the low inertia motors; it is used to deflect the beam in the X and Y directions. The scanner has a laser beam input, into which the beam is fed, and a beam output, through which the laser beam is emitted. Such scanners are prone to produce barrel-shaped distortion of the marking field which is unavoidable when using a 2-axis deflection unit. In addition, if an ordinary spherical lens is used for focusing the laser beam, the focus lies on the sphere; in a flat image, field results in a varying spot size. In order to resolve this problem, F-theta lens is used after the deflection unit. It focuses the laser beam at uniform quality at any position in the marking field and provides partial optical compensation for barrel-shaped distortion. However, the laser beam distortion on the bed is affected by the scan angle, if scan angle increases the beam distortion will increase as seen in Figure 3.8 (left).

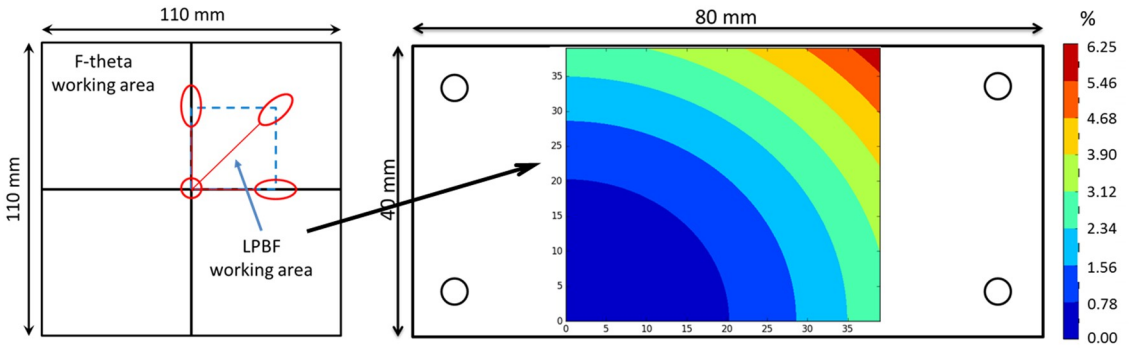

Figure 3.8: Change in Spot Diameter (40 x 40 mm^2) with F-theta lens

In order to keep this angle smaller, the F-theta lenses are made as big as the working field. In this setup, F-theta ronar lens with a focal distance of 163 mm is used which provides working area 110x110 mm^2, although the LPBF system has a working area of 40 x 40 mm^2 and it can be selected anywhere in the total field. However, to reduce back reflection, the area was selected in the starting corner of one quadrant. The scan angle varies from 0º to 28.5º for the full working area (110 x 110 mm^2), however for LPBF working area 40 x 40 mm^2 the scan angle varies up to ~12º, the resulting beam diameter distortion is shown in Figure 3.8 (right). The beam diameter varies (increases) up to 6.25% in the entire working field of the f-theta; and approximately 3.12% variability over the LPBF system's working area.

3.4.3 Power Measurement

In order to measure the laser optical power output, a laser power meter Power Max -Pro HP sensor from Coherent Inc. was used [132]. This power meter is the most advanced system for infrared laser power measurement up to 15 kW, as it has novel, thin-film technology to sense thermal changes rapidly; the response time is below 10 µs. In addition, the power meter comes with its software called LABMAX-PRO and a control box which provides a terminal for the quick trigger on and off laser system. In an effort to investigate the actual power incident onto the powder bed and to measure power losses in the optics, a set of measurements were performed. As explained previously, the laser parameters including power setting are the input of the SCAPS scanning software which is connected with laser system using USC-2 control card.

In the first set, direct laser power (without any optics) was measured, for this, power was set in software and variesd from 50 W to 300 W with the increment of 50 W. Subsequently, the power measurements were performed separately when the beam passed through F-theta lens, then from F-theta lens to fused silica 2 mm optical window fitted on

shielding gas chamber. In addition, power measurement was performed on the dirty fused silica window, after the long run of experiments some smoke got on the window. In the all measurements except direct (5 mm), the laser beam diameter was approximately 10 mm (after the focus) to avoid water cooling for the power meter.

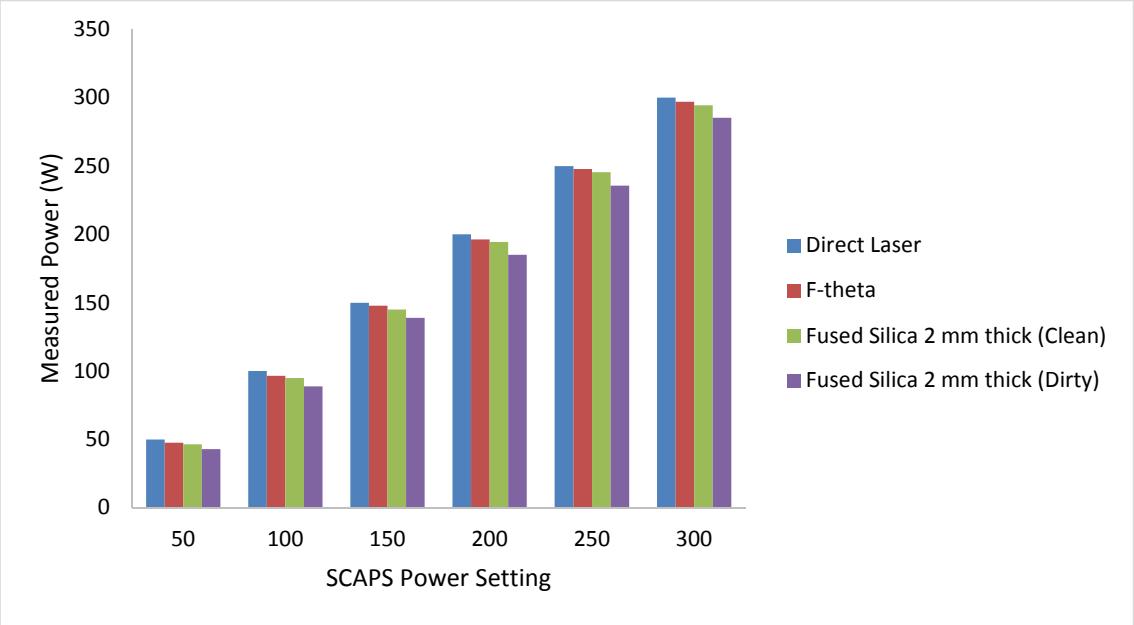

Figure 3.9: Power measurement and losses in optics

Figure 3.9 shows, a graph plotted between the SCAPS power setting and measured power for different cases. As it can be seen, the power is decreasing as different optical components are added to the path. The most striking result is from the dirty window, power loss was more prominent than what was expected. In the results, measured power loss in scanner and f-theta was ~2%, till optical window (clean) was ~3% and in dirty window was~12%. Thus, the optical window was regularly cleaned, and the output laser power was measured before every experiment, and at the end of the experiment, the readings from the power meter were used to calibrate the laser source to achieve a desired power on the workpiece.

3.5 Results

Whilst the design of the LPBF system was originally determined by the requirements for x-ray access, portability and remote operation, the resulting open architecture design enables access for other in-situ measurements for fundamental process studies and for the development of process control. In this section, we validate that the LPBF system produces single tracks and volume builds of acceptable quality to demonstrate that the process is representative for such measurements. For these experiments, we used gas-atomised

stainless steel 316L powder (Renishaw PLC) with particle diameters in the range 15 to 45 µm and a mean diameter of 30 µm [133]; the morphology of the powder material is shown in Figure 3.10. SS316L was chosen to validate the performance of the system because it has comparable properties to titanium but is significantly easier to handle. The 80 × 40 mm^2 build plates (coupons) were made from 2 mm stainless steel (304L). For all the experiments reported, light from the laser was focussed to a spot with a Gaussian beam profile and 4Dσ diameter of 50 µm in both the x- and y-directions.

Figure 3.11 shows single tracks produced at different laser scanning speeds and two laser powers. A single powder layer of thickness 50 µm was spread directly on to the build coupon surface, where the thickness was set with the feeler gauge between the 'front' spreader and the build plate. Thinner tracks are produced as the laser power is decreased or the laser scan speed is increased. The thin tracks at the highest scan speeds demonstrate balling due to Plateau-Rayleigh instabilities in the molten metal and reduced penetration into the substrate.

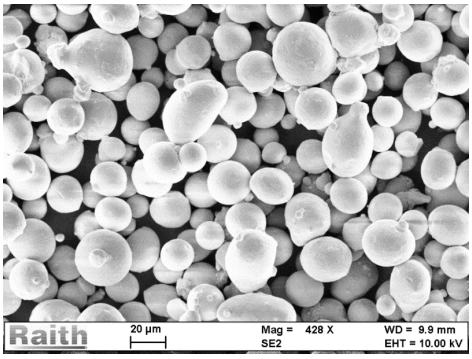

Figure 3.10: Morphology of SS316L powder, taken from Raith scanning electron microscopy (SEM) [134].

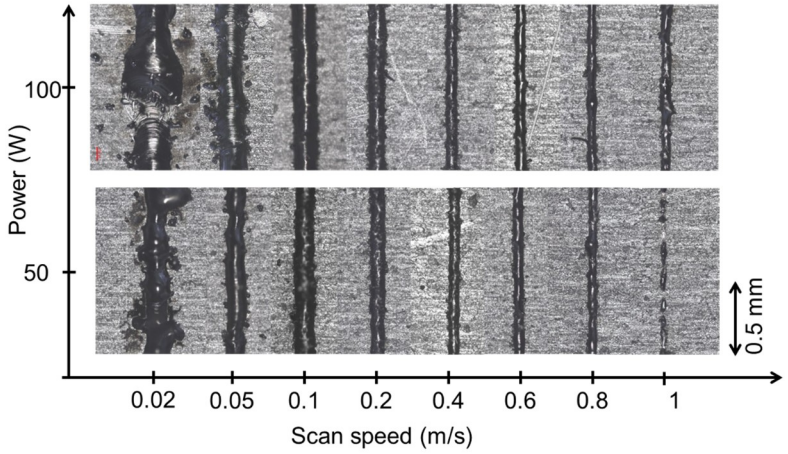

Figure 3.11: Typical tracks at different laser scan speeds for laser powers of 50 and 100 W. Laser beam diameter 50 µm and powder layer thickness 50 µm.

Conversely, the wider tracks at the lowest scan speeds are irregular and broken, with obvious spatter, due to the decreased viscosity at higher temperatures and instabilities in the melt-pool produced by the Marangoni flow. The tracks are continuous and straight for scan speeds from 0.1 to 0.4 m/s at 50 W and 0.2 to 0.6 m/s at 100 W.

For volume builds, the spreader height above the build plate was again set to 50 µm and the downwards motion of the z-stage between successive layers was set to 40 µm. For a laser power and scan speed of 50 W and 0.120 m/s respectively, layers were built by scanning adjacent parallel tracks. The adjacent tracks in each layer were scanned in alternating directions. Between layers, the scan direction was rotated by 90°, i.e. parallel to the x-axis for odd layers and parallel to the y axis for even layers. Figure 3.12(a) shows a staircase object built in this way. Figure 3.12(b) shows a profile measurement for the staircase of the mean height across the step in the x-direction that was measured at each y-value when the staircase had been removed from the powder bed.

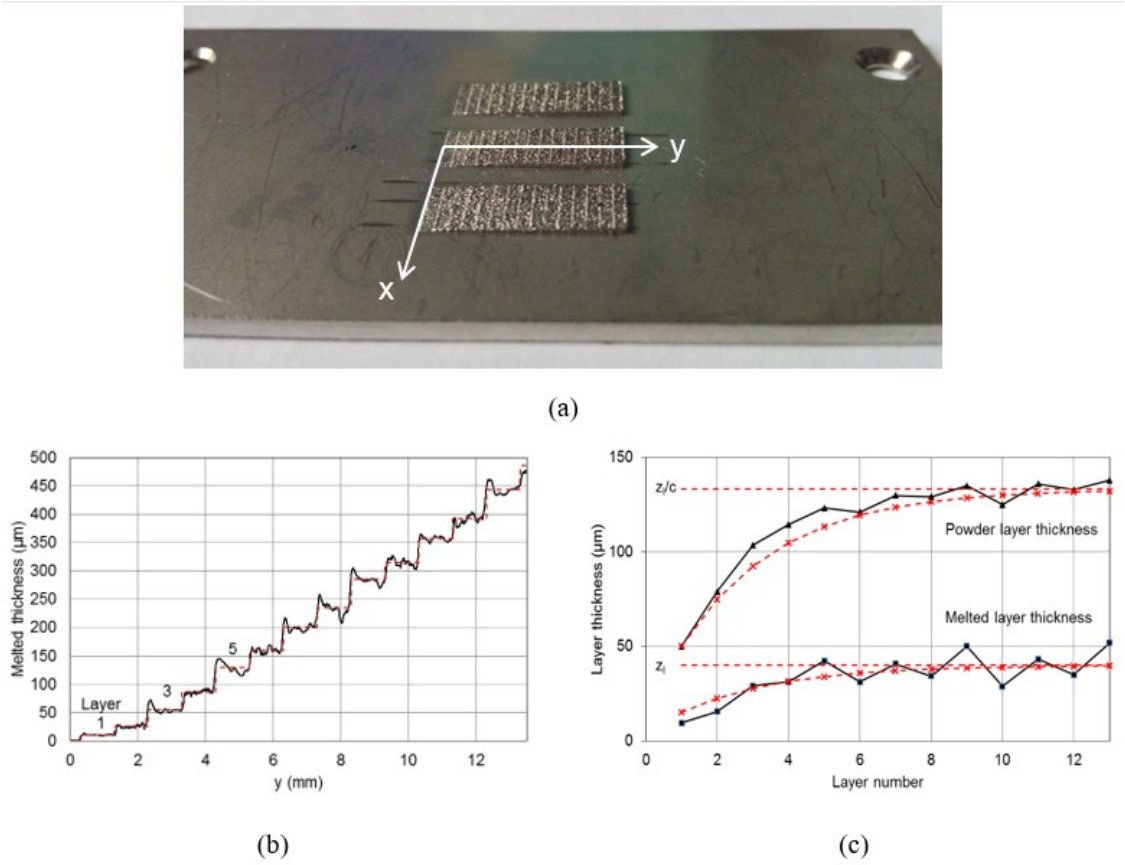

Figure 3.12: (a) Staircase objects built to investigate powder layer shrinkage. (b) Mean height across the step in the x-direction (solid line) and mean height over each step (dashed line). (c) The measured thickness of each melted layer. Also shown is the powder layer thickness that produced each layer, calculated from the measured thickness of the preceding melted layer, the known downwards motion of the z-stage between layers (40 µm) and the height of the 'front' spreader above the build plate (50 µm). The dashed lines show the melted layer and powder layer thicknesses calculated using the powder consolidation of 0.3 calculated from Figure 3.12(b).

The well-known edge effect [39], in which the first scanned line in a layer has a larger height than adjacent scans, is clearly seen in the odd-numbered layers where the scan in the x-direction is parallel to the edge of the step. The mean height of each step was calculated from the profile in Figure 3.12(b) and is plotted in the figure as a dotted line. The powder layer thickness, and consequently the melted layer thickness, develop during the first few layers of a build until the steady state for the process is achieved. Figure 3.12(c) shows the evolution of the melted layer thickness that was calculated as the difference between the mean height of consecutive layers from the measurements in Figure 3.12(b).

The evolution of the powder layer and melted layer thicknesses for the first three layers is shown schematically in Figure 3.13. Each layer in the figure shows the spread powder thickness prior to melting it. For layer 1, the powder layer thickness, t_{p1}, corresponds to the height of the spreader above the build plate, t_{sp}. In our system, the spreader was adjusted to be 50 μm above the surface plate with a feeler gauge, and the surface plate and built plate (coupon) surfaces were adjusted to the same height, giving $t_{p1} = t_{sp} = 50$ μm. For layer 2, the build plate surface moves down by z_l and the powder layer thickness now corresponds to the height of the spreader above the build plate, t_{sp}, plus the difference between the z_l and the thickness of the first melted (consolidated) layer, t_{m1}. Similarly, for layer 3, the build plate surface has moved down an additional step of z_l and the powder layer thickness changes by z_l-t_{m2}, where t_{m2} is the thickness of the second melted layer. In this way, it is straightforward to show that the powder layer thickness for layer n for n≥2 is given by the geometric series:

$$t_{pn} = t_{sp} + \left(z_l - ct_{sp}\right)\sum_{i=0}^{n-2}\left(1-c\right)^i \tag{3.2}$$

where $c = t_{mn}/t_{pn}$ is the consolidation ratio that relates the thickness of a melted layer produced by shrinkage of the powder layer. The change in powder layer thickness between consecutive layers, $\left(z_l - ct_{sp}\right)\left(1-c\right)^{n-2}$ tends to zero. Therefore, the powder layer thickness in the steady state can be determined by summing the geometric series in Eq. (3.2) to infinity:

$$t_p = t_{sp} + \left(z_l - ct_{sp}\right)\frac{1}{1-\left(1-c\right)} = \frac{z_l}{c} \tag{3.3}$$

The melted powder thickness is obtained by multiplying Eq. (3.2) by c, so that the melted layer thickness is

$$t_{mn} = ct_{sp} + c\left(z_l - ct_{sp}\right)\sum_{i=0}^{n-2}(1-c)^i \tag{3.4}$$

and the melted layer thickness is in the steady state is $t_m = z_l$.

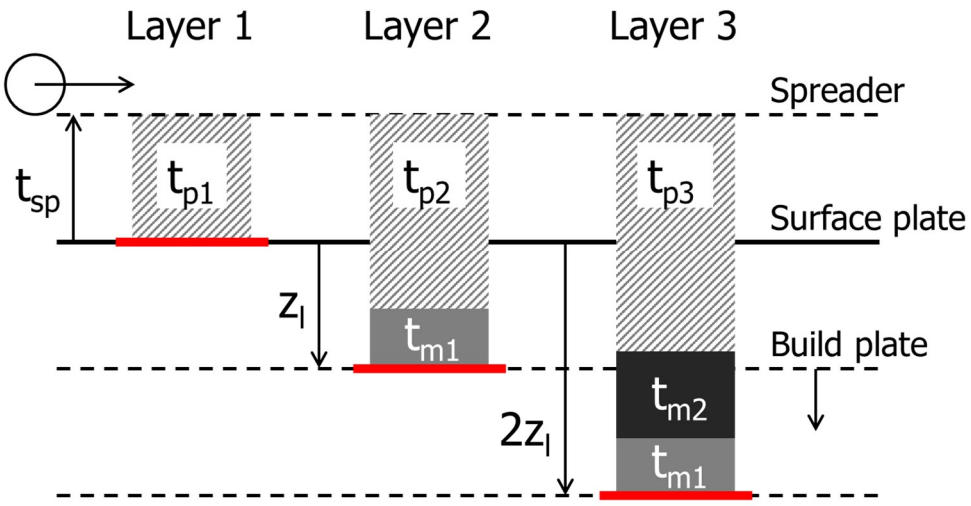

Figure 3.13: Schematic of the powder layer thickness evolution for the first three layers. t_{sp} is the distance between the spreader and the surface plate and z_l is the z motion of the build plate for each layer. t_{pn} and t_{mn} are the powder and melted layer thicknesses, respectively, for layer n.

The measured melted thickness for each layer in the staircase object in Figure 3.12(b) enables the thickness of the subsequent powder layer spread over it to be calculated from the known spreader height above the build plate t_{sp} = 50 μm and the build step increment of z_l = 40 μm. The powder layer thickness calculated for each layer is shown in Figure 3.12(c). The consolidation ratio for each layer can then be calculated, and its mean value was approximately 0.3. The consolidation ratio includes both the powder packing density as well as the powder particles being thrown away by the laser plume. Figure 3.12(c) includes the melted layer thickness and powder layer thickness, calculated from Eqs. (3.4) and (3.2) respectively, for these experimental values of t_{sp}, z_l and c. Steady state melted layer thickness of $t_m = z_l$ = 40 μm, and powder layer thickness of $t_p = z_l/c$ = 133 μm are established after approximately 10 layers. Such a low consolidation could be due to the entrained powder particle being thrown away by the laser plume which is explained in detail in further Chapters of this thesis.

For volume builds, an acceptable distance between parallel adjacent tracks in each layer, the scan spacing *s*, was determined by experiment. For laser power and scan speed of 50 W and 0.120 m/s, specimens were produced with scan spacing reduced from 110 μm to 50 μm in steps of 20 μm.

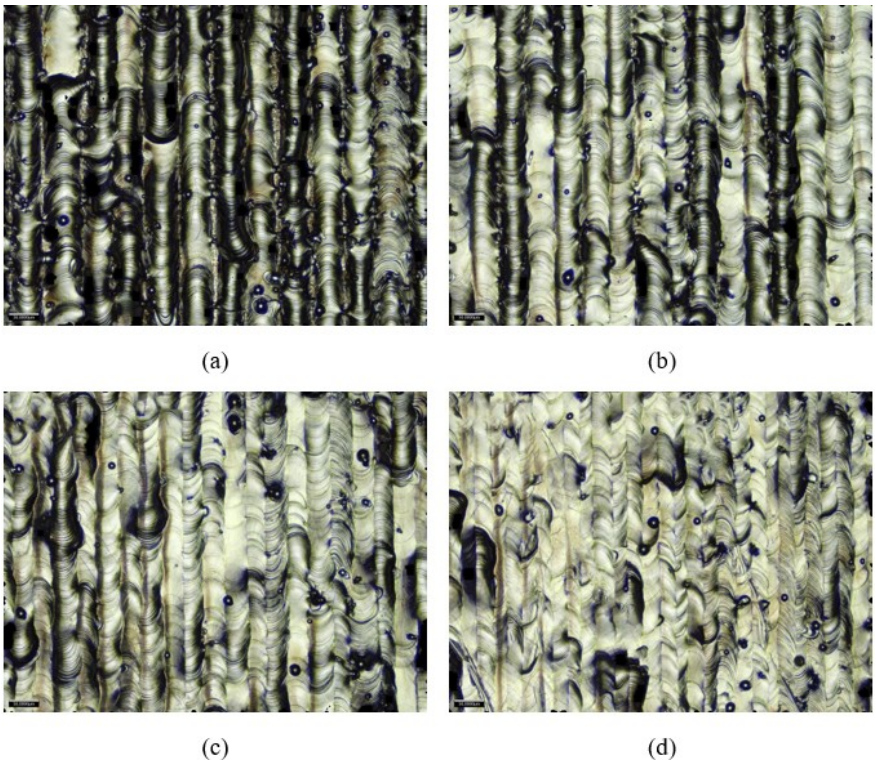

Figure 3.14: Optical microscope images of melted areas with scan spacing factors of a) 1.1 (110 µm), b) 0.9 (90 µm), c) 0.7 (70 µm) and d) 0.5 (50 µm) for laser power 50 W, scan speed 0.12 m/s, laser spot diameter 50 µm and powder layer thickness 50 µm.

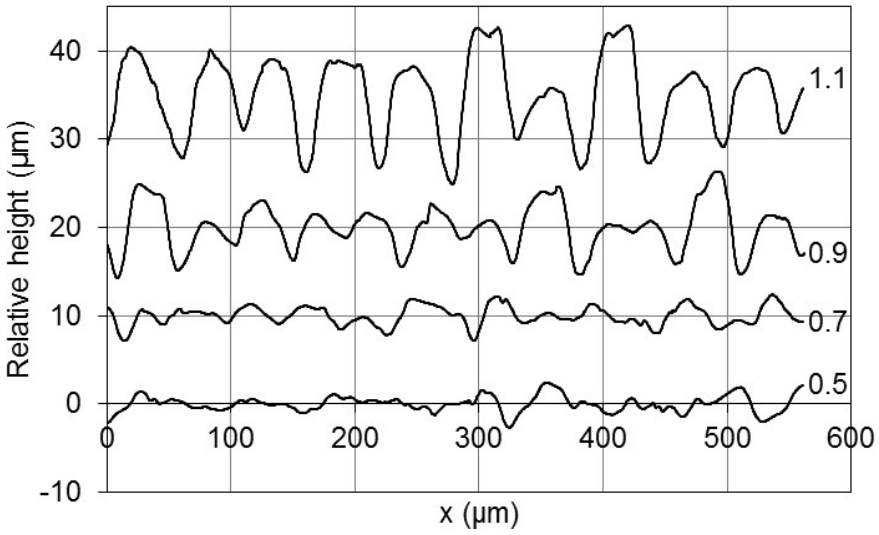

Figure 3.15: Surface profile measured along a line at the centre of the microscope images shown in Figure 7. An offset of 10 µm, 20 µm and 30 µm has been added to the lines for scan spacing factor 0.7, 0.9 and 1.1 respectively, in order to separate the lines on the graph.

These scan spacing values corresponded to scan spacing factors *s/2d* of between 1.1 at 110 µm to 0.5 at 50 µm, where *d* is the laser spot diameter. The surface quality of each specimen was inspected under an optical microscope, Figure 3.14, and the surface profile was measured orthogonal to the adjacent tracks, Figure 3.15. For a scan spacing factor of 1.1 the tracks are clearly separated and no overlapping is observed. The surface flatness only

increases marginally in passing from a scan spacing factor of 0.7 to 0.5 with an approximate 20% increase in processing time.

Three cubes of size 5 × 5 × 5 mm^3 were manufactured on a single coupon with scan spacing factors of 1.1, 0.9 and 0.7 and with the same laser parameters, Figure 3.16. The build time of the components was around 1.5 hours, which is dominated by the scan speed of the powder spreader which was ~0.01 m/s. Three such coupons were produced, making a total of 9 cubes, i.e. three cubes at each scan spacing factor. The cubes were separated from the build coupon using a low speed diamond cutter. The density of each of the nine cubes was measured by applying Archimedes' immersion method following the procedure described in [16] We used a KERN analytical balance (AJS/ACS, resolution ±0.1 mg) with a density measurement attachment for solid materials (ABT-A01) and deionised water as the immersion fluid. The density is expressed as a percentage of the density of bulk stainless steel 316L (7.9 g/cm^3). Air buoyancy was included in the calculation [135] which typically reduces the density by approximately 0.1% compared to the non-corrected value. A density exceeding 99% was achieved for a scan spacing ratio of 0.7, Figure 3.17(a).

One cube for each scan spacing ratio was sectioned, embedded in epoxy resin and polished using diamond suspension paste. Optical micrographs at ×5 magnification were recorded from the centre of the cubes, Figure 3.16(b) and (d). At the largest scan spacing factor of 1.1, the pores are uniformly distributed in a regular pattern due to insufficient overlapping of the individual single tracks resulting in a low density. The micrographs show the increase in density with decreasing scan spacing factor. At 0.9 scan spacing factor the overlap of adjacent tracks is close to a threshold where any necking (thinning) of a track results in porosity. At 0.7 scan spacing factor, the track overlap was sufficient to accommodate any track necking without loss of track overlap.

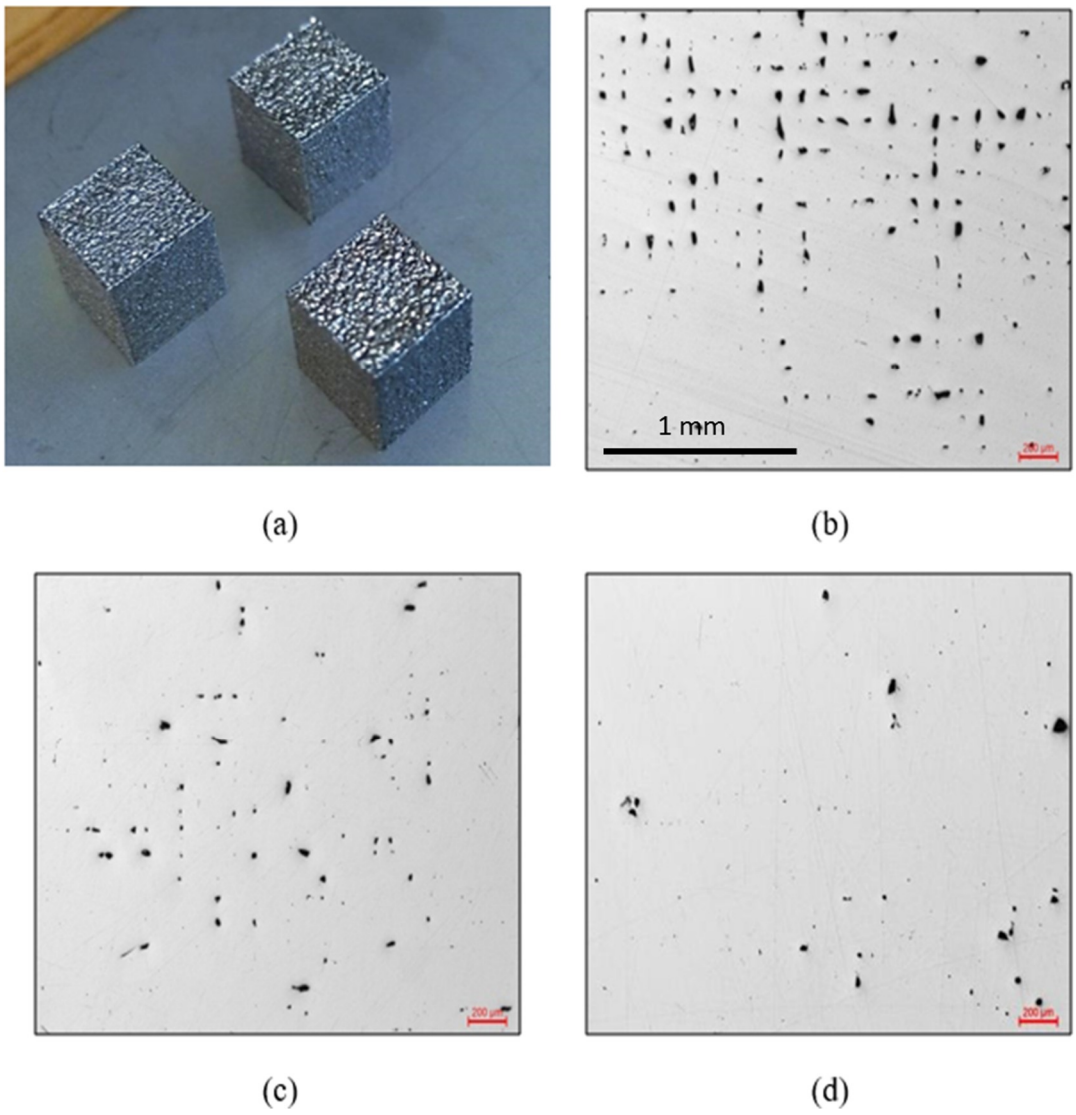

Figure 3.16: Effect of scan spacing factor on component density. (a) Cube samples for density measurements. (b) Microscope images of sectioned cubes at ×5 magnification for scan spacing factors of (b) 1.1, (c) 0.9 and (d) 0.7.

These images were analysed in ImageJ to measure the area of pores, and the values expressed as a percentage are plotted in Figure 3.17(b). Again, a density >99% was measured for a scan spacing factor of 0.7. Both Figure 3.17(a) and Figure 3.17(b) indicate that further increasing in the scan spacing factor might improve the density still further if required, but obviously at the expense of an increased processing time and residual stresses (due to increased heat input per unit volume of powder). We have found that the density measured by immersion produces a systematically lower result than by imaging and that this is consistent with other studies using optical and SEM imaging, Figure 3.17(c). In general, the Archimedes method gives the fastest measurement although obviously no information is obtained regarding the distribution of defects.

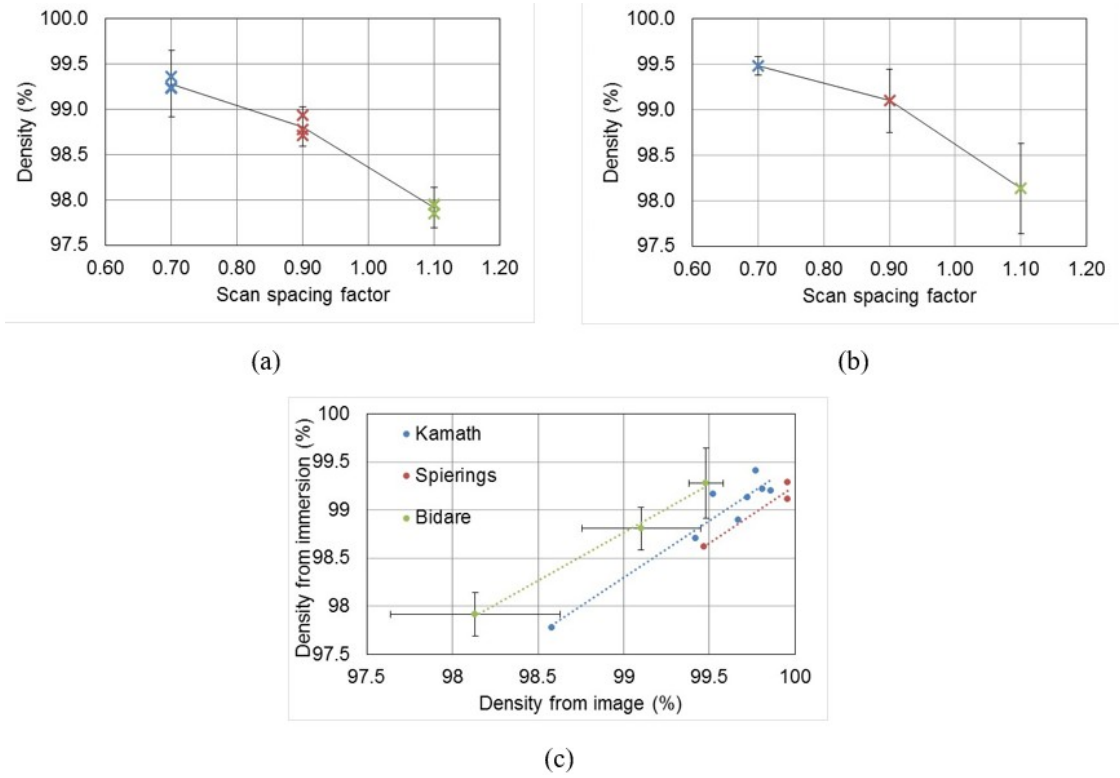

Figure 3.17: Effect of scan spacing factor on component density. Density measurements using (a) Archimedes immersion method (3 cubes at each scan spacing factor) and (b) analysis of optical microscope images (one cube at each scan spacing factor). (c) Relationship between density measurement methods including a comparison with results reported by Kamath [21] and Spierings [20].

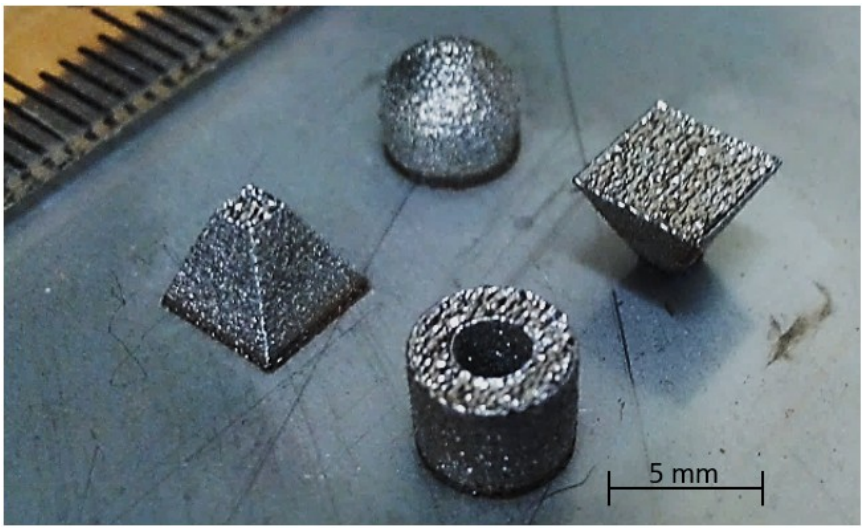

Figure 3.18: Cylinder, dome, pyramid and inverted pyramid produced by the open architecture LPBF system. Each component is contained in a cube of 5 × 5 × 5 mm^3.

Figure 3.18 shows four complex shapes built with the system. The CAD model was prepared using Creo 2.0, sliced using the open source software Slice3r [136] and each sliced geometry processed on the LPBF system using the SCAPS scan software. Processing parameters were chosen based on the previous experiments: power 50 W, scanning speed 0.12 m/s, scan spacing factor 0.7 and a stable powder layer thickness of 130 µm. The built

components were inspected visually and found to be of good quality with almost no exterior defects. The depth of the components was 5 mm or approximately 125 layers. The dimensional accuracy, in particular heights, widths and diameters, were checked with a CMM and were accurate to within ±0.1 mm. The surface finish was measured with an optical confocal profilometer (Alicona) profilometer: the top surface finish <20 μm R_z and side surface finish <25 μm R_z.

3.6 Preliminary X-ray Monitoring Results

3.6.1 Flash X-ray Measurement

One of the objective of this work was the feasibility study of high power flash x-rays for in-situ imaging of the LPBF process. In order to achieve sufficient contrast, stainless steel 316l powder particle size 15 – 45 μm with three type of substrates stainless steel 304, Aluminum AlSiMg10 and Perspex sheet of two different thickness 1 mm and 2 mm were used. The coupons were cut in dimensions of 80 x 40 mm^2, and a thin paper double sided tape (~0.5 mm thickness) of dimension 40 x 40 mm^2 was stacked (Figure 3.19 right). Subsequently, the powder was applied manually on the tape and lightly pressed so that it does not fall when tilted vertically. As seen in Figure 3.19 (left and right), the prepared samples were mounted in the front of the x-ray source. In order to achieve high and low magnification, the detector was moved from far (1.5 m) to near (0.5 m) to the sample.

In the x-ray images, sufficient intensity and spatial resolution were achieved. However, the powder particles were not seen on the any of the samples. Instead, other metal components such as washer, screw and clamps were visible. Because, the broadband source produced high-energy x-rays that were absorbed by the detector but not by the stainless-steel powder particles, producing insufficient contrast to image individual particles as seen in Figure 3.20.

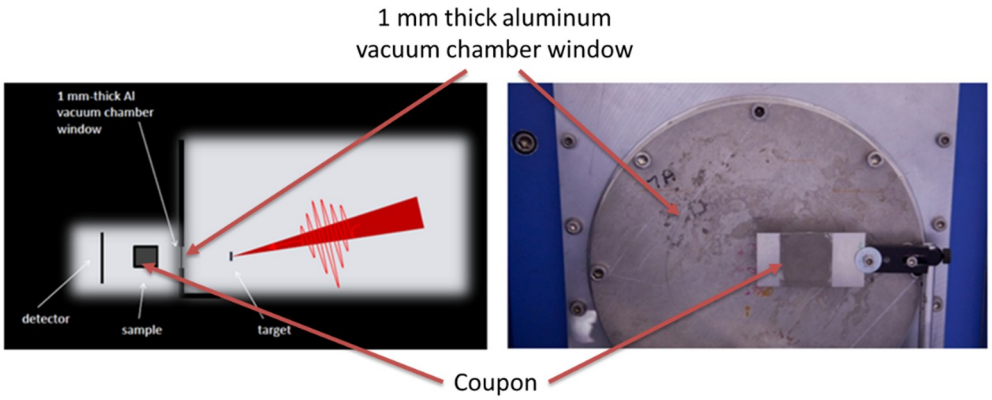

Figure 3.19: Flash x-rays source and sample mounting location (left), powder on an aluminium substrate mounted near to x-ray source.

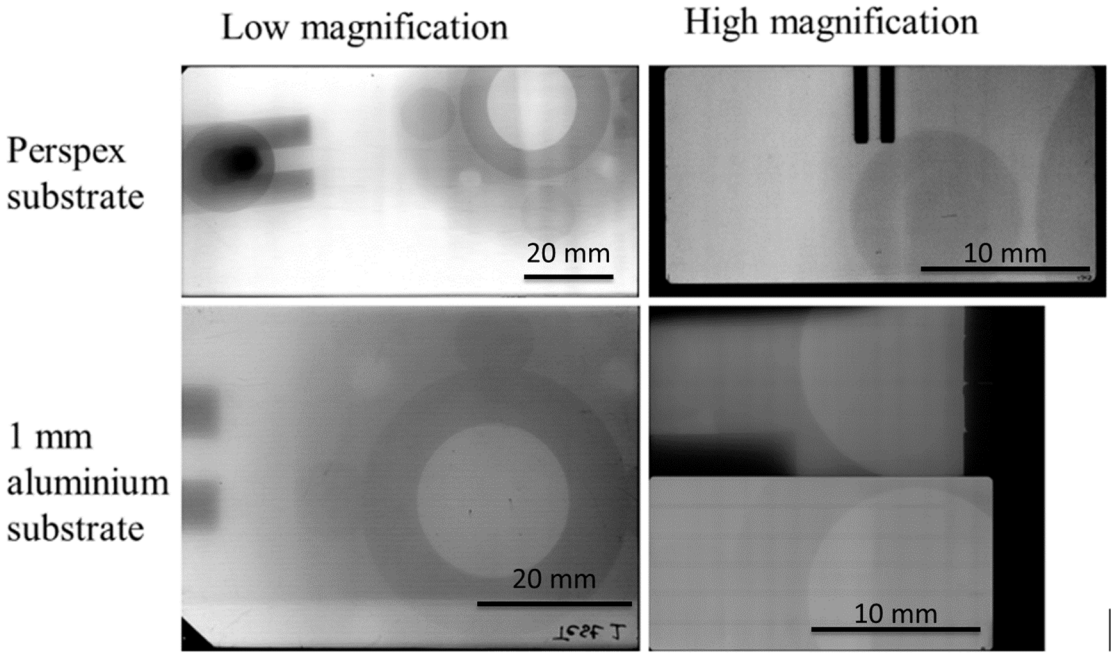

Figure 3.20: X-ray images of low-density substrates (Perspex and Aluminum) at high and low magnification

3.6.2 Phase Contrast X-ray Imaging

In an effort to achieve high contrast and spatial resolution in x-ray imaging, we have worked on a feasibility study of phase contrast x-ray (PCX) imaging in LPBF. The PCX imaging is an attractive emerging method when the classical x-ray absorption method does not provide sufficient contrast. In PCX imaging, in addition to attenuation, information concerning phase change of x-ray beam is also added while creating an image on the detector. For these experiments, Phase-Contrast Microscopy using high x-ray energy 80 keV developed at University College London, UK was used. The setup is characterised by low-intensity source then the flash x-rays, but the more prolonged exposure can be used to get sufficient contrast.

Samples were prepared as described previously in flash x-ray imaging using two different powder size distribution stainless steel 316l powders 15 – 45 µm and 100 – 150 µm. In addition, 2 mm thick steel washer was added to locate the powder in the output image easily. Figure 3.21 shows the samples (left) and x-ray setup (right); the samples were prepared using different material substrates such as stainless steel, aluminium, Perspex and thick paper, the thickness of coupon was varied from 0.5 mm to 2 mm for stainless steel. The main reason behind using dissimilar material substrate is to characterise the contrast possible on these micro metal powder particles.

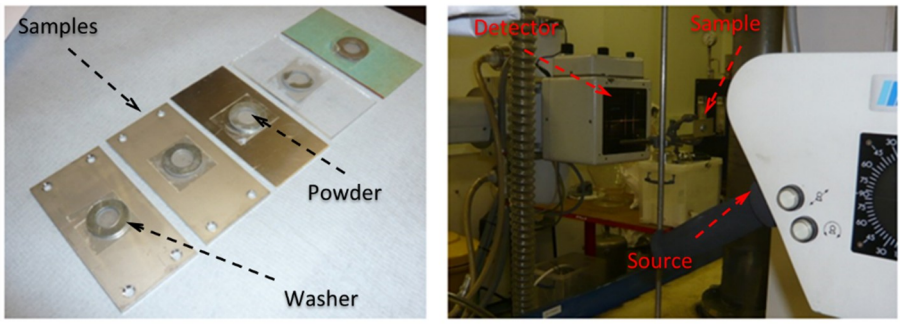

Figure 3.21: Phase-contrast x-ray imaging, SS 316l powder coupons (left), the setup (right)

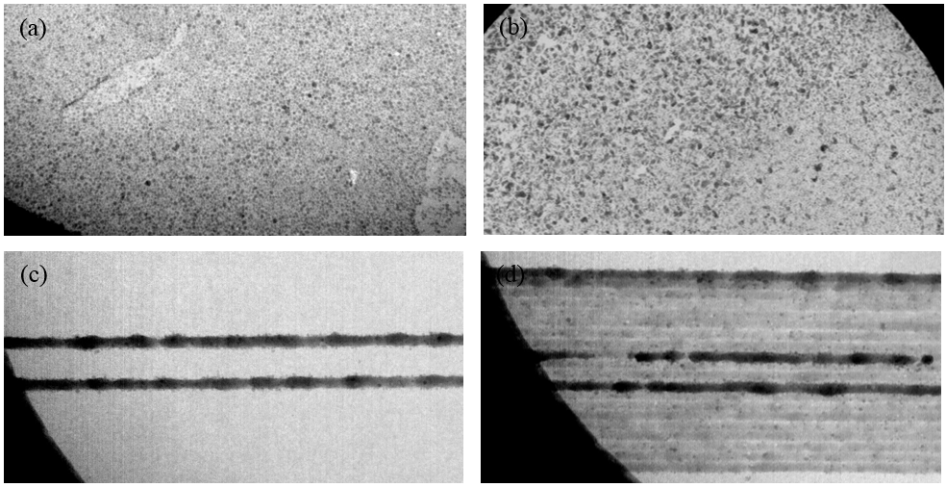

Figure 3.22: Phase-contrast images from 1 mm thick SS 304 substrate, (a) SS316l 15 – 45 µm powder (b) SS316l 100 – 150 µm powder (c) tracks of melted single layer using SS316l 15 – 45 µm powder (d) tracks of melted second layer SS316l 15 – 45 µm powder

In the results, as our primary interest is stainless steel substrate, the Figure 3.22 (a) and (b) shows the image of SS 316l 15 – 45 µm powder (left) and SS 316l 100 – 150 µm powder (right) on 1 mm thick SS 304 substrate for 10 min exposure. The particles are visible; however, lack of spatial resolution noticed which can be further improved by increasing exposure time. In order to identify the PCX imaging suitability with melted tracks: single layer and multi-layer (2 layers) tracks were produced using 50 W of laser power at 0.1 m/s scanning speed. Figure 3.22 (b) and (c) show the output image of the same, the tracks are

visible in both cases single layer and multi-layer. The PCX imaging was found to be the most suitable imaging for the LPBF process, however shorter exposure time is required to freeze the fast-moving melt pool.

3.6.3 X-ray CT Measurement

This work was aimed to use ex-situ (pseudo in-situ) high-resolution x-ray computed tomography (XCT) to characterise powder packing in the bed as spread and the retained defects in melted layers, to support the experiments and modelling. The XCT imaging creates a 3D image by directing x-rays at an object from multiple orientations and measuring the decrease in intensity along series linear paths. The system chosen for such measurement in LPBF is the High Flux Nikon XTEK bay at the x-ray imaging facility, University of Manchester. The XCT setup has a high resolution capability from 2 to 119 μm for specimen areas from < 8 mm up to 202 mm diameters respectively. In order to use the LPBF system for XCT imaging, some modifications were determined by the requirements for the XCT access and those are:

- The XCT scan head needs to be as close as possible to the powder bed.
- The powder spread must be circular to reduce diffraction and to later construct the 3D image.
- To get higher resolution faster, the powder bed must not be bigger than 10 mm diameter.
- The XCT table is a rotating type so no obstacles should be in the path of the scan head.

The LPBF system was modified by changing the powder bed build plate. As can be seen in Figure 3.23, the moving build plate is replaced with a fixed plate with a hole of 10 mm diameter. In addition, a plunger with diameter 10 mm was mounted onto the Z stage, which makes a piston-cylinder arrangement with the fixed plate hole and provides a flat surface for powder.

To deposit a powder layer, the spreader completes the cycle as explained previously and then taken out from the system. Subsequently, the plunger was moved up by 20 mm for obstacle free imaging. For workability of the system, serval powder spreading trails have been made as shown in Figure 3.23.

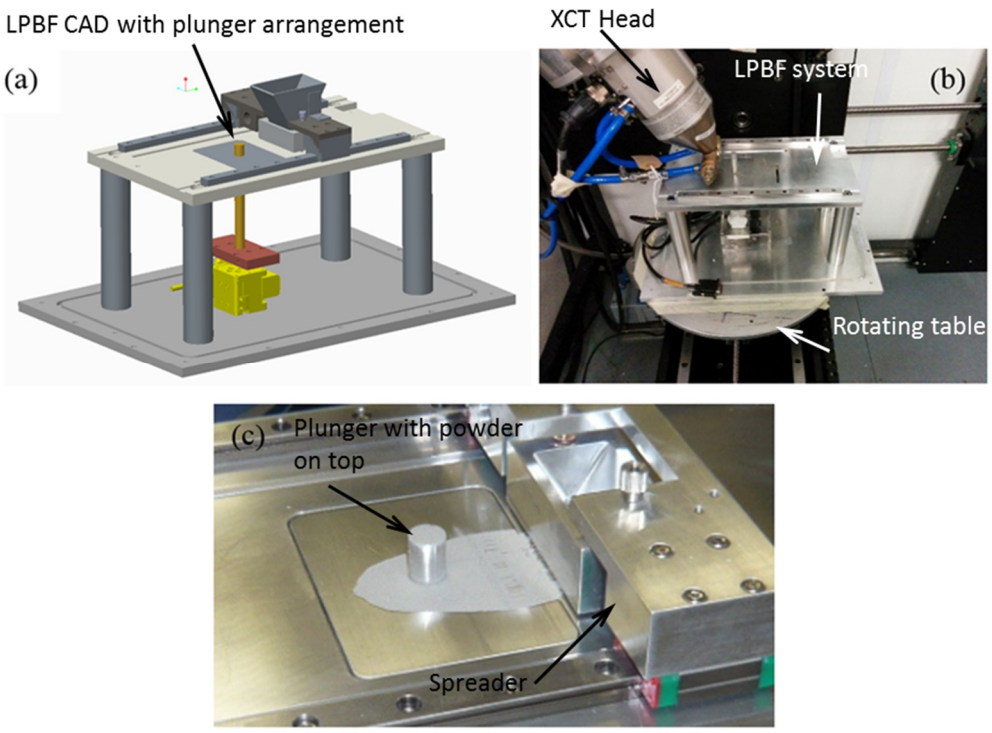

Figure 3.23: XCT setup (a) CAD model of modified LPBF (b) LPBF in XCT machine (c) Powder trials

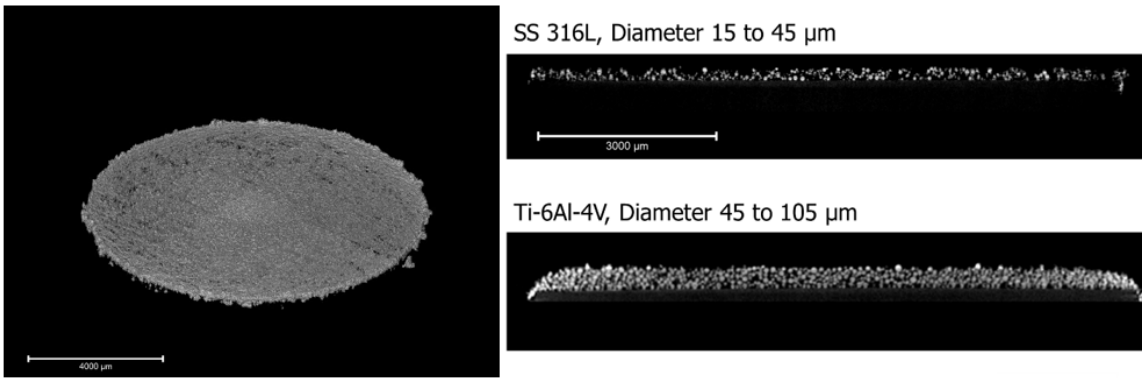

Figure 3.24: XCT 3D constructed image (left) and sliced 3D images of two different powders

The LPBF system with XCT scan head in the machine is shown in the Figure 3.23(b). There were two different powders used, first, stainless steel 316L powder size 15 – 45 µm, second, titanium alloy Ti-6Al-4V size 45 – 105 µm. After the test, 3D images were constructed (Figure 3.24 left) and sliced from the middle shown in Figure 3.24 right. The difference can be clearly seen in particle distribution of both the powder materials; Ti-6Al-4V powder resulted higher packing density than stainless steel powder.

3.7 Summary

A compact and automated system for powder bed fusion additive manufacture has been reported. Its design was determined by the requirements for x-ray access, portability and

remote operation. In particular, the system can accommodate both horizontal viewing through a very thin powder bed, and oblique imaging at 12 to 57° from the horizontal from below the powder bed through a full-width powder bed for more representative heat conduction. In both cases, single track, area and multiple layer builds can be implemented automatically. The system was characterised and it was demonstrated that parts with >99% density are produced by the system. The design is simple and very few components require precision machining, making it an approach that is accessible to most research groups. Furthermore, its open-architecture design enables access to the build area for a range of other in-situ measurement techniques discussed further in this thesis.

Chapter 4. High-speed Imaging in LPBF

4.1 Introduction

Detailed imaging of the interaction between the laser beam and the powder bed whilst building multiple layer islands with laser powder bed fusion (LPBF) has not been reported previously. It is extremely challenging to record images through the viewing window of commercial LPBF systems with sufficient magnification or contrast to see individual powder particles in the powder bed. Higher magnification images have so far focussed on the melt pool whilst scanning a single laser track in a representative powder layer. In this Chapter, detailed in-process imaging of the interaction of the laser beam with the powder bed during the LPBF build of fully dense parts is reported. It is demonstrated that the LPBF process is more dynamic than is generally appreciated and involves considerable motion of the powder particles and agglomerates in and above the powder bed. This motion is driven by the laser-induced plume of metal vapour and plasma above the melt pool. As an outcome of this work, a journal article entitled "**Fluid and particle dynamics in laser powder bed fusion**" was published in the peer-reviewed Acta Materialia journal as an open access. Supplementary data (Videos) associated with this Chapter can be found at the online version of published article [137].

In the work presented here, detailed high-speed imaging of the interaction of the laser with the powder bed is shown at a range of laser powers and scan speeds. It was observed that powder particles entrained in the atmospheric gas flow were drawn in towards the melt pool and ejected backwards with respect to the scan direction or vertically upwards at different process settings, as reported previously in Chapter 2. But by imaging the wider powder bed, the denudation produced by these effects are observed for the first time. In addition, effects that have not been reported previously at other process settings, including the forwards ejection of entrained particles and denudation arising due to their interaction with the laser plume, and particles being driven away from the melt track at atmospheric pressure are reported here. More importantly, the imaging has been extended from single tracks to multilayer builds, in order to observe how these effects manifest in the powder bed during a full build. Furthermore, high-speed schlieren imaging for gas flow visualisation of the density gradients in the gas flow, not attempted for LPBF previously, both to elucidate aspects of the physical phenomena involved in the process are reported in this Chapter.

4.2 Experimental System

The design and characterisation of an open architecture LPBF system for in-situ measurements during LPBF have been reported in Chapter 3, which is shown schematically in Figure 4.1. A key feature of the system is computer control for the automated build of fully dense components. The computer controls the vertical movement of the build plate between layers, the movement of the silicon cord powder spreader and the laser illumination and scanning. The system has complete flexibility for laser power and speed, and scan geometry including hatching. Hence it is possible to achieve high resolution imaging not only whilst melting single tracks in the powder bed, but also during multiple layer builds under conditions known to produce parts with >99% density. Minor modifications were made to the top and end faces of the Perspex shielding chamber to incorporate viewing windows. For top views of the powder bed, a window of diameter 50 mm made from infra-red absorbing KG glass was added, Figure 4.1. Side viewing windows were added, made from Zerodur glass flats of diameter 75 mm, polished to λ/4 on both surfaces.

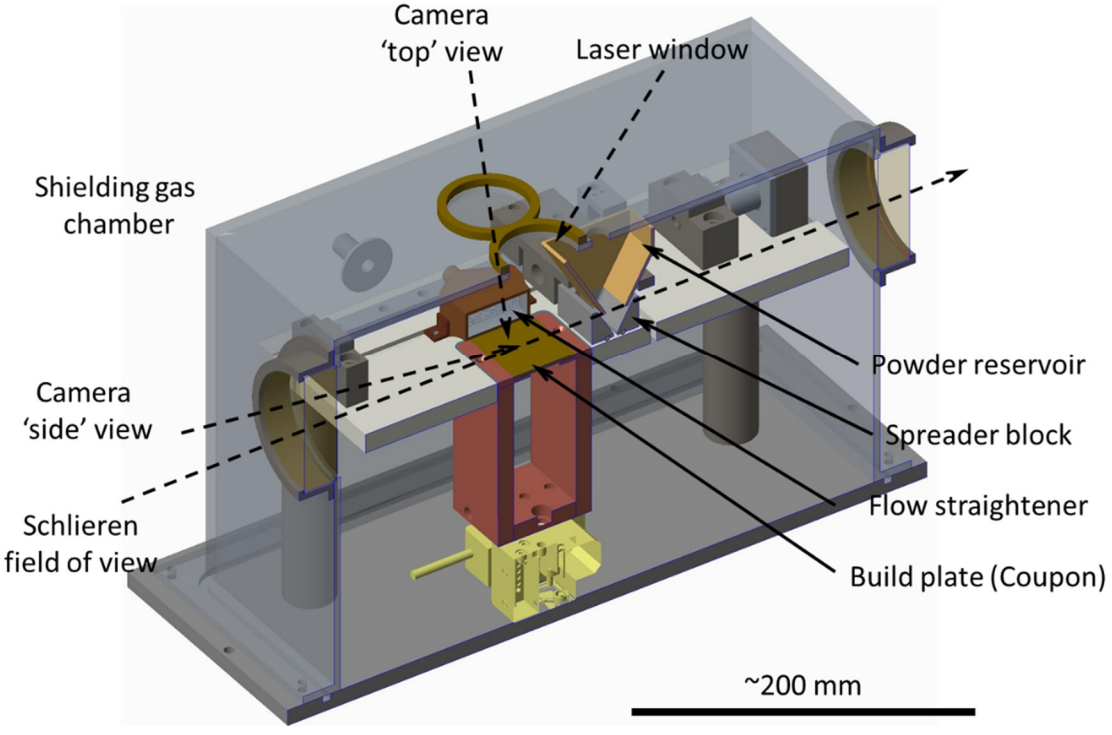

Figure 4.1: Schematic of the open-architecture LPBF system with modifications for high-speed imaging and schlieren imaging.

All the experiments reported here were undertaken with gas-atomised stainless steel 316L powder (Renishaw PLC) with particle diameters in the range 15 to 45 μm and a mean diameter of 30 μm [133]. Powder layers were melted on to 80 × 40 mm^2 stainless steel

304L build plates (coupons) of thickness 2 mm, using a single mode fibre laser (SPI 400 W continuous wave, 1070 nm) which was scanned over the powder surface (Raylase MS-II-14 scanner with 163 mm focal length f-theta lens). The coupon surfaces were roughened by manual, circular rubbing with P400 sandpaper. The powder layer thickness for particular experiments is noted in the relevant sections below. Light from the laser was focussed to a spot with a Gaussian beam profile and 4Dσ diameter of 50 μm in both the x- and y-directions, measured with an Ophir Spiricon SP928 beam profiling camera. The shielding chamber was purged with argon until the measured oxygen concentration was <0.1%. The experiments were performed with an exchange of clean argon into the chamber between experiments, exhausted through a water bath to remove potentially harmful nanoparticles produced by the process. The pressure in the chamber remained at 1 atm.

A Photron Fastcam Mini UX100 monochrome camera [138] was used for high-speed imaging. The full resolution for this camera is 1,280 × 1,024 pixels up to 4,000 fps. The direct imaging experiments reported here were recorded at 8,000 fps and 1,280 × 616 pixels. The camera was fitted with a C-mount QiOptiq Optem Fusion lens, configured to provide a zoom of 7:1 and a working distance of 135 mm. At this working distance, the region of interest could be varied between approximately 14 × 11 mm^2 (depth of field 2 mm) and 2 × 1.5 mm^2 (depth of field 0.2 mm).

The top viewing window was used for direct imaging from above the powder bed with the camera angled at ~20° to the vertical as seen in Figure 4.2(a). One side window was used for direct imaging from the side of the powder bed, with the camera positioned at approximately 10° to the horizontal as seen in Figure 4.2(b). For the side views, an infra-red absorbing filter was placed in front of the camera lens. The camera was mounted on a tilt stage to change the area of the powder bed that was imaged, which enabled multiple areas to be scanned and imaged on the same coupon. This feature was particularly useful for side imaging with high magnification and a small depth of field: the tilt stage was used to select the build region on the powder bed followed by a fine adjustment of the lens focus as necessary. Illumination was provided by a 300 W tungsten filament lamp that was focussed through the top of the Perspex shielding chamber on to the powder bed in a rectangle of approximately 15 × 5 mm^2. The illumination was switched on for a few seconds during imaging and produced negligible heating of the powder bed.

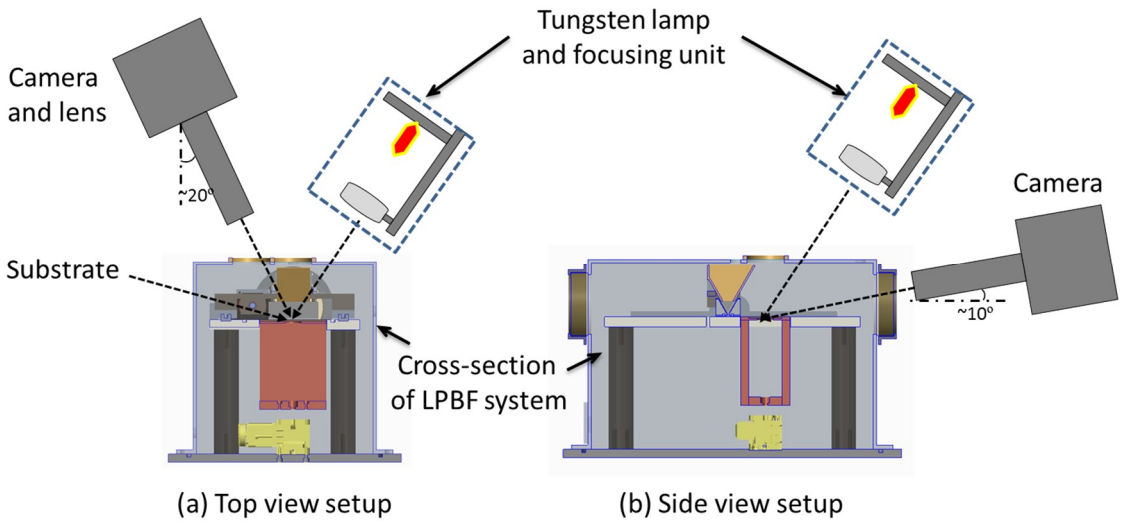

Figure 4.2: High-speed direct imaging experimental setup (a) top view (b) side view

Schlieren imaging to view and optimise shielding gas coverage during welding applications have been previously reported by Bitharas et al. [87,139]. Schlieren imaging enables refractive index gradients due to temperature, pressure and concentration gradients to be visualised. Figure 4.3 shows a schematic of the optical setup that used Toepler's double parabolic mirror schlieren arrangement [140]. The Toepler's portable z-type schlieren system was incorporated into the LPBF system as seen in Figure 4.3. Two 100 mm diameter, parabolic field mirrors with a focal length of 1.27 m, Mirror 1 and Mirror 2, were located approximately two focal lengths apart. Aligned in a Z-type arrangement, Mirror 1 collimated the light from the 300 W tungsten lamp source while Mirror 2 focused it to a spot. Ideally the included 'Z' angles should be less than 3° in order to reduce the separation of the tangential and sagittal focus planes of Mirror 2. However, in order to incorporate LPBF system between the mirrors, while keeping the distance between the mirrors within the confines of the lab space, it was necessary to increase the 'Z' angles of the mirrors to approximately 8°. The result was a small amount of astigmatism in the recorded images. Tungsten lamp that was focussed on to a 2 × 5 mm^2 rectangular source slit with its long edge vertical through condenser lens of focal length 120 mm. The slit was placed at the focus of the first schlieren Mirror 1 to produce a collimated beam that passed across the LPBF system via the windows in the side of the Perspex shielding chamber, Figure 4.1. A second, mirror (Mirror 2) focussed the collimated beam to produce an image of the source slit on a vertical knife-edge filter. The knife-edge filter was positioned with a micrometer to block 50% of the image of the source slit in the horizontal (x) direction, producing images with a uniform measurement range in which the intensity was proportional to the gradient of the refractive index $\partial n/\partial x$. Schlieren images were recorded with the high-speed camera using a variable focus telephoto lens (focal length 75 to 300 mm) at 16,000 fps and

1,280 × 312 pixels. An additional infra-red absorbing filter, and a polariser to remove glare, were placed in front of the camera lens.

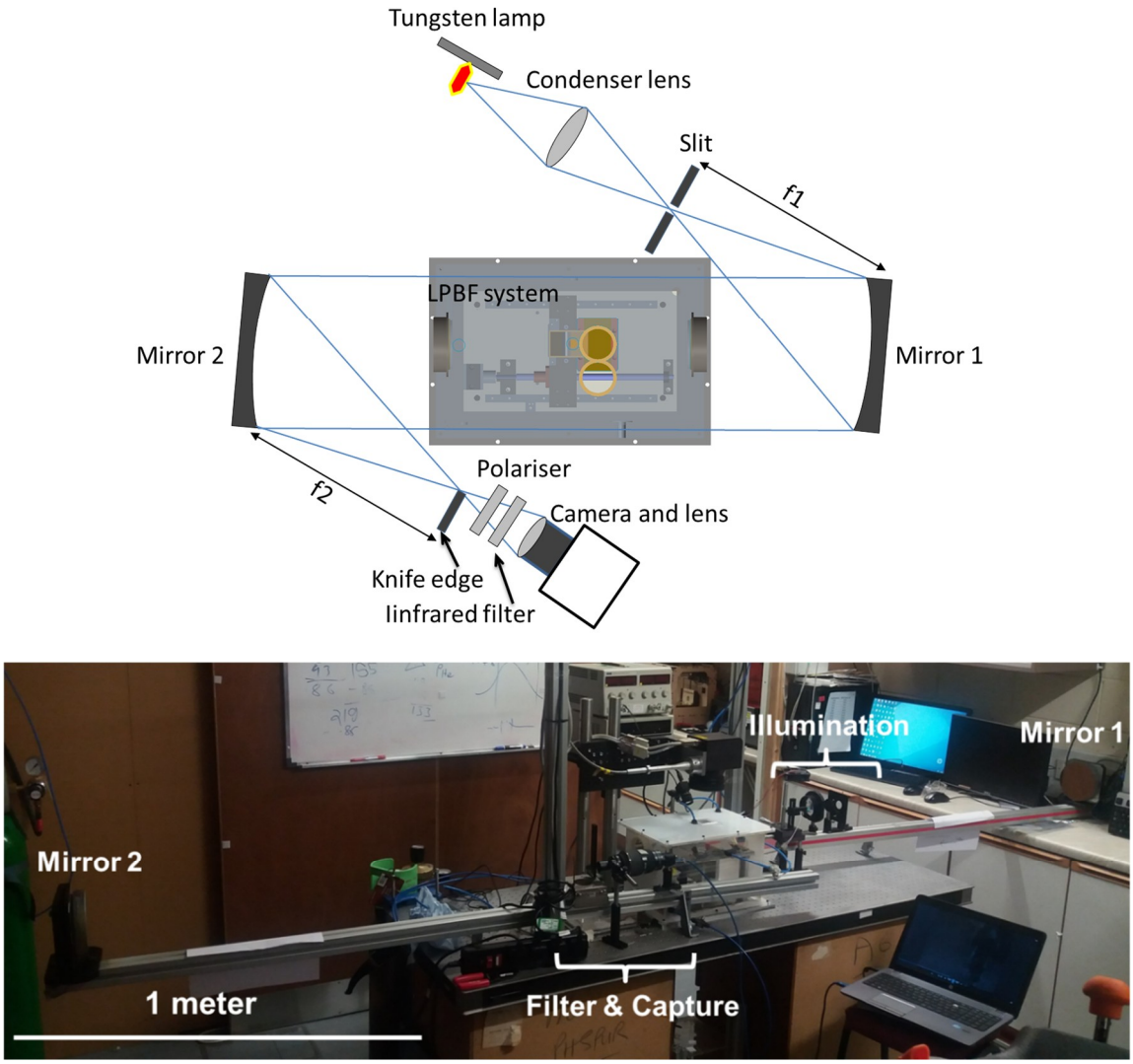

Figure 4.3: Schlieren imaging setup for laser powder bed fusion, top, schematic of z-type schlieren setup [140], bottom, image of the lab setup with LPBF system

4.3 Results

The high-speed direct imaging results are divided into single track and multilayer builds in the following sections. These are followed by sections for the results of high-speed schlieren imaging and finite element modelling. All the results in this section were recorded without a flow of shielding gas across the powder bed in order to focus attention on the gas movement due to the laser's interaction with the powder bed. The effect of an additional flow of shielding gas across the powder bed is introduced in the Discussion Section 4.4.

4.3.1 High-speed Imaging: Single Tracks

Figure 4.4 and Videos Figure 4.4(a-f) show high-speed imaging for side and top views of the powder bed during laser scans of individual tracks. Three different laser power and scan speed combinations are shown: 50 W and 0.1 m/s, 100 W and 0.5 m/s, and 200 W and 1 m/s. The 100 and 200 W laser power conditions have the same line energy (laser power divided by scan speed) at 200 J/m while the 50 W condition has a line energy of 500 J/m. The 50 W and 100 W laser power conditions have been shown to build parts with >99% density in Chapter 3. These results are for the first powder layer of thickness 50 µm spread on the coupon. We had access to only one high-speed camera and so the side and top views were recorded in separate experiments.

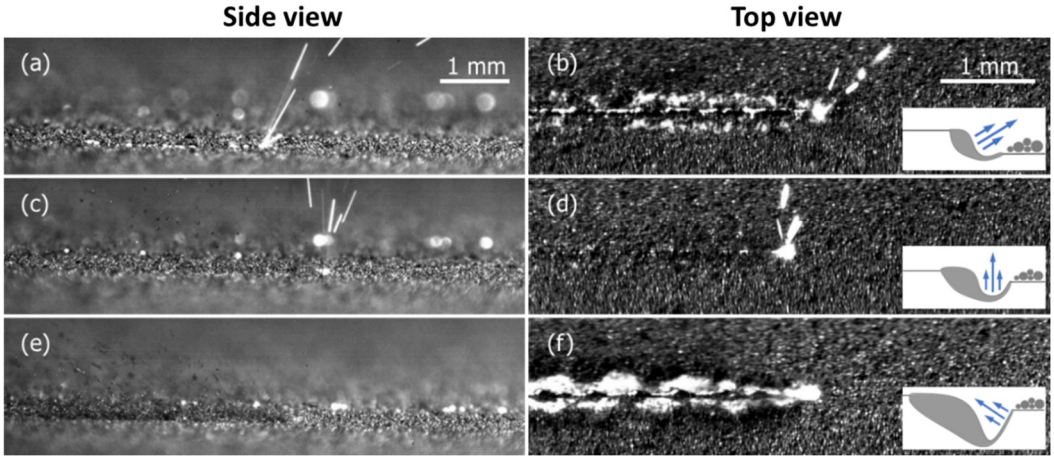

Figure 4.4: High-speed images for side and top views when scanning single tracks (left to right scan direction) with laser power and scan speeds of (a) and (b) 50 W and 0.1 m/s; (c) and (d) 100 W and 0.5 m/s and (e) and (f) 200 W and 1 m/s. Inset is a schematic of the melt pool shape, which determines the laser plume direction. The videos for all figures are included in the supplementary material.

The results show that the direction of spatter ejection with respect to the laser scan direction and the denudation mechanism both change with process parameters. At the 50 W condition, the plasma jet is established forwards with respect to the laser scan direction. The induced flow of the ambient gas entrains powder particles in towards the melt pool from all directions on the powder bed. Entrained powder particles are either consolidated into the track or ejected forwards, due to the inclination of the plasma jet and induced gas flow as seen in the side view Figure 4.4(a). At the 100 W condition, the plasma plume and spatter are directed predominantly vertically upwards, resulting in less momentum in the shielding gas flow at the powder level and consequently less denudation. At the 200 W condition, the plasma and spatter are directed backwards with respect to the scan direction. The plume is at a sufficiently low angle that it impinges directly on the powder bed and causes denudation by blowing particles *away* from the track.

4.3.2 High-speed Imaging: Multiple Layer Builds

Multiple layer builds were undertaken at laser power and scan speed of 100 W and 0.5 m/s, respectively. Figure 4.5 and Videos Figure 4.5(a) and (b) show high-speed imaging of side views of the first and second layers of a rectangular island of approximately 2.6 x 1.8 mm^2. The powder layer thickness for the first layer was again t_{sp} = 50 µm, which was determined by the height of the powder spreader above the coupon surface. The z-stage was lowered by z_l = 40 µm between layers from which the powder layer thickness for each layer is calculated (Chapter 3) and given in the caption for Figure 4.5. The scan spacing was s = 60 µm between adjacent tracks, corresponding to a scan spacing factor s/2d of 0.6, where d is the laser spot diameter. The laser was switched off for ~500 µs at the end of each line before returning in the opposite direction; the rectangular outline to the island was not scanned at the start.

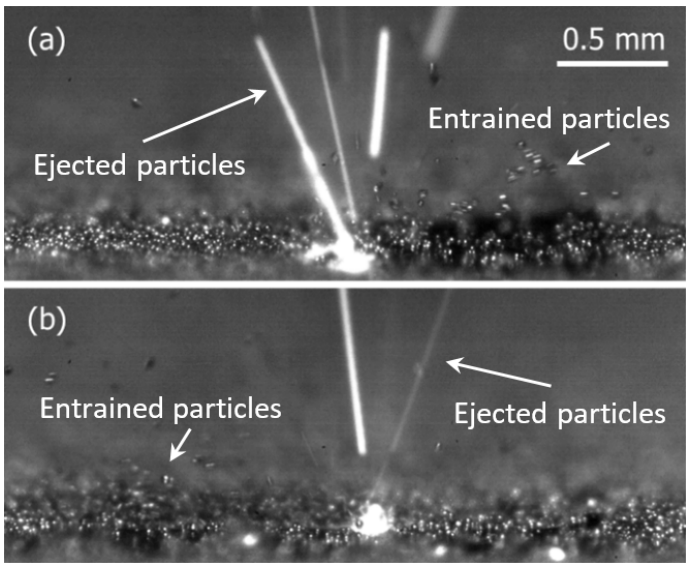

Figure 4.5: Side views during island scans at 100 W and 0.5 m/s. (a) Layer 1, laser scan path front to back in the image. (b) Layer 2, scan path left to right. The powder layer thickness is 50 µm and 75 µm for layers 1 and 2, respectively, as it increases towards its steady state value.

For the first track of layer 1, Figure 4.5(a) shows vertical ejection from the melt pool as expected. From the second track onwards, the laser plume and entrained particles are angled away from the previously melted track. Powder particles and agglomerates alike are entrained by the shielding gas flow induced by the laser plume: their exact motion on and above the powder bed is determined by the specific scan strategy of the laser. The videos show instances where these agglomerates are melted directly into the track or melted into larger spherical beads in the atmosphere. Both views emphasise the dynamic nature of the powder bed when moving from single track to island scanning and the importance of the laser plume in driving that process.

Figure 4.6 and Videos Figure 4.6(a-d) show top views whilst building the rectangular island through multiple layers using the same laser scan parameters. The same region of the powder bed was imaged as the layers were built and the scan direction was rotated by 90° between successive layers. For the first layer, Figure 4.6(a), the first scan line shows relatively little denudation and the laser plasma is vertical as observed in Figure 4.4(b) and Figure 4.4(e). From the second scan lines onwards, the laser plume points away from the previously built, adjacent track as observed in Figure 4.5(a).

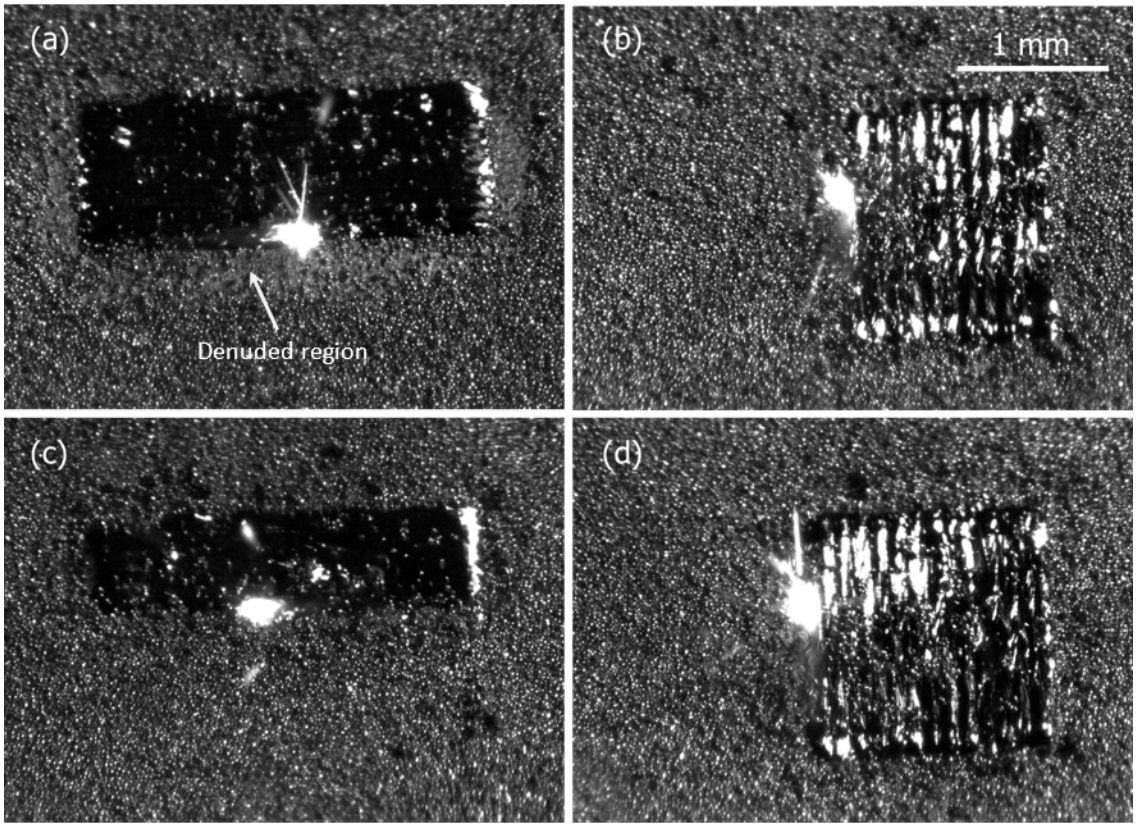

Figure 4.6: Top views of island scans at 100 W and 0.5 m/s for (a) layer 1, (b) layer 2, (c) layer 5 and (d) layer 6. Denudation is reduced after the first layer due to the increasing powder layer thickness and the surface roughness of built layers. The powder layer thickness is 113 µm and 119 µm for layers 5 and 6, respectively, as it increases towards its steady state value.

As the first layer progresses, the video shows an increase in temperature around the melt pool, through increased emission of light from plasma in the laser plume, and the denudation increases. For subsequent layers in the build, Figure 4.6(b-d), the denudation is less severe as the layer number increases, both between adjacent tracks in a layer and around the edges of the island. This decrease in denudation is in part due to the increase in powder layer thickness between layers as it evolves towards the steady state thickness. By the sixth layer, Figure 4.6(d), the powder layer thickness is already 89.5% of the steady state value of ~130 µm as shown in Chapter 3. Additional images sequences recorded for layers seven through ten showed no significant change in behaviour from that of layer six.

At the steady state powder layer thickness, it appears that there is sufficient powder adjacent to the track for it to roll towards the track without leaving a completely denuded region. However, the rough surface of the previously built layer also seems to contribute towards decreasing denudation compared to the first layer, which is discussed later.

4.3.3 Schlieren High-speed Imaging

Schlieren imaging was conducted for the first layer only. This was because the powder reservoir and the spreader block obstructed the collimated schlieren illumination passing across the powder bed. Hence, for the schlieren experiments only, the spreader block assembly was used to spread a powder layer on the coupon and was then carefully removed. The Perspex shielding chamber was fitted and purged with argon.

Figure 4.7 and Videos Figure 4.7(a-c) show high-speed schlieren imaging for single track laser scans across the powder bed at the three laser power and scan speed combinations used in Figure 4.4. The images were recorded at 16,000 fps, but the video playback speed has been doubled to produce the same apparent time dilation as for Videos Figure 4.4. The telephoto lens gave a lower magnification than for direct imaging of the powder bed in order to capture the gas motion above it. Therefore, individual cold powder particles cannot be resolved but the refractive index gradient around hot particles expelled by the laser plume can be seen. The direction of the laser plume and ejection of entrained particles with respect to the laser scan direction for the three process conditions is consistent with Figure 4.4. At the 50 W condition, the low scan speed combined with the forward plasma ejection causes the laser beam to traverse a considerable distance of heated gas, metal vapour and plasma before it reaches the powder bed surface. It is not possible to separate the relative contribution due to temperature, pressure and metal vapour concentration on the measured refractive index gradient from the images. However, these refractive index gradients are undesirable as they can contribute to process instability through defocus and lateral wander of the laser spot. At the 100 W condition, the laser beam is apparently just in front of the region of high refractive index gradients once the large convection plume from the initial laser incidence on the powder bed has been cleared. Circular plumes of vapour can be seen when vertically ejected particles are vaporised by the laser beam. For the 200 W condition, interaction between the laser beam and the heated gas, metal vapour and plasma is not an issue due to the high laser scan speed, although these conditions were previously seen to produce a balled track.

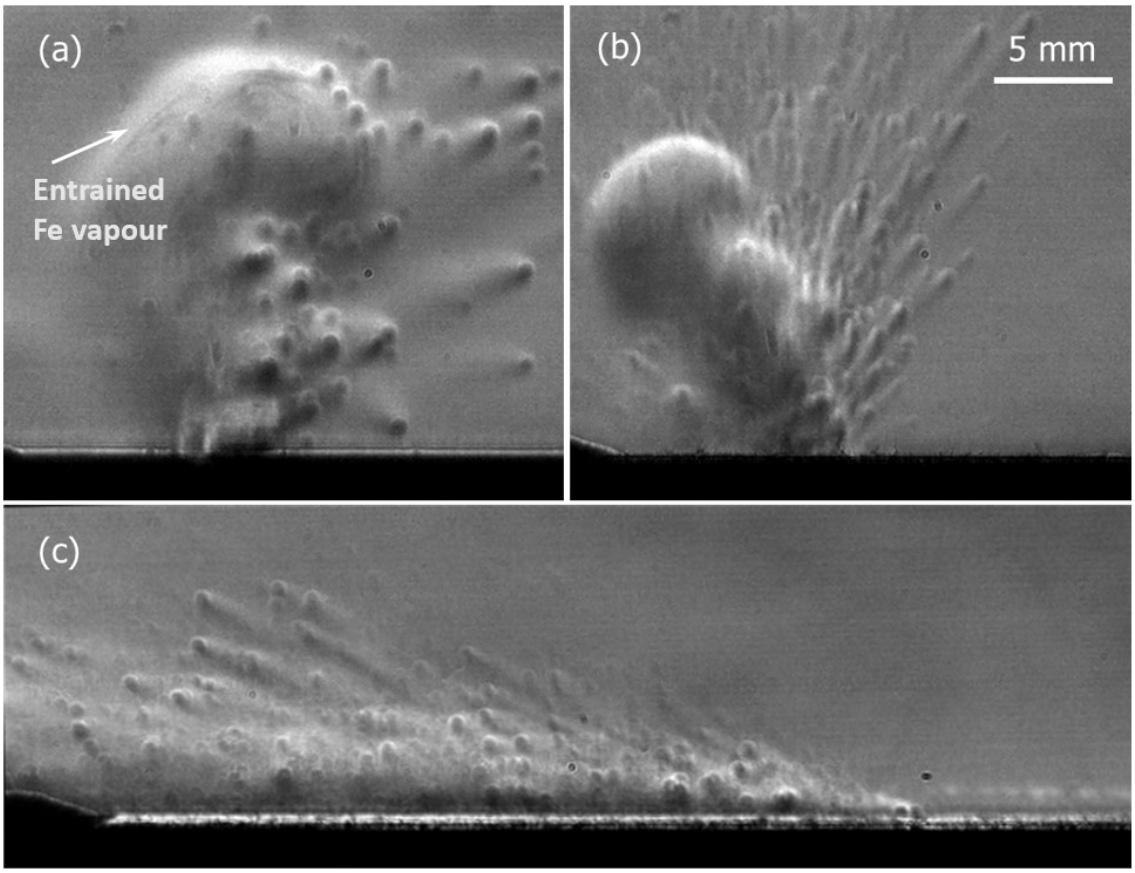

Figure 4.7: Schlieren images during left to right line scans at (a) 50 W and 0.1 m/s, (b) 100 W and 0.5 m/s, and (c) 200 W and 1 m/s. The characteristic refractive index gradients due to convection are visible in (a) and (b) but not present in (c) due to the backwards tilt of the laser plume. Entrained Fe vapour is visible behind the convection front in (a).

Figure 4.8 shows a composite schlieren image sequence at the times indicated after initial illumination of the powder by the laser for a single-track laser scan across the powder bed towards the camera, taken from Video Figure 4.8.

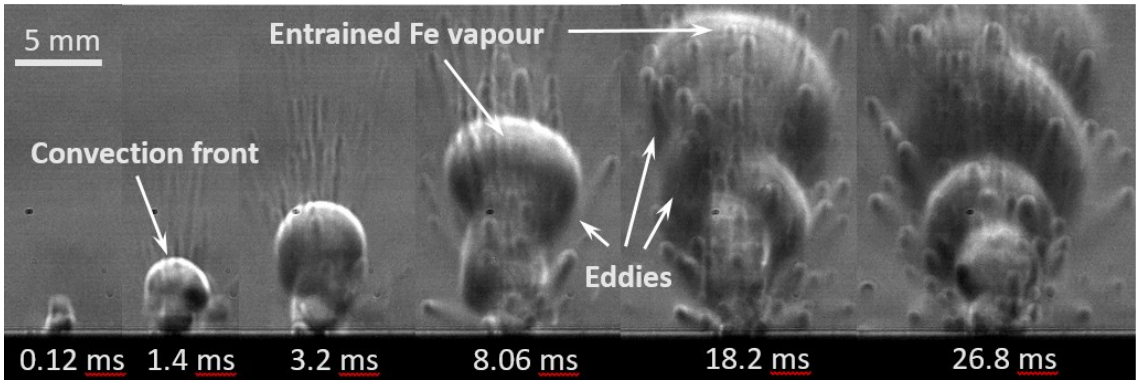

Figure 4.8: Composite image of the heated gas rising due to convection at the times indicated for laser power 100 W and scan speed 0.5 m/s towards the viewing direction. Radial momentum is imparted to the atmosphere by eddies trailing the convection fronts.

Upwards momentum carried by the plume is imparted to the surroundings, as indicated by the observed convection front while radial gas motion is induced by the eddies trailing it. Dark lines in the initial convection front are particularly clear, and are due to entrained iron

vapour. They are also visible in the Video Figure 4.7(a). The plume of heated gas continues to be fed by the laser plume: intermittent bursts of gas and vapour could be caused by laser-supported absorption waves (LSAW) although the spatial and temporal resolution of these measurements is insufficient to resolve directly the shock front or light emission associated with those events.

4.4 Discussion

This research shows the importance of the laser plume and ambient atmosphere for a full understanding of the LPBF process, because of the influence on denudation but also on the production and subsequent transport of debris. A detailed numerical model which includes plume dynamics and temperature distribution is included in the published article but not shown here. From the article [137], the plume includes Fe vapour and an optically thin plasma of metal ions. The plume velocity is of the order of several hundred m/s and scales with laser power. The laser plume induces an inwards flow in the surrounding atmosphere that reaches velocities of the order of tens of m/s. This flow exerts a significant drag on powder particles and agglomerates in the proximity of the melt pool, altering the local particle distribution and powder availability. When scanning islands, the temperature build-up increases the density of the plasma and the number of powder agglomerates that form. Agglomerates can also be affected by the laser plume-induced flow: they can be drawn back into the melted track, presumably with an increased likelihood of producing porosity, or ejected into the atmosphere and produce large molten beads if they interact sufficiently with the laser beam, hot gas, or a combination of both. Particles that are “heat-treated” and ejected act as an inclusion if reincorporated into the build at a later time, due to microstructure mismatch and oxide layer formation, as shown by previous studies for maraging steels in [34], stainless steel, Al-Si10Mg, and Ti-6Al-4V in [80] and Ni-based superalloys in [123]. These entrained powder particles, agglomerates and larger solidified beads are also routinely found in the filters of commercial LPBF systems, which is explained by these results. When building multiple layers, the denudation caused by the plume-induced flow of the atmosphere becomes less significant as the powder layer thickness increases towards its steady state value.

The motion of particles entrained in the flow of the inert atmosphere immediately around the melt pool produced by the high-speed vapour jet has been observed previously [58,69,85]. Our description of the jet as a laser plume recognises that it contains plasma in addition to metal vapour. Entrained particle motion has been proposed as a mechanism for

denudation [58] but the results presented here are the first direct observation of this denudation process. Entrained particles are generally drawn towards the melt pool, Figure 4.4(b) and Figure 4.4(d), but we also observed denudation arising due to particles being blown away from the melt pool, Figure 4.4(f). The diameter of the induced flow increases with distance from the melt pool, and for the laser scan conditions in Figure 4.4(f), it was angled backwards sufficiently to impinge directly on the powder bed and blow particles away from the scan track. It is perhaps worth emphasising that denudation due to particle motion away from the melt track was inferred in [58], but that was only at very low ambient pressures and was therefore due to uniform expansion of the Fe vapour and not due to the angle of the plume.

The evolution of vertical to backwards ejection of material from the melt pool as the laser scan speed increases has been observed in laser welding [141] and LPBF [58,84]: the ejection direction is taken to be normal to the surface of the melt pool under the laser spot which varies due to a complex interaction of the laser plume recoil pressure and the liquid metal, as indicated by the schematics in Figure 4.4(d) and Video Figure 4.4(d). We also observed the laser plume directed forwards from the melt pool for the first time, Figure 4.4(b). Previous studies have reported particle ejection from the melt pool in the forward direction, due to interfacial surface tension forces resulting in droplet detachment, rather than the laser plume directed in the forward direction. We believe a forward direction of the laser plume is specific to LPBF and is not seen in welding. The presence of additional material (i.e. powder) in LPBF enables a build-up of molten material in a bead at the back of melt pool, as indicated by the schematic in Figure 4.4(b). We speculate that there is a gradual transition between these regimes, and hence in the direction of the laser plume, in particular from vertically upwards to backwards. Hence the denudation caused by particles entrained in the gas flow could transition from an upwards plume pulling inwards towards the track, observed in Figure 4.4(d), through an intermediate stage of a backwards tilted plume still pulling inwards (not observed), to a plume tilted sufficiently far backwards that the flow impinges on the bed and blows away from the track, Figure 4.4(f). The onset of Plateau-Rayleigh instability (balling) may be enhanced by the drag forces exerted by the plume on the liquid surface, but the characterisation of this interaction would require a unified model of the melt pool and plume.

The vertical plume could be investigated further as a favourable process setting, both with respect to reduced denudation and uniform direction of spatter within the build chamber. However, the detailed imaging of rectangular islands at 100 W showed that the

laser plume tilts away from the adjacent track, which we again attribute to the modified shape of the melt pool. Hence spatter, entrained particles and agglomerates are ejected away from the build towards fresh powder in the bed. The interaction of particles and agglomerates above the powder bed is entirely dependent on the scan pattern of the laser within the island. Particles carried by the flow can be dragged towards the scan line without being sintered or ejected upwards by the flow and can interact with the beam at a later time. This effect becomes more prevalent as the layer number increases and more powder is available in the build area. We have not undertaken a detailed analysis of the particle velocities because only its component in the image plane is available; furthermore, the particles are of different diameters and the force acting on them varies with distance from the melt pool making any inferences rather speculative. Nevertheless, cold particles raised off the powder bed typically move at ~2 m/s, and the maximum length of image streaks from the ejection of hot particles corresponds to ~6 m/s. These speeds are in agreement with the simulated velocity of the induced flow as shown in the published article [137].

The extent of denudation in the first layer can be significant as the powder bed temperature increases and the effects of many adjacent tracks accumulate, Figure 4.6(a). Whilst this observation can be taken into account in process planning, its effect should not be over-exaggerated. Firstly, a commercial LPBF build typically has ~100 sacrificial layers for support structures before layers of the actual component are deposited. Hence relatively small areas in the first layer are actually scanned and the powder can be pulled in from surrounding regions. Secondly, the first layer is relatively thin and is spread directly on to the coupon. The powder layer thickness for the first layer was t_{sp} = 50 μm, which is determined by the height of the powder spreader above the coupon surface and the z-stage was lowered by z_l = 40 μm between layers. A geometric series describes the evolution of the powder layer thickness between layers (in Chapter 3). In the steady state, the melted layer thickness is z_l and the powder layer thickness from which it was produced is z_l/c, where c is the consolidation ratio (equal to the thickness of a melted layer divided by the thickness of the powder layer that produced it). For c = 0.3 measured in our system, the steady state powder layer thickness of ~130 μm and the denudation is less severe as observed in the results. However, it appears the surface roughness of previously built layers also contribute to the reduced denudation in later layers. In a separate experiment, we spread a thicker first layer of 130 μm directly on to the roughened coupon surface. The denudation was less than for the 50 μm first layer but larger than for layer 6, because the particles could move more freely on the plane coupon surface compared to a built layer. It highlights that caution is required if trying to extract general conclusions from single track

and single layer observations, which are not typical of the conditions observed in building a complete, fully dense part.

Schlieren imaging enabled the effect of refractive index gradients, associated with the laser plume (metal vapour and plasma) and the heated atmosphere, above the melt pool to be visualised. These gradients are undesirable and can cause variations in the laser position and focus. In a commercial system, these hot fluids should be cleared by a flow of shielding gas across the powder bed during the process, which can also serve to extract 'airborne' particles and prevent them from landing back on the powder bed. All the results presented so far have excluded this cross-flow, in order to focus on the effects of the plume-induced flow. Indeed, these cross-flows are typically of the order of a few m/s, and so will not interfere with the plasma flow directly. It is instructive to observe the interaction of the laser-plume induced flow with a laminar cross-flow of 10 l/min across the powder bed from the flow-straightener.

A cross flow system for shielding gas flow across the powder bed was added in the same way as available in commercial machines. A typical cross flow system consists of flow diffuser and flow straightener. The design of the system was inspired from commercial machines, and an [76]. The challenges in designing such system were the LPBF system's small working area 40 x 40 mm and space limitations in the build chamber. Several design iterations were made, and fitment was cross-checked in Creo 2.0 CAD modelling software (Figure 4.9(a)). The iterations were mainly for the flow diffuser design, as the gas inlet was from a tube of 4 mm diameter, to diffuse the gas efficiently in limited space, a solid cone of base diameter 8 mm and height 10 mm was added immediately after the inlet. Furthermore, a honeycomb structure of thickness 5 mm with the edge of 0.75 mm (Figure 4.9b) was added to make flow uniform and distributed over the entire working area. In addition, a fluid flow model of the system was prepared in COMSOL Multiphysics to validate the design and performance. The cross-flow system was made from ABS plastic using FDM 3D printing technology. The outlet system (Figure 4.9(d)) was also added to the front of the cross-flow system in the build chamber to protect the sliding rail from spatter and contamination. The flow rate used in these experiments was 10 l/min.

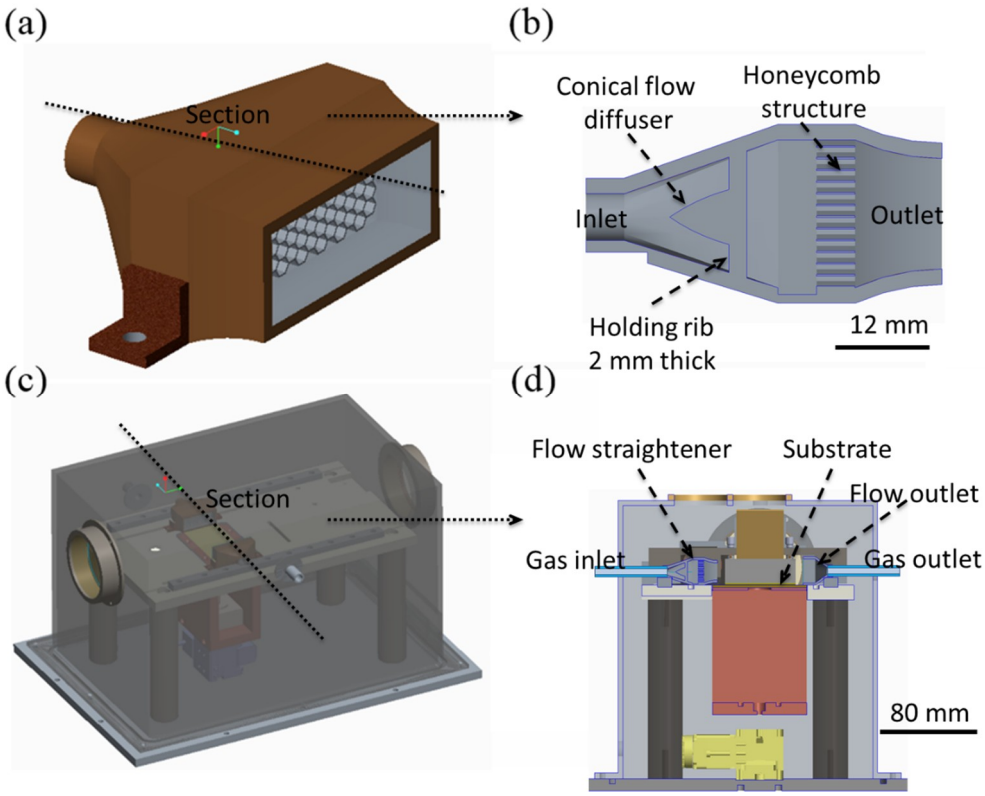

Figure 4.9: Cross-flow system in the LPBF system (a) cross-section of flow straightener (b) cross-section of flow straightener (c) cross-flow system assembled in the LPBF system (d) cross-section of flow system assembled in the LPBF system

Due to the relatively low velocities in the decelerated flow a few mm above the powder bed, a lower frame rate is more suitable for this application. Figure 4.10 and Videos Figure 4.10 show schlieren imaging with the high-speed camera replaced with a standard CMOS camera operating at 150 fps. An additional 633 nm ±1 nm full width at half maximum band-pass filter was included to eliminate incandescence from the melt pool and plasma light. Figure 4.10(a) shows the plume with no cross draft. Figure 4.10(b) and Figure 4.10(c) show the introduction of a cross draft for laser powers of 100 and 200 W respectively, which indicate the need to match the cross draft to process setting if the plume and particles are to be removed effectively. Another interesting observation is that ejected particles carry enough upwards momentum so as not to be affected by the cross-flow initially, but are swept to the side upon re-entry to the stream after free-falling. It is difficult to separate the relative contribution due to temperature, pressure and metal vapour concentration on the measured refractive index gradient from these images. However, Figure 4.10(d) shows the effect of introducing a helium inert atmosphere. The refractive index sensitivity to temperature and pressure gradients is lower in helium than argon due to its lower density, and as a consequence the metal vapour can be distinguished. A full study of the effect of cross drafts and of the He atmosphere are beyond the scope of this thesis, and will form part of future research. However, this discussion highlights the importance of fluid and

particle dynamics on the cross-draft requirements in commercial systems and in the usefulness of schlieren imaging to determine the effectiveness of the extraction system during builds.

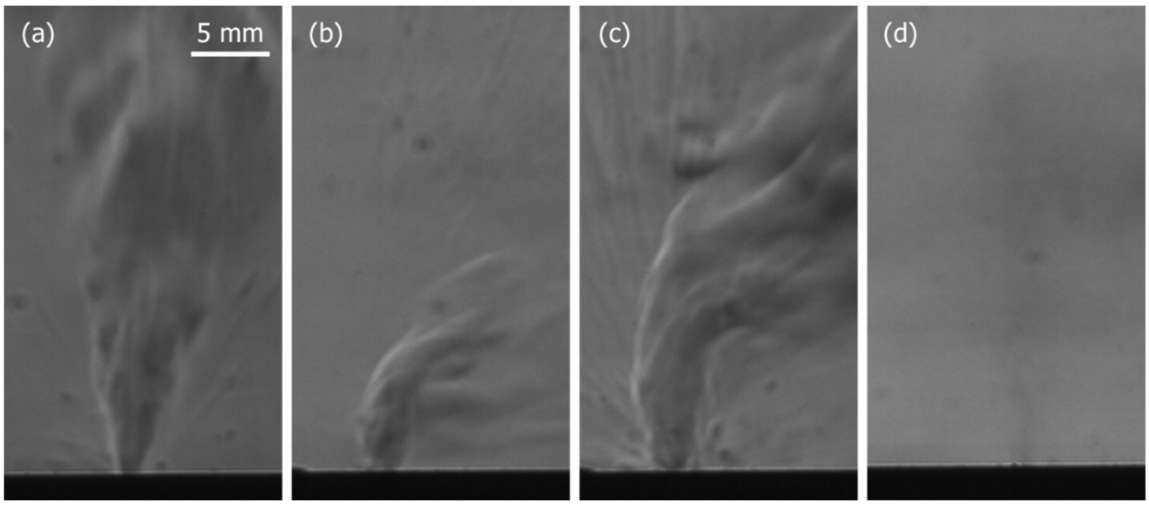

Figure 4.10: Long exposure schlieren images. (a) 100 W laser power and no cross flow, (b) 100 W laser power with 10 l/min cross-flow, (c) 200 W laser power with 10 l/min cross-flow. (d) Vapour stream in Helium atmosphere. Refractive index gradients due to temperature and pressure are reduced in He with schlieren sensitivity tuned for Ar.

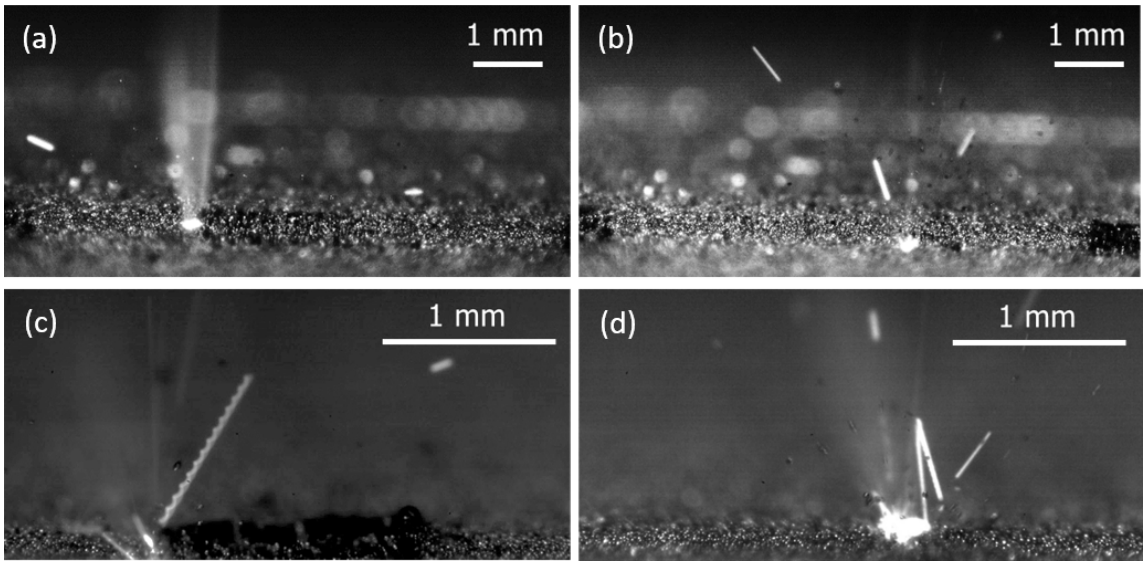

Figure 4.11: (a) Laser plume radiation during an island scan at 200 W and 0.5 m/s, where surface temperature is increased. (b) Scattering of the laser beam by ejected particulate from the plume. (c) Swirling hot particle ejection (d) Ejection of hot particle followed by collision, deflecting the particle back towards the bed.

The video sequences provide many interesting local effects which cannot all be discussed individually. A particularly nice example around 150 ms in Video Figure 4.5(a) is the formation of a powder agglomerate close to the scan track, which is lifted off the powder bed by a subsequent scan, fused into a molten bead whilst ‘airborne’ and ejected from the build region. To finish, Figure 4.11 shows some other interesting events not in the videos

selected for this thesis. Figure 4.11(a) is a clear example of the laser plume at 200W to compare with the emitted light distribution from the plasma as shown in the article. Figure 4.11(b) shows scattering of the laser beam by ejected particulate from the plume. Figure 4.11c shows emission from a partially vaporised particle that was swirling (rotating) as it was emitted. Figure 4.11(d) shows a Λ-shaped streak, formed by a change in the trajectory of a hot ejected particle due to a collision. High-speed particles which are turned towards the bed in this manner can form impact craters in the powder layer, unsettling nearby particles.

4.5 Summary

The results presented in this work elucidate the dynamic phenomena that arise from the complex interaction between the laser and the molten metal during LPBF, which are related to the quality of the manufactured part. The open architecture design of the system enabled detailed high-speed imaging to be performed for single tracks and multiple layer builds, as well as schlieren imaging for flow visualisation. It was shown that the Fe vapour, plasma and induced Ar gas flow determine the pattern in which powder is denuded from the vicinity of the melt pool. Single line scans showed that the direction of particle ejection with regards to the scanned direction changes from forwards to backwards with increasing laser power and scan speed. When the scan speed and power were relatively high, the plume was pointed fully backwards and towards the powder layer, which was heavily disrupted as a result. Upward ejection resulted mostly in particles being pulled towards the laser spot due to the aerodynamic drag. Particles that approached the plume were either sintered or melted and subsequently ejected according to their accumulated heat and momentum. The high temperatures of the plume promoted the formation and ejection of agglomerates (particles sintered together) and large spherical beads (particles fused together) which may result in defects and inclusions if reincorporated into the build after landing. Imaging of the process after several layers showed that denudation has a reduced impact on the powder availability compared to the first layer, due to increased powder layer thickness and surface roughness.

Schlieren imaging enabled the visualisation of the plume, facilitating flow characterisation. It was observed that convection fronts originating from the melt pool propagate in the atmosphere above the powder bed. Momentum was conveyed radially with respect to the plume axis through transient eddies trailing the convection fronts. The jet of vapourised material becomes entrained in the hot gas, accentuating the refractive index

gradient presented to the laser beam. Refractive index gradients were observed around ejected particles, confirming that both heat and momentum is transferred from the plume. High-speed observation of the convection patterns in the atmosphere correlated well with the denudation effect observed through the direct imaging. Vapour jet visibility was enhanced in a He atmosphere, due to weaker refractive index gradients. This difference suggests that heat and mass transfer in the plume can vary significantly with a change in ambient gas, warranting further investigation.

Chapter 5. Laser Powder Bed Fusion in Vacuum

5.1 Introduction

The perceived advantages of laser powder bed fusion (LPBF) at reduced pressure include a more stable melt pool and reduced porosity, although it has not been realised to date. In this study, high-speed imaging is used to investigate the interaction of the laser beam with the powder bed at sub-atmospheric pressures. As an outcome of this work, a journal article entitled "**Laser powder bed fusion at sub-atmospheric pressures**" was published in the peer-reviewed International Journal of Machine Tools and Manufacture journal as an open access. Supplementary data (Videos) associated with this Chapter can be found at the online version of published article [142].

To date, very few researchers have investigated laser powder bed fusion (LPBF) of metals at sub-atmospheric pressures [57,114,115]. The perceived advantages of sub-atmospheric pressure include reduced porosity and surface roughness in the fabricated part, similar to that achieved with laser welding. Remaining pores that are not filled with shielding gas would be removed more effectively by hot isostatic pressing [143]. However, the findings from this thesis are somewhat contradictory: the pressure and laser settings required for a successful process have not been established and no multi-layer builds have been undertaken. In this Chapter, first high-speed imaging of the interaction of the laser with the powder bed at sub-atmospheric pressures are reported to provide some process understanding for future implementation in LPBF. In this work, only single powder layers are investigated in order to resolve the inconsistences in the LPBF literature regarding suitable process settings for sub-atmospheric pressures. Similar process where a vacuum is used as atmosphere is called electron beam melting (E-Beam). The E-Beam process is different than the LPBF process as it uses the electron beam as an energy source so no detailed literature study of the same is reported here.

The Clapeyron equation describes the gradient of the coexistence curve on the phase diagram of a material, for which two phases exist in thermodynamic equilibrium, $dP/dT = L/(T\,\Delta v)$, where P is the pressure, T is the absolute temperature and Δv and L are the change in specific volume and the latent heat of the phase transition, respectively. For vaporisation well below the critical point, the change in specific volume of the vapour is significantly larger than that of the liquid, enabling the specific volume to be replaced using the ideal gas law to obtain the Clausius-Clapeyron equation [57,114]:

$$\ln\left(\frac{P_2}{P_1}\right) = \frac{L_{vap}}{R}\left(\frac{1}{T_1} - \frac{1}{T_2}\right) \tag{5.1}$$

where R is the specific gas constant and (P_1, T_1) and (P_2, T_2) are two points on the phase boundary. The change in vaporisation temperature with ambient pressure is plotted in Figure 5.1 for stainless steel 316L, taking the boiling point of 3090 K at atmospheric pressure and the latent heat of vaporisation, L_{vap} = 7.45 MJ/kg. The plot also includes the empirical line:

$$\log(P) = 11.1183 - \frac{18{,}868}{T} \tag{5.2}$$

which is determined from a fit to experimental data in the range 1750 to 5000 K [144,145] with the pressure in Pa. The melting point is essentially independent of pressure, and the $T_{liquidus}$ is marked on the Figure 5.1. The pressures for the experiments reported here are marked in Figure 5.1 and the lowest pressure is just above the sublimation region.

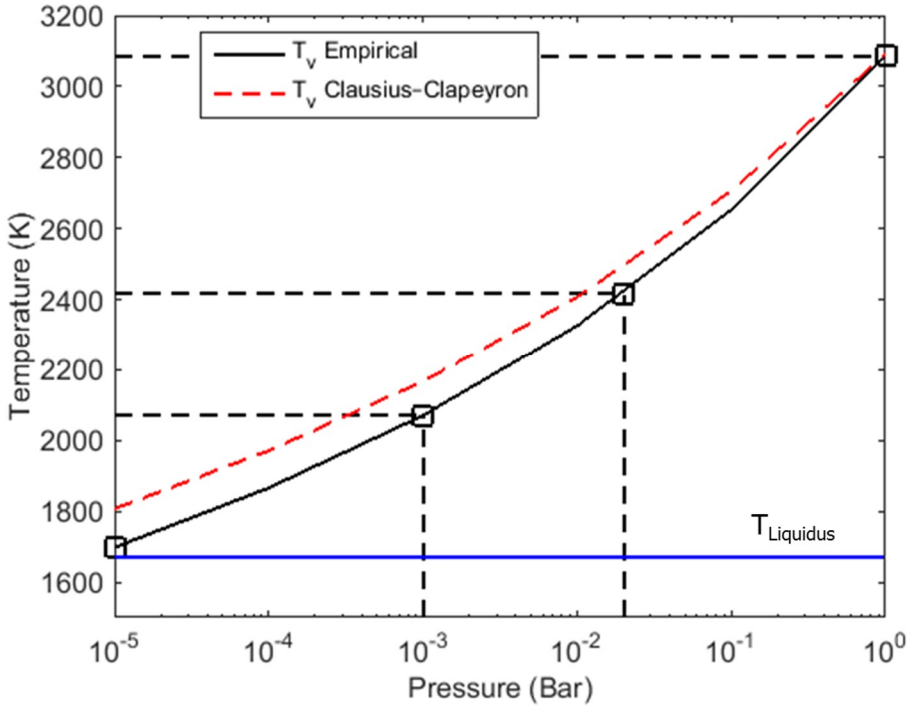

Figure 5.1: Plot of vaporisation temperature against pressure. The pressures reported here are marked and the corresponding of vaporisation temperatures are: 1698 K at 10 µbar; 2071 at 1 mbar; 2415 K at 20 mbar and 3087 K at 1 bar.

5.2 Experimental System

The design and characterisation of an open-architecture LPBF system for in-situ measurements have been previously reported in Chapter 3. For this work, the system was

encased in a custom-made vacuum chamber, Figure 5.2. A key feature of the LPBF system is computer control for the automated build of fully dense components, enabling in-process measurements under realistic build conditions. However, for this study, the laser interaction with a single powder layer was investigated in order to understand the process conditions that might enable multiple layers to be built in the future.

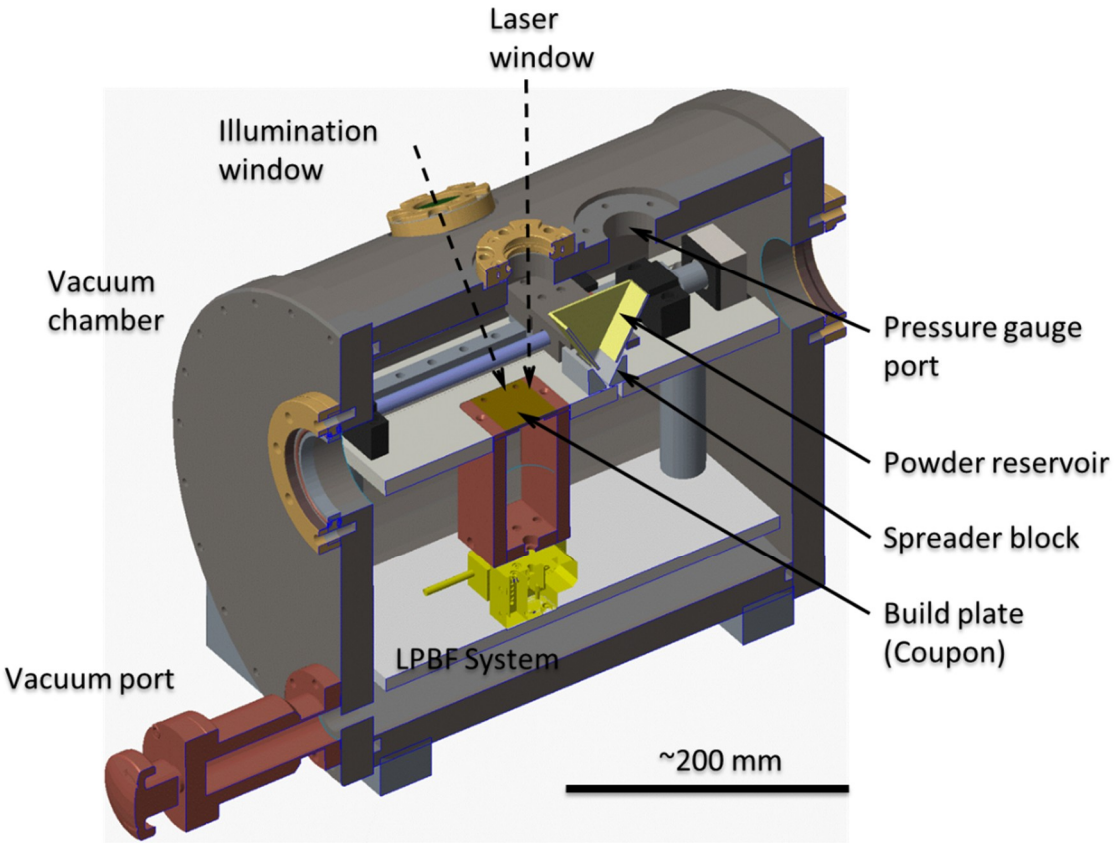

Figure 5.2: Schematic of the open-architecture LPBF system with vacuum chamber.

The vacuum chamber incorporated access windows to illuminate and image the powder bed. The window for the LPBF laser was an anti-reflection coated, high-vacuum viewport assembly (Thorlabs VPCH42-C) providing ~30 mm clear aperture. Similar viewport assemblies, but without anti-refection coatings on the windows, were used for white light illumination and imaging of the powder bed. These two windows were positioned asymmetrically with respect to the vertical so as to avoid direct scatter of the illumination into the camera, Figure 5.3. The imaging window provided a top view of the powder bed with the camera angled at ~20° to the vertical. The two end windows were not used in this study.

Experiments were performed on layers of gas-atomised stainless steel 316L powder (Renishaw PLC) with particle diameters in the range 15 to 45 µm and a mean diameter of 30 µm [133]. These layers were spread on stainless steel 304L build plates (coupons) which

had been roughened by manual, circular rubbing with P400 sandpaper. The powder layer thickness for all experiments was 60 µm, determined by the height of the powder spreader above the coupon surface (Chapter 3). Individual tracks were melted with a single mode fibre laser (SPI 400 W continuous wave, 1070 nm) focussed to a spot with a Gaussian beam profile and 4Dσ diameter of 50 µm in both the x- and y-directions.

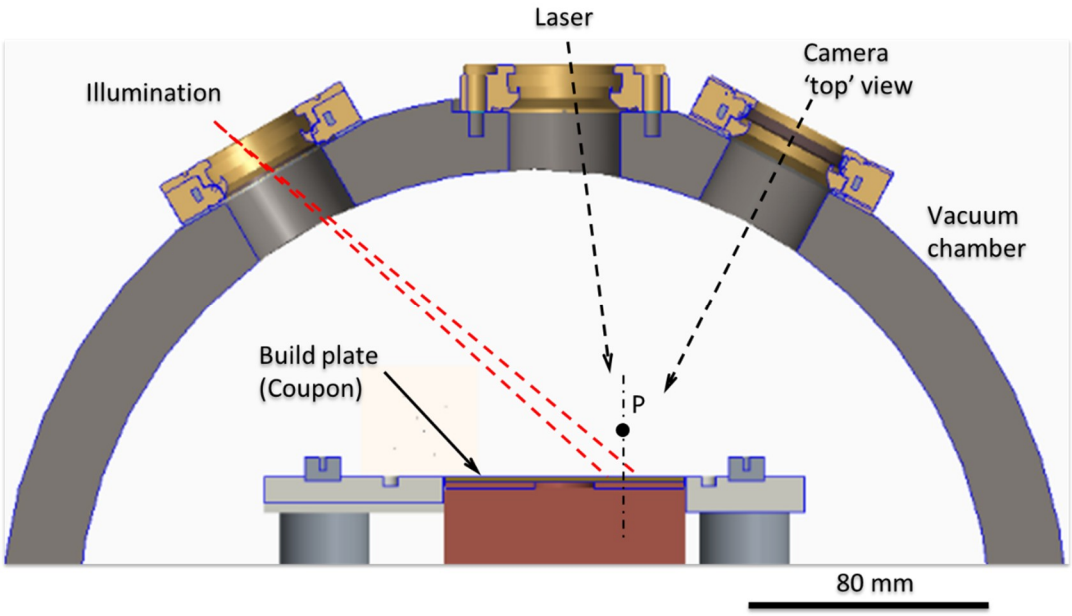

Figure 5.3: Cross-section of the chamber showing the build area and imaging arrangement.

The vacuum port included a T-piece and isolation valves (not shown in the figure) to connect the chamber to both the vacuum pump and the Ar shielding gas supply. Initially the chamber was purged with Ar by continuously filling for 10 minutes, with the pressure gauge port intentionally opened. Air was displaced through the pressure gauge port due to the denser Ar entering at the bottom of the chamber, a process known to reduce O_2 concentration to <0.1% (Chapter 3). The pressure gauge (Edwards APG100-XM, NW16) was then tightened in position and the system pumped down to just below the pressure required, using an oil-free, scroll pump (Edwards XDS35i). Finally, the chamber was slowly back-filled with Ar until the test pressure was reached. The lowest pressure tested was 10 µbar, limited by the pump performance. The pressure increase due to leakage was negligible during the time required to scan the laser tracks at a given pressure.

Image sequences were recorded with a Phantom V2512 monochrome high-speed camera. The full resolution for this camera is 1,280 × 800 pixels up to 25,700 fps. The results reported here were recorded at 40,000 fps and 768x368 pixels. The camera was fitted with a C-mount adaptor and a QiOptiq Optem Fusion lens, configured to provide a zoom of 7:1 and a working distance of 155 mm. At this working distance, the region of

interest could be varied between approximately 6 × 8 mm^2 (depth of field 2.6 mm) and 0.9 × 1.2 mm^2 (depth of field 0.2 mm). Vignetting due to the mismatch between the 35 mm format of the camera sensor and the C-mount lens was not an issue because of the reduced image size at high frame rates. The camera was fitted with a band-stop filter to block light from the LPBF laser (Thorlabs NF1064-44). The powder bed was illuminated with a white light source guided via a liquid light guide and collimator (Lumencor SOLA SM light engine) to illuminate a circle of ~10 mm diameter on the powder bed. The illumination was switched on for a few seconds during imaging and produced negligible heating of the powder bed.

5.3 Results

At each pressure, results were recorded for three different laser power and scan speed combinations that provided the same line energy (laser power divided by scan speed) of 250 J/m: 50 W and 0.2 m/s, 100 W and 0.4 m/s, and 200 W and 0.8 m/s. The 100 W laser power condition has been shown to build parts with >99% density in our system. All pressures reported are absolute, i.e. 1 bar corresponds to atmospheric pressure. High-speed images sequences were recorded for the 'top' view of the powder bed for single track laser scans.

Figure 5.4 and Videos Figure 5.4(a-c) show baseline measurements recorded at 1 bar. The results are consistent with our previous observations at atmospheric pressure: both the direction of spatter ejection and the denudation mechanism change with different process parameters (Chapter 4). At the 50 W condition, Figure 5.4(a), the laser plume is established forwards with respect to the laser scan direction. The induced flow of the ambient gas entrains powder particles in towards the melt pool from all directions on the powder bed, which are consolidated into the track or ejected forwards. At 100 W, Figure 5.4(b), the plume and spatter are directed predominantly vertically upwards, resulting in less momentum in the shielding gas flow at the powder level and consequently in less denudation. At 200 W, Figure 5.4(c), the plume and spatter are directed backwards with respect to the scan direction, at a sufficiently low angle to impinge on the powder bed and to blow particles away from the track. Clearly the parameters at 200 W are not suitable due to the onset of balling. However, the higher frame rate used here (40,000 fps) compared to that used in the previous study (8,000 fps) in Chapter 4 enabled the balling process to be observed directly, for the first time for LPBF to the best of our knowledge. Molten metal from the melt track is drawn backwards into the 'ball' due to the increase in surface tension

as it cools. Once the ball has solidified sufficiently, the next instability begins to draw in molten material backwards from the melt pool, and the process repeats in a reasonably regular pattern.

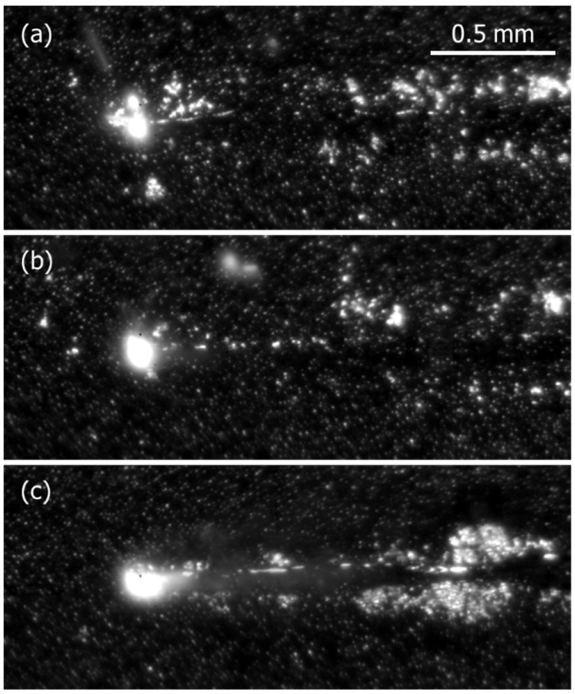

Figure 5.4: High-speed images for top view when scanning single tracks (right to left scan direction) at 1 bar. Laser power and scan speeds of (a) 50 W and 0.2 m/s, (b) 100 W and 0.4 m/s and (c) 200 W and 0.8 m/s. The videos for all figures are included in the supplementary material.

Figure 5.5 and Videos Figure 5.5(a-c) show the results recorded at 20 mbar. Despite the low pressure, a far larger number of powder particles are entrained in the flow induced by the laser plume, and they are drawn in from considerably further away on the bed. It is inferred that the vertical speed of the laser plume is larger than at 1 bar, but at the same time the inward flow begins to be offset by the lateral expansion of the laser plume that is associated with the transition to molecular flow. The flow transition with reduced pressure can be characterised by a Knudsen number Kn ≈ 1, from a hydrodynamic flow where Kn<<1 to a molecular flow where Kn>>1 [146]. The Knudsen number was of the order 0.018 and 0.9 at 1 bar and 20 mbar, respectively, assuming a temperature of 2,000 K and particle diameter of 40 μm [58] and the dynamic viscosity and the atomic mass of Ar to be 89 kg/(ms) and 6.67×10^{-26} kg respectively.

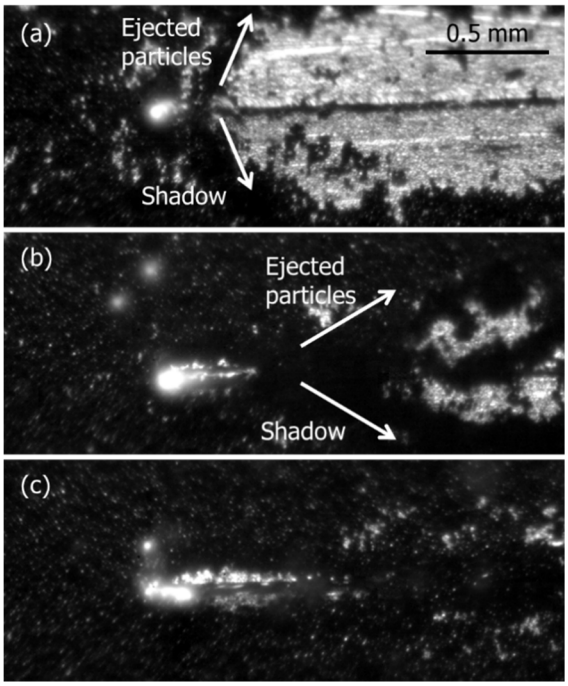

Figure 5.5: High-speed images at 20 mbar. Laser power and scan speeds of (a) 50 W and 0.2 m/s, (b) 100 W and 0.4 m/s and (c) 200 W and 0.8 m/s.

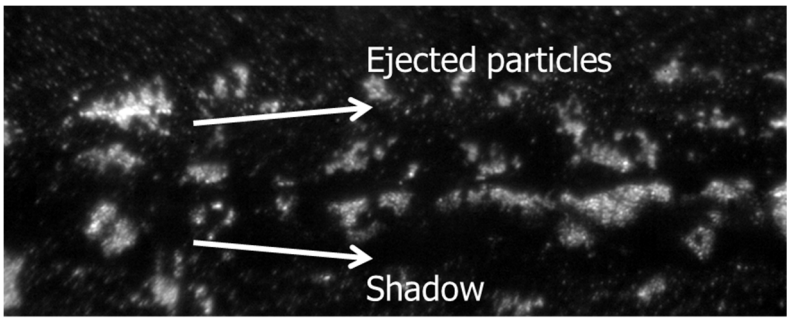

Figure 5.6: High-speed image at 20 mbar for 200 W and 0.8 m/s. The symmetry of the entrained particles and their shadow are particularly clear when the laser spot has exited the field of view.

The dense jet of entrained particles casts a shadow on to the powder bed, due to the angle of illumination and observation. Point P in Figure 5.3 represents an entrained particle vertically above the laser scan line: in the camera image it appears above the scan line, whilst its shadow appears below the scan line. The jet of entrained particles and its shadow are marked in Figure 5.5(a) and Figure 5.5(b). The effect is most obvious for the highest scan speed once the laser beam has passed out of the field of view: the correlation between features in the jet of particles and its shadow are apparent, which can be observed in Video Figure 5.5(c) and are labelled in a single frame in Figure 5.6.

At 1 mbar, Figure 5.7 and Videos Figure 5.7(a-c), powder particles are still drawn in from a considerable distance away on the powder bed. At the lowest scan speed, Figure 5.7(a), the bare metal surface of the coupon is just visible in a distinct gap between the front

of the melt pool and the powder in front of the track: the outward flow of the laser plume carries sufficient momentum to overcome the inward flow of entrained particles and to clear the laser track. The Knudsen number is approximately 18 and the flow is still in the transition region between the hydrodynamic and molecular regimes. At 0.4 m/s, the scan speed of the laser matches more closely the speed at which particles are repelled by the vapour, whilst at 0.8 m/s the particles do not have sufficient speed to escape and are still incorporated into the melt pool.

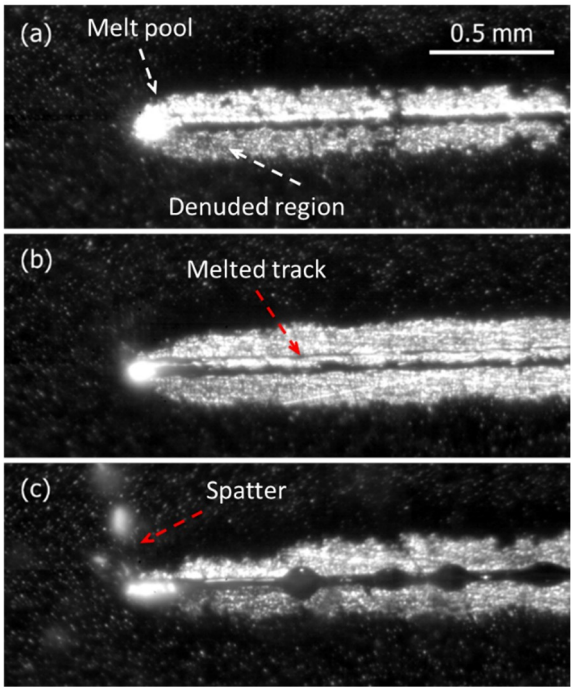

Figure 5.7: High-speed images at 1 mbar. Laser power and scan speeds of (a) 50 W and 0.2 m/s, (b) 100 W and 0.4 m/s and (c) 200 W and 0.8 m/s.

The laser scan speed is acting cumulatively with the inwards drag forces exerted on particles by the induced ambient flow, whilst competing with the vapour expansion velocity which repels particles from the melt pool.

Finally, at 10 µbar, Figure 5.8 and Videos Figure 5.8(a-c), no inward flow of entrained particles from the powder bed is observed and the flow has become fully molecular, Kn ≈ 1,800. The outward flow of particles directly affected by the laser plume at 0.2 and 0.4 m/s is slightly increased with respect to 1 mbar, indicating that the velocity of the plume in the plane of the powder bed has increased between the two pressures. However, the 0.8 m/s scan speed is still sufficiently fast to prevent particles escaping the melt pool.

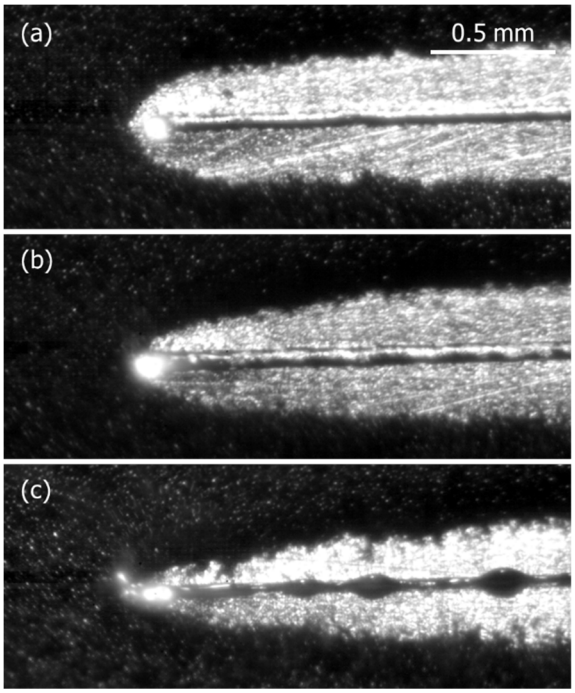

Figure 5.8: High-speed images at 10 µbar. Laser power and scan speeds of (a) 50 W and 0.2 m/s, (b) 100 W and 0.4 m/s and (c) 200 W and 0.8 m/s.

Typical track profiles are shown in Figure 5.9. These are presented according to laser processing condition in order to observe the effect of pressure in each case. At 50 W and 0.2 m/s, Figure 5.9(a), the cross-sectional area of the bead is significantly reduced at 20 mbar and below. It is clear from Figure 5.6(a) and Figure 5.7(a), and the associated videos, that the profiles at 1 mbar and 10 µbar are melted substrate and do not contain any powder. The profile at 20 mbar similarly contains almost no powder, despite the large entrainment of powder towards the melt-pool. Of the pressures tested, 20 mbar was apparently on the cusp of these entrained particles being expelled by the expansion of the laser plume, for the 50 W condition. The profiles for 100 W and 0.4 m/s, Figure 5.9(b), are also significantly reduced at pressures below 1 bar, although slightly larger than for 50 W and 0.2 m/s: the front of the melt pool and the powder always interact, even at 50 µbar. Finally, Figure 5.9(c) shows the profiles for the 200 W and 0.8 m/s. Powder is incorporated into the melt pool at all pressures due to the high scan speed, although balling occurs in each case.

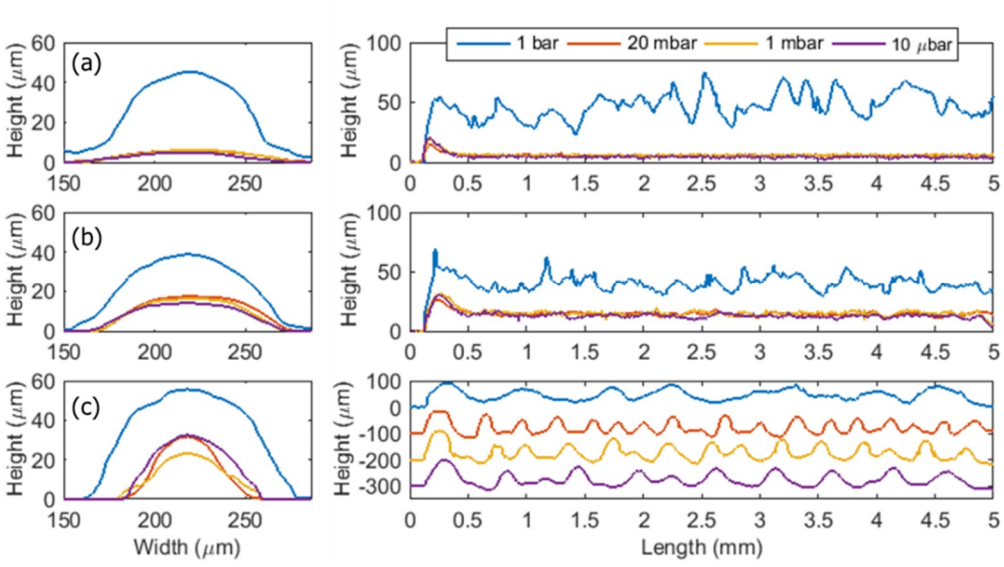

Figure 5.9: Transverse (left-hand column) and longitudinal (right-hand column) profiles of the laser tracks. Laser power and scan speeds of (a) 50 W and 0.2 m/s, (b) 100 W and 0.4 m/s and (c) 200 W and 0.8 m/s.

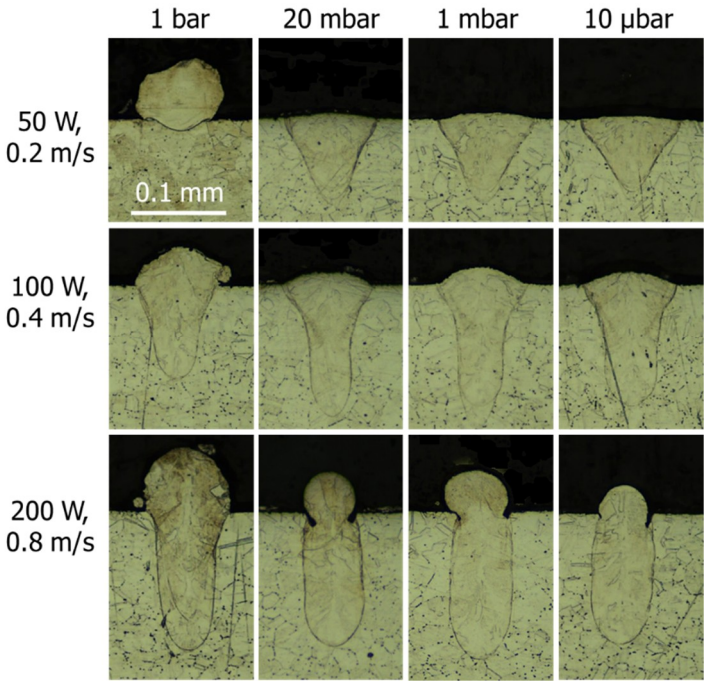

Figure 5.10: Cross-sections of laser tracks.

Typical track cross-sections are shown in Figure 5.10. In general, the penetration increased with a decrease in ambient pressure but became independent of pressure at some threshold pressure above 20 mbar.

5.4 Discussion

The results show that the reduced bead profile at sub-atmospheric pressure is primarily due to increased denudation, rather than increased metal vaporisation as reported previously [57,114]. The apparent contradiction between these two references regarding suggested

processing parameters at sub-atmospheric pressures is resolved: it is most likely that the 100% density reported at 100 µbar and very low scan speeds ≤0.02 m/s [114] was in fact measured from the coupon substrate which had been completely cleared of powder, under conditions similar to Figure 5.8(a). We have scanned islands at these pressures, Figure 5.11(a) and Video Figure 5.11(a), and it is clear that the substrate is cleared of powder throughout the scan and that no powder is incorporated.

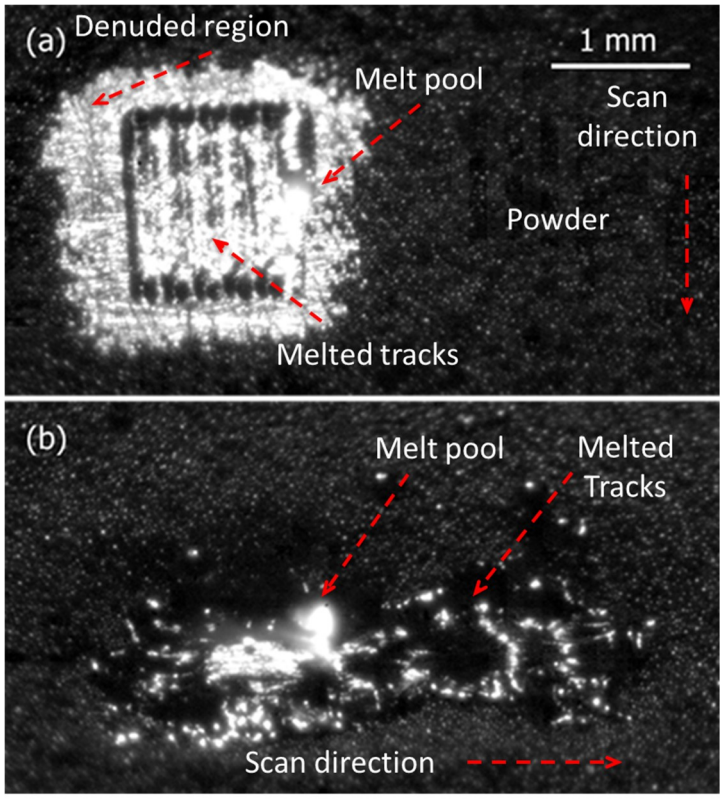

Figure 5.11: Top view of island scans for (a) 50 µm powder layer spread on baseplate at 10 µbar for 50 W and 0.1 m/s and (b) 130 µm powder layer spread on a LPBF surface at 10 µbar for 100 W and 0.4 m/s.

It also explains why the measured density decreased steadily to 70% as the laser scan speed was increased to 0.6 m/s [114]: powder was eventually incorporated into the track by conditions similar to Figure 5.8(b) and Figure 5.8(c). The observation by the same group that no powder was consolidated below 100 mbar at 0.1 m/s scan speed [57] is consistent with the results reported here, for example the track profiles shown in Figure 5.9(a). However, simply increasing the scan speed (or a reducing the power) of the laser [57] does not inform the choice of process parameters: the results presented here show that unwanted balling can indeed occur at high scan speeds, even for sub-atmospheric pressures.

The extremely low surface roughness and lack of spatter observed at 50 nbar and 0.01 m/s [115] is again most likely due to measurements made from the coupon substrate, which had been completely cleared of powder. Indeed, a previous publication by the same

group includes images of these low roughness surfaces which are completely devoid of any residual powder [147]. It also explains why they observed both the surface roughness and spatter to increase at 0.1 m/s: powder was eventually incorporated into the track by conditions similar to Figure 5.8(b) and Figure 5.8(c). The appearance of spatter as the laser scan speed increases and eventually incorporates powder into the track is evident when comparing Video Figure 5.8(a) and Figure 5.8(c), for example.

The Figure 5.11(a) showed how the powder is cleared from the substrate during area scans at low pressure (10 μbar). This image is for a powder layer thickness of 50 μm spread directly on to the baseplate for which the denudation is greatest. The effect of denudation is reduced as the steady state build condition is reached, due to the increase in the powder layer thickness as described in Chapter 3 and surface irregularities of previously built layers constraining the particle motion as described in Chapter 4. Figure 5.11(b) and Video Figure 5.11(b) show the laser interacting at 10 μbar with a 130 μm thick powder layer spread on to a LPBF surface (built under standard atmospheric conditions). Even under these conditions, which are representative of the steady build state, the substrate is cleared by the outward expansion of the evaporation plume

The videos presented here enabled the first direct observation of the outward expansion of the evaporation plume counter-acting and eventually dominating any inward flow of the ambient gas as the pressure decreases, for example Figure 5.4(a), Figure 5.5(a) and Figure 5.7(a) for the 50 W condition. They confirm that denudation due to asymmetrical heating of particles close to the laser spot being propelled away by the vapour flux generated, was correctly discounted in [58]. The pressures at which the flow regime transitions from hydrodynamic to molecular, and the trends in the resulting denudation, are also generally consistent with those inferred from measurements of the size of the denuded region.

The Figure 5.10 showed an increase in penetration depth with reduced pressure. This increase is attributed to the reduction in vaporisation temperature at low pressure as explained in the introduction of this Chapter (Figure 5.1), and similar to that observed in laser keyhole welding.

For laser welding at low speeds, the threshold pressure below which there is no noticeable effect on the penetration depth has been approximated at ~$P_c/10$, where $P_c = \sigma/r$ is the pressure in the keyhole due to surface tension, σ, and r is the radius of the keyhole [118] A plot of the variation in surface tension with temperature for stainless steel

316L is given in [148] from which the approximate relation for surface tension (in N/m) of $\sigma = -0.45\times10^{-3}T + 2.65$ was determined in the temperature range 2,000 to 4,000 K. Using the vaporisation temperature at 1 bar from Figure 5.1, combined with an approximate keyhole radius of 25 μm from Figure 5.10, yields a threshold pressure of 50 mbar. This estimate applies to low weld speeds [118], so in practice the threshold pressure is likely to be somewhat higher for LPBF because the higher laser scan speed will make a small pressure contribution in addition to the surface tension pressure. This estimate of the threshold pressure requires further experiments to be validated, but it is consistent with Figure 5.10 where the deepest penetration has already been reached by 20 mbar.

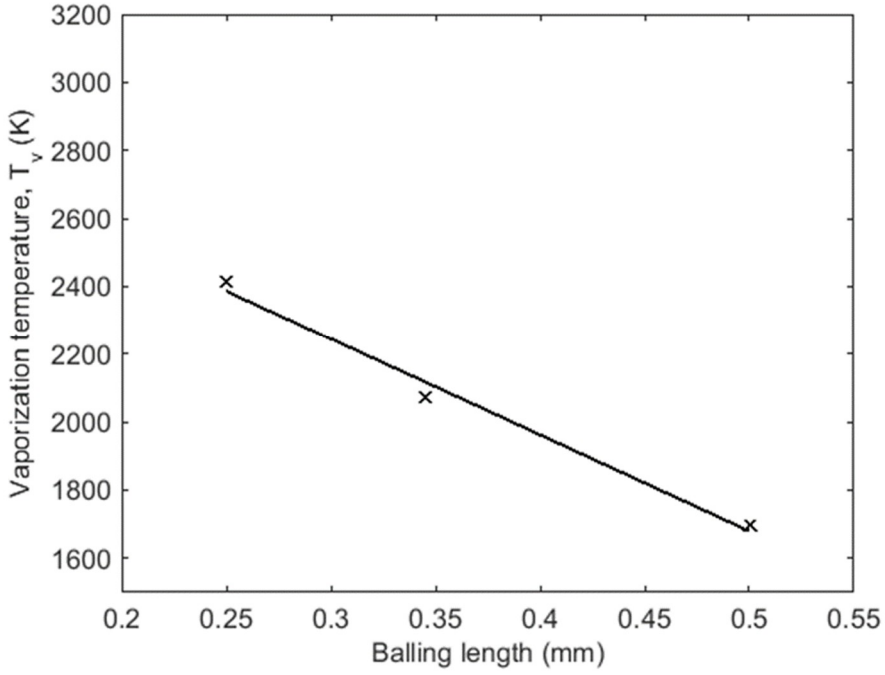

Figure 5.12: Vaporisation temperature (which is linearly related to surface tension in this temperature range) plotted against distance between balls from Fig. 7(c).

The reduced vaporisation temperature and its effect on the surface tension also appears to affect the balling frequency seen at the highest scan speed. A fast-Fourier transform of the longitudinal scan profiles in Figure 5.9(c) yielded the balling spatial frequency, from which the typical length between balls was calculated. The vaporisation temperature was plotted against this balling length, Figure 5.12, shows a linear relationship. The balling length is considerably shorter than predicted for a Plateau-Rayleigh instability [36]: the melted substrate shown in the cross-sections in Figure 5.10 indicate that the mechanism was not a molten 'cylinder' breaking into droplets. A Kelvin-Helmholtz hydrodynamic instability can arise when the velocity of the liquid metal at the surface of the melt-pool is lower than the velocity of the atmosphere [149] but this effect is less well understood and it is not straightforward to predict the balling length from the process parameters.

5.5 Summary

The reduced bead profiles seen at sub-atmospheric pressure are primarily due to increased denudation, rather than increased metal vaporisation. As the pressure decreases in the transition region between hydrodynamic and molecular flows, entrainment of particles towards the melt pool increases but is in competition the repelling of particles away from the melt pool by the expansion of the laser plume. Eventually, in the molecular flow regime, particles are only repelled by the plume away from the melt pool. The resulting disruption to the powder bed means that most pressures would require a pre-sinter for the process to be viable, with a concomitant increase in processing time and complexity. The regime between 1 bar and ~50 mbar (the threshold pressure at which the penetration depth no longer increases) could provide an interesting window for processing without a pre-sinter, but further investigation is required. In E-Beam process, pre-sinter holds the powder from being thrown away by means of vapour expansion.

Chapter 6. Laser Powder Bed Fusion in High-pressure Atmosphere

6.1 Introduction

A combination of high-speed imaging and schlieren imaging as well as cross sectioned micrographs were used to investigate the interaction of the laser beam with the powder bed at atmospheric pressures up to 5 bar, in argon and helium atmospheres. As an outcome of this work, a journal article entitled "**Laser powder bed fusion in high-pressure atmosphere**" has been submitted to The International Journal of Advanced Manufacturing Technology as an open access and is currently under review. Supplementary data (Videos) associated with this Chapter can be found at the online version of the article.

As reported in the Chapter 2, an increase in ambient pressure might reduce denudation, due to a decrease in the laser plume velocity and the resulting induced flow in the shielding gas leading to less entrainment of powder particles. A reduction in the recoil pressure from the laser plume might lead to a more stable melt pool and a smoother build. It might also reduce condensation coating on the machine windows from evaporation of metal from the melt pool. It increases the vaporisation temperature that might allow use of higher energy densities and increased scan speed without boiling the material.

The Clausius-Clapeyron equation describes the coexistence curve on the phase diagram for vaporisation of a material, for which the liquid and vapour phases exist in thermodynamic equilibrium [57,150]. For stainless steel 316L, an empirical fit to experimental data in the range 1750 to 5000 K plot is given by [144,145].

$$\log(P) = 11.1183 - \frac{18{,}868}{T} \tag{6.1}$$

with the pressure in Pa. This change in vaporisation temperature with ambient pressure is plotted in Figure 6.1and the vaporisation temperatures at the pressures tested are marked.

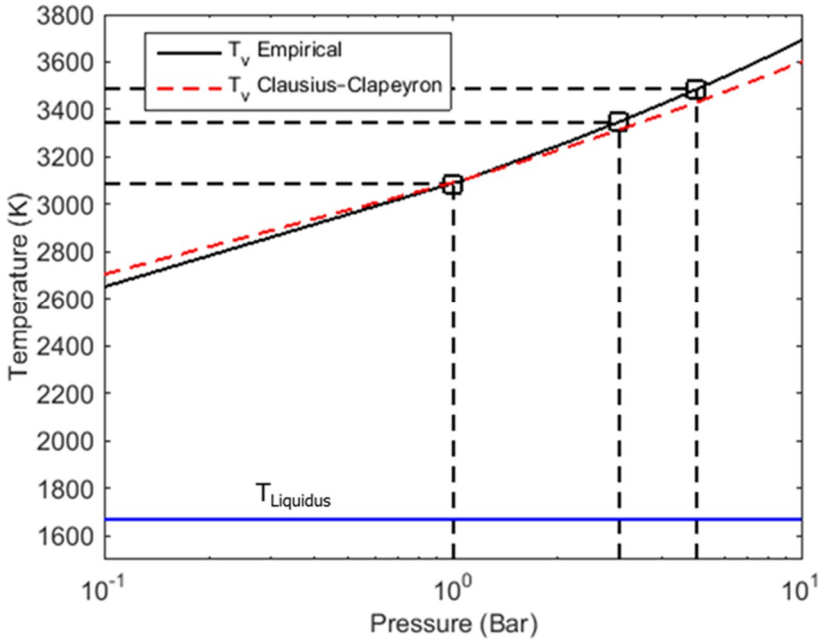

Figure 6.1: Plot of vaporisation temperature against pressure. The empirical line is a plot of Eq. (6.1) and the Clausius-Clapeyron line is taken from Chapter 5. The experimental pressures reported here are marked for which the corresponding vaporisation temperatures are: 3087 K (1 bar); 3348 (3 bar) and 3485 K (5 bar).

6.2 Experimental System

The design and characterisation of an open-architecture LPBF system for in-situ measurements have been reported in the Chapter 3. The LPBF system is computer controlled for the automated build of fully dense components, enabling in-process measurements under realistic build conditions. However, for this study, the laser interaction with a single powder layer was investigated in order to understand the process conditions at high pressures that might enable multiple layers to be built in the future. The open-architecture LPBF system was encased in a custom-made pressure chamber shown in Figure 6.2. The pressure chamber was essentially the same as a vacuum chamber used to perform LPBF at sub-atmospheric pressures down to 10 µbar in Chapter 5 and so it is not described in detail again here. The key difference was that the high-vacuum viewport assemblies, which were used to provide optical access to the power bed, were reinforced externally with stainless steel adapter plates and additional O-rings to prevent them from blowing out under high pressure. The top of the pressure chamber contained a viewport for the LPBF laser, and two symmetrical viewports for white light illumination and imaging of the powder bed, each with a ~30 mm clear aperture. For this study, two additional viewports (Thorlabs VPCH42-C without anti-refection coatings) in the ends of the chamber enabled a collimated white light beam to pass across the powder bed for schlieren imaging.

The pressure chamber was connected directly to the shielding gas cylinder through a non-return inlet valve. For argon, the chamber was purged by continuously filling for 10 minutes, with the pressure gauge port in the top of the chamber intentionally opened, to reduce the O_2 concentration to <0.1%. The pressure gauge was then tightened in position and the chamber pressure increased to the required value. For helium the process was reversed: the pressure chamber was filled from the top in the initial purging process so that the heavier air was displaced via the bottom of the chamber. The pressure chamber including viewport windows were hydrostatic pressure tested to 10 bar, although the highest pressure tested in these experiments was 5 bar. The pressure decrease due to leakage was negligible during the time required to scan the laser tracks and islands at a given pressure.

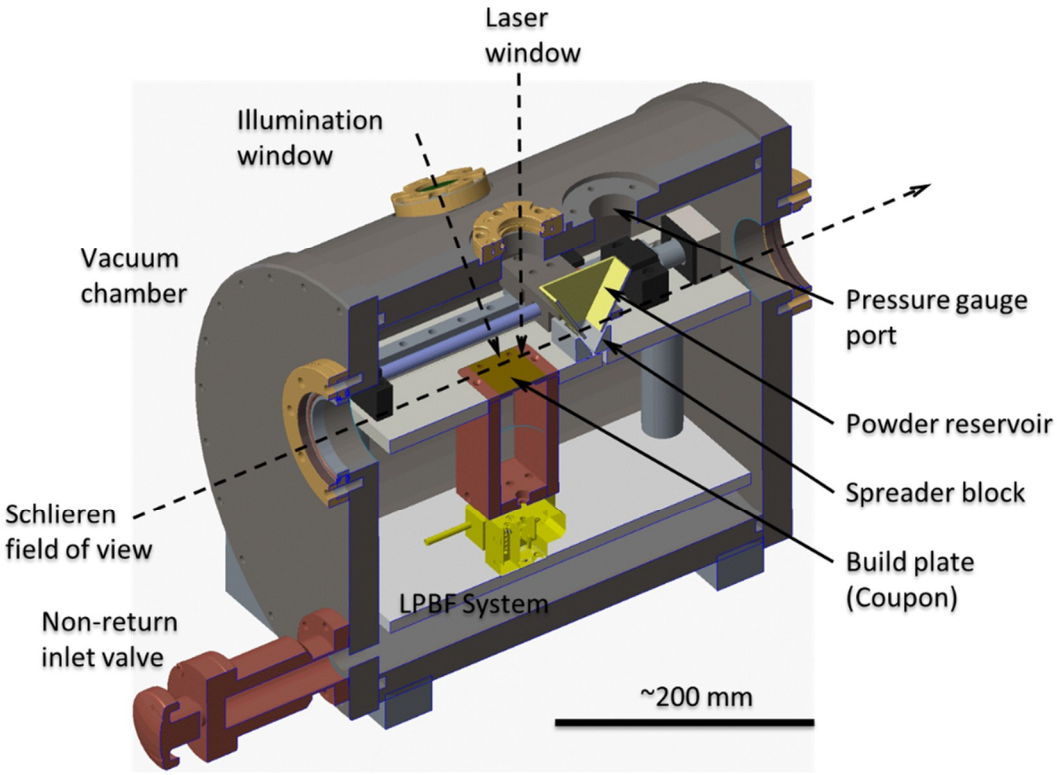

Figure 6.2: Schematic of the open-architecture LPBF system with pressure chamber.

Experiments were performed on gas-atomised stainless steel 316L powder (Renishaw PLC) with particle diameters in the range 15 to 45 µm and a mean diameter of 30 µm [133]. Powder layers of thickness 50 µm were spread on stainless steel 304L build plates (coupons) which had been roughened by manual, circular rubbing with P400 sandpaper. The powder was melted with a single mode fibre laser (1070 nm) focussed to a spot of diameter 50 µm (Chapter 3). High-speed image sequences were recorded with a Phantom V2512 monochrome camera at 40,000 frames per second (fps) and 768x368 pixels resolution, with illumination of the powder bed by a Lumencor SOLA SM white light

source. The camera was fitted with a band-stop filter to block light from the LPBF laser. The images recorded correspond to a top view of the powder bed with the camera angled at ~20° to the vertical. The portable z-type schlieren system used a 300 W tungsten lamp for illumination and images were recorded with the high-speed camera using a variable focus telephoto lens (focal length 200 – 500 mm) at 80,000 fps and 384 x 512 pixels resolution. The playback speed for the schlieren results have been adjusted to produce the same apparent time dilation as for the direct imaging videos. For the schlieren experiments, the camera was fitted with a polariser to remove glare in addition to the band-stop filter; the powder layer was spread on the coupon and the spreader block assembly was then carefully removed so that it did not obstruct the collimated schlieren illumination passing across the powder bed similar to described in the Chapter 4.

6.3 Results

Similar to Chapter 5, results were recorded for three different laser power and scan speed combinations that provided the same line energy (laser power divided by scan speed) of 250 J/m: 50 W and 0.2 m/s, 100 W and 0.4 m/s, and 200 W and 0.8 m/s. The 100 W laser power condition have been shown to build parts >99% density at atmospheric pressure (1 bar) previously. Single tracks and rectangular islands of 1 x 2 mm^2 were scanned at pressures of 1, 3 and 5 bar (absolute pressure). For the island scans, the scan spacing was 50 µm between adjacent tracks and the laser was switched off for ~500 µs at the end of each line.

6.3.1 Argon Atmosphere

Figure 6.3 and Videos Figure 6.3(a-e) show direct imaging for top views of the powder bed for single track scans, recorded with increasing pressure in argon. Concentrating on the 100 W and 0.4 m/s condition as typical of a good build condition, the results at 1 bar in Figure 6.3(a) were consistent with our previous observations (Chapter 4 and 5). The laser plume points vertically upwards and induces a flow in the shielding gas that entrains particles from all directions on the powder bed. Entrained powder particles are either consolidated into the track or ejected upwards. Some of these particles are incandescent due to their interaction with the laser beam or the laser plume. The laser plume also ejects incandescent spatter due to instabilities in the melt pool.

At 3 and 5 bar, Figure 6.3(b) and (c), the powder particle entrainment and the resulting denudation do indeed decrease as the pressure increases. However, the amount of

plasma generated in the laser plume above the melt pool increases significantly as the pressure increases. The amount of molten spatter and the size of the spatter particles also both increase; plasma can even be seen around some of these spatter particles, particularly at 5 bar, which suggests that the spatter is at a high enough temperature to produce metal vapour (an effect observed even at ambient pressure, similar to the Leidenfrost effect) which is then ionised via the transfer of thermal energy from the plume. This increased ionisation indicates that the temperature of the laser plume increases at high pressure. These observations are discussed in detail in discussion Section 6.4.

Figure 6.3(d), (c) and (e) show the effect of changing the process setting at 5 bar. The 50 W and 200 W conditions are consistent with our previous observations (Chapter 4 and 5) where the laser plume points forwards and backwards respectively with respect to the laser scan direction. In all cases, the denudation at 5 bar was less than the corresponding process setting at 1 bar; however there was more plasma, and more and larger spatter particles were generated. Less plasma was produced at the 200 W condition that at 50 and 100 W at 5 bar: the higher scan speed and backwards direction of the laser plume meant that the incident laser beam had less time to interact with the laser plume. Many of the spatter particles produced at 200 W do not produce vapour or plasma, for the same reason.

The build height measured relative to the build plate for the single track scans are inset in Figure 6.3. These bead profiles are for the full 5 mm scan length of the track and are therefore at a different scale to the images in the figure. In general, the smoothness and continuity of the track worsened with an increase in pressure at a given laser power and scan speed, due to an increase in absorption, scattering and shadowing of the incident laser beam. Generally, the smoothness and continuity of the track improved with an increase in laser power and scan speed at high pressure. These effects are discussed in Section 6.4.

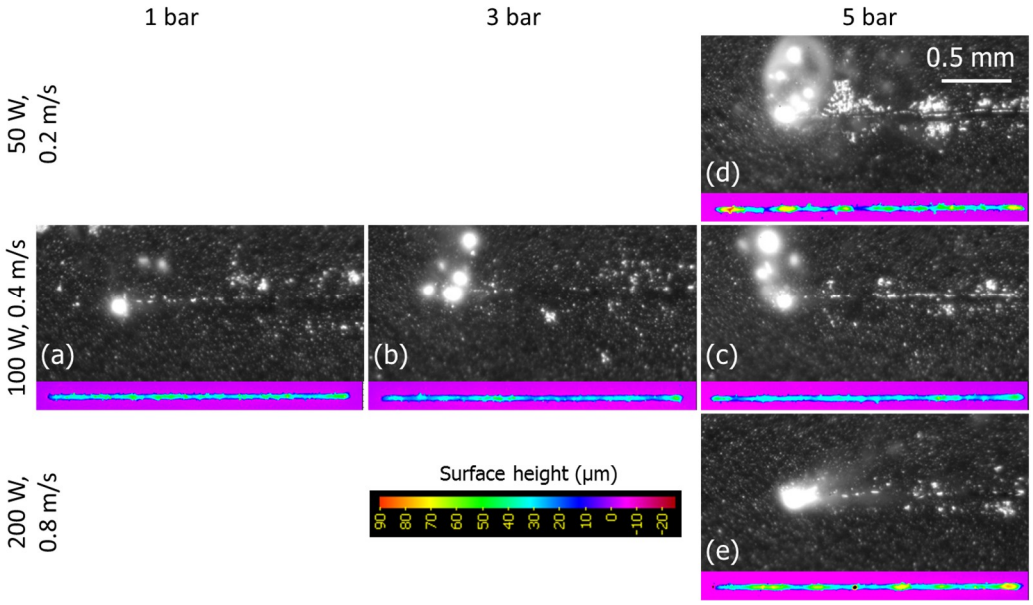

Figure 6.3: High-speed images for top views of the powder bed in argon when scanning single tracks at the pressures and process settings (laser power and scan speed) indicated. Scan direction is right to left. Denudation is reduced as the pressure increases at a laser power of 100 W and scan speed of 0.4 m/s; the formation of plasma and spatter increases as the laser power and scan speed are increased at 5 bar. Inset is the height profile for the entire length (5 mm) of each bead, i.e. not to the same scale as the image.

Figure 6.4 and Video of Figure 6.4(a-e) show direct imaging for side views of the powder bed for single track scans, at 1 and 5 bar in argon. Side images were captured at 80,000 fps and the video playback speed was not adjusted to match with top view to see better particle movements. Although the contrast between the incandescent spatter and cold particles is worse in the side images than for the top images, because the illumination direction is less favourable, the cold particles can still be discerned. The results at 1 bar, Figure 6.4(a) and (c), for both 100 and 200 W, are consistent with our previous observations. The laser plume contains metal vapour, which can be observed directly when it is ionised. The flow in the shielding gas induced by the laser plume entrains individual powder particles, which can become airborne: some particles are incandescent due to their interaction with the laser beam or the laser plume. Powder agglomerates are also entrained and some can be melted by the laser beam to produce incandescent spatter. The laser plume also ejects spatter due to instabilities in the melt pool. At 5 bar, Figure 6.4(b) and (d), the amount of plasma and number of powder agglomerates increased compared to 1 bar, indicating an increased process temperature. The amount and average size of molten spatter therefore increased at high pressure. As noted above, the amount of plasma and spatter was less for 200 W than for 100 W at 5 bar, because the interaction time of the laser beam with the laser plume was reduced. Figure 6.4(e) shows the 100 W condition at 5 bar with an additional 632 nm filter inserted in front of the camera lens, to reduce saturation in the image from incandescent spatter particles. The plasma around molten spatter can be clearly seen in the video.

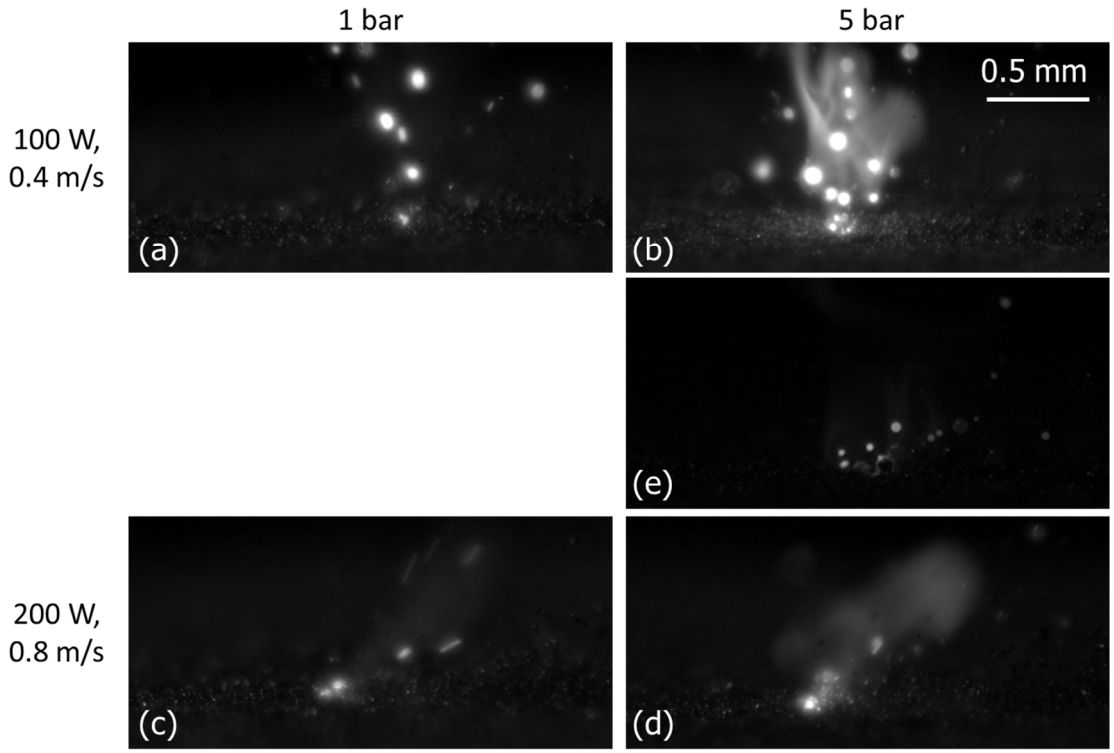

Figure 6.4: High-speed images for side views of the powder bed in argon when scanning single tracks at the pressures and process settings indicated (the images captured at 80,000 fps and playback speed of the videos is 24 fps). Scan direction is right to left. The formation of plasma and spatter increases as the laser power is increased at 5 bar; less plasma and spatter was formed at the higher scan speed due to less interaction between the laser and the laser plume. An additional 632 nm filter was included for Fig. 3(e), in order to image the incandescent spatter more clearly.

Schlieren imaging was conducted for the single-track scans. Figure 6.5 and Video Figure 6.5 show high-speed video sequences with the laser travelling towards the camera. It is not possible to resolve either individual cold powder particles, or the laser plume immediately above the melt pool, due to the lower magnification than that used for the direct imaging. However, the thermal plume of heated shielding gas and metal vapour rising above the melted track, as well as spatter and heated particles, can be seen. The images in Figure 6.5 were taken with the laser spot at the same distance from the start of the scan line (4 mm) so as to compare the evolution of the thermal plume. At higher laser scan speeds, less time is required to scan 4 mm and so the plume rises less far above the powder bed. At high pressure, the thermal plume is constrained closer to the powder bed due to the lower velocity of the laser plume from the melt pool. This effect is less pronounced at 200 W because the laser plume is angled backwards with respect to the laser scan direction.

The schlieren features arise from refractive index gradients due to temperature, pressure and concentration gradients in the shielding gas. However, the schlieren system sensitivity to pressure and concentration gradients across the thermal plume is relatively small compared to the sensitivity to the temperature gradients. The sensitivity of the

schlieren system was constant for all the measurements in Figure 6.5. Therefore, the darker schlieren features confirm an increase in the temperature of the plume as the pressure increases, as inferred from direct imaging of the plasma in Figure 6.3 and Figure 6.4.

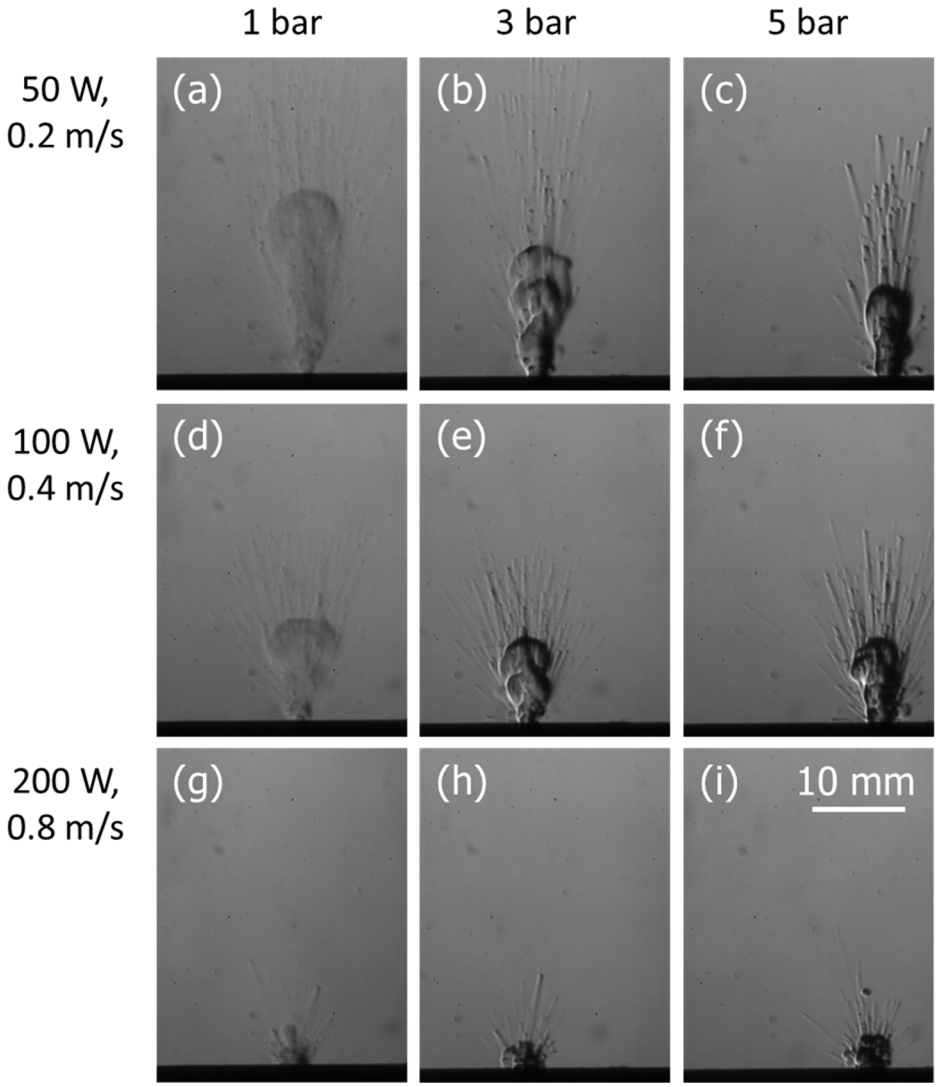

Figure 6.5: High-speed schlieren images during single track scans towards the camera at the pressures and process settings (laser power and scan speed) indicated. In each case, the schlieren sensitivity is the same and the image is taken when the laser had scanned 4 mm on the powder bed surface. At high pressure, the thermal plume rises less due to the reduced velocity of the laser plume; the schlieren image features are darker due to the increased temperature of the plume.

The left-hand column of Figure 6.6 and Video Figure 6.6 show the laser spot scanning from right to left for a single track. The results were recorded with the same schlieren sensitivity as in Figure 6.5. The images in Figure 6.6 were taken with the laser spot at the same distance from the start of the scan line (8 mm) so as to compare the evolution of the thermal plume. At 200 W, the laser beam traverses less of the thermal plume than at 100 W, due to its higher scan speed and because the laser plume is angled backwards with respect to the laser scan direction.

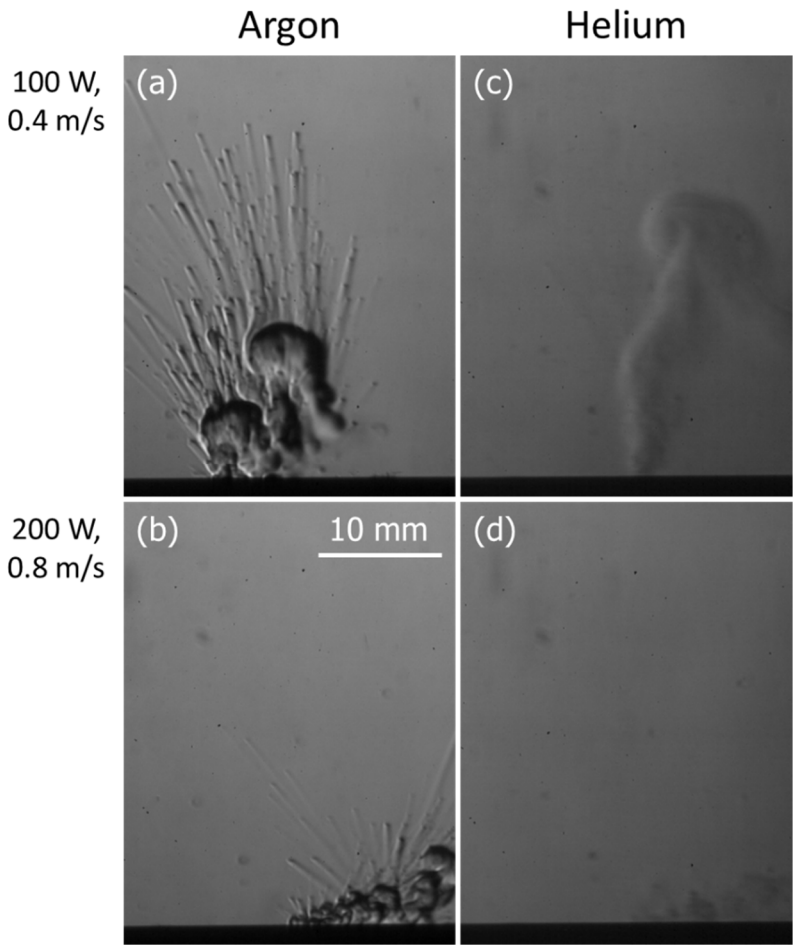

Figure 6.6: High-speed schlieren images at 5 bar during single track scans from right to left when the laser had scanned 8 mm on the powder bed surface. The schlieren sensitivity is the same as in Fig. 6. The incident laser beam traverses more of the heated gas and metal vapour produced by the melt pool at 200 W than at 100 W; the thermal plume rises faster in helium.

Figure 6.7 shows cross-sections of single track scans. In general, the penetration depth decreases as the pressure increases at each laser setting, which suggests that the physical processes which generate the keyhole are weaker at higher pressure. The penetration at 200 W at 5 bar is similar to that for 100 W at 1 bar. These points are discussed further in Section 6.4.

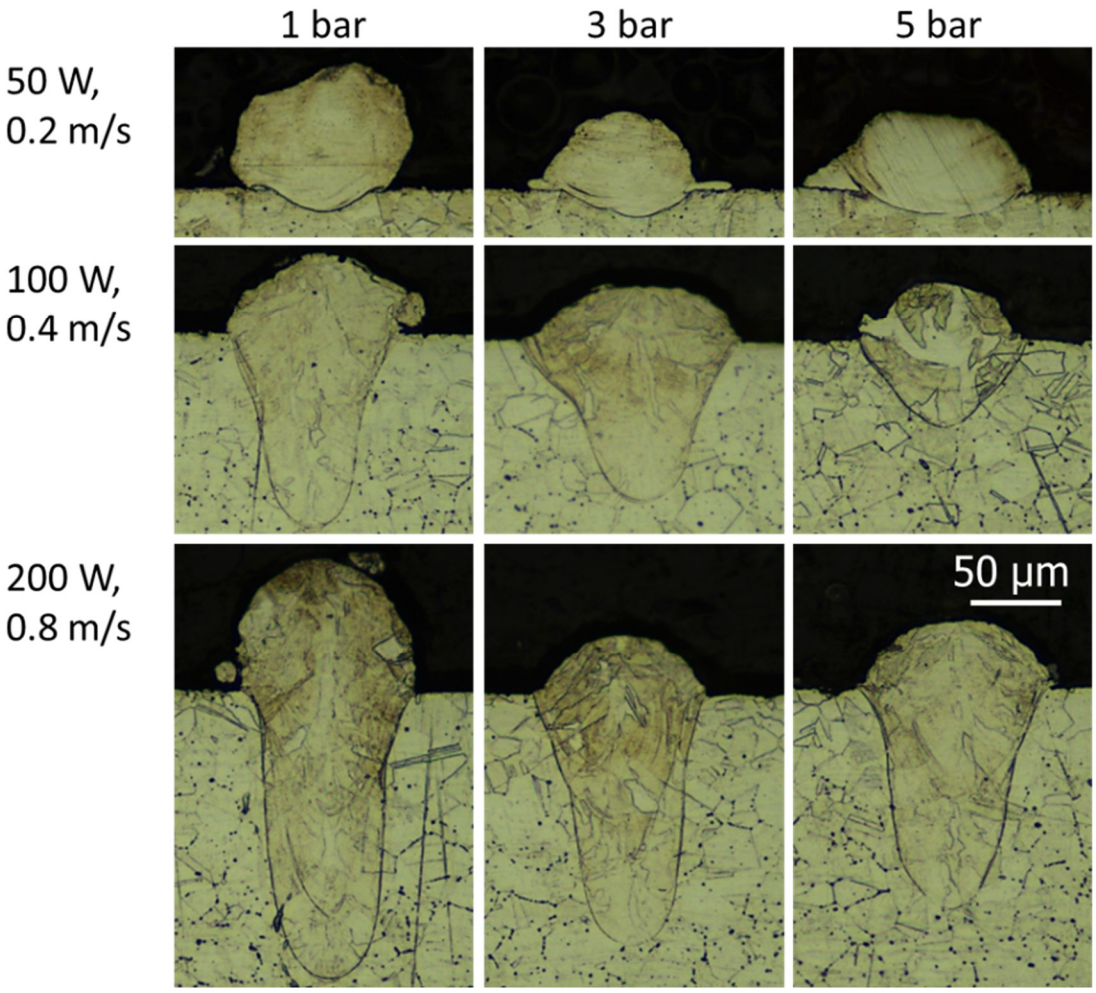

Figure 6.7: Cross-sections for single track scans at the pressures and process settings (laser power and scan speed) indicated. The penetration depth decreases with an increase in pressure.

Figure 6.8 and Video Figure 6.8(a-e) show direct imaging of island scans recorded with increasing pressure in argon. The first scanned line of the island is equivalent to the single track scans of Figure 6.3, and the direction of the laser plume and the particle entrainment are consistent at each laser setting and pressure. For subsequent tracks in the island, the laser plume is directed away from the previously melted track. The extent of denudation in the first layer can be significant, as the effects of adjacent tracks accumulate and the temperature of the powder bed increases. However, its effect should not be over-exaggerated: the first layer is relatively thin and is spread directly on to the coupon. It has been shown that the change in the powder layer thickness between layers is described by a geometric series and that in the steady state build after 6 to 10 layers the denudation is less severe due to the increased powder layer thickness (Chapter 3) and the surface roughness of previously built layers (Chapter 4).

Some denudation is still evident at 5 bar, which causes the laser spot to interact with different amounts of powder as the island scan progresses. The production of plasma and

spatter is greatest when more powder is present, indicating that the plasma primarily consists of ionised metal vapour rather than ionised argon, and that variations in the amount of powder incorporated into the melt pool cause melt pool instabilities which contribute to spatter.

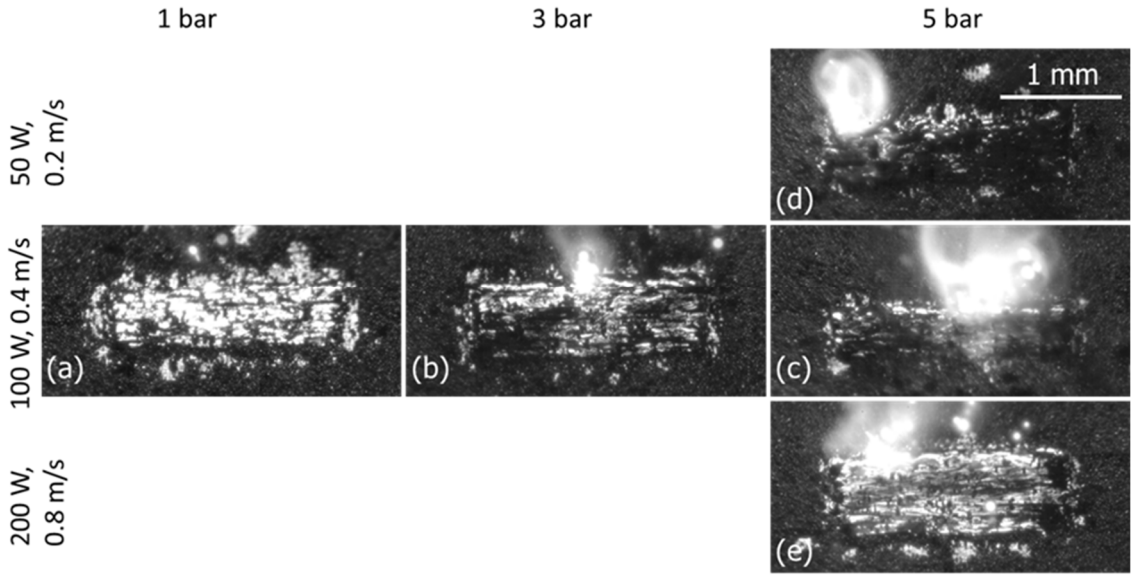

Figure 6.8: High-speed images for top views of the powder bed in argon when scanning rectangular islands at the pressures and process settings indicated. Denudation is reduced as the pressure increases at a laser power of 100 W and scan speed of 0.4 m/s; the formation of plasma and spatter increases as the laser power and scan speed are increased at 5 bar.

Figure 6.9 shows the build height relative to the build plate for the island scans shown in Figure 6.8. The first track of each scan is much higher than the subsequent ones, as powder denudation is significantly reducing mass consolidation in the first layer. At 3 bar, Figure 6.9(b), tracks beyond the first are higher on average compared to 1 bar, Figure 6.9(a), showing the effect of reduced denudation. At 5 bar, Figure 6.9(c), the effects of the interaction between the plasma and laser significantly disrupt the process. In general, the smoothness and continuity of the layer worsened with an increase in pressure, but improved with an increase in laser power and scan speed.

The islands produced at 5 bar were sectioned orthogonal to the laser scan direction, left-hand column of Figure 6.10. Adjacent laser scan lines progress from left to right in the images. As seen in Video Figure 6.8, none of the builds at 5 bar in argon produced a stable build due to the increase in spatter from the melt pool and plasma in the laser plume.

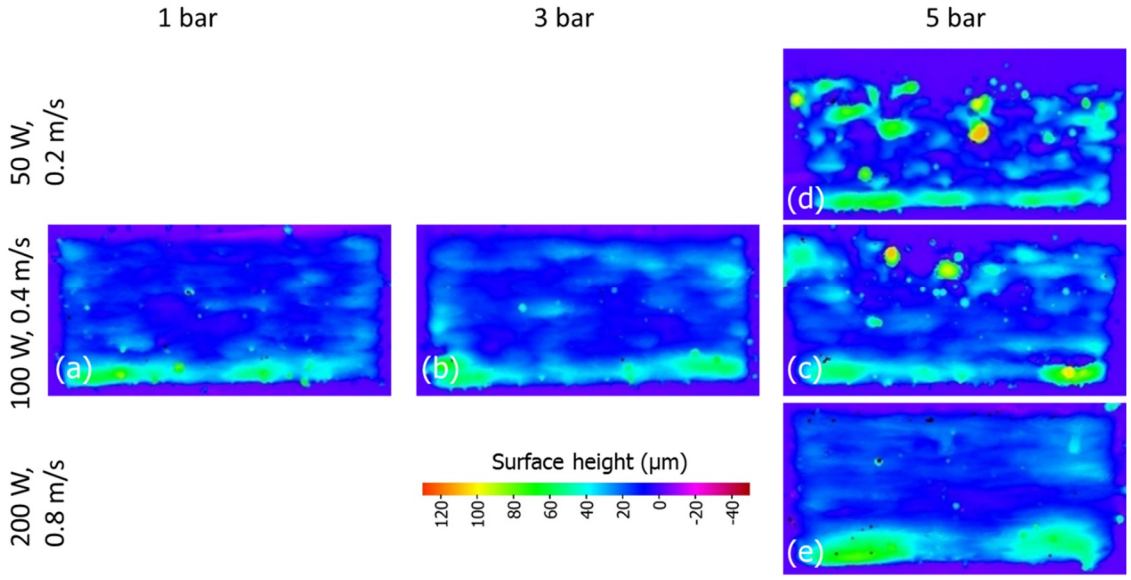

Figure 6.9: Surface height maps for the island scans of Figure 6.3

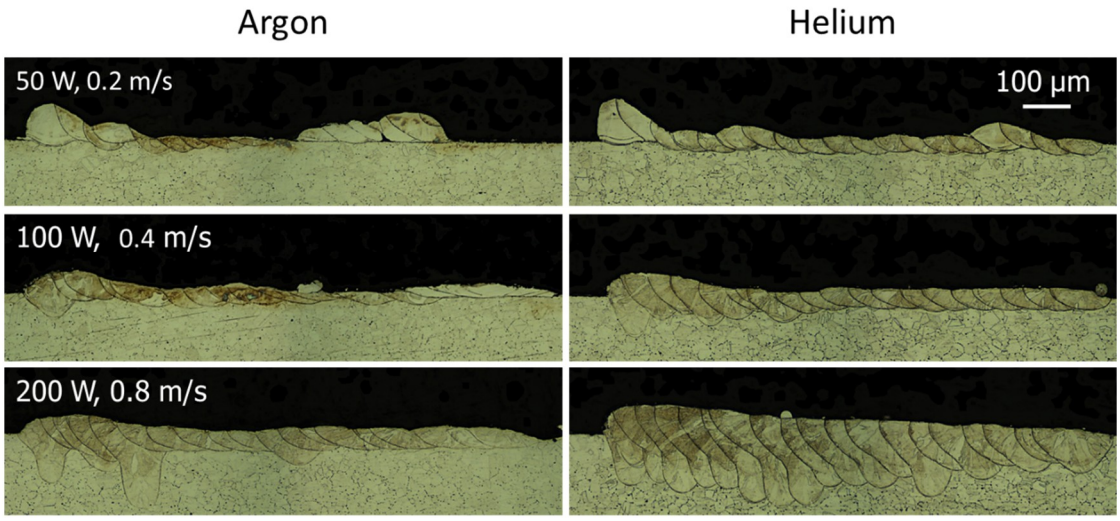

Figure 6.10: Cross-sections orthogonal to the laser scan direction for the island scans at 5 bar of Figure 6.3 and Figure 6.8. Adjacent laser scan tracks progress from left to right in the images.

The build and penetration depth are greatest at the beginning of each island. As the island progresses, the penetration depth stabilises but at a decreased value: the change in the shape of the melt pool cross-section is consistent with an increase in laser spot diameter during the island build. This effect was due to accumulation of metal vapour above the powder bed causing the laser spot to defocus and condensed particulate scattering some of the incident laser beam: all the experiments were recorded without a flow of shielding gas across the powder bed from the flow straightener in order to observe only the laser's interaction with the powder bed.

6.3.2 Helium Atmosphere

Figure 6.11 and Video Figure 6.11(a-d) show direct imaging of island scans recorded with increasing pressure in helium. For the 100 W condition, Figure 6.11(a) and (b), show that the denudation decreased as the pressure increased to 5 bar as observed previously for argon. However, in helium the amount of plasma generated in the laser plume and the size and number of spatter particles remained the same at 5 bar compared to 1 bar. These observations indicate that the laser plume in helium was at a lower temperature than at the corresponding pressure in argon. Figure 6.11(c), (b) and (d) show the effect of changing the process setting at 5 bar. Unlike argon, the amount of plasma, and the amount and size of the spatter, did not increase at higher laser powers: it remained the same in each of the three process conditions. The surface height maps measured from these island scans, Figure 6.12, were smoother and more continuous than for argon, and indicate that the process was more stable at high pressure in helium.

The islands produced at 5 bar in helium were sectioned orthogonal to the laser scan direction, right-hand column of Figure 6.10. The solidified bead cross-sections of the first track in each island are larger than those at the corresponding process setting in argon, indicating that the energy input was increased.

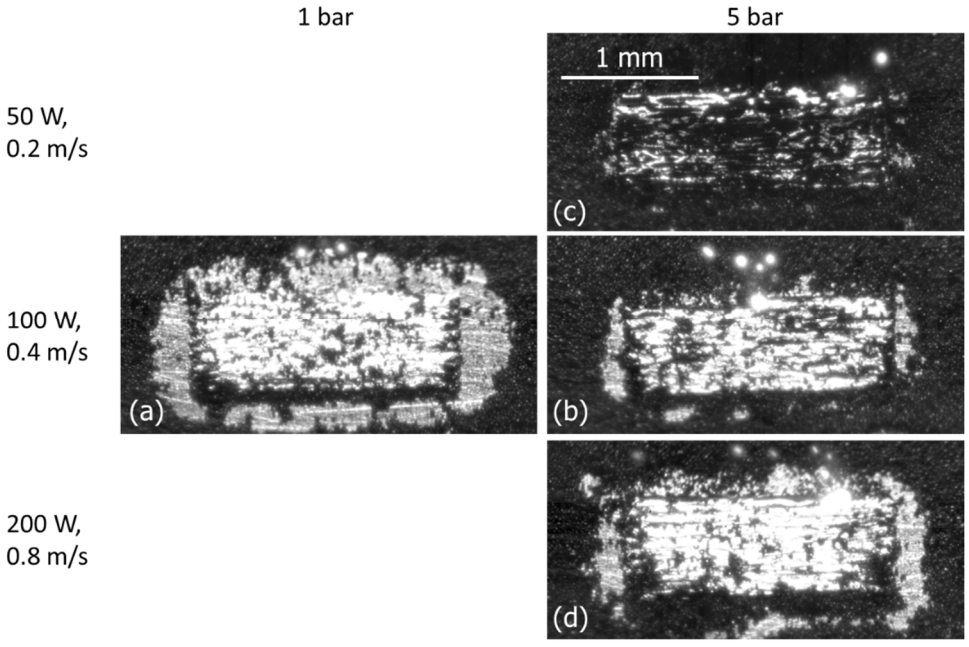

Figure 6.11: High-speed images for top views of the powder bed in helium when scanning rectangular islands at the pressures and process settings (laser power and scan speed) indicated. Denudation is larger than at the corresponding setting in argon. Denudation is reduced as the pressure increases at a laser power of 100 W and scan speed of 0.4 m/s; the formation of plasma and spatter does not increase at high pressure.

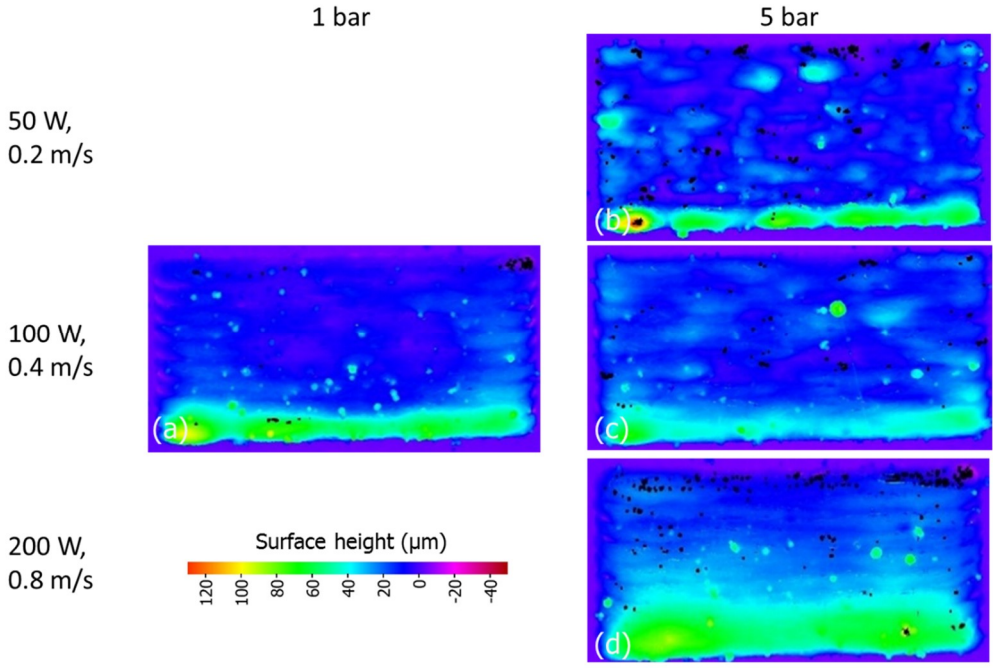

Figure 6.12: Surface height maps for the island scans of Figure 6.11.

The penetration depth in Figure 6.10 was again deeper at the beginning of each island, and stabilised at a decreased value as the island progressed. The decreased penetration began later in the island build than for argon, showing that more time was required in helium for the accumulated metal vapour to defocus the laser beam and for scatter from particulate to reduce its apparent intensity on the powder bed.

Finally, the right-hand column of Figure 6.6 shows schlieren imaging for the helium atmosphere at 5 bar, recorded with the same schlieren sensitivity as for argon in Figure 6.5 and Figure 6.6. The thermal plume rises faster in helium due to its lower density and kinematic viscosity than for argon. The increased convection in the resulting thermal plume is consistent with the increased number of laser scans required before the accumulated vapour and particulate affected the penetration depth of the melt pool. Although the imaged flow features are less dark in helium, it is not possible to infer directly the relative temperature of the thermal plume compared to argon, because the refractive index sensitivity to temperature gradients is lower in helium due to its lower density. However, the absence of significant amounts of ionised metal vapour in the direct imaging results, Figure 6.10, enables the inference of a lower temperature plume in helium than in argon.

6.4 Discussion

In an argon environment, particle entrainment (and hence denudation) was reduced at increased ambient pressure, due to the reduction in the speed of the laser plume and the

associated reduction in the speed of the induced flow of the shielding gas. However, it was accompanied by more plasma in the laser plume, and by an increase in the number and size of spatter particles ejected from the melt pool, making the process less stable. The increased amount of plasma is due to an observed increase in the temperature of the laser plume at high pressure. The increased internal energy of the plume, combined with an inferred increase in the temperature of the melt pool at high pressure, leads to more powder agglomerates which produce more and larger spatter particles.

The increase in vaporisation temperature of the metal at higher pressure suggests that higher temperatures can be reached in the melt pool as described in the Introduction Section 6.1. For laser welding [117] and LPBF experiments at sub-atmospheric pressures (Chapter 5), the penetration depth increases as the pressure is reduced. By analogy, the reduction in penetration observed in Figure 6.7 with an increase in pressure is partially explained by this increase in vaporisation temperature. At high pressure, the same incident laser power is absorbed in a shallower melt pool to keep it molten at high pressure: effectively, more energy is required to create and maintain a weld pool of a given size. A complementary interpretation is that the recoil pressure (the difference between the pressure exerted by the laser plume on the melt pool and the ambient pressure) is reduced at high pressure, so that more energy is required to overcome ambient pressure to open and then maintain a keyhole.

The second effect that reduces the penetration at high pressure is a decrease in laser energy that reaches the workpiece, due to increased absorption and scattering of the beam by the atmosphere. For a fibre laser operating at a wavelength of 1 μm at atmospheric pressure, losses due to Rayleigh scattering (from small particles of condensed metallic atoms with diameter ~100 nm) dominate both inverse Bremsstrahlung absorption by the plasma and Mie scattering (from larger agglomerations of condensation particles) [120]. The effect of each of these scattering and absorption mechanisms increases at high pressure due to the increase in density of the atmosphere. This effect, combined with the increased vaporisation temperature, accounts for the reduction of the penetration depth observed at high pressure.

The increased temperature of the laser plume observed at high pressure is more difficult to analyse analytically or numerically, due the large number of unknown thermophysical properties at high pressure. However, it is possible to infer information about the ionisation state of the plasma in the laser plume as the pressure, and hence

temperature, increases. The first ionisation state of a plasma can be approximated by the Saha equation [119]:

$$\frac{N_e N_i}{N_0} = \frac{g_i g_e}{g_0} \frac{(2\pi m_e k T_e)^{3/2}}{h^3} exp\left(\frac{-E_i}{kT_e}\right) \tag{6.2}$$

Where N_e, N_i and N_0 are the electron, ion and neutral atom densities, T_e is the electron temperature and constants g_e, g_i and g_0 is the degeneracy of the electrons, ionised and neutral states E_i the first ionisation potential of the atom, m_e is the electron mass, k is the Boltzmann constant and h is the Planck constant. For quasi-neutral, weakly ionised plasma N_e=N_i and N_0>>N_e, and using the equation of state $P = N_0 k T_e$ gives:

$$N_e^2 = \frac{g_i g_e}{g_0} \frac{(2\pi m_e)^{3/2}}{h^3} (kT_e)^{1/2}\, P\, exp\left(\frac{-E_i}{kT_e}\right) \tag{6.3}$$

For stainless steel, the metal vapour is predominantly iron vapour (~66% by mass of the powder) but also contains some of the alloying elements, including chromium (~17%), nickel (~12%) and manganese (~2%). Selective vaporisation during laser processing of a metallic alloys may lead to a slightly different vaporisation rates of the alloying elements, and hence composition of the plasma. At 1 bar, the laser plume has an expected temperature of ~6,000 K, primarily depending on the laser power (Chapter 4), which is supported by experimental data for the electron density in the laser plume above a laser key-hole weld in iron [119]. There is no comparable experimental data available at high-pressure. The electron density for iron at atmospheric pressure given by Eq. (6.3) is plotted in Figure 6.13(a) for the atomic constants given in Table 6.1. Clearly the temperature varies with position in the laser plume, and two values are included in the figure: 6,000 K corresponding to a typical temperature and 8,000 K to a high estimate of the increased temperature at 5 bar. From Eq. (6.3) at 6,000 K, the degree of ionisation (N_e/N_0) for iron is 2.3% and for argon is only 0.002%. Even if the electron temperature in the plasma at 5 bar rises to as much as 8,000 K, the degree of ionisation of argon is still only 0.09% which supports the observation that the plasma at high pressure was predominantly ionised metal vapour. The threshold for the optical breakdown of gases decreases at high pressure, but its value for argon at 5 bar is ~3×10^9 W/cm^2 for a laser wavelength of 1064 nm [151] which is significantly higher than the highest value in our experiments (1×10^6 W/cm^2 at 200 W for a 50 μm diameter laser spot). Figure 6.13(b) shows that the degree of ionisation actually decreases as the pressure increases. However, the overall number of ions increases, as shown in Figure 6.13(a) and observed experimentally.

Table 6.1: Atomic constants for atoms and ions of interest [152] **, used in Eq. (6.3) and Figure 6.13. Note g_e=2**

	g_i	g_o	E_i (eV)
Iron	30	25	7.9024678
Argon	2	1	15.7596112
Helium	2	1	24.587387936

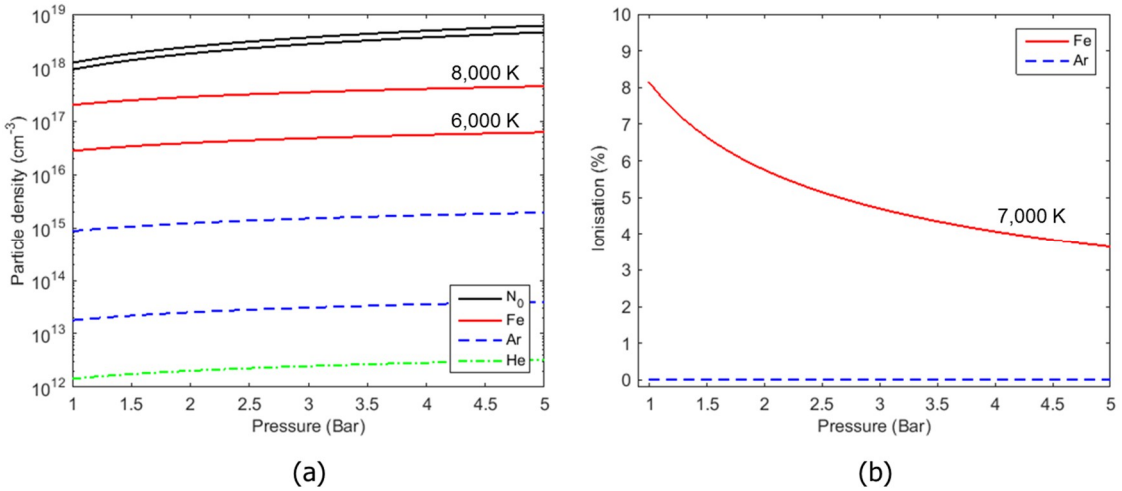

Figure 6.13: (a) Plot of electron density against pressure for a weak plasma of iron, argon and helium from Eq. (6.3) using the atomic values in Table 6.1. For each element, the upper and lower lines correspond to Te of 6,000 K and 8,000 K, respectively. For helium, Ne < 1012 at 6,000 K. (b) Plot of the degree of ionisation for iron and argon at Te = 7,000 K.

Increased thermal ionisation of the metal vapour contributes to the increased plasma in the laser plume, due to the increased temperature of the melt pool and laser plume. It is conceivable that as seed electrons are present within the laser's focal volume, cascade photoionisation processes add to the overall degree of ionisation of the metal vapour. This effect would explain the large increase in plasma observed when spatter was expelled upwards, in the direction of the laser beam, compared to that observed during backwards ejection of the laser plume. Theoretical analyses suggest that the intensity threshold for cascade photoionisation is inversely proportional to the pressure squared [153], while competing processes such as recombination are less favourable within the high energy argon plume.

Denudation around the melt track was always greater in helium than in argon at the corresponding pressure and process setting. The drag force on an entrained powder particle (due to the flow induced in the shielding gas by the laser plume) is proportional to the density of the fluid and the square of its velocity. Hence the velocity of the laser plume in helium must be greater than in argon. The denudation decreased at high pressure due to a reduction in the laser plume velocity, but with no increase in ionisation of the metal vapour or spatter from the melt pool. The thermal conductivity of helium is approximately ten

times that of argon across a range of temperatures, effectively conducting the heat away and preventing the formation of plasma. Any ionisation of helium is even less than argon, due to its higher ionisation potential, Figure 6.13(a), and the optical breakdown intensity threshold is even higher [151]. The thermal plume rises faster in helium due to its lower density and kinematic viscosity, assisting with the convective transport of metal vapour and plasma away from the melt pool. Hence, more energy arrived at the metal surface, resulting in a larger melt bead at the corresponding process setting than in argon. However, even so, the accumulation of vapour and particulate above the powder bed did eventually cause defocus of the laser beam and a reduction in the apparent laser intensity reaching the powder bed, causing the penetration to be reduced in the island scans.

Although denudation was reduced at high pressure, the increased ionisation of metal vapour and spatter from the melt pool degraded the islands in argon: no advantage in using high pressure was identified, at least for the conditions investigated. The helium atmosphere mitigated the negative effects of plasma and spatter to some extent. There is a similarity in denudation and penetration achieved in argon at 1 bar, 100 W and 0.4 m/s and in helium at 5 bar, 200 W and 0.8 m/s with a comparable smoothness and continuity of the built layer. As discussed above, this effect can be attributed to a reduction in recoil pressure at 5 bar, resulting in lower kinetic energy in the melt pool and more stable flow. Therefore, a high-pressure atmosphere could potentially enable an increase in processing speed, provided that the metal vapour generated is extracted to prevent laser defocus and excess plasma generation. The advantages of high pressure in helium at the conditions tested would not appear to be sufficiently decisive to recommend the additional complexity and expense required in the LPBF system. However, the enhanced heat transfer observed when using helium certainly warrants further study on the potential benefits of gases and mixtures beyond pure argon. The effects of helium or mixtures with other gases on material properties (such as hardness) and fluid-particle interactions would also need to be considered.

6.5 Summary

The entrainment of powder particles in the laser powder bed fusion can be reduced by increasing the ambient pressure, which in principle reduces the associate effects of powder denudation and porosity. However, in argon, the associated increase in the temperature of the melt pool and the laser plume produced more spatter and ionised metal vapour: the smoothness and continuity of built layers was degraded. Due to laser defocus and excess

plasma formation, no advantage in using high pressure could be identified. In helium, the plasma and spatter were limited by its higher thermal conductivity and diffusivity, and a comparable smoothness and continuity of built layers was achieved to that in argon at atmospheric pressure but at an increased process speed. However, this marginal potential advantage at the conditions tested would not appear to justify the additional complexity and expense in the LPBF system required.

Chapter 7. Conclusion and Future Work

The goal of this work was to address the issues in the process and create more in-depth knowledge through in-situ process monitoring. The data acquired, in combination with the understanding that has been gained, can be used to aid the selection of robust process parameters and to act as the foundations for development of in-process feedback control. A modular open-architecture LPBF system was designed to maximise accessibility, ensuring ease of modification for specific process monitoring techniques with a high level of flexibility in varying the process parameters. The underlying design was determined by the requirements of access for various in-situ process monitoring techniques such as x-ray imaging, high-speed imaging, thermal sensing, schlieren imaging and other in-situ strain measurements.

7.1 Key Conclusions

The completed work presented in the thesis has produced many interesting results. A number of key conclusions can be made in each of the following subject areas:

An open-architecture modular laser powder bed fusion system for in-situ monitoring:

- A compact, automated and modular open-architecture LPBF system was developed with tremendous flexibility in parameter modification, remote operations and build view access modifications. The system was fully characterised for producing parts with >99% density.

- The developed LPBF system supported various sensors mounting options inside the build chamber for the fixation of equipment such as; strain gauges, thermocouples, dynamometers, spectrometers. Various optical systems such as optical cameras, pyrometers could be mounted as close as 45 mm from the powder bed.

- The built LPBF ensured a high level of reproducibility and repeatability in building parts.

- The LPBF system enabled systematic investigation of shrinkage in powder layers, and powder layer thickness evolution in the multiple layers build. The steady-state melted layer thickness of 40 μm and powder layer thickness of ~130 μm are established after approximately 10 layers. The steady-state melted layer thickness was found equal to the build step increment for each layer in z-stage.

- High resolution (2 μm) x-rays computer tomography (XCT) imaging enabled pseudo in-situ powder layer packing density measurement. The measured packing density from the 3D image was ~56 % for stainless steel 316L for a powder particle size of 15 – 45 μm. A higher packing density of > 60% was observed in Ti64 for a large powder particle size distribution of 45 – 105 μm.

In situ x-ray measurements

- High energy flash x-rays were found to be unsuited for the powder bed for in-situ monitoring, as the high energy x-rays were not attenuated by the micron size powder particles.

- Long-exposure phase contrast x-ray imaging has sufficient contrast to visualise individual particles and was found to be suitable for in-situ monitoring. Stainless steel 316l powder particles of size 15 – 45 μm can be clearly seen on the 1 mm thick 304 stainless-steel coupon.

High-speed imaging of laser powder bed fusion

- High-speed imaging enabled visualisation of several of the complex phenomena within the LPBF process. Single line scans showed that the direction of particle ejection changes with regards to scanned direction from forwards to backwards with increasing laser power and scan speed. When the scan speed and power are relatively high, such as 200 W and 1 m/s for our case, the plume was tilted fully backwards which heavily disrupted the powder bed behind. Furthermore, it was observed that the ejected laser plume creates a low-pressure region and that induces gas flow (Ar), which determines the pattern in which powder is denuded from the vicinity of the melt pool.

- For island scanning, the plume was tilted away from the previously melted track, towards fresh powder that further disrupted the powder layer. The powder availability for consecutive tracks depends on the induced gas flow pattern which further proved the concept of dynamic packing density in LPBF. Large denudations were observed within the first layer in both the adjacent tracks and around the island itself.

- Imaging of the process after several layers showed that the denudation has reduced impact on powder availability compared to the first layer due to the increased powder layer thickness and surface roughness.

- Schlieren imaging enabled visualisation of plume propagation in the atmosphere above the powder bed, facilitating flow characterisation. High-speed observations of the plume propagation correlated well with the denudation effect observed in the direct imaging. The refractive index gradients observed in the videos were undesirable and caused variation in the laser position and focus. However, in commercial systems, the hot fluid should be cleared away by the shielding gas cross flow. Schlieren imaging was found to be a useful tool for the optimisation of a cross-flow system.

Laser powder bed fusion in vacuum

- Vacuum was found to be unsuitable for the laser powder bed fusion without any pre-processing of the powder layer.

- Considerable disruption to the powder bed was observed at sub-atmospheric pressures. As the pressure decreases, particle entrainment increases, however the expansion of the laser plume prevents the particles reaching the melt pool: profiles and track cross-sections revealed a drastic reduction in the cross-sectional area.

- The reduced bead profiles seen at sub-atmospheric pressures are primarily due to increased denudation, rather than increased metal vaporisation as reported in the literature.

- In the molecular flow regime, particles are only repelled by the plume away from the melt pool. The resulting disruption to the powder bed means that most pressures would require a pre-sinter for the process to be viable, with a corresponding increase in processing time and complexity.

- For the regime between 1 bar and ~50 mbar, a mild vacuum (the threshold pressure at which the penetration depth no longer increases) could provide an interesting window for processing without a pre-sinter, but further investigation is required.

Laser powder bed fusion in high pressure atmosphere

- The entrainment of powder particles in LPBF can be reduced by increasing the ambient pressure, which in principle mitigates the associate effects of powder denudation and porosity.

- The associated increase in the temperature of the melt pool and the laser plume produced more spatter and ionised metal vapour: the smoothness and continuity of the built layers was degraded. These effects combine to reduce penetration of the melt pool.

- Helium can stabilise the process at high pressure. Higher scan speeds could then be implemented than at atmospheric pressure, although at the expense of significant complexity in the system.

7.2 Future Work

The work presented in this thesis has produced many interesting results, while also leaving several opportunities.

With regards to an open-architecture LPBF system, areas of interest for future work include:

I. Increase laser power capacity up to 1 kW and application of different laser sources such diode lasers in LPBF.

II. The building of version 2.0 LPBF system with more enhanced sensor mounting facility. Feedback control for layer spreading quality, oxygen concentration measurement and melt pool monitoring.

III. Addition of multi-material modular spreader and auto-hiding for schlieren imaging (to perform schlieren in multilayer components).

IV. Addition of heated bed for residual stress mitigation studies.

V. Building more complex geometries and monitoring build performance.

With regards to in-situ monitoring:

I. Further tests for in-situ phase contrast x-ray measurement while melting single tracks and multilayer builds. A short exposure up to 1 picosecond phase contrast x-ray source at Gemini laser is already located.

II. Further high-speed imaging tests using a high zoom lens and ultra-high-speed camera to visualise the powder particle level interactions and observe the presence of laser supported combustion and detonation waves in LPBF.

III. High-speed imaging for exotic aerospace alloy metal powders such Titanium alloys, Aluminum alloys, nickel alloys etc.

With regards to temperature and residual stresses measurements:

I. In-situ characterisation of residual stresses for process setting in metal powder-bed fusion

II. Multi-sensor (thermocouple, thermal camera and pyrometer) temperature measurements for single track to multilayer build for validation of numerical simulation and equivalent heat source.

Appendix A – CAD Drawing of LPBF System

Main Assembly with Scanner and F-theta

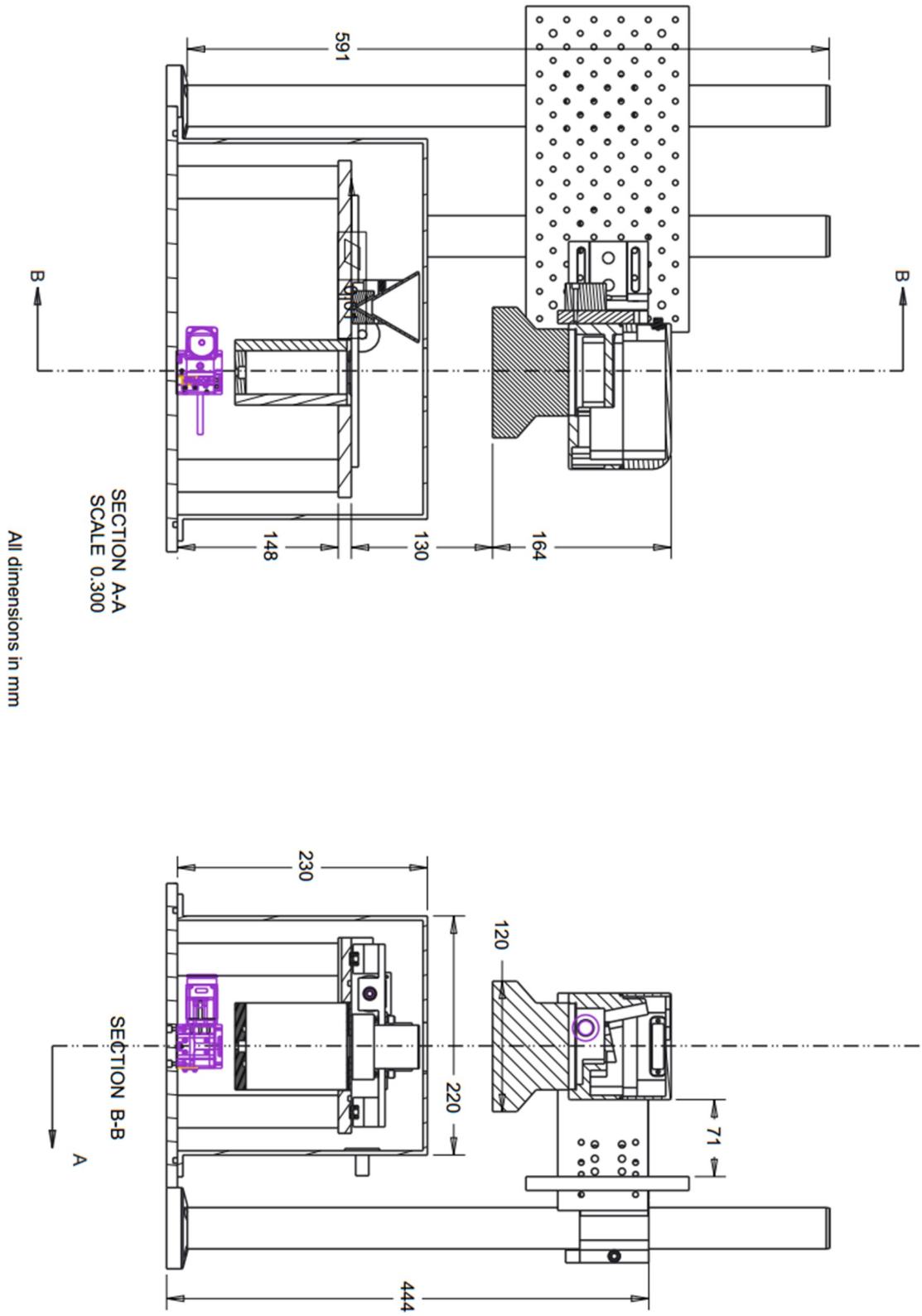

LPBF Powder Spreading System

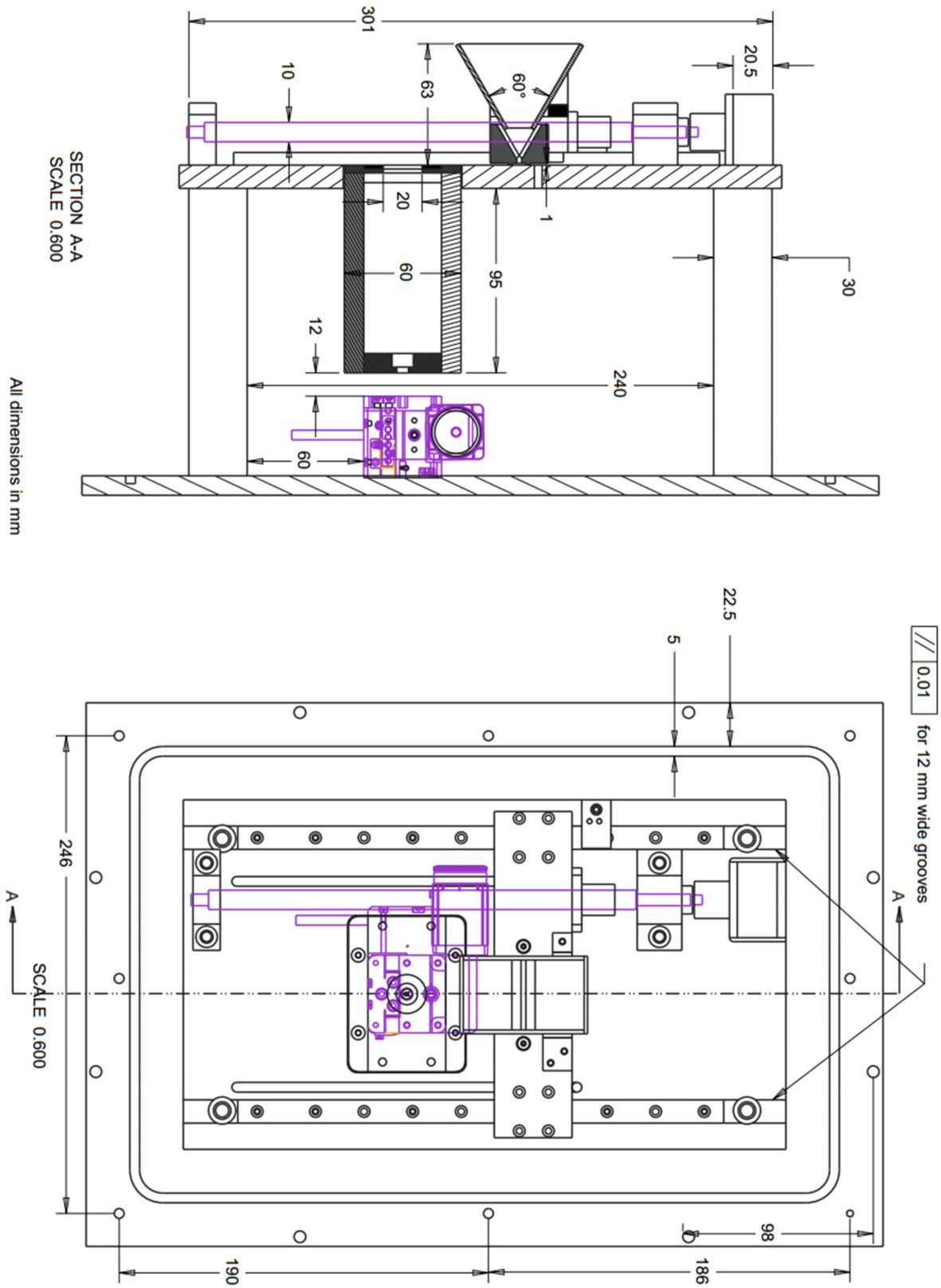

Appendix B – Vacuum and High-pressure Chamber Drawings

Main Tube

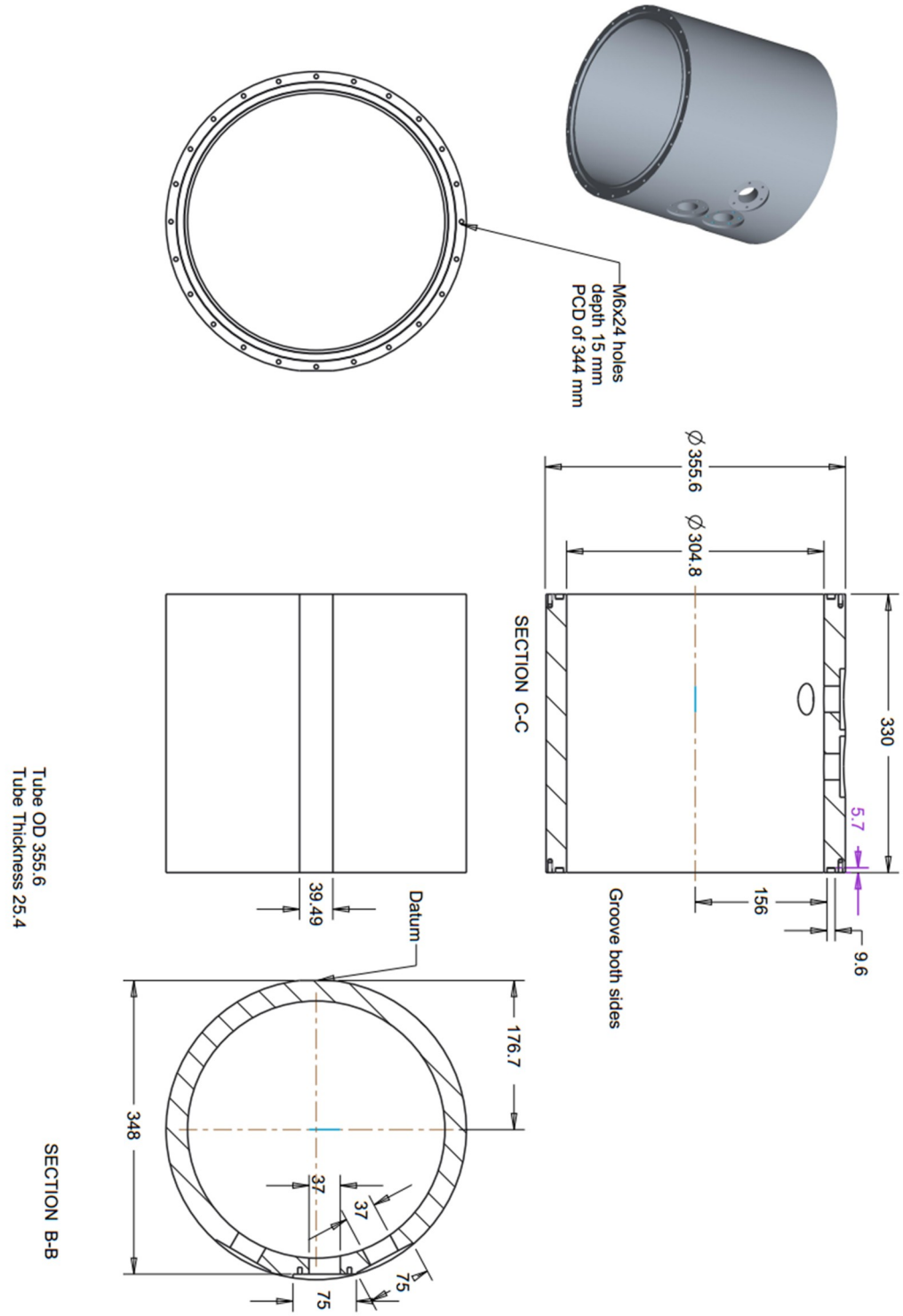

Cover Plate

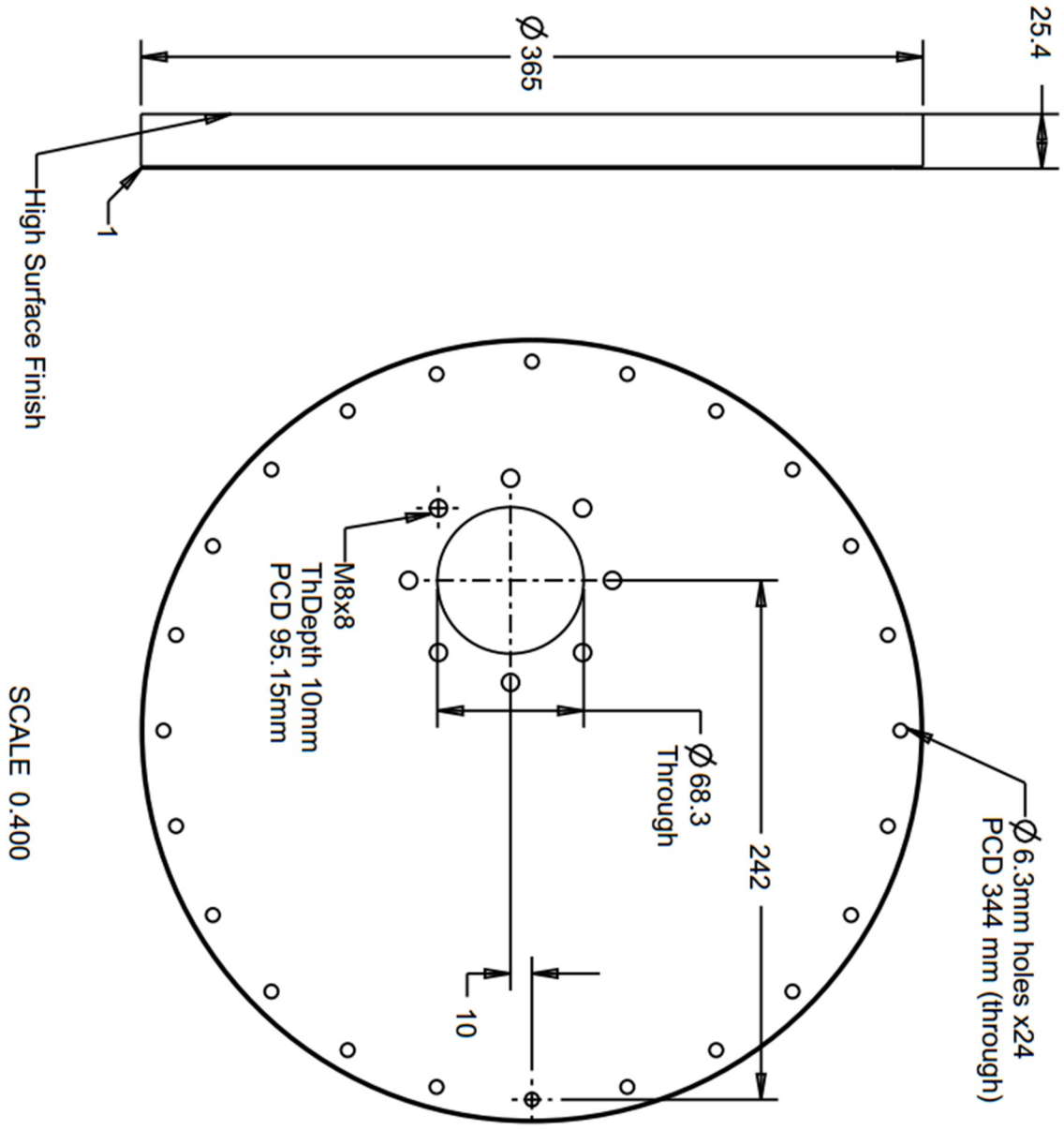
25.4
Ø 365
High Surface Finish
1
M8x8
ThDepth 10mm
PCD 95.15mm
Ø 68.3
Through
242
10
Ø 6.3mm holes x24
PCD 344 mm (through)
SCALE 0.400

Pressure Support Plate 1

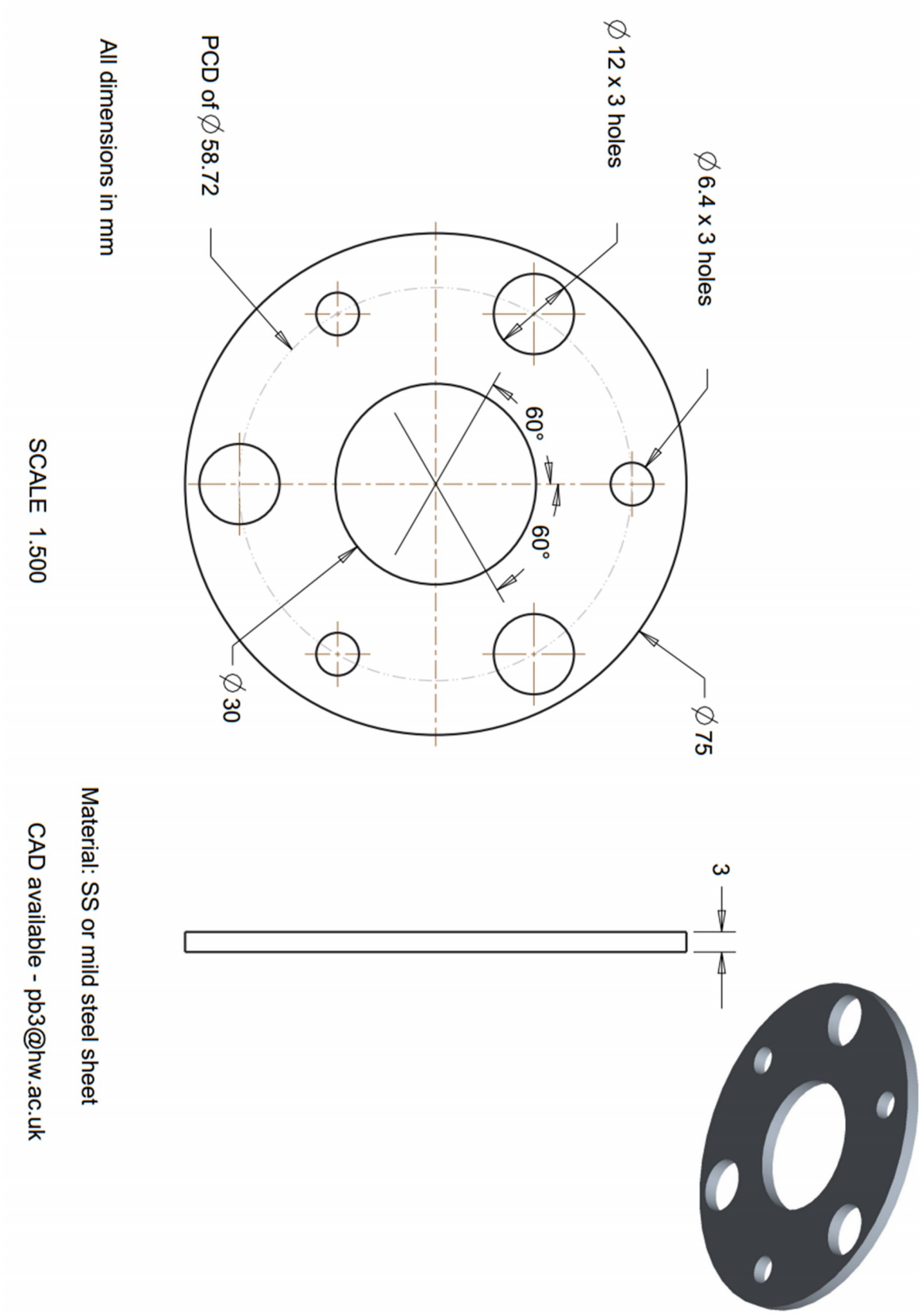

Pressure Support Plate 2

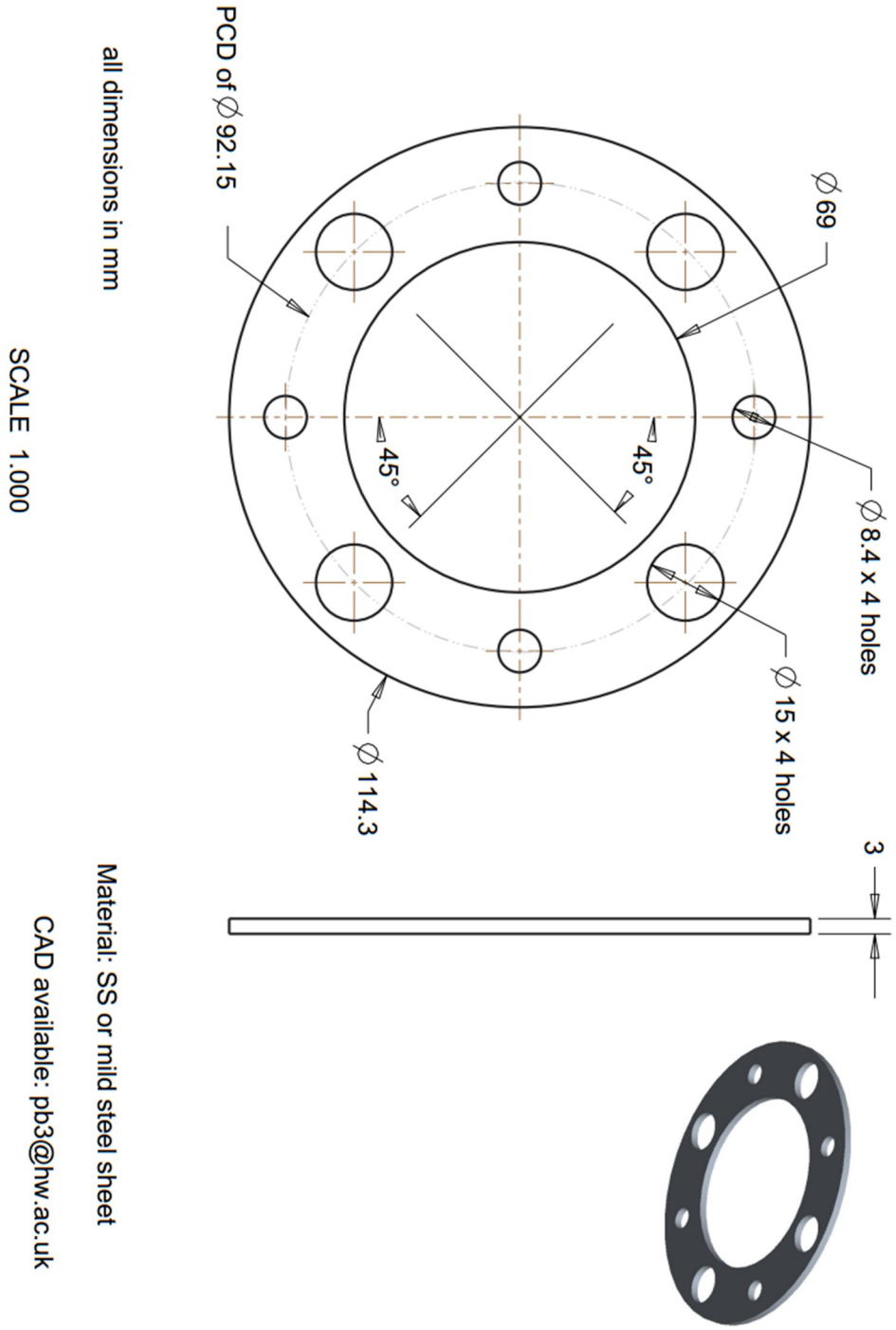

Appendix C - Flow Straightener

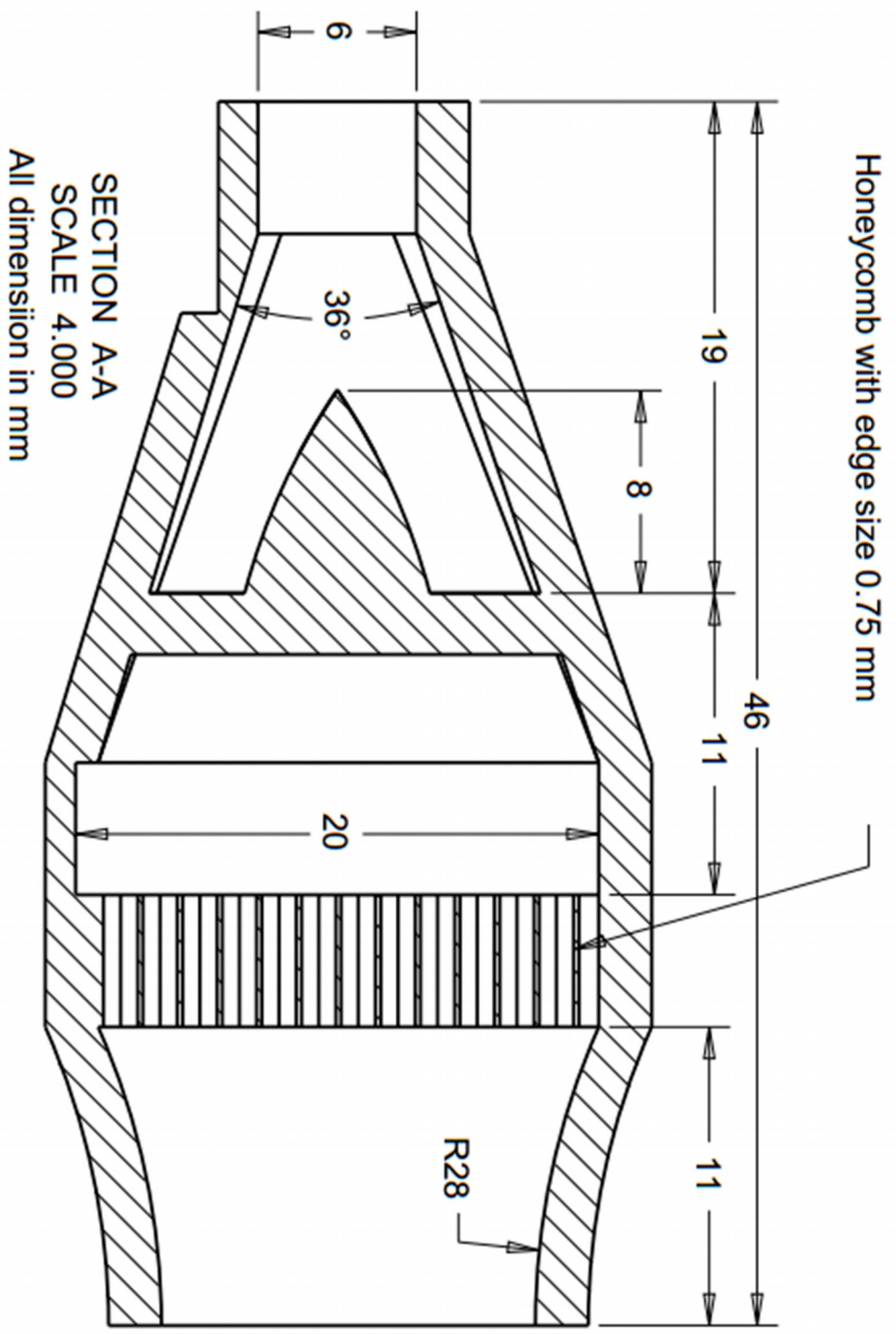

Appendix D - LabVIEW Program Architecture

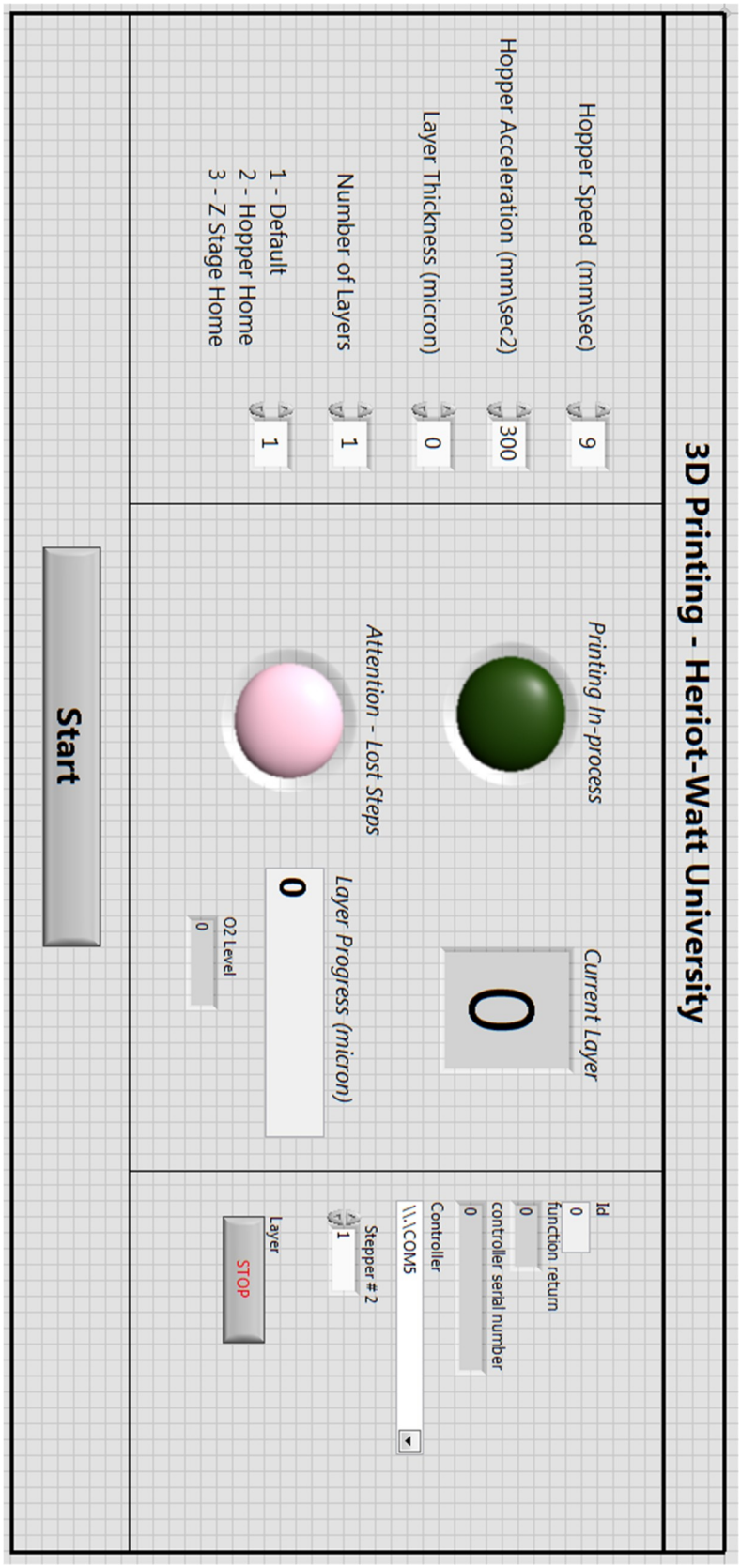

LabVIEW Program Code

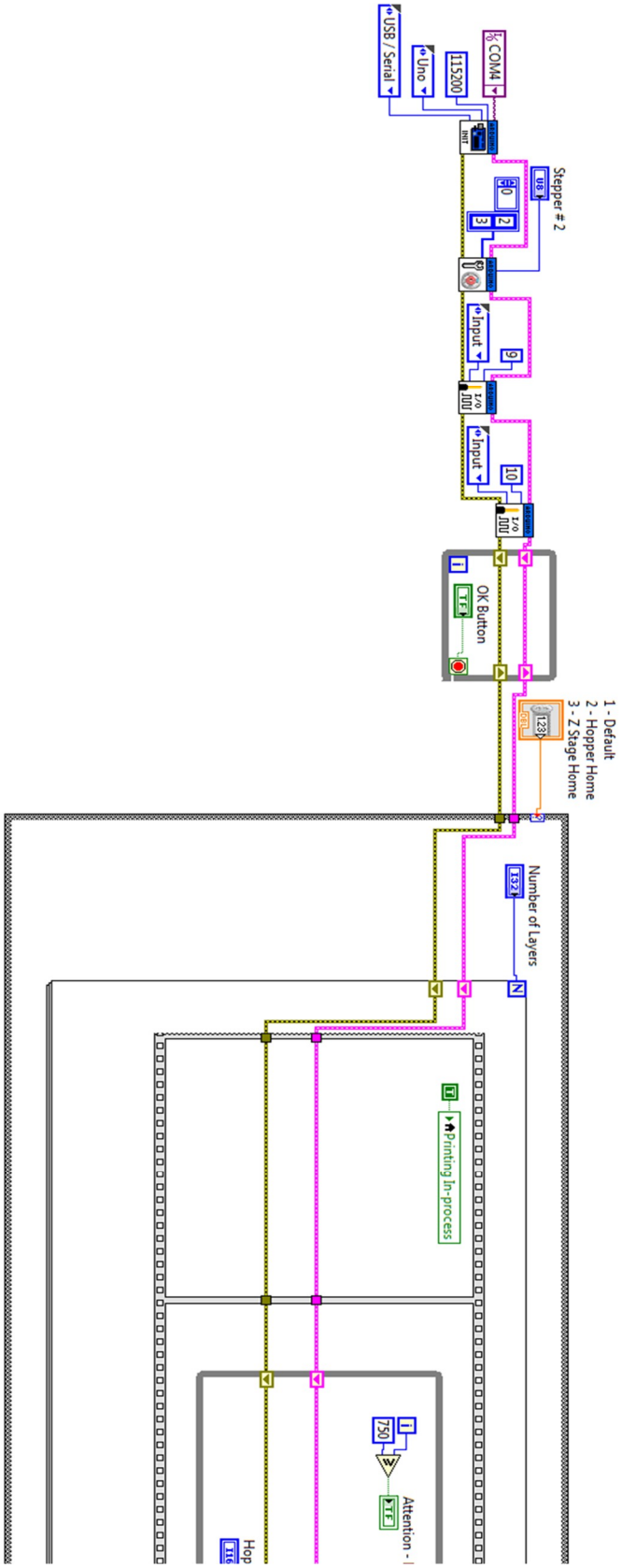

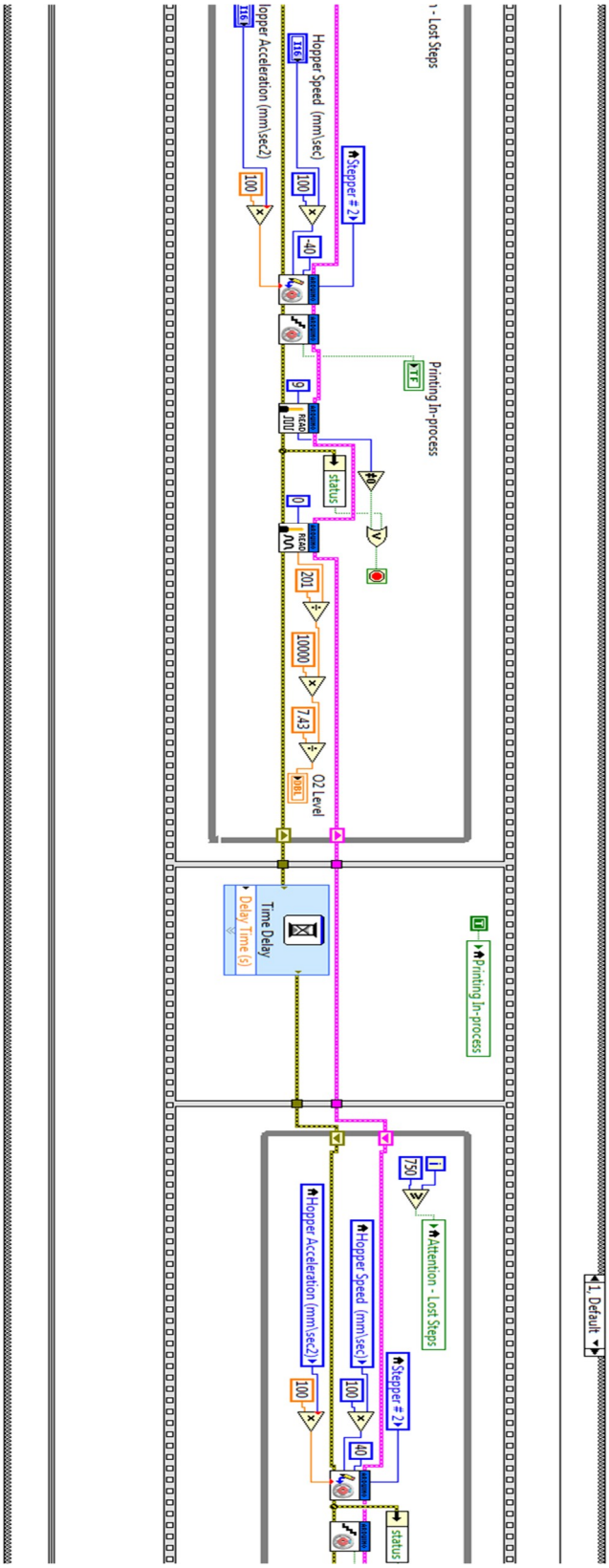
1 - Lost Steps
Hopper Speed (mm\sec)
Hopper Acceleration (mm\sec2)
Stepper # 2
Printing In-process
status
201
10000
7.43
O2 Level
Time Delay
Delay Time (s)
Printing In-process
750
Attention - Lost Steps
Hopper Acceleration (mm\sec2)
Hopper Speed (mm\sec)
Stepper # 2
status
1 Default

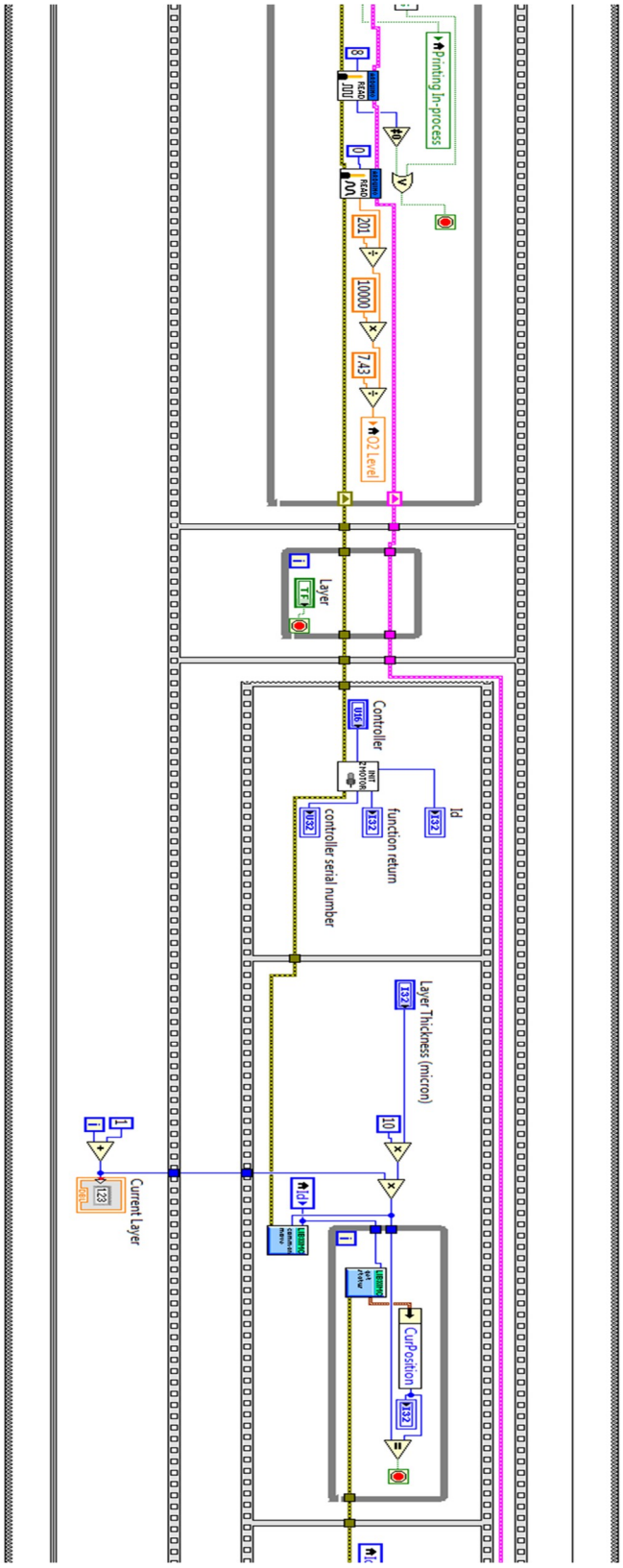
Printing In-process
201
10000
7.43
O2 Level
Layer
Controller
function return
Id
controller serial number
Layer Thickness (micron)
10
Current Layer
CurPosition

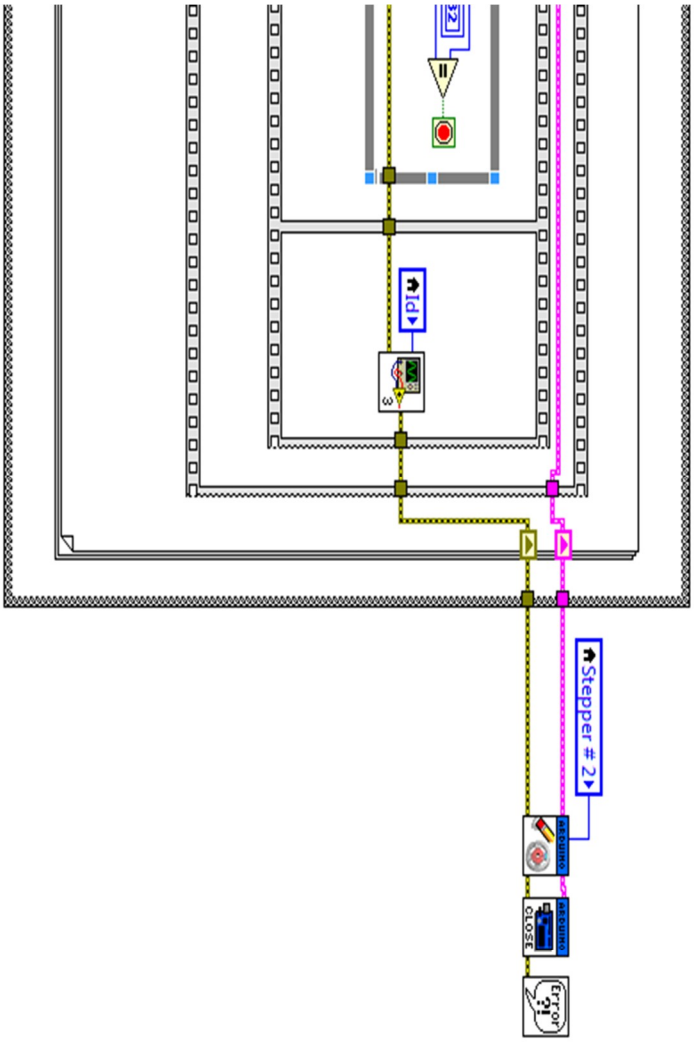
Stepper # 2
CLOSE
Error

References

[1] W.E. Frazier, Metal Additive Manufacturing: A Review, J. Mater. Eng. Perform. 23 (2014) 1917–1928. doi:10.1007/s11665-014-0958-z.

[2] D. Herzog, V. Seyda, E. Wycisk, C. Emmelmann, Additive manufacturing of metals, Acta Mater. 117 (2016) 371–392. doi:10.1016/j.actamat.2016.07.019.

[3] SpaceX, SpaceX Launches 3D-Printed Part to Space, Creates Printed Engine Chamber _ SpaceX, 2014. http://www.spacex.com/news/2014/07/31/spacex-launches-3d-printed-part-space-creates-printed-engine-chamber-crewed.

[4] V. Bhavar, P. Kattire, V. Patil, S. Khot, K. Gujar, R. Singh, A Review on Powder Bed Fusion Technology of Metal Additive Manufacturing, in: 4th Int. Conf. Exhib. Addit. Manuf. Technol., 2014: pp. 1–2.

[5] Renault, Renault Trucks Prints Engine Components, 2017. https://www.spotlightmetal.com/renault-trucks-prints-engine-components-a-661708/.

[6] TCT Magazine, Airbus division 3D prints aluminium component for Eurostar E3000 satellite, (n.d.). https://www.tctmagazine.com/3d-printing-news/airbus-division-3d-prints-aluminium-components-for-new-eurostar-satellite/ (accessed April 9, 2018).

[7] P. Graff, B. Ståhlbom, E. Nordenberg, A. Graichen, P. Johansson, H. Karlsson, Evaluating Measuring Techniques for Occupational Exposure during Additive Manufacturing of Metals: A Pilot Study, J. Ind. Ecol. 0 (2016) 1–10. doi:10.1111/jiec.12498.

[8] J.P. Kruth, L. Froyen, J. Van Vaerenbergh, P. Mercelis, M. Rombouts, B. Lauwers, Selective laser melting of iron-based powder, J. Mater. Process. Technol. 149 (2004) 616–622. doi:10.1016/j.jmatprotec.2003.11.051.

[9] I. Yadroitsev, P. Bertrand, I. Smurov, Parametric analysis of the selective laser melting process, Appl. Surf. Sci. 253 (2007) 8064–8069. doi:10.1016/j.apsusc.2007.02.088.

[10] K.A. Mumtaz, P. Erasenthiran, N. Hopkinson, High density selective laser melting

of Waspaloy??, J. Mater. Process. Technol. 195 (2008) 77–87. doi:10.1016/j.jmatprotec.2007.04.117.

[11] W.E. King, H.D. Barth, V.M. Castillo, G.F. Gallegos, J.W. Gibbs, D.E. Hahn, C. Kamath, A.M. Rubenchik, Observation of keyhole-mode laser melting in laser powder-bed fusion additive manufacturing, J. Mater. Process. Technol. 214 (2014) 2915–2925. doi:10.1016/j.jmatprotec.2014.06.005.

[12] A.B. Spierings, N. Herres, G. Levy, C. Buchs, Influence of the particle size distribution on surface quality and mechanical properties in additive manufactured stainless steel parts, Rapid Prototyp. J. Spec. Issue SFF 2010. 17 (2011) 195–202. doi:10.1108/13552541111124770.

[13] B. Liu, R. Wildman, C. Tuck, I. Ashcroft, R. Hague, Investigation the Effect of Particle Size Distribution on Processing Parameters Optimisation in Selective Laser Melting Process, Solid Free. Fabr. Proc. (2011) 227–238.

[14] I. Yadroitsev, L. Thivillon, P. Bertrand, I. Smurov, Strategy of manufacturing components with designed internal structure by selective laser melting of metallic powder, Appl. Surf. Sci. 254 (2007) 980–983. doi:10.1016/j.apsusc.2007.08.046.

[15] M. Simonelli, C. Tuck, N.T. Aboulkhair, I. Maskery, I. Ashcroft, R.D. Wildman, R. Hague, A Study on the Laser Spatter and the Oxidation Reactions During Selective Laser Melting of 316L Stainless Steel, Al-Si10-Mg, and Ti-6Al-4V, Metall. Mater. Trans. A. 46 (2015) 3842–3851. doi:10.1007/s11661-015-2882-8.

[16] A.B. Spierings M. Schneider R. Eggenberger, Comparison of density measurement techniques for additive manufactured metallic parts, Rapid Prototyp. J. 17 (2011) 380–386. doi:10.1108/13552541111156504.

[17] P. Bidare, R.R.J. Maier, R.J. Beck, J.D. Shephard, A.J. Moore, An open-architecture metal powder bed fusion system for in-situ process measurements, Addit. Manuf. 16 (2017). doi:10.1016/j.addma.2017.06.007.

[18] A.R. Saad A. Khairallah, Andrew T. Anderson, Laser powder-bed fusion additive manufacturing: physics of complex melt flow and formation mechanisms of pores, spatter and denudation zone Saad, Igarss 2014. (2014) 1–5. doi:10.1007/s13398-014-0173-7.2.

[19] I. Gibson, D.W. Rosen, B. Stucker, Additive Manufacturing Technologies, 2010. doi:10.1007/978-1-4419-1120-9.

[20] M. Agarwala, D. Bourell, J. Beaman, H. Marcus, J. Barlow, Direct selective laser sintering of metals, Rapid Prototyp. J. 1 (1995) 26–36. doi:10.1108/13552549510078113.

[21] H. Gong, K. Rafi, N. V. Karthik, T. Starr, B. Stucker, Defect morphology in Ti-6Al-4V parts fabricated by Selective Laser Melting and Electron Beam Melting, in: 24th Int. SFF Symp. - An Addit. Manuf. Conf. SFF 2013, 2013: pp. 440–453. doi:10.1007/s11665-013-0658-0.

[22] S.L. Sing, J. An, W.Y. Yeong, F.E. Wiria, Laser and electron-beam powder-bed additive manufacturing of metallic implants: A review on processes, materials and designs, J. Orthop. Res. 34 (2016) 369–385. doi:10.1002/jor.23075.

[23] K. Mumtaz, N. Hopkinson, Top surface and side roughness of Inconel 625 parts processed using selective laser melting, Rapid Prototyp. J. 15 (2009) 96–103. doi:10.1108/13552540910943397.

[24] M. Saunders, Real-time AM monitoring opens up new process control opportunities, 2018. https://www.linkedin.com/pulse/real-time-am-monitoring-opens-up-new-process-control-marc-saunders.

[25] C. Bryant, Design and development of layer-based additive manufacturing process for realization of metal parts of designed mesostructure, 2008.

[26] C.D. Boley, S.A. Khairallah, A.M. Rubenchik, Calculation of laser absorption by metal powders in additive manufacturing., Appl. Opt. 54 (2015) 2477–82. doi:10.1364/AO.54.002477.

[27] W.E. King, A.T. Anderson, R.M. Ferencz, N.E. Hodge, C. Kamath, S.A. Khairallah, A.M. Rubenchik, Laser powder bed fusion additive manufacturing of metals; physics, computational, and materials challenges, Appl. Phys. Rev. 2 (2015) 41304. doi:10.1063/1.4937809.

[28] T. Wohlers, T. Gornet, History of Additive Manufacturing, Wohlers Rep. 2014 - 3D Print. Addit. Manuf. State Ind. (2014) 1–34. doi:10.1017/CBO9781107415324.004.

[29] Renishaw plc, First metal 3D printed bicycle frame manufactured by Renishaw for Empire Cycles, (n.d.). http://www.renishaw.com/en/first-metal-3d-printed-bicycle-frame-manufactured-by-renishaw-for-empire-cycles--24154 (accessed April 10, 2018).

[30] R. Li, Y. Shi, Z. Wang, L. Wang, J. Liu, W. Jiang, Densification behavior of gas and water atomized 316L stainless steel powder during selective laser melting, Appl. Surf. Sci. 256 (2010) 4350–4356. doi:10.1016/j.apsusc.2010.02.030.

[31] Renishaw PLC, RenAM 500Q multi-laser AM system, 2017. http://resources.renishaw.com/en/details/data-sheet-renam-500q--99032.

[32] Additive Industries, Industrialising 3D printing for functional parts, Re. (2015) 1–2. https://additiveindustries.com/systems/metalfab1.

[33] W.J. Sames, F.A. List, S. Pannala, R.R. Dehoff, S.S. Babu, The metallurgy and processing science of metal additive manufacturing, Int. Mater. Rev. 6608 (2016) 1–46. doi:10.1080/09506608.2015.1116649.

[34] L. Thijs, J. Van Humbeeck, K. Kempen, E. Yasa, J.-P. Kruth, Investigation on the inclusions in maraging steel produced by Selective Laser Melting, in: 5th Int. Conf. Adv. Res. Virtual Rapid Prototyp., 2011: pp. 297–304. doi:doi:10.1201/b11341-48\r10.1201/b11341-48.

[35] W. King, A.T. Anderson, R.M. Ferencz, N.E. Hodge, C. Kamath, S.A. Khairallah, Overview of modelling and simulation of metal powder bed fusion process at Lawrence Livermore National Laboratory, Mater. Sci. Technol. 31 (2015) 957–968. doi:10.1179/1743284714Y.0000000728.

[36] I. Yadroitsev, A. Gusarov, I. Yadroitsava, I. Smurov, Single track formation in selective laser melting of metal powders, J. Mater. Process. Technol. 210 (2010) 1624–1631. doi:10.1016/j.jmatprotec.2010.05.010.

[37] A.B. Spierings, G. Levy, Comparison of density of stainless steel 316L parts produced with selective laser melting using different powder grades, in: Proc. Solid Free. Fabr. Symp., 2009: pp. 342–353.

[38] Y. Pupo, J. Delgado, L. Serenó, J. Ciurana, Scanning space analysis in Selective Laser Melting for CoCrMo powder, Procedia Eng. 63 (2013) 370–378.

doi:10.1016/j.proeng.2013.08.228.

[39] I. Yadroitsev, I. Smurov, Surface morphology in selective laser melting of metal powders, Phys. Procedia. 12 (2011) 264–270. doi:10.1016/j.phpro.2011.03.034.

[40] G. Strano, L. Hao, R.M. Everson, K.E. Evans, Surface roughness analysis, modelling and prediction in selective laser melting, J. Mater. Process. Technol. 213 (2013) 589–597. doi:10.1016/j.jmatprotec.2012.11.011.

[41] S. Berretta, O. Ghita, K.E. Evans, A. Anderson, C. Newman, Size, shape and flow of powders for use in Selective Laser Sintering (SLS), in: 6th Int. Conf. Adv. Res. Virtual Phys. Prototyping, VR@P 2013, Oct. 1, 2013 - Oct. 5, 2013, 2014: pp. 49–54.

[42] F.J. Gürtler, M. Karg, M. Dobler, S. Kohl, I. Tzivilsky3, M. Schmidt, Influence of powder distribution on process stability in laser beam melting: Analysis of melt pool dynamics by numerical simulations, in: Solid Free. Symp. Texas, 2014: pp. 1099–1117.

[43] P.A. Carroll, A.J. Pinkerton, J. Allen, W.U.H. Syed, H.K. Sezer, P. Brown, G. Ng, R. Scudamore, L. Li, The effect of powder recycling in direct metal laser deposition on powder and manufactured part characteristics, in: Proc. AVT-139 Spec. Meet. Cost Eff. Manuf. via Net Shape Process. NATO Res. Technol. Organ., 2006: pp. 1–8. http://eprints.lancs.ac.uk/59645/.

[44] Renishaw plc, Investigating the effects of multiple re-use of Ti6Al4V powder in additive manufacturing, Report. (2016) 1–10. http://resources.renishaw.com.

[45] S. Dadbakhsh, L. Hao, Effect of layer thickness in selective laser melting on microstructure of Al/5 wt.%Fe2O3 powder consolidated parts., Sci. World J. 2014 (2014) 1–10. doi:10.1155/2014/106129.

[46] Renishaw PLC, InfiniAM Spectral – Energy input and melt pool emissions monitoring for AM systems, 2018. http://resources.renishaw.com/en/details/data-sheet-renam-500q--99032.

[47] ConceptLaser, Achieve the highest possible quality in series production thanks to LaserCUSING ®, Report. (2015) 1–4. https://www.concept-laser.de/fileadmin/user_upload/1603_QM_Prospect_EN.pdf.

[48] EOS, Monitoring of industrial 3D printing processes, (2017) 1–4. https://www.eos.info/software/monitoring-software.

[49] SLM Solutions GmbH, Selective Laser Melting Eine produktive Fertigungstechnologie, Report. 49 (2013) 1–26. http://www.stage.slm-solutions.com/index.php?downloads_en#cpid214.

[50] M.L. Vlasea, B. Lane, F. Lopez, S. Mekhontsev, A. Donmez, Development of powder bed fusion additive manufacturing test bed for enhanced real-time process control, in: Solid Free. Fabr. Proc., 2015: pp. 527–539.

[51] J.C. Fox, B.M. Lane, H. Yeung, Measurement of process dynamics through coaxially aligned high speed near-infrared imaging in laser powder bed fusion additive manufacturing, in: 2017: pp. 1021407–1021417. http://dx.doi.org/10.1117/12.2263863.

[52] S.M. Kelly, P.C. Boulware, L. Cronley, G. Firestone, J. Marchal, T. Stempky, C. Reichert, In-Process Sensing of Laser Powder Bed Fusion Additive Manufacturing, in: A Work. Predict. Theor. Comput. Approaches Addit. Manuf., 2015. http://sites.nationalacademies.org/cs/groups/pgasite/documents/webpage/pga_168775.pdf.

[53] M. Jamshidinia, P. Boulware, J. Marchal, H. Mendoza, L. Cronley, S. Kelly, S. Newhouse, In-Process Monitoring of Cross Contamination in Laser Powder Bed Fusion (L-PBF) Additive Manufacturing (AM), in: Proc. Solid Free. Fabr. Symp., 2016: pp. 1366–1380.

[54] B.K. Foster, E.W. Reutzel, A.R. Nassar, B.T. Hall, S.W. Brown, C.J. Dickman, Optical, layerwise monitoring of powder bed fusion, in: Proc. Solid Free. Fabr. Symp., 2015: pp. 295–307. doi:10.1017/CBO9781107415324.004.

[55] Fraunhofer ILT, Component and System Development for Selective Laser Melting (SLM), Report. (2014) 1–2. https://www.ilt.fraunhofer.de.

[56] S.P. Baker, Design and Fabrication of an Open-Architecture Selective Laser Melting System, Massachusetts Institute of Technology, 2017.

[57] A. Masmoudi, R. Bolot, C. Coddet, Investigation of the laser – powder – atmosphere interaction zone during the selective laser melting process, J. Mater.

Process. Tech. 225 (2015) 122–132. doi:10.1016/j.jmatprotec.2015.05.008.

[58] M.J. Matthews, G. Guss, S.A. Khairallah, A.M. Rubenchik, P.J. Depond, W.E. King, Denudation of metal powder layers in laser powder bed fusion processes, Acta Mater. 114 (2016) 33–42. doi:10.1016/j.actamat.2016.05.017.

[59] M. Islam, T. Purtonen, H. Piili, A. Salminen, O. Nyrhila, Temperature profile and imaging analysis of laser additive manufacturing of stainless steel, Phys. Procedia. 41 (2013) 835–842. doi:10.1016/j.phpro.2013.03.156.

[60] W.M. Steen, M. J., Laser Material Processing, 2010. doi:10.1007/978-1-84996-062-5.

[61] C. Qiu, C. Panwisawas, M. Ward, H.C. Basoalto, J.W. Brooks, M.M. Attallah, On the role of melt flow into the surface structure and porosity development during selective laser melting, Acta Mater. 96 (2015) 72–79. doi:10.1016/j.actamat.2015.06.004.

[62] C. Van Gestel, Study of physical phenomena of selective laser melting towards increased productivity, École Polytechnique Fédérale De Lausanne Pour, 2015.

[63] T. Craeghs, S. Clijsters, J.-P. Kruth, F. Bechmann, M.-C. Ebert, Detection of Process Failures in Layerwise Laser Melting with Optical Process Monitoring, Phys. Procedia. 39 (2012) 753–759. doi:10.1016/j.phpro.2012.10.097.

[64] T. Craeghs, S. Clijsters, E. Yasa, J.-P. Kruth, Online quality control of selective laser melting, in: Solid Free. Fabr. Proc., 2011: pp. 212–226.

[65] S. Clijsters, T. Craeghs, S. Buls, K. Kempen, J.-P. Kruth, In situ quality control of the selective laser melting process using a high-speed, real-time melt pool monitoring system, Int. J. Adv. Manuf. Technol. 75 (2014) 1089–1101. doi:10.1007/s00170-014-6214-8.

[66] S. Berumen, F. Bechmann, S. Lindner, J.-P. Kruth, T. Craeghs, Quality control of laser- and powder bed-based Additive Manufacturing (AM) technologies, Phys. Procedia. 5 (2010) 617–622. doi:10.1016/j.phpro.2010.08.089.

[67] J. Kruth, P. Mercelis, J. Van Vaerenbergh, T. Craeghs, Feedback control of Selective Laser Melting, in: Proc. 3rd Int. Conf. Adv. Res. Virtual Rapid Prototyp.,

2007: pp. 1–7.

[68] T. Craeghs, F. Bechmann, S. Berumen, J.P. Kruth, Feedback control of Layerwise Laser Melting using optical sensors, Phys. Procedia. 5 (2010) 505–514. doi:10.1016/j.phpro.2010.08.078.

[69] C. Zhao, K. Fezzaa, R.W. Cunningham, H. Wen, F. De Carlo, L. Chen, A.D. Rollett, T. Sun, Real-time monitoring of laser powder bed fusion process using high-speed X-ray imaging and diffraction, Sci. Rep. 7 (2017) 3602. doi:10.1038/s41598-017-03761-2.

[70] I. Yadroitsev, P. Krakhmalev, I. Yadroitsava, Selective laser melting of Ti6Al4V alloy for biomedical applications: Temperature monitoring and microstructural evolution, J. Alloys Compd. 583 (2014) 404–409. doi:10.1016/j.jallcom.2013.08.183.

[71] M. Pavlov, M. Doubenskaia, I. Smurov, Pyrometric analysis of thermal processes in SLM technology, Phys. Procedia. 5 (2010) 523–531. doi:10.1016/j.phpro.2010.08.080.

[72] Y. Chivel, I. Smurov, On-line temperature monitoring in selective laser sintering/melting, Phys. Procedia. 5 (2010) 515–521. doi:10.1016/j.phpro.2010.08.079.

[73] M.A. Doubenskaia, I.V. Zhirnov, V.I. Teleshevskiy, P. Bertrand, I.Y. Smurov, Determination of True Temperature in Selective Laser Melting of Metal Powder Using Infrared Camera, Mater. Sci. Forum. 834 (2015) 93–102. doi:10.4028/www.scientific.net/MSF.834.93.

[74] P. Lott, H. Schleifenbaum, W. Meiners, K. Wissenbach, C. Hinke, J. Bültmann, Design of an Optical system for the In Situ Process Monitoring of Selective Laser Melting (SLM), Phys. Procedia. 12 (2011) 683–690. doi:10.1016/j.phpro.2011.03.085.

[75] U. Thombansen, A. Gatej, M. Pereira, Process observation in fiber laser–based selective laser melting, Opt. Eng. 54 (2014) 11008. doi:10.1117/1.OE.54.1.011008.

[76] B. Ferrar, L. Mullen, E. Jones, R. Stamp, C.J. Sutcliffe, Gas flow effects on selective laser melting (SLM) manufacturing performance, J. Mater. Process.

Technol. 212 (2012) 355–364. doi:10.1016/j.jmatprotec.2011.09.020.

[77] G. Repossini, V. Laguzza, M. Grasso, B.M. Colosimo, On the use of spatter signature for in-situ monitoring of Laser Powder Bed Fusion, Addit. Manuf. 16 (2017) 35–48. doi:10.1016/j.addma.2017.05.004.

[78] A. Ladewig, G. Schlick, M. Fisser, V. Schulze, U. Glatzel, Influence of the shielding gas flow on the removal of process by-products in the selective laser melting process, Addit. Manuf. 10 (2016) 1–9. doi:10.1016/j.addma.2016.01.004.

[79] A.J. Dunbar, E.R. Denlinger, J. Heigel, P. Michaleris, P. Guerrier, R. Martukanitz, T. Simpson, Development of experimental method for in situ distortion and temperature measurements during the laser powder bed fusion additive manufacturing process, Addit. Manuf. 12 Part A (2016) 25–30. doi:10.1016/j.addma.2016.04.007.

[80] M. Simonelli, C. Tuck, N.T. Aboulkhair, I. Maskery, I. Ashcroft, R.D. Wildman, R. Hague, A Study on the Laser Spatter and the Oxidation Reactions During Selective Laser Melting of 316L Stainless Steel, Al-Si10-Mg, and Ti-6Al-4V, Metall. Mater. Trans. A Phys. Metall. Mater. Sci. 46 (2015) 3842–3851. doi:10.1007/s11661-015-2882-8.

[81] Y. Liu, Y. Yang, S. Mai, D. Wang, C. Song, Investigation into spatter behavior during selective laser melting of AISI 316L stainless steel powder, Mater. Des. 87 (2015) 797–806. doi:10.1016/j.matdes.2015.08.086.

[82] F. Bayle, M. Doubenskaia, Selective Laser Melting process monitoring with high speed infra-red camera and pyrometer, in: Proc. SPIE, 2008: p. 698505. doi:10.1117/12.786940.

[83] B. Lane, S. Moylan, E.P. Whitenton, L. Ma, Thermographic measurements of the commercial laser powder bed fusion process at NIST, Rapid Prototyp. J. 22 (2016) 778–787. doi:10.1108/RPJ-11-2015-0161.

[84] S. Ly, A.M. Rubenchik, S.A. Khairallah, G. Guss, M.J. Matthews, Metal vapor micro-jet controls material redistribution in laser powder bed fusion additive manufacturing, Sci. Rep. 7 (2017) 4085. doi:10.1038/s41598-017-04237-z.

[85] V. Gunenthiram, P. Peyre, M. Schneider, M. Dal, F. Coste, R. Fabbro, Analysis of

laser–melt pool–powder bed interaction during the selective laser melting of a stainless steel, J. Laser Appl. 29 (2017) 22303. doi:10.2351/1.4983259.

[86] D.M. Bauer, K. Dietrich, M. Walter, P. Forêt, F. Palm, G. Witt, Effect of Process Gas and Powder Quality on Aluminum Alloys Processed by Laser Based Powder Bed Melting Process, in: Proc. Solid Free. Fabr. Symp., 2016: pp. 419–425.

[87] I. Bitharas, S.W. Campbell, A.M. Galloway, N.A. McPherson, A.J. Moore, Visualisation of alternating shielding gas flow in GTAW, Mater. Des. 91 (2016) 424–431. doi:10.1016/j.matdes.2015.11.085.

[88] S. Dadbakhsh, L. Hao, N. Sewell, Effect of selective laser melting layout on the quality of stainless steel parts, Rapid Prototyp. J. 18 (2012) 241–249. doi:10.1108/13552541211218216.

[89] A.J. Dunbar, Analysis of the Laser Powder Bed Fusion Additive Manufacturing Process Through Experimental Measurement and Finite Element Modeling, The Pennsylvania State University, 2016. https://etda.libraries.psu.edu/files/final_submissions/11675.

[90] C. Sutcliffe, Residual Stresses in Powder Bed Laser Melting, in: RESIDUAL Stress Meas. Temp. Perform., 2016. events.imeche.org/residualstresses.

[91] M. Shiomil, T. Yamashital, K. Osakada, M. Shiomi, T. Yamashita, F. Abe, K. Nakamura, Residual Stress within Metallic Model Made by Selective Laser Melting Process, in: Ann. CIRP, 2004: pp. 195–198. doi:10.1016/S0007-8506(07)60677-5.

[92] L. van Belle, G. Vansteenkiste, J.C. Boyer, Investigation of Residual Stresses Induced during the Selective Laser Melting Process, Key Eng. Mater. 554–557 (2013) 1828–1834. doi:10.4028/www.scientific.net/KEM.554-557.1828.

[93] A.S. Wu, D.W. Brown, M. Kumar, G.F. Gallegos, W.E. King, An Experimental Investigation into Additive Manufacturing Induced Residual Stresses in 316L Stainless Steel, Metall. Mater. Trans. A. 45 (2014) 6260–6270. doi:10.1007/s11661?014?2549-x.

[94] S.A. Khairallah, A.T. Anderson, A. Rubenchik, W.E. King, Laser powder-bed fusion additive manufacturing: Physics of complex melt flow and formation

mechanisms of pores, spatter, and denudation zones, Acta Mater. 108 (2016) 36–45. doi:10.1016/j.actamat.2016.02.014.

[95] M. Erler, A. Streek, C. Schulze, H. Exner, Novel machine and measurement concept for micro machining by selective laser sintering, in: Proc. Solid Free. Fabr. Symp., 2014: pp. 12–21.

[96] A. Neef, V. Seyda, D. Herzog, C. Emmelmann, M. Schönleber, M. Kogel-Hollacher, Low coherence interferometry in selective laser melting, Phys. Procedia. 56 (2014) 82–89. doi:10.1016/j.phpro.2014.08.100.

[97] J.A. Kanko, A.P. Sibley, J.M. Fraser, In situ morphology-based defect detection of selective laser melting through inline coherent imaging, J. Mater. Process. Technol. 231 (2016) 488–500. doi:10.1016/j.jmatprotec.2015.12.024.

[98] A. Wegner, G. Witt, Process monitoring in laser sintering using thermal imaging, in: Proc. Solid Free. Fabr. Symp., 2011: pp. 405–414.

[99] V.S. Sufiiarov, A.A. Popovich, E. V. Borisov, I.A. Polozov, D. V. Masaylo, A. V. Orlov, The Effect of Layer Thickness at Selective Laser Melting, Procedia Eng. 174 (2017) 126–134. doi:10.1016/j.proeng.2017.01.179.

[100] G. Jacob, A. Donmez, J. Slotwinski, S. Moylan, Measurement of powder bed density in powder bed fusion additive manufacturing processes, Meas. Sci. Technol. 27 (2016) 115601. doi:10.1088/0957-0233/27/11/115601.

[101] J.S. Kallman, S. Depiero, S. Azevedo, Effects of Powder Morphology and Particle Size on CT Number Estimates, Report. (2014) 1–15. https://e-reports-ext.llnl.gov/pdf/768411.pdf.

[102] R.W. McVey, R.M. Melnychuk, J. a. Todd, R.P. Martukanitz, Absorption of laser irradiation in a porous powder layer, J. Laser Appl. 19 (2007) 214. doi:10.2351/1.2756854.

[103] S. Zhoum, Absorption of some powder materials to YAG laser, Sci. China. 44 (2001) 489–494. http://www.cnki.com.cn/Article/CJFDTotal-JAXG2001S1077.htm.

[104] S. Wu, I. Golosker, M. Leblanc, S. Mitchell, J. Stanley, G. Gallegos, Direct

Absorptivity Measurements of Metallic Powders Under 1-Micron Wavelength Laser Light, in: Proc. Solid Free. Fabr. Symp., 2014: pp. 1–18.

[105] A. Rubenchik, S. Wu, S. Mitchell, I. Golosker, M. LeBlanc, N. Peterson, Direct measurements of temperature-dependent laser absorptivity of metal powders, Appl. Opt. 54 (2015) 7230. doi:10.1364/AO.54.007230.

[106] M. Grasso, V. Laguzza, Q. Semeraro, B.M. Colosimo, In-Process Monitoring of Selective Laser Melting: Spatial Detection of Defects Via Image Data Analysis, J. Manuf. Sci. Eng. 139 (2016) 51001. doi:10.1115/1.4034715.

[107] J. Schilp, C. Seidel, H. Krauss, J. Weirather, Investigations on temperature fields during laser beam melting by means of process monitoring and multiscale process modelling, Adv. Mech. Eng. 2014 (2014). doi:10.1155/2014/217584.

[108] H. Krauss, T. Zeugner, M.F. Zaeh, Layerwise monitoring of the Selective Laser Melting process by thermography, Phys. Procedia. 56 (2014) 64–71. doi:10.1016/j.phpro.2014.08.097.

[109] S. Kleszczynski, J. zur Jacobsmuhlen, J.T. Sehrt, G. Witt, Error Detection in Laser Beam Melting Systems by High Resolution Imaging, in: Proc. Solid Free. Fabr. Symp., 2012: pp. 1–14.

[110] J. Jacobsmühlen, S. Kleszczynski, A. Ladewig, G. Witt, D. Merhof, In-Situ Surface Roughness Measurement of Laser Beam Melted Parts – a Feasibility Study of Layer Image Analysis, in: Fraunhofer Direct Digit. Manuf. Conf., Berlin, 2016: pp. 1–6. www.lfb.rwth-aachen.de/bibtexupload/pdf/JAC16b.pdf.

[111] J. zur Jacobsmuhlen, S. Kleszczynski, D. Schneider, G. Witt, High resolution imaging for inspection of laser beam melting systems, in: IEEE Int. Instrum. Meas. Technol. Conf., 2013: pp. 707–712. doi:10.1109/I2MTC.2013.6555507.

[112] M. Aminzadeh, A Machine Vision System for In-Situ Quality Inspection in Metal Powder-Bed Additive Manufacturin, Georgia Institute of Technology, 2016. https://smartech.gatech.edu/handle/1853/56291.

[113] U. Scipioni Bertoli, A.J. Wolfer, M.J. Matthews, J.P.R. Delplanque, J.M. Schoenung, On the limitations of Volumetric Energy Density as a design parameter for Selective Laser Melting, Mater. Des. 113 (2017) 331–340.

doi:10.1016/j.matdes.2016.10.037.

[114] B. Zhang, H. Liao, C. Coddet, Microstructure evolution and density behavior of CP Ti parts elaborated by Self-developed vacuum selective laser melting system, Appl. Surf. Sci. 279 (2013) 310–316. doi:10.1016/j.apsusc.2013.04.090.

[115] Y. Sato, M. Tsukamoto, S. Masuno, Y. Yamashita, K. Yamashita, D. Tanigawa, N. Abe, Investigation of the microstructure and surface morphology of a Ti6Al4V plate fabricated by vacuum selective laser melting, Appl. Phys. A Mater. Sci. Process. 122 (2016) 1–5. doi:10.1007/s00339-016-9996-8.

[116] T. Arata, Y., Abe, N., Oda, Fundamental phenomena in high power CO2 laser (Report II) – Vacuum laser welding, Trans. JWRI. 14 (1985) 17–22.

[117] S. Katayama, A. Yohei, M. Mizutani, Y. Kawahito, Development of deep penetration welding technology with high brightness laser under vacuum, Phys. Procedia. 12 (2011) 75–80. doi:10.1016/j.phpro.2011.03.010.

[118] R. Fabbro, K. Hirano, S. Pang, Analysis of the physical processes occurring during deep penetration laser welding under reduced pressure, J. Laser Appl. 28 (2016) 22427. doi:10.2351/1.4944002.

[119] R.F. and G.D. A. Verwaerde, Experimental study of continuous CO2-laser welding at subatmospheric pressures, J. Appl. Phys. 78 (1995) 2981–2984.

[120] N.M. and S.K. Y. Kawahito, K. Kinoshita, Visualization of refraction and attenuation of near-infrared laser beam due to laser-induced plume, J. Laser Appl. 21 (2009) 96–101.

[121] W.S.O. Rodden, S.S. Kudesia, D.P. Hand, J.D.C. Jones, Use of “assist” gas in the laser drilling of titanium, J. Laser Appl. 13 (2001) 204. doi:10.2351/1.1404415.

[122] M. Gieseke, C. Noelke, S. Kaierle, V. Wesling, H. Haferkamp, Selective Laser Melting of Magnesium and Magnesium Alloys, in: Magnes. Technol. 2013, Springer International Publishing, Cham, 2013: pp. 65–68. doi:10.1007/978-3-319-48150-0_11.

[123] X. Wang, N. Read, L.N. Carter, R.M. Ward, M.M. Attallah, Defect Formation and Its Mitigation in Selective Laser Melting of High J â€™ N L -Base Superalloys, in:

Superalloys 2016 13th Int. Symp., 2016: pp. 351–358. doi:\url{10.1002/9781119075646.ch38}.

[124] R.D. Edwards, M.A. Sinclair, T.J. Goldsack, K. Krushelnick, F.N. Beg, E.L. Clark, A.E. Dangor, Z. Najmudin, M. Tatarakis, B. Walton, M. Zepf, K.W.D. Ledingham, I. Spencer, P.A. Norreys, R.J. Clarke, R. Kodama, Y. Toyama, M. Tampo, Characterization of a gamma-ray source based on a laser-plasma accelerator with applications to radiography, Appl. Phys. Lett. 80 (2002) 2129–2131. doi:10.1063/1.1464221.

[125] A.M. Shaikh, C. Romesh, T.S. Kolage, A. Sharma, Flash X-ray Radiography with Phosphor Imaging Plate, E-Journal Nondestruct. Test. 20 (2015) 2–9.

[126] C.M. Brenner, S.R. Mirfayzi, D.R. Rusby, C. Armstrong, A. Alejo, L.A. Wilson, R. Clarke, H. Ahmed, N.M.H. Butler, D. Haddock, A. Higginson, A. McClymont, C. Murphy, M. Notley, P. Oliver, R. Allott, C. Hernandez-Gomez, S. Kar, P. McKenna, D. Neely, Laser-driven x-ray and neutron source development for industrial applications of plasma accelerators, Plasma Phys. Control. Fusion. 58 (2016) 14039. doi:10.1088/0741-3335/58/1/014039.

[127] Scaps, SCAPS: USC-2, (n.d.). http://www.scaps.com/index.php?id=26 (accessed April 16, 2018).

[128] Scaps, SCAPS: SAMLight, (n.d.). http://www.scaps.com/index.php?id=10 (accessed April 16, 2018).

[129] Ophir, Introduction to Camera-Based Profilers | Ophir Photonics, (n.d.). http://www.ophiropt.com/laser--measurement/beam-profilers/introduction-camera-based-profilers (accessed April 16, 2018).

[130] G.E.S. Gerald F. Marshall, Handbook of Optical and Laser Scanning, 2004.

[131] SPI Lasers, Industrial Laser Solutions Manufacturer | Fiber Laser Products | SPI Lasers, (n.d.). http://www.spilasers.com/ (accessed April 16, 2018).

[132] Coherent, PowerMax-Pro Sensor | Coherent, (n.d.). https://www.coherent.com/measurement-control/measurement/powermax-pro-sensor (accessed April 23, 2018).

[133] Renishaw PLC, SS 316L-0407 powder for additive manufacturing, 2001 (2001) 0–1.

[134] Raith, Nanopatterning with ELPHY MultiBeam, (n.d.). https://www.raith.com/products/elphy-multibeam.html (accessed April 23, 2018).

[135] C.K. Bassem, G.F. Gallegos, W.E. King, A. Sisto, Density of additively-manufactured , 316L SS parts using laser powder-bed fusion at powers up to 400 W, Int. J. Adv. Manuf. Technol. (2014) 65–78. doi:10.1007/s00170-014-5954-9.

[136] Slice3r, Slic3r - G-code generator for 3D printers, (n.d.). http://slic3r.org/ (accessed April 16, 2018).

[137] P. Bidare, I. Bitharas, R.M. Ward, M.M. Attallah, A.J. Moore, Fluid and particle dynamics in laser powder bed fusion, Acta Mater. 142 (2017) 107–120. doi:10.1016/j.actamat.2017.09.051.

[138] Photron, FASTCAM Mini UX100 – Photron, (n.d.). https://photron.com/mini-ux/ (accessed April 23, 2018).

[139] V. Beyer, S.W. Campbell, G.M. Ramsey, A.M. Galloway, A.J. Moore, N.A. McPherson, Systematic study of effect of cross-drafts and nozzle diameter on shield gas coverage in MIG welding, Sci. Technol. Weld. Join. 18 (2013) 652–660. doi:10.1179/1362171813Y.0000000143.

[140] G.S. Settles, Toepler's Schlieren Technique, in: Schlieren Shad. Tech., Springer Berlin Heidelberg, Berlin, Heidelberg, 2001: pp. 39–75. doi:10.1007/978-3-642-56640-0_3.

[141] R. Fabbro, S. Slimani, I. Doudet, F. Coste, F. Briand, Experimental study of the dynamical coupling between the induced vapour plume and the melt pool for Nd–Yag CW laser welding, J. Phys. D. Appl. Phys. 39 (2006) 394–400. doi:10.1088/0022-3727/39/2/023.

[142] P. Bidare, I. Bitharas, R.M. Ward, M.M. Attallah, A.J. Moore, Laser powder bed fusion at sub-atmospheric pressures, Int. J. Mach. Tools Manuf. 130–131 (2018) 65–72. doi:10.1016/j.ijmachtools.2018.03.007.

[143] S. Tammas-Williams, P.J. Withers, I. Todd, P.B. Prangnell, The Effectiveness of

Hot Isostatic Pressing for Closing Porosity in Titanium Parts Manufactured by Selective Electron Beam Melting, Metall. Mater. Trans. A. 47 (2016) 1939–1946. doi:10.1007/s11661-016-3429-3.

[144] C.S. Kim, Thermophysical properties of stainless steels, 1975.

[145] International Atomic Energy Agency (IAEA), Thermophysical properties of materials for nuclear engineering: A tutorial and collection of data, 2008.

[146] G. A. Bird, Molecular Gas Dynamics and the Direct Simulation of Gas Flows, Oxford University Press, Oxford, 1994.

[147] Y. Sato, M. Tsukamoto, Y. Yamashita, Surface morphology of Ti–6Al–4V plate fabricated by vacuum selective laser melting, Appl. Phys. B. 119 (2015) 545–549. doi:10.1007/s00340-015-6059-3.

[148] J.M. H. Ki, P.S. Mohanty, Modeling of laser keyhole welding: Part I. Mathematical modeling, numerical methodology, role of recoil pressure, multiple reflections, and free surface evolution, Metall. Mater. Trans. A. 33A (2002) 1817–1830.

[149] T. Debroy, H.L. Wei, J.S. Zuback, T. Mukherjee, J.W. Elmer, J.O. Milewski, A.M. Beese, A. Wilson-heid, A. De, W. Zhang, Additive manufacturing of metallic components – process, structure and properties, Prog. Mater. Sci. 92 (2017) 112–224. doi:10.1016/J.PMATSCI.2017.10.001.

[150] B. Zhang, L. Dembinski, C. Coddet, The study of the laser parameters and environment variables effect on mechanical properties of high compact parts elaborated by selective laser melting 316L powder, Mater. Sci. Eng. A. 584 (2013) 21–31. doi:10.1016/j.msea.2013.06.055.

[151] E. Panarella, Theory of laser-induced gas ionization, Found. Phys. 4 (1974) 227–259. doi:10.1007/BF00712689.

[152] W. Han, Computational and experimental investigations of laser drilling and welding for microelectronic packaging, Worcester Polytechnic Institute, 2004.

[153] C. G. Morgan, Laser-induced breakdown of gases, Reports Prog. Phys. 38 (1975) 621–665.